

Energy Yield and Electricity Management of Thin-Film and Crystalline Silicon Solar Cells: from Devices to Systems

THÈSE N° 6894 (2016)

PRÉSENTÉE LE 15 JANVIER 2016

À LA FACULTÉ DES SCIENCES ET TECHNIQUES DE L'INGÉNIEUR
LABORATOIRE DE PHOTOVOLTAÏQUE ET COUCHES MINCES ÉLECTRONIQUES
PROGRAMME DOCTORAL EN SCIENCE ET GÉNIE DES MATÉRIAUX

ÉCOLE POLYTECHNIQUE FÉDÉRALE DE LAUSANNE

POUR L'OBTENTION DU GRADE DE DOCTEUR ÈS SCIENCES

PAR

Yannick Samuel RIESEN

acceptée sur proposition du jury:

Prof. P. Murali, président du jury
Prof. C. Ballif, Dr N. Würsch, directeurs de thèse
Prof. R. Gottschalg, rapporteur
Dr A. Virtuani, rapporteur
Prof. M. K. Nazeeruddin, rapporteur



ÉCOLE POLYTECHNIQUE
FÉDÉRALE DE LAUSANNE

Suisse
2016

Résumé

La part d'énergie solaire effectivement utilisable dans le cas d'une intégration de masse du photovoltaïque (PV) dans le réseau électrique dépend de deux facteurs : le rendement énergétique du système ainsi que des pertes due à la gestion de cette énergie. Ce second facteur résulte du caractère volatile de l'énergie solaire et du besoin d'éviter les pics de production à midi qui peuvent déstabiliser le réseau électrique. L'objectif global de cette thèse est d'établir des lignes directrices pour maximiser l'énergie utilisable en quantifiant les différentes pertes en fonction des conditions d'exploitation au niveau de la cellule solaire et du système PV. Les cellules solaires sont habituellement optimisées pour des conditions standards de test (STC). Cependant, pendant leur fonctionnement, elles sont soumises à des conditions différentes. Notre but est donc d'étudier comment les matériaux et la conception d'une cellule solaire peuvent être optimisés pour des conditions de fonctionnement spécifiques. Nous avons particulièrement mis l'accent sur les cellules en couches minces de silicium car leur comportement n'est pas encore bien compris.

Pour cela, nous avons mesuré la dépendance en température des performances des cellules en couche mince en silicium amorphe (a -Si:H) et en silicium microcristallin (μc -Si:H) en fonction de leurs conditions de dépôt et de leur conception. Nous avons notamment observé qu'en variant l'épaisseur de la couche intrinsèque d'une cellule (a -Si:H), la cellule la plus efficace dans des conditions standard n'a pas forcément le meilleur rendement énergétique. Nous avons aussi trouvé une explication à la présence d'un maximum au facteur de remplissage (fill-factor, FF) en fonction de la température. Puis, nous avons étendu notre analyse à des cellules en couches minces à multi-jonctions, en silicium cristallin à hétérojonction et en silicium cristallin standard.

Pour les cellules en couches minces de silicium, le rendement énergétique est significativement influencé par les effets spectraux et les effets de dégradation/récupération des performances (dus à l'effet Staebler-Wronski). En se basant sur des mesures de dégradations/récupération à l'intérieur (en laboratoire) et à l'extérieur (en conditions réelles), nous avons démontré qu'il est difficile de décrire cet effet avec un modèle de diode pour cellule solaire. Cependant, un tel modèle avec un courant de recombinaison et avec une dépendance supplémentaire en température du courant de saturation et du facteur d'idéalité permet de reproduire les caractéristiques courant-tension d'une cellule solaire a -Si:H sur plusieurs ordres de grandeur d'illumination et pour des températures de 0 °C à 80 °C.

Au niveau du système, nous avons modélisé un système PV avec stockage local pour évaluer différentes stratégies visant à diminuer les pics d'injection (injection=production PV-

consommation électrique locale) néfastes pour le réseau et évaluer l'impact de ces mesures sur l'énergie utilisable. Dans ce cadre, nous avons développé un algorithme de contrôle simple pour la gestion d'une batterie qui permet de minimiser les pertes dues à une limite d'injection dans le réseau et de maximiser la consommation propre. Cet algorithme donne de bons résultats sans avoir besoin de prévision de production PV. Nous avons établi que le stockage thermique avec une pompe à chaleur ou un boiler est comparables, quant à son efficacité à diminuer les pics d'injection, au stockage électrique dans une batterie. En général, l'imposition d'une limite d'injection permet de significativement réduire les pics de production tout en induisant des pertes relativement petites. De plus, ces pertes peuvent être réduites massivement avec une batterie relativement petite. En variant l'orientation et l'inclinaison des modules solaires (par exemple orientation est-ouest au lieu de plein sud), les pertes dues à une limite d'injection peuvent aussi être réduites, tout comme la différence entre la production en été et en hiver qui peut diminuer d'un facteur de deux. Nous avons aussi développé une méthode statistique qui permet d'extraire l'utilisation des différents appareils électriques d'un ménage en se basant sur des mesures de la courbe de charge au quart d'heure et de quelques informations à propos de ce ménage. Grâce à ce modèle, nous avons déterminé qu'environ 8 % de la consommation électrique peut-être déplacée autour de midi, réduisant de ce fait les pics d'injections durant cette période. Finalement, en combinant les résultats de la partie cellule avec la méthodologie de la partie système, nous avons mis en évidence que la variation du type de technologie de cellule solaire (avec, entre autre, différentes dépendances en température) influent peu sur la réduction des pics d'injection, la consommation propre et les variations saisonnières de production en comparaison avec les autres influences (par exemple la limite d'injections ou la capacité de stockage de la batterie). Néanmoins ces variations ne sont pas négligeables.

Mots clefs : Photovoltaïque, couche mince en silicium amorphe, rendement énergétique, effet Staebler-Wronski, effets de température, intégration réseau électrique, stockage de l'électricité, flexibilisation de la consommation.

Abstract

In the case of high photovoltaic (PV) penetration into the electricity grid, the energy produced by a PV system that is effectively used (useful energy) depends on the energy yield and on how this energy is managed to avoid detrimental effects occurring at high PV injection, e.g. during the midday peak. The overall goal of this thesis is to provide guidelines for maximizing the useful energy of a PV system by quantifying losses incurred during operation at both the solar cell device and the system levels. Solar cells are usually optimized for the standard test conditions (STC). However, the conditions are generally different during operation. This work assesses how solar cell materials and designs can be optimized to maximize the energy yield for specific operating condition. We mainly focus on thin-film silicon solar cells because of their challenging metastable behavior.

The temperature dependence of the performance of thin-film amorphous silicon (a -Si:H) and microcrystalline silicon (μc -Si:H) solar cells is thus measured for different deposition parameters and cell designs. We observe that, by tuning the intrinsic layer thickness of a -Si:H cells, the cells with the best (STC) efficiency do not necessarily provide the highest energy output. We also explain the presence of a maximum in the value of the fill factor as a function of temperature. The temperature dependence study is then extended to thin-film silicon multi-junction, crystalline silicon heterojunction (SHJ) and other crystalline silicon solar cells. For thin-film silicon solar cells, spectral effects and degradation or recovery effects due to the metastable character of a -Si:H (due to the Staebler-Wronski effect) significantly impact the energy yield. Based on indoor and outdoor degradation/recovery experiments, we show that it is challenging to describe this metastability with a diode model. However, such a model with a current loss term and an additional temperature dependence for the saturation current and ideality factors accurately reproduces the current-voltage characteristics of a -Si:H solar cells over a wide range of irradiance levels and operating temperatures.

On the system level, we model a PV system with local storage to evaluate several strategies to reduce the detrimental midday injection peaks. The impact of such measures on the useful energy is also investigated. We develop a simple control algorithm that minimizes the losses due to a feed-in limit and maximizes self-consumption without the need of a production forecast. We show that heat storage using a boiler or a heat pump performs as well as battery storage. In general, a feed-in limit reduces significantly peak injection but only a relatively small storage capacity is needed to reduce losses (due to this limit). Changes in tilt and orientation of modules also reduce losses resulting from feed-in limits and shrink the winter/summer production ratio by more than a factor of two. We also develop a

statistical method that estimates – from loads measured every 15 min–when different electrical appliances in a household are commonly used. This model indicates that about 8 % of the total load could be shifted easily to the midday period, thereby reducing the midday injection peak. Finally, we combine device and system aspects to show that varying cell technology (e.g. with different temperature response) has a limited but not negligible impact on system output.

Key words: Photovoltaic, amorphous silicon, thin-film silicon solar cell, energy yield, Staebler-Wronski effect, temperature behavior, grid integration, electricity storage, demand side management.

Contents

Abstract	iii
List of figures	ix
List of tables	xiii
1 Introduction	1
1.1 Motivation	1
1.2 Photovoltaics	2
1.2.1 Basic principles of a silicon-based solar cell	2
1.2.2 PV-systems	4
1.2.3 PV integration into the electricity grid	5
1.3 Useful energy	6
1.3.1 Cell level	6
1.3.2 Module level	7
1.3.3 System level	8
1.4 Objectives	8
1.4.1 Structure of this thesis	8
1.4.2 Contribution of this thesis to the research field	10
2 Materials and measurements techniques	13
2.1 Solar cells	13
2.1.1 Amorphous silicon cells	13
2.1.2 Microcrystalline silicon cells	15
2.1.3 Multijunction silicon thin film solar cells	16
2.1.4 Hetero-junction solar cells	16
2.2 Measurements tools	17
2.2.1 Current-voltage characterisation	17
2.2.2 Solar simulators	18
2.2.3 External quantum efficiency (EQE) measurements	19
2.3 Light-soaking	19
2.4 Monitoring station	20

Contents

3	Diode equation for solar cells	23
3.1	Introduction	23
3.2	Basic equations	24
3.3	Diode models for amorphous silicon cells	25
3.4	Shunts	26
3.5	Amorphous silicon solar cell fitting with diode models	27
3.5.1	One-diode with current loss term	27
3.5.2	Temperature fitting of the one-diode model with current loss term	29
3.5.3	Temperature fitting of the 2 diode model with current loss term	32
3.6	Simulating multi-junction solar cells using diode equation based models	33
3.7	Conclusion	34
4	Temperature dependence of thin-film and crystalline silicon-based solar cells	35
4.1	Introduction	36
4.2	Amorphous Si cells temperature behavior	38
4.2.1	Experimental details	39
4.2.2	Results and discussion	41
4.3	Microcrystalline Si cells temperature behavior	53
4.3.1	Experimental details	53
4.3.2	Results and discussion	54
4.4	Multi-junction thin-film silicon cell temperature behavior	58
4.4.1	Experimental details	58
4.4.2	Results and discussion for micromorph cells	59
4.4.3	Results and discussion for the triple cells.	61
4.5	Temperature behavior of silicon heterojunction solar cells	62
4.5.1	Experimental details	62
4.5.2	Results and discussion	63
4.6	Temperature dependence of silicon-based solar cells	67
4.6.1	Temperature coefficient comparison	67
4.6.2	Impact on the energy yield of irradiance-dependence of the temperature coefficient	70
4.6.3	Temperature dependence over a large temperature range	72
4.7	Conclusion	73
5	Spectral dependence of micromorph solar cells	75
5.1	Introduction	75
5.2	Model	78
5.3	Results and discussion	79
5.3.1	Modeled spectrum	79
5.3.2	Energy output	80
5.4	Conclusion	81

6	Annealing and degradation of amorphous silicon solar cells	83
6.1	Introduction	84
6.1.1	Material level metastability	84
6.1.2	Module level metastability	86
6.1.3	Motivation and objectives	88
6.2	Indoor light-soaking and annealing	89
6.2.1	Experimental details	89
6.2.2	Results	89
6.3	Outdoor results	96
6.3.1	Small amorphous silicon cell monitoring	96
6.3.2	Micromorph minimodules	98
6.3.3	Micromorph and amorphous tandem module	100
6.4	Diode modeling	102
6.4.1	Description of the model	102
6.4.2	Before and after degradation fit	103
6.4.3	Model validation	104
6.5	Conclusion	105
7	Photovoltaic generation and the local electricity grid	107
7.1	Introduction	108
7.1.1	PV integration in the Swiss grid	109
7.1.2	PV integration in the local grid	111
7.2	Photovoltaic and storage for households	113
7.2.1	System configurations and description of the simulation	113
7.2.2	Control algorithms	116
7.2.3	Comparison of different electricity pricing scheme for peak-shaving	119
7.2.4	Comparison of the different control algorithms with feed-in limit	120
7.2.5	Loss analysis	124
7.2.6	Load shape sensitivity analysis	125
7.2.7	Household local storage compared to district storage	125
7.2.8	Variable feed-in limit	127
7.2.9	Electricity and heat storage comparison	128
7.3	Module orientation and peak shaving	130
7.3.1	Simulation details	130
7.3.2	Households level results	131
7.3.3	Swiss level results	132
7.4	Demand-side management potential for households	134
7.4.1	Methodology	135
7.4.2	Results	137
7.5	Solar cells influence on self-consumption, PV-loss and seasonal production	140
7.5.1	Simulation details	140
7.5.2	Results	141

Contents

7.6 Conclusion	143
8 Conclusion	147
8.1 Cell level	148
8.1.1 Temperature dependence	148
8.1.2 Spectral dependence	149
8.1.3 Annealing and degradation	149
8.2 System level	150
8.3 Outlook	151
A ASA simulation input parameters	153
B Activity and load classification	155
C Inverter efficiencies	157
Glossary	159
Bibliography	181
Acknowledgment/Remerciements	183
Curriculum Vitae	185

List of Figures

1.1	Swiss raw energy consumption	1
1.2	Swiss electricity production and module cost time evolution	3
1.3	Losses of a PV system	6
2.1	Amorphous cell schematic	14
2.2	ZnO Pyramids	15
2.3	Microcrystalline cell schematic	16
2.4	SHJ schematic	17
2.5	I(V) curve	18
2.6	Solar simulator spectra	19
2.7	Measurement block for light-soaking	20
2.8	Monitoring station	21
3.1	Equivalent circuit of a solar cell	25
3.2	IV parameters of a fit with the one-diode with current loss term	28
3.3	Simulated and modeled temperature behavior of the IV parameters	31
3.4	Fitted ideality factor and mobility lifetime product vs. T	32
3.5	Simulated and modeled temperature behavior IV parameters for a thicker cell	33
3.6	Micromorph diode circuit	34
4.1	I(V) parameters as a function of T for different <i>a</i> -Si:H materials	42
4.2	TC_{Voc} as a function of V_{oc} for <i>a</i> -Si:H cells	45
4.3	FF vs temperature and TC_{FF} vs FF for <i>a</i> -Si:H	46
4.4	Temperature of the $FF(T)$ maximum as a function of J_{sc} and $FF(T, J_{sc})$	47
4.5	I(V) curves of <i>a</i> -Si:H cells at different temperatures and irradianations	47
4.6	ASA modeled and measured <i>a</i> -Si:H cell	48
4.7	Temperature dependent band diagram	49
4.8	EQE of <i>a</i> -Si:H as a function of temperature	50
4.9	TC_{Jsc} as a function of FF for <i>a</i> -Si:H cells	50
4.10	FF and P_{mpp} of the reference <i>a</i> -Si:H cell	51
4.11	P_{mpp} as a function of temperature and intensity for <i>i-thick</i> . series	52
4.12	Simulated energy output for different <i>i</i> -layers thickness	52
4.13	IV parameters of μc -Si:H cell as a function of temperature	55
4.14	TC of different μc -Si:H cells	56

List of Figures

4.15	$TC_{V_{oc}}$ as a function of the V_{oc} of μc -Si:H cells	57
4.16	CMM results of I(V) parameters	59
4.17	TC and temperature behavior of a micromorph cell	60
4.18	Triple multijunction cell: FF and P_{mpp} and EQE	62
4.19	I(V) parameters as a function of temperature for SHJ solar cells	64
4.20	I(V) curve of SHJ vs temperature and efficiency vs T and G	65
4.21	Activation energy of SHJ barrier	66
4.22	$TC_{V_{oc}}$ as a function of V_{oc} of silicon-based solar cells	68
4.23	TC of silicon-based solar cells as a function of their J_{sc}	69
4.24	TC comparison and yearly irradiance histogram	71
4.25	V_{oc} and FF temperature dependence for silicon-based solar cells.	72
5.1	Spectra and EQE	77
5.2	Micromorph efficiency as a function of in plane irradiance	77
5.3	Spectrum influence model	79
5.4	EQE of a top and bottom limited micromorph cells	79
5.5	Contribution to energy yield of the different spectra	80
5.6	Monthly energy output for top and bottom limited micromorph cell	81
6.1	Relative variation as a function of irradiance and temperature	90
6.2	Light-soaking kinetics for 500h	91
6.3	Light-soaking kinetics for 20h	92
6.4	RV and log slope as a function of temperature and irradiance value	93
6.5	Light-soaking and annealing	95
6.6	Annealing kinetics for different temperature and irradiances	96
6.7	Time evolution of small a -Si:H solar cell outdoor monitored	98
6.8	FF of micromorph minimodules indoor measurements as function of mismatch and time	100
6.9	Micromorph minimodules outdoor measurements	101
6.10	Outdoor FF and P_{mpp} time dependence for micromorph and a -Si:H/ a -Si:H modules.	102
7.1	CH load and PV production for a week in May 2014	110
7.2	Excess PV as a function of PV coverage and monthly PV production and Swiss load for 2014	111
7.3	Schematic of the two different configurations of a of PV system with storage	114
7.4	Schematic of PV system with heat storage	114
7.5	Forecasted, measured and clear sky PV production	115
7.6	Schematic of minimize cost algorithm	117
7.7	Effect on SC of different el. pricing	120
7.8	PV-loss	121
7.9	PV-loss and self-consumption (SC) for a single household	122
7.10	Cashflow	123

7.11 Losses of the system	124
7.12 Mean PV loss and self consumption as a function of battery size	126
7.13 PV loss as a function of aggregation and grid flux	126
7.14 Histogram for a variable feed-in limit	128
7.15 Heat pump grid flux and water tank temperature	129
7.16 PV-loss as a function of the feed-in limit	129
7.17 Clear sky PV production for different module orientations	131
7.18 PV-loss and SC as a function of module orientation	132
7.19 Swiss PV excess as a function of tilt and azimuth share	133
7.20 Monthly PV production as a function of module tilt and azimuth	134
7.21 Schematic of the appliance recognition methodology	136
7.22 Measured and synthetic load	137
7.23 Load repartition	138
7.24 Monthly electric devices use	139
C.1 Inverter and converter efficiency	157

List of Tables

3.1	Diode parameter: one-diode with current loss	29
4.1	Summary of the temperature coefficients and I(V) parameters	43
4.2	Power at STC (Wp) and estimation of yearly energy output for the <i>i-thick</i> series.	53
4.3	Activation energies of the s-shape and T_{FFmax}	66
4.4	I(V) parameters of the different silicon-based solar cells.	68
4.5	TC_{Pmpp} at STC from highest to lowest	70
4.6	Modeled yearly energy output using different methods to simulate temperature dependence	72
5.1	Energy output simulation of spectral effects	80
6.1	IV results of indoor measurements of the <i>a</i> -Si:H/ <i>a</i> -Si:H module	101
6.2	Diode fit for initial and degraded state	104
7.1	<i>PV-loss</i> , <i>SC</i> and cash-flow for comparison between disseminated and centralized storage.	127
7.2	Relative <i>PV-loss</i> with as a function of storage type and feed-in limit	130
7.3	Efficiency, TC_{Pmpp} , optimized inverter sizes and inverter losses as a function of module technology	141
7.4	<i>SC</i> , <i>PV-loss</i> and P_{nom} as a function of module technology	142
7.5	Winter/summer production ratio as a function of module technology	143

1 Introduction

1.1 Motivation

Since the 20th century, world energy consumption has been increasing continuously. In Switzerland, the raw (primary) energy consumption increased by a factor of 10 from 1940 to 2013 (see Fig. 1.1 left) [OFEN 15]. Today, the highest energy vectors are based on fossil fuels. In Switzerland 2014, 36 % of the total raw energy was used for motor fuel, 25 % for electricity and 15 % for heating oil. Note that in Fig. 1.1 left, the "gray energy" caused by the manufacturing of imported goods is not taken into account. This significant energy demand causes high carbon dioxide (CO₂) emissions which are a main cause for climate change. Figure 1.1 right shows the global temperature increase from the mid-19th century to 2014 [Clim 15, Broh 06]. This change is summarized by the Intergovernmental Panel on Climate Change (IPCC) as "*Climate change will amplify existing risks and create new risks for natural and human systems. Risks are unevenly distributed and are generally greater for disadvantaged people and communities in countries at all levels of development*" [Pach 14].

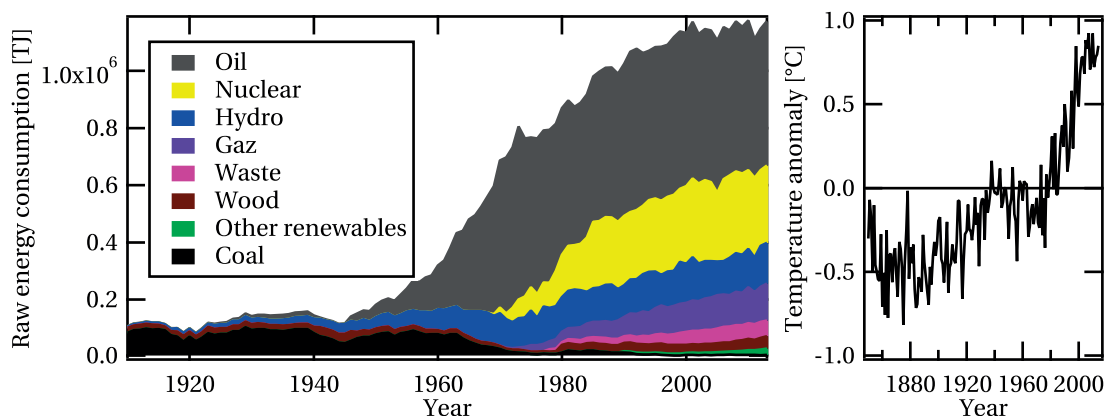


Figure 1.1 – (Left) Swiss primary (raw) energy consumption from 1910 to 2013 [OFEN 15] (Right) Global temperature increase [Clim 15, Broh 06]

Hence we need to move to energy sources with low carbon emissions. Moreover, in Switzerland, the Energy Strategy 2050 decided by the Federal Council [Mess 13] envisions the withdrawal of all Swiss nuclear power plants at the end of their lifetime. Therefore about 40 % of Swiss electricity generation must be replaced, preferably with renewable energy sources.

In one and a half hours the Earth receives more solar energy than the worldwide energy consumption of 2001 [Tsao 06]. Part of this energy can be converted directly into electricity with photovoltaic (PV) installations. Due to its decreased price and relatively low CO₂ emission (15-50 grams CO₂ equivalent per kilowatt hour (kWh), produced mostly during manufacturing [Wild 13, Nuge 14]), PV power is a promising technology that is beginning to play a major role in supplying energy. Regarding the total Swiss energy consumption, PV energy could in the future replace a part of the energy that is used to produce electricity (replace nuclear power generation), a part of the oil used for heating through heat pumps, and even a part of the combustible energy used for motor fuel through rechargeable electric or hydrogen-powered vehicles.

Research institutes and industry are working hard to improve the solar cells efficiency, and thus reduce the cost, of PV modules. Thanks to those efforts, module prices have decreased considerably during the last decade. Since the fabrication of the first PV module, the cost followed an exponential learning curve shown at the right in Fig. 1.2, which shows module cost as a function of cumulative module shipments. Nowadays, in sunny area the cost of utility-scale solar dropped to prices around 0.05 \$/kWh in the U.S or in Dubai [Boli 15]. In Dubai this energy cost is even lower than the current local gas price [Park 15] reaching wholesale grid parity. Those prices makes only sense if the electricity can be used when it is produced. Moreover, in much more countries retail grid parity¹ has already been reached [Brey 13].

Hence, PV will certainly play an important role in worldwide electricity generation. Every year more and more PV power is installed throughout the world, which has led to a global capacity of more than 150 GW (status 2014) [Phil 14]. The International Energy Agency regularly updates its PV capacity roadmap: *e.g.* in 2010 900 GW were predicted for 2030, and four years later, in 2014, this forecast was increased to 1720 GW [Fran 10, Phil 14]. To illustrate this PV capacity expansion, the left of Fig. 1.2 shows the evolution of the yearly Swiss PV energy production, which reached a value of over 1.2 % of the total Swiss electricity production in 2014.

1.2 Photovoltaics

1.2.1 Basic principles of a silicon-based solar cell

A semiconductor such as silicon is a material whose electrical conductivity is lower than that of a conductor (*e.g.* copper) but higher than that of an insulator (*e.g.* glass). This low conductivity is explained by a band of energy levels called the band gap that are forbidden for electrons

¹Retail grid parity is reached when the LCOE (levelized cost of electricity) of PV power is equal or lower to the electricity price paid by the end customer.

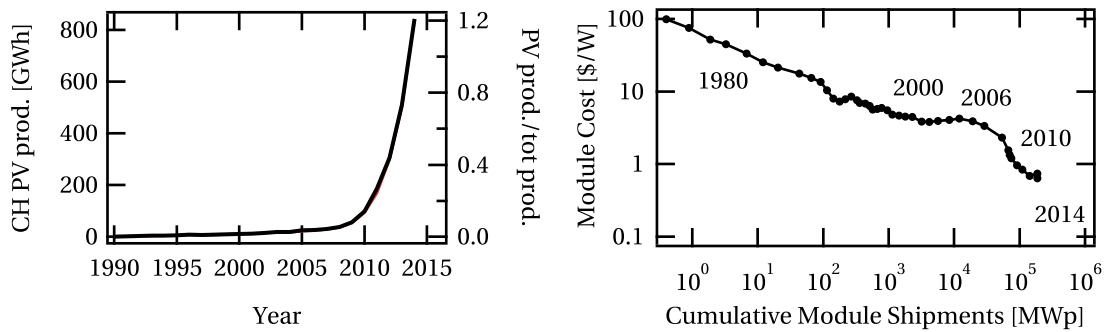


Figure 1.2 – (Left) Evolution of the Swiss PV electricity production in GWh relative to the total Swiss electricity production [OFEN 15]. (Right) Global module cost evolution as a function of cumulative module shipments for *c*-Si cells [Metz 15].

and holes and the fact that the Fermi-level is within this forbidden energy region. The band below this gap is called the valence band (VB) and the band above is called the conduction band (CB). At 0°K in equilibrium the electrons are immobilized in the VB and therefore no conduction is possible. If the electrons are excited across the band gap to the CB they are able to move in the corresponding conduction states. The same is true for positive-charged holes left behind which can move in the VB (allowing conduction). The electrons can *e.g.* be excited from the VB to CB by photons with higher energy than the band gap.

A working solar cell relies on an absorber such as *e.g.* a semiconductor. There the incoming light (photon) excites electrons into the CB and a hole is generated in the VB. These so-called electron-hole pairs have to be separated and the carriers extracted from the cells. This process is induced with carrier-selective contacts that attract or repel the other carrier type. For example, for standard silicon-based solar cells, the *pn* junction generates these selective contacts². Note that this junction is not necessary for a functioning solar cell [Wurf 15, Geis 15]. If there are defects in the material, the electron can recombine with a hole and hence both carriers are lost. They do not contribute to the power generation and the cell conversion efficiency is reduced. If the electron- and hole-collecting sides of a solar cell are connected forming an electrical circuit, this charge separation induces a potential that drives a current (the electrons leave the circuit on one side and at the same time on the other side an electron enters the device recombining with a hole). This current and potential can then be used to power electrical devices.

Several types of PV technologies exist on the global market. In 2014, 55 % of the total produced solar modules were multi-crystalline silicon, 36 % mono-*c*-Si, 4 % cadmium-telluride (CdTe), 3.6 % CIGS and 1.7 % were thin-film silicon-based [Burg 15].

Thin-film silicon solar cells are based on amorphous silicon (*a*-Si:H) or microcrystalline silicon (μ c-Si:H). Their name reflects the fact that their absorber layer are thinner (0.2 μ m to 2 μ m)

²A *pn* junction is created if we stack a *p*-doped semiconductor with an *n*-doped semiconductor.

than *c*-Si solar cells (100 μm to 300 μm). *a*-Si:H and μc -Si:H exhibit a larger number of defects (higher defect density) leading to enhanced recombination and hence to a reduction of the cell efficiency. Moreover, if they are *p*- or *n*-doped, the defect density increases considerably which makes these materials not usable as an absorber in a PV cell due to too low carrier lifetime. Therefore an intrinsic layer (*i*-layer) with a lower defect density than doped layers is used as the absorber, surrounded by thin *p*- and *n*-layers. This structure is called a *p-i-n* configuration (or superstrate configuration) when the *p*-layer is the first to be deposited and *n-i-p* configuration (or substrate configuration) when the *n*-layer is deposited first. Note that light is usually entering the device from the *p*-side to improve hole collection and as a consequence cell efficiency. Such cells can be stacked to form multi-junction cells, as for example micromorph cells constituted by an *a*-Si:H top cell and a μc -Si:H bottom cell. Multi-junction cells have higher efficiencies as they can use the solar spectrum more efficiently. Compared to other technologies, thin-film silicon photovoltaic (TF-Si) technologies deposited by plasma-enhanced chemical vapor deposition (PECVD) show certain advantages: (1) potential for cost reduction, (2) short energy pay-back time³ [Wild 13], (3) large availability of the main materials (silicon, zinc oxide) and (4) suited for building integrated photovoltaic due to a favorable temperature behavior and visually pleasing integration. Moreover, concerning their energy yield (see Sec. 1.3), depending on location thin-film silicon modules have a better performance ratio than crystalline cells⁴. However conversion efficiencies are rather low compared to other technologies. Presently, the best silicon thin-film cells surpassed 13.6% stable efficiency [Sai 15]. This technology is also one of the most challenging in terms of energy yield modeling due to the presence of spectral effects and metastable effects that change the efficiency of the cell during operation. In this thesis special attention will therefore be given to this technology.

Recently, due to the significant decline of the price for *c*-Si solar cells and reduced fraction of the cell cost in the total system cost, thin-film silicon cells are losing market share. We hence also considered other technologies in part of chapter 4.

1.2.2 PV-systems

In order to warrant lifetimes of over 25 years, solar cells have to be protected against humidity, mechanical impacts and dirt. Generally this is achieved by encapsulating the cells with glass on the front side and a back-sheet or also glass at the back side. Between the glass and the cell, an encapsulant is added to allow adhesion of the two components. If more than one module is installed, they can be connected in series or in parallel to reach the desired voltage and current. The output of PV modules is a direct current (DC). The PV modules are connected to a DC/AC (alternating current) inverter or a DC/DC converter depending on the needed output and system configuration. Those converters generally include a maximum power point

³Payback time is the time that is needed by a system to produce the energy that was used for its manufacturing

⁴The performance ratio is the ratio of how a module/system is performing in a given time interval under real operating conditions compared to how it would perform if the efficiency would always have the same constant value as at STC.

tracker, keeping the module at its ideal working point, to maximize the generated power. PV systems are divided into two categories:

- *Grid-connected installations*, in which the inverter is connected to the electricity grid and the power that is not directly used locally is injected into the grid. Today this represents the majority of installed systems.
- *Stand-alone installations* are not connected to the grid and the power that cannot be directly used is either stored in a battery or lost. This type of installation is generally found where no electricity grid is available as e.g. in rural regions in developing countries, huts in the mountains or solar-powered airplanes.

1.2.3 PV integration into the electricity grid

PV is an intermittent power source. The only control we have is the possibility to limit its output. With high penetration of PV into the grid, the midday peak production occurring during sunny days that cannot be consumed locally can have detrimental effects on the stability of the grid. For example, over-voltages in the electricity lines or overheating transformers could occur due to high injection of PV power [Denh 07, Umla 12, Buch 13b]. There are several ways to mitigate this midday peak (peak-shaving). For example:

- *Local storage with battery*. A part of the midday production is stored in a battery to reduce the injection peak. This energy is then used to supply electricity in the evening and at night when there is no PV production [Riff 11, Schm 10].
- *Module orientation variations*. Usually, PV modules are, if possible, south oriented to maximize yearly PV production. However, if modules are east-west oriented, more modules need to be installed to reach the same energy yield but the midday production peak will be reduced. Varying the tilt and orientation of modules also reduces the discrepancy between the high summer and low winter PV production.
- *Demand-side management*. A part of the electricity consumption could be shifted to the high PV production period. As the power is consumed locally, the injection peaks diminish.

Moreover these solutions increase local consumption of the PV power thereby reducing grid-related losses and mitigate instability. There are several ways to encourage PV system owners to use these solutions, for example by introducing a maximum feed-in limit. This means that if the excess power (produced PV power minus the local electricity consumption – including battery charging) is higher than the feed-in limit (injection is higher than the feed-in limit) this power has to be curtailed and is lost. PV system owners are then pushed to implement schemes to minimize energy losses.

1.3 Useful energy

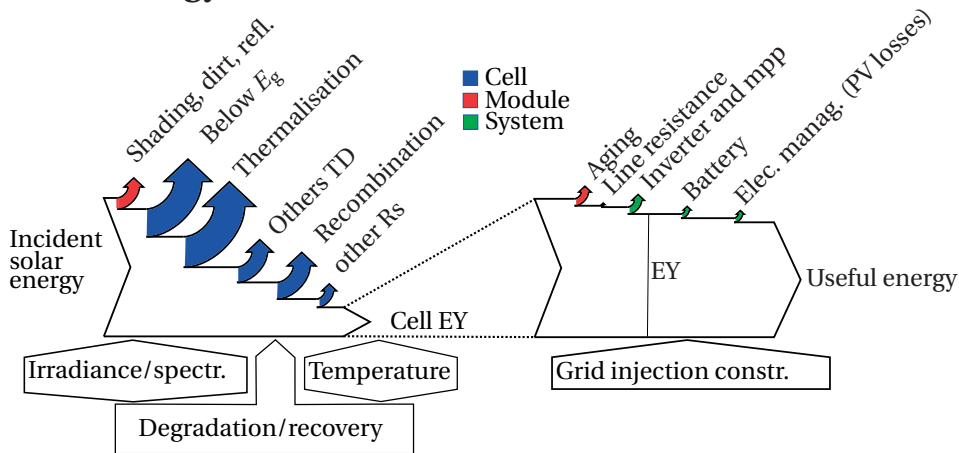


Figure 1.3 – Schematic of losses during conversion of solar energy into useful electricity energy.

The conversion of solar energy into electricity implies several losses at cell, module and system level which depend on operating conditions (see Fig. 1.3). We define the useful energy as the solar energy that can be effectively used. It is the energy yield minus the losses induced by the electricity management which is needed at high PV penetration (*e.g.* due to feed-in limit or storage). The energy yield⁵ is defined as the total amount of energy generated by a PV module divided by the installed power capacity (in kWh/W_p) during a period (generally one year) at a specific location for given installation conditions (*e.g.* inclination, orientation and thermal properties of the setup). It can also be defined as the total incoming solar energy minus the cell, module and for instance DC/AC inverter losses divided by the installed power capacity.

1.3.1 Cell level

PV modules are rated by their efficiency in standard test conditions (STC: 1000 W m⁻², AM1.5g spectrum, 25 °C). However, it is not the PV installation efficiency but its generated energy output or energy yield⁶ that matters for end users. The energy yield is always bound to the local operating conditions: the local climate and the installation characteristics of the modules. To calculate a financial yield, users need to "buy" energy (kWh) and not power (W). Modules with the same efficiency will not produce the same amount of energy in the Sahara desert and in continental Europe.

As PV modules are rated by their efficiency at STC, cells have so far been optimized for this condition. However, real operating conditions are almost never at STC. For example module temperatures easily reach 60 °C and hotter under full sun illumination, even in temperate climate zones like Switzerland. PV modules should be optimized for a specific climate and operating conditions. Such optimized designs can increase electricity production and hence

⁵Generally defined as the energy production measured after the DC/AC inverter divided by the installed capacity. However in this thesis we also sometimes use the energy yield for a cell or module.

⁶Energy yield = $\frac{\text{energy output}}{\text{installed capacity}}$

contribute to the development of renewable electricity generation. Moreover, high PV penetration in electricity grids will require smart energy management because of the intermittency of this type of power. Thus electricity storage solutions and precise power and energy yield predictions will be essential for grid managers.

Several parameters related to operating conditions (as location and orientation) influence the output power and hence the energy yield. For silicon-based PV systems these are (on the cell level):

- The operating temperature of a cell. During outdoor operation, cells undergo large temperature variations (*e.g.* from -10°C to 80°C). Since solar modules lose generally 0.2 % (for amorphous silicon cells) to 0.5 % (for multi-crystalline silicon cells) relative efficiency per $^{\circ}\text{C}$, temperature considerably affects cells performance.
- The intensity of the incoming irradiance.
- The spectrum of the incoming light. The sun's irradiation spectrum varies as a function of the sun's position, the meteorological conditions and the albedo. The spectral effects on cell's performance are dependent on its spectral response. *a*-Si:H and multi-junction cells are significantly affected by spectral variations.
- Degradation and recovery effects. During solar cell operation, the electronic properties of thin-film silicon and especially *a*-Si:H-layers degrade due to illumination. This light-induced degradation of the material is known as the Staebler-Wronski effect (SWE) [Stae 77]. This degradation depends mainly on illumination intensity and temperature. However, it can be partially recovered with increased temperature (annealing effect). Degradation and recovery of a cell or module will thus depend on its operating history.

In this work on cell level, the recombination losses dependence on operating conditions plays the most important role (see Fig. 1.3).

1.3.2 Module level

Different parameters influence the energy yield of a module. These include:

- Soiling and shadowing losses.
- Optical losses from the front glass.
- Current or operating condition mismatch between the cells of a module (the total module current is always limited by the weakest cell).
- Physiologic and degradation mechanisms such as adhesion failure, junction box separation, encapsulant browning, corrosion of the metal lines and cell cracking [DeGr 10, Jord 13, Duml 06].

1.3.3 System level

To calculate the energy that will effectively be available to the end-user (useful energy), the system losses, *e.g.* inverter and cable losses, also have to be taken into account. Moreover, feed-in limit regulations, storage solutions or different module orientations and tilt configurations (see Sec. 1.2.3) significantly affect the useful energy of systems by inducing additional losses.

1.4 Objectives

The main objective of this thesis is to provide guidelines for maximizing the useful energy of a PV system by quantifying losses incurred during operation at both the solar cell device and the system levels. Publications discussing energy yield from a materials perspective are relatively rare. Most models that describe energy yield contain parameters without any link to actual material properties. On the other hand, many papers link material parameters to solar cell efficiency, but not to energy yield. The aim of this work is to fill this gap. We will first focus on the cell level, taking into account the three main operating parameters affecting energy yield. Our objectives are to:

- Evaluate spectral effects on micromorph modules using a diode-based model.
- Understand the temperature dependence of *a*-Si:H and μc -Si:H as a function of their material properties and its impact on energy yield. Building on this knowledge, to understand the temperature dependence on the performance of thin-film silicon multi-junction solar cells. And then compare the temperature behavior of thin-film silicon solar cells to silicon heterojunction and other silicon-based solar cells.
- Provide a better understanding of the way the SWE influences cell performance and develop and test a model for the SWE linked to material properties.

On the system level, our main objective is to quantify how storage and corresponding control management, module orientation configurations and demand-side management can support the grid in the case of high PV penetration and to identify the additional losses that affect the useful energy. We limit the scope mainly to households. Finally, we combine cell level and system level results to quantify the impact of different solar cells technology on those additional losses.

Note that the effects of module parameters on energy yield were not considered in this thesis.

1.4.1 Structure of this thesis

This thesis is organized as follows.

In chapter 2, we describe the different solar cells and measurement tools, as well as the

simulation program, used in this thesis. A description of the cell simulation program used is also included.

In chapter 3, the diode equations that are used for represent current as a function of voltage $I(V)$ behavior of solar cells are reviewed with focus on a -Si:H solar cells. A fitting methodology is then described and the models are evaluated in function of their ability to fit the $I(V)$ curves. The temperature dependence of the diode fitting parameter is investigated resulting in the proposal of an extension of an existing diode model which takes into account the temperature dependence of a -Si:H solar cells.

In chapter 5, the spectral effects of a micromorph multi-junction cell are quantified by modeling for the case of Bern in Switzerland.

In chapter 4, the temperature dependence of the performance of silicon-based solar cells is investigated. First, the mechanism behind the temperature effects on a -Si:H solar cells is investigated by experiment and simulation. The influence of material parameters and cell designs on the temperature behavior is determined as well. A similar approach is followed for μc -Si:H solar cells. Next, the temperature dependence of micromorph and triple-junction cells (a -Si:H/ μc -Si:H/ μc -Si:H) is also analyzed. Then, we extend the discussion to the temperature behavior of silicon heterojunction cells which shows some similarity with thin-film silicon devices. Last, we compare our results with the temperature dependence of the performance of other silicon-based solar cells.

Chapter 6 is dedicated to the SWE effect in a -Si:H-based thin-film silicon solar cells. The results of indoor light-soaking experiments performed at different irradiances and temperatures are presented. Then the results of outdoor monitoring of a -Si:H cells, micromorph and a -Si:H/ a -Si:H tandem modules are reported. Finally, a diode-based model for the SWE is discussed.

We move then from a device perspective to a system perspective in chapter 7. We investigate several measures that could support the grid in the case of high PV penetration and evaluate the corresponding expected losses for the useful energy of the whole system. This chapter is divided into three parts:

1. *Local storage*: we programmed a MATLAB simulation to model a grid-connected PV-system with local storage. With this tool we quantify how such systems can support the grid and the losses depending on different control algorithms for the battery. Moreover we compare heat storage and battery storage, the effect of aggregating loads and the influence of PV production forecast errors on the performance of such systems.
2. *Module orientation*: we investigate the losses and peak shaving ability on a local and national level (in Switzerland) as a function of module orientation.
3. *Demand-side management*: we describe a method that allows us to statistically extract the time use for electrical appliances from a 15-minute-time-step load curve. With this

method we estimate the potential of load shifting for a sample of hundred households with individually measured load curves.

4. *Device and system*: we combine the device and system parts to quantify the effects of different solar cells dependence on temperature and irradiance on self-consumption, losses due to feed-in limit and seasonal production ratio.

1.4.2 Contribution of this thesis to the research field

The main contributions of this thesis to the PV field are:

- We improve the one-diode model with a recombination term [Mert 98b] to be able to describe the temperature behavior of *a*-Si:H solar cells.
- By modeling and measurement results we provide a better and comprehensive understanding of the different mechanisms influencing the temperature dependence of thin-film silicon solar cells.
- By studying how different material properties (controlled by different PECVD conditions during cell fabrication) and cell designs influence the *a*-Si:H cell temperature response, we provide guidelines to optimize cell performance for specific operating temperatures. This should benefit cell design with the best energy yield for specific climate conditions.
- We demonstrate the more favorable temperature coefficient of silicon heterojunction cells compared to other silicon-based technologies.
- We show that the SWE cannot be easily modeled with the one-diode model with a recombination term.
- We examine how the SWE influences *a*-Si:H solar cell performance as a function of temperature and irradiance conditions during light-soaking. This opens the way for developing a more precise model for *a*-Si:H cell performance.
- We show that our simple control algorithm for battery management in the presence of a feed-in limit using no PV production forecast performs as well as an algorithm with forecasts.
- We develop a method for estimating the part of electrical consumption that can be shifted to midday. This tool can help to estimate how PV penetration can be enhanced by demand-side management for households.
- We quantified the influence of different solar cell technologies on the system ability to reduce PV injection peaks.

Finally, this work led to one peer-reviewed publication [Ries 15], one conference proceedings as first author [Ries 13] with and oral presentation and various contribution as co-author [Stuc 12, Stuc 14b, Stuc 14a, Fran 12a, Fran 12b, Wyr 11, Wyr 13b, Wyr 13a, Wyr 15a, Wyr 15b]. Moreover three more publications based on this work are in preparation [Ries 16c, Ries 16a, Ries 16b].

2 Materials and measurements techniques

In this chapter we introduce the main solar cell types and measurement techniques used in this thesis.

2.1 Solar cells

2.1.1 Amorphous silicon cells

This paragraph relies mainly on those two references [Shah 09, Stuc 14c] which contain extensive information on amorphous silicon cells. Hydrogenated amorphous silicon (a -Si:H) is a class of thin-film silicon materials. In contrast to highly ordered crystalline silicon material where each silicon atom is bonded to four other silicon atoms forming a diamond cubic structure amorphous silicon a -Si:H is a disordered semiconductor. It still possess a short-range order (the nearest atomic neighbors are almost placed as in c -Si) this is why many physical properties (*e.g.* the presence of a band gap) are similar to those of c -Si. However over longer distances the deviation in bond angles and bond lengths becomes very large inducing defects in the structure in the form of missing bonds called dangling bonds. These dangling bonds result in electronic state that lies near the mid-gap and act as recombination center. Adding hydrogen during deposition passivates these dangling bonds, reducing recombination and enabling the use of hydrogenated amorphous silicon for solar cells. For simplification will call this material amorphous silicon.

a -Si:H is a metastable material as the defect density increases with illumination and can be recovered by thermal annealing (Staebler-Wronski effect [Stae 77] see Sec. 6). Compared to c -Si (1.12 eV), a -Si:H has a higher bandgap (1.7 eV) and band tails caused by the disorder in the lattice induced by different bonding angles, incorporated hydrogen and vacancies [Smet 12]. Moreover a -Si:H material has a higher absorption at photon energies higher than the band gap than c -Si due to the relaxation of the selection rules for optical transition (due to the disorder). This allows for much thinner a -Si:H layers than c -Si in solar cells.

Chapter 2. Materials and measurements techniques

The cell design of the *a*-Si:H solar cells used in this thesis is showed in Fig. 2.1. They were deposited in the *p-i-n* (superstrate) configuration. We enumerate the process steps of such a cell:

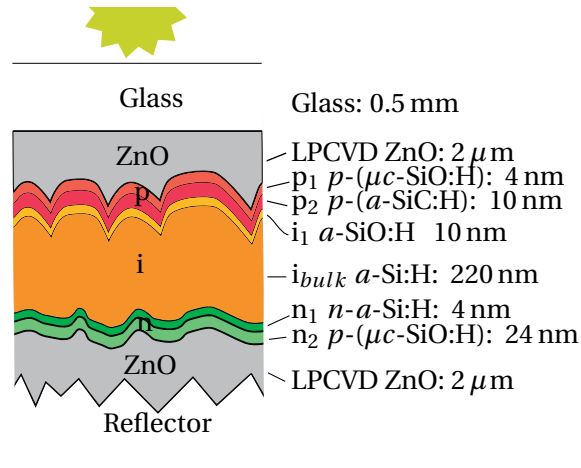


Figure 2.1 – Schematic of an amorphous silicon solar cell stack used as top cell for an micro-morph solar cell.

1. The cells are deposited on a 0.5-mm-thick Schott AF 32 glass substrates.
2. The first layer is a transparent conductive oxide (TCO) is a 2.3- μm -thick boron doped Zinc oxide (ZnO:B) deposited by low pressure chemical vapor deposition (LP-CVD).
3. The doped and active layers are all deposited by plasma-enhanced chemical vapor deposition (PE-CVD). They comprise:
 - (a) A *p*-type microcrystalline silicon-oxide layer (*p*-(μc -SiO:H)) for a good electrical contact with ZnO.
 - (b) A wide-bandgap *p*-type *a*-SiC:H layer for a strong electric field with generally a thickness of about 10 nm.
 - (c) An undoped wide-bandgap *a*-SiO:H buffer layer is deposited (PE-CVD) at the interface between the *p*- and the intrinsic (*i*-) *a*-Si:H layer.
 - (d) An *i*-*a*-Si:H layer as absorber layer.
 - (e) A *n*-type *a*-Si:H layer for the electrical field
 - (f) A *n*-type μc -SiO:H layer for a good contact with the next layer.
4. An another 2.3- μm -thick boron doped Zinc oxide TCO

The cell are then structured by a lift-off technique to an nominal cell area of 25 mm². Further details about the PE-CVD system, the deposition parameters, and substrates can be found elsewhere [Stuc 13, Stuc 14b, Stuc 14c].

2.1.2 Microcrystalline silicon cells

Microcrystalline silicon (μc -Si:H) also referred as nanocrystalline silicon is made of small crystalline grains embedded in an amorphous matrix [Vall 00]. The Raman crystallinity factor which quantifies the crystalline fraction of μc -Si:H is an important parameter of characterization. This fraction yields a value of about 50 % to 70 % for best efficiency cells [Droz 04]. A high crystallinity allows for a higher current of the solar cell however it decreases its V_{oc} [Hann 14]. The band-gap of this material is equivalent to the band-gap of c -Si (1.12 eV).

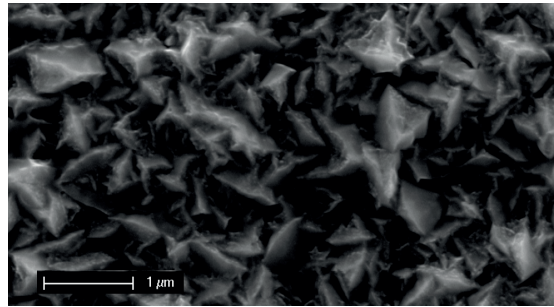


Figure 2.2 – Scanning electron microscope image of a rough ZnO TCO with pyramids

As for a -Si:H cells LP-CVD ZnO is used as TCO for the front electrode. This TCO layer is deposited such as to have a pyramidal surface morphology increasing light trapping into the device (Fig. 2.2). The more light is trapped in the device the higher will be the photogenerated current and hence the conversion efficiency of the cell. Usually we use a 5- μm -thick ZnO layer (called internally in the PVLAB as Z5). Its roughness can be tuned by varying the argon (Ar) plasma treatment time after deposition [Ding 13]. Due to the indirect bandgap of μc -Si:H the surface roughness of the front electrode ZnO plays an even more important role than for a -Si:H solar cells. The rougher the electrode, the more porous zones in the μc -Si:H layers (also known as cracks) are appearing at the bottom of the valley of the pyramids [Pyth 08]. This porous zone reduces diode properties affecting mainly the V_{oc} value of a solar cell. Usually, a 20 minutes Ar treatment time of the TCO still results in a rough substrate, while a 45 minutes treatment time leads to a smoother substrate.

Figure 2.3 shows a scanning electron microscope (SEM) image with a superposed electron-beam induced current (EBIC) image and the schematic of the standard μc -Si:H solar cell used in this thesis. The fabrication of such a cell is very similar to a -Si:H. It is basically the deposition condition during PE-CVD that are changed in order to obtain μc -Si:H material. We first deposit the ZnO front electrode, followed by the different doped and intrinsic active layers deposited by PE-CVD: a p -(μc -SiO:H) layer (about 10 nm) is sometimes followed by a very thin SiO_x layer to reduce the effect of porous zones. Then the i - μc -Si:H layer is deposited. This layer is generally thicker than the i -layer of a standard a -Si:H cell because of lower absorption. Finally a n -type μc -SiO:H layer is deposited. To passivate the interface, this layer can be replaced by i - a -Si:H/ n - a -Si:H/ n - μc -Si:H layers (see Sec. 4.3). More information on these cells can be found in [Hann 14, Ding 13, Bugn 13].

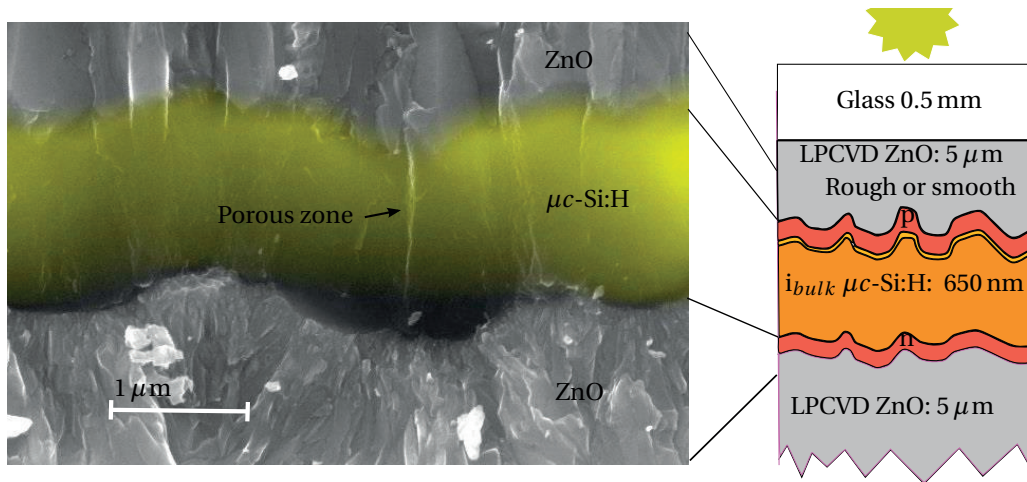


Figure 2.3 – (Left) SEM image superposed with an electron-beam induced current (EBIC) image (yellow) of a μc -Si:H solar cell. The stronger the yellow the higher the induced current. We can observe the increased collection at the p side (top of the cell). (Right) schematic of a μc -Si:H solar cell stack.

2.1.3 Multijunction silicon thin film solar cells

The efficiency of thin-film silicon technologies can be increased by stacking two or more cells together. Those device are known as tandem or triple junction cells. A widely use structure is the micromorph (or hybrid) thin-film silicon cell [Meie 94]. This cell is composed of an a -Si:H top cell and an μc -Si:H bottom cell. Due to its high band-gap, the top cell absorbs the blue part of the sun spectrum with relatively small thermal relaxation losses. The μc -Si:H bottom cell with lower band-gap absorbs the infrared light for which the top cell is transparent. Because of this better use of the solar spectrum than with a single junction cell, the efficiency can be increased. As both cells are connected in series the current of the two sub-cells should be matched in order to maximize the efficiency of the whole cell (otherwise the current of the total cell is limited by the sub-cell with less generated current). Triple (a -Si:H/ μc -Si:H/ μc -Si:H) junction cells will also be studied in this thesis; they could allow for an even higher efficiency than for micromorph cells.

2.1.4 Hetero-junction solar cells

Generally in homojunction c -Si solar cells a part of the efficiency losses are due to carrier recombination at the absorber/metal contact. Those recombination losses can be reduced by passivating the surface of the absorber with a few nanometer intrinsic a -Si:H-layer deposited on a c -Si wafer [Tana 93]. This heterojunction passivation is due to the hydrogenation of the c -Si surface state from the a -Si:H material. In addition, the carrier type selective contacts are generated with p - and n - a -Si:H on both sides of the wafer sandwiching the two i -layers. These type of cells are called silicon heterojunction solar cells (SHJ). Moreover, with *e.g.* a n -type

c-Si wafer a back surface field is generated at the *c*-Si/*i*-*a*-Si:H/*n*-*a*-Si:H junction repelling the minority carriers and hence reducing further the recombination rate. This reduced surface recombination due to passivation allows essentially to have a high V_{oc} (e.g. 750 mV [Masu 14]) which is near the theoretical limit of *c*-Si (769 mV for a 100 μm thick wafer [Tied 84]). A review on this topic can be read in De Wolf *et al.* [De W 12].

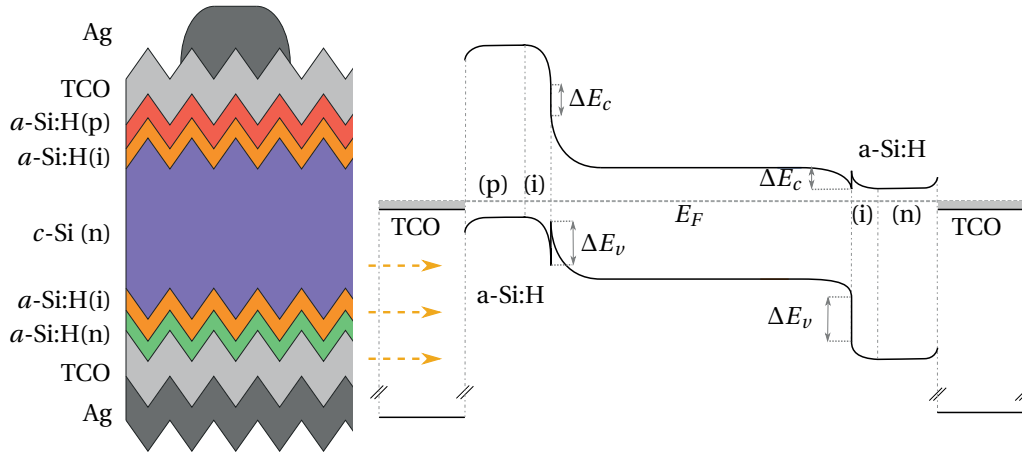


Figure 2.4 – (Left) Schematic of a front emitter silicon heterojunction cell layer stack. (Right) Schematic of the band-diagram. Note that both schematics are not to scale.

Schematics of the layer stack and the band-diagram of a standard SHJ used in this thesis are showed in Fig. 2.4. The SHJ cells studied in this thesis were deposited in our laboratory with a front emitter and a cell size of $2 \times 2 \text{ cm}^2$. The thickness of the *n*-type wafer is 240 μm and we uses indium thin oxide (ITO) as TCO.

2.2 Measurements tools

2.2.1 Current-voltage characterisation

One of the standard characterization technique for solar cells is to measure its current-voltage ($I(V)$) characteristics. The cells are connected with four probes (to suppress contact and line resistances) to a sourcemeter. Figure 2.5 shows the $I(V)$ and power-voltage ($P(V)$) curve of a back-contacted *c*-Si solar cell measured at -40°C . Three points indicated by the circles in the plot are particularly important:

- Short circuit condition: At this point ($V = 0$) we evaluate the short-circuit current density J_{sc} and the short-circuit resistance (R_{sc}) which is defined as the inverse slope at this point.
- Open circuit condition: At this point ($J = 0$) we evaluate the open-circuit voltage (V_{oc}) and the open-circuit resistance R_{oc} which is defined as the inverse slope at this point.

Chapter 2. Materials and measurements techniques

- Maximum power point: The P_{mpp} is defined as the point where the cell produces the maximum power (maximum current x voltage product, see Fig. 2.5 right).

With those points we can define the fill factor as $FF = \frac{V_{mpp} \cdot J_{mpp}}{V_{oc} \cdot J_{sc}} = \frac{P_{mpp}}{V_{oc} \cdot J_{sc}}$ which corresponds to the ratio of the areas of the two rectangles (formed by the red lines and x-/y- axis) showed at the left in Fig. 2.5.

The conversion efficiency (η) is defined as the ratio between the P_{mpp} and the power intensity of incoming irradiance.

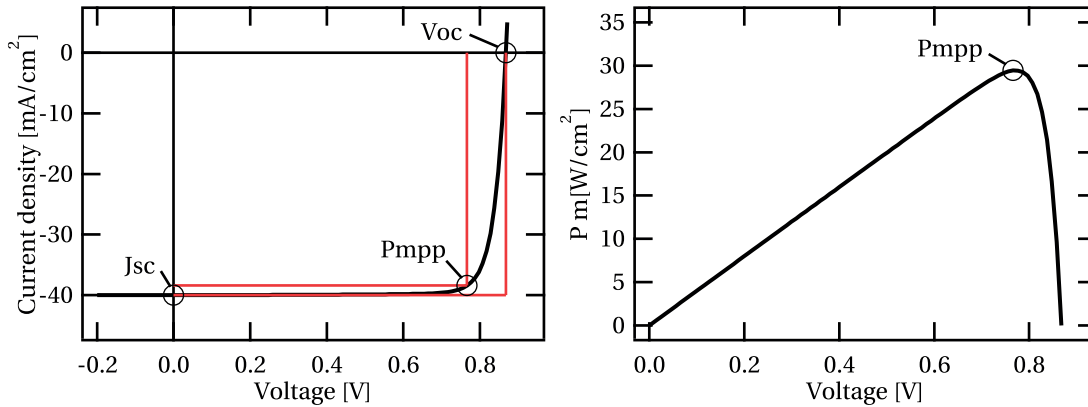


Figure 2.5 – I(V) and P(V) curve schematic of a back contacted crystalline silicon solar cells measured at -70°C with $V_{oc} = 0.868\text{V}$, $J_{sc} = 40\text{mA cm}^{-2}$, $FF = 85\%$ and $P_{mpp} = 29.4\text{W m}^{-2}$

2.2.2 Solar simulators

In this work, we used five different (quasi-) steady state solar simulators that can be grouped in two different categories:

LED and halogen lamp source Those simulator have several light emitting diodes (LED) with different colors to cover the blue-green part and halogen lamps to cover the red/infrared part of the solar spectrum. The intensities of the different lamps can be easily tuned individually allowing variable spectrum and illumination. For low illumination (generally lower than 60W m^{-2} , only LED light sources can be used. Moreover, the incoming light is not collimated, inducing an angular distribution of the light that depends on light sources. We used three different simulators (R&D systems) depending on sample size:

- Large-area solar simulator with a test area of $1.5 \times 2\text{ m}^2$ for measuring full-size modules [Desp 14]. During the measurement period the irradiance non-uniformity was below $\pm 3\%$.
- Medium-area solar simulator denoted "sunsim" with a test area of $0.85 \times 0.85\text{ m}^2$ for minimodules [Lo 10]. The irradiance non-uniformity was measured below $\pm 2\%$. It can be classified as AAA according to the IEC norm [IEC 08b].

- Cell tester with a test area of $30 \times 30 \text{ cm}^2$ for measuring cells. The irradiance non-uniformity was measured below $\pm 1.5\%$.

Xenon and halogen lamp source We also performed measurements using a Wacom commercial simulator model WXS-220S-L2 (denoted here Wacom2 with four lamps - three halogen and one Xenon- and a $220 \text{ mm} \times 220 \text{ mm}$ illuminated area) and a Wacom commercial simulator WXS-90S-L2 model (denoted here Wacom with two lamps - one halogen and one Xenon -with a $90 \text{ mm} \times 90 \text{ mm}$ illuminated area). Both are class AAA simulators.

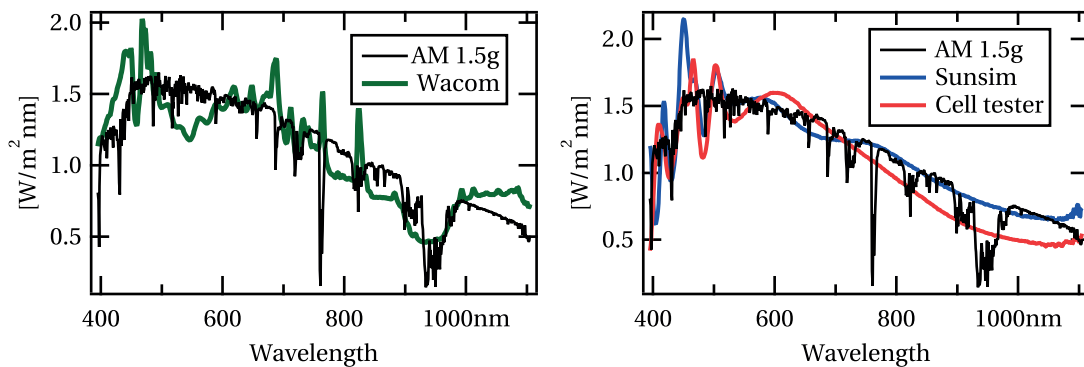


Figure 2.6 – Spectra of the Wacom (green), sunsim (blue) and cell tester (red) in comparison with the AM1.5g spectrum (black). Note that the spectral values above a wavelength of 1000 nm are not reliable.

Figure 2.6 shows the spectra of the Wacom, Sunsim and cell tester in comparison with the AM1.5g spectrum.

2.2.3 External quantum efficiency (EQE) measurements

The EQE is the ratio between collected electron-hole pairs to incident photons at a given wavelength and it describes the spectral response of a solar cell. Our setup has a spot size of about $1 \text{ mm} \times 2 \text{ mm}$ at the focal point. Measurements were performed with white back-reflector placed at the back of the cell. For measuring the spectral response of each sub-cells of a multi-junction cell, bias-lights are used such that only the wanted sub-cell limits the current. The setup is described in [Domi 09].

2.3 Light-soaking

For light-soaking of *a*-Si:H cells, we mostly used an in house built fully LED-based solar simulator allowing to vary the spectra and the irradiance (up to three-sun-equivalent) [Stuc 14a]. The temperature of the cells could be varied from $5 \text{ }^\circ\text{C}$ until $90 \text{ }^\circ\text{C}$ using a temperature controlled plate. During light-soaking, in-situ I(V) curves of the solar cells could be recorded by placing

Chapter 2. Materials and measurements techniques

them on a measurement block that is in thermal contact with the plate (see Fig. 2.7 for a sketch).

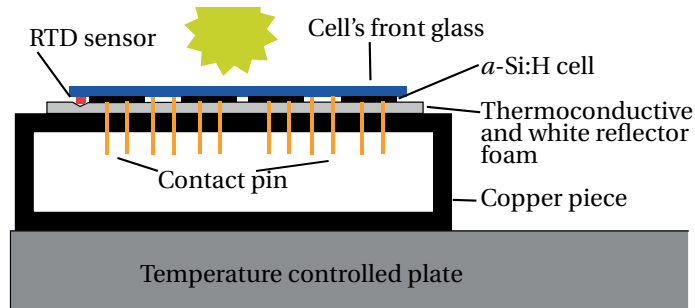


Figure 2.7 – Measurement block for in-situ I(V) measurements of *a*-Si:H during light-soaking with resistance temperature device (RTD) sensor

For some light-soaking experiments at 50 °C and 1000 W m^{-2} , we also used a solar simulator from Soloronix. This simulator uses two microwave-excited Na lamps and the cell temperature is controlled using a cooling plate [Sola].

2.4 Monitoring station

Some results of this thesis are based on results of the PV monitoring station located on the roof of our institute in Neuchâtel, Switzerland. The weather station comprise the following sensors:

- A CM21 pyranometer from Kipp and Zonen [Kipp] used for global horizontal irradiance measurements (GHI).
- A CM11 pyranometer from Kipp and Zonen with a shadow ring to measure diffuse horizontal irradiance (DHI).
- A SP Lite2 pyranometer with the same tilt and orientation (plan-of-array, POA) as the full size module.
- A supplementary pyranometer measuring the global POA irradiance of the small cells.
- A reference encapsulated *c*-Si solar cells whose J_{sc} is used for the measurement of the sun irradiance at the same tilt as the full size modules.
- Air temperature and humidity sensor.
- Wind speed and direction sensor.
- All-sky camera from Vivotek; a picture is showed in Fig. 2.8 b).

2.4. Monitoring station

The PV monitoring system measures each 3 minutes the I(V) curve of each (full size) modules. In between each module is kept at its maximum power point (MPP tracker) and every minutes the P_{mpp} is recorded. The back of module temperature is recorded too¹ at its back. The modules have a 15° tilt and an azimuth of 175°. The measured P_{mpp} and irradiances during the day of the eclipse in 2015 are shown in Fig. 2.8 a).

A second monitoring system for measuring minimodules and lab-size cells was also set up. The I(V) curve of the cells or modules are measured every minutes together with their temperature. When not measured the devices are left in open-circuit. The devices have a 30° tilt and an azimuth of 175°.

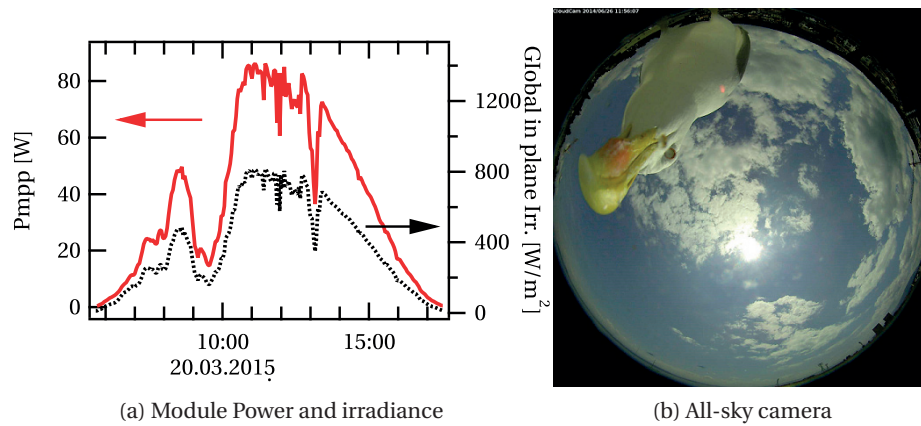


Figure 2.8 – (a) P_{mpp} of a Micromorph full size PV module and irradiance during the eclipse on March 20, 2015. (b) All sky-camera picture with a curious gull.

¹The temperature is measured by an RTD sensor fixed and insulated from air cooling with foam.

3 Diode equation for solar cells

Summary

I(V) characteristics of solar cells can be described using diode equation based models. For thin-film silicon solar cells, an additional current loss term which takes in account the electrical voltage dependent recombination in the intrinsic layer can be added according to literature. A good fit can be obtained with this current loss term for our thin amorphous silicon cells with relatively high fill factor (FF) over several range of intensities. We could show that the temperature dependence can also be reproduced well with this model by introducing a temperature dependence for some parameters. Even the non-linear FF as a function of temperature curve can be reproduced. However, for thicker cells with a high defect density and hence a lower FF , the modeled FF value is too high compared to the measurement. This discrepancy arises because the model does not take into account electrical field deformation. Adding a second diode does not allow reducing this discrepancy significantly.

3.1 Introduction

Solar cells I(V) characteristics can be described using diode equation based models. As those equations have a physical background, a fit with those models of real measured curve allows gaining insight into cells characteristics. Moreover, such a model should be able to simulate solar cells performances at different conditions (varying temperature and irradiation) which will be useful for the next chapters. In this chapter several existing diode based models are analyzed. We here focus on the fitting of thin-film silicon solar cells and verify the ability of the model to fit the I(V) curves at different irradiation and temperatures.

In section 3.2, we discuss the diode based models in general. In section 3.3, the recombination term developed by Merten *et al.* for amorphous silicon cells (a -Si:H) modeling and an explicit formulation of the reverse saturation currents for a two diode model are reviewed. Moreover different expression for shunt currents found in literature are discussed.

In section 3.5, in a first part, a procedure developed for a -Si:H cell fitting with the one-diode

model is explained. This procedure is partially based on existing procedures from literature. Fitting results are showed and analyzed. In a second part, the temperature dependence of the diode based model is discussed. A fitting procedure taking into account temperature behavior is presented and the discussion is extended to a 2 diode model. The limitation of the two models are discussed as well.

Section 3.6 presents briefly the method to model multi-junction cells with diode based models.

3.2 Basic equations

We consider an ideal p-n junction in the dark [Sah 57] and the following hypothesis:

- Outside the space charge region the semi-conductor is neutral.
- The space charge region is abrupt.
- The electron (n) and holes (p) concentration are linked to the potential through the junction in the space charge region.
- The injection is kept low.
- Recombination and generation are neglected in the space charge region.
- An infinitely thick device is assumed.

Using the continuity equations and the Poisson equation and taking into account the drift and diffusion of the carrier we get the $J(V)$ characteristic of a diode in the dark:

$$J(V) = J_0(e^{\frac{qV}{kT}} - 1) \quad (3.1)$$

$$J_0 = \frac{qD_p}{L_p} p_n + \frac{qD_n}{L_n} n_p \quad (3.2)$$

Where q is the elementary charge, $D_{n,p}$ are the diffusion constant of electrons and holes, p_n/n_p the minority carrier concentration for holes and electrons and L_p/L_n the diffusion length, k the Boltzmann constant, V the applied voltage and T the temperature. For non-ideal solar cells the dark I(V) characteristic is often given by three recombination currents [Ghos 80]:

$$J = J_0(e^{qV/n_d kT} - 1) + J_{0t}(e^{qV/n_t kT} - 1) + J_{or}(e^{qV/n_i kT} - 1) \quad (3.3)$$

with J_0 for the reverse saturation current due to diffusion (same as in Equ. 3.3), n_d is the ideality factor for the diffusion current with generally a value of 1 as for an ideal diode. J_{0t} is the reverse saturation current due to the thermionic emission for MIS or SNO_2/Si or ITO/Si cells and is generally negligible. $J_{or} = qn_i W/2\tau^1$ is the reverse saturation current due to

¹ n_i is the saturation current and W the width of the absorber layer

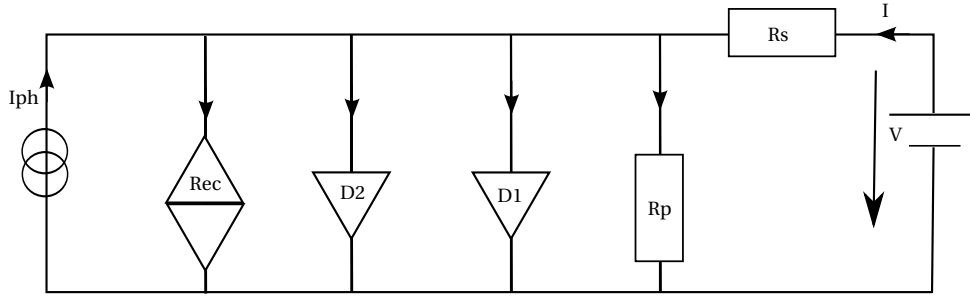


Figure 3.1 – Equivalent electrical circuit of a solar cell with 2 diode (D_1 and D_2), the Merten recombination current (J_{rec}), the light generated current (I_{ph}), series resistance (R_s) and shunt resistance (R_p).

recombination in the space charge region, generally $n_r = 2$. [Sah 57, Wolf 77]. Neglecting the second term we get the often used 2 diode model. The recombination components dominates at low currents and the diffusion component at high currents. In practice the ideality factor and the reverse saturation current can depend on illumination level and voltage [Stut 99].

Coming back to the ideal diode, under illumination, a generation term can be added to the equations and we get the superposition principle. It means the $I(V)$ curve under illumination is given by the sum (superposition) of the dark $I(V)$ curve and the photogenerated current J_{ph} . Especially for a -Si:H, it is far from being true mainly because of voltage dependent charge collection. For hetero-junction solar cells this principle is also not precisely applicable mainly due to irradiation dependent recombination path or charge accumulation. To complete further the model, a parasitic series resistance (due *e.g.* to the TCO or contact resistances) and shunt currents represented by a parallel resistance can be added to the equation (Fig. 3.1 and Equ. 3.4 without the recombination current).

3.3 Diode models for amorphous silicon cells

Merten *et al.* [Mert 98b] added a current loss term (J_{rec}) to the diode equation in order to take into account enhanced recombination in the i -layer and the drift characteristic of the carrier transport. They assumed a constant electrical field (E -field) within the i -layer. Hence this assumption is only valid for small external voltages, cells with thin i -layer and low defect densities. Using the recombination function from [Hubi 92] they proposed the following equation:

$$J = J_{ph} - J_{ph} \frac{d_i^2}{(\mu\tau)_{eff}[V_{bi} - (V + JR_s)]} - J_0 \left[e^{\left(q \frac{V + JR_s}{nkT} \right)} - 1 \right] - \frac{V + J \cdot R_s}{R_p} \quad (3.4)$$

with d_i the thickness of the i -layer, V_{bi} the built-in voltage. The effective lifetime mobility product is given by:

$$(\mu\tau)_{eff} = 2 \frac{\mu_n^0 \tau_n^0 \cdot \mu_p^0 \tau_p^0}{\mu_n^0 \tau_n^0 + \mu_p^0 \tau_p^0}. \quad (3.5)$$

Here $\tau_{n,p}^0$ are the capture times (lifetimes) of the electrons and holes by the neutral dangling bonds and $\mu_{n,p}^0$ are the band mobilities of the free carrier.

Later, Voswinckel *et al.* [Vosw 13] added a second diode to the Merten model to enable a physical interpretation of the irradiation independent recombination path (the equivalent circuit is shown in Fig. 3.1). The first diode with saturation current $J_{0,int}$ describes the so called interface recombination current which models the recombination of the charge carriers at the p/i - and i/n -interfaces of the $p-i-n$ solar cell [Rech 97]. The n_1 ideality factor value was set to a value of 1.2 because the recombination does not exactly occur at interfaces. The second diode with saturation current $J_{0,bulk}$ is the bulk recombination current and represents the recombination in the i -layer which is very similar to J_{or} in Equ. 3.3. The saturation currents and the resulting equation are thus described as:

$$J_{0,int} = \frac{qp_p \cdot e^{-qV_{bi}/kt} \sqrt{\mu_p kT/q}}{\sqrt{\tau/q} \sinh(d_i / \sqrt{\mu_p kT\tau/q})} + \frac{qp_e \cdot e^{-qV_{bi}/kt} \sqrt{\mu_e kT/q}}{\sqrt{\tau/q} \sinh(d_i / \sqrt{\mu_e kT\tau/q})} \quad (3.6)$$

$$J_{0,bulk} = \frac{qd_i n}{\tau} \quad (3.7)$$

$$J = J_{ph} - J_{ph} \frac{d_i^2}{(\mu\tau)_{eff} [V_{bi} - (V + JR_s)]} - J_{0,int} \left[e^{\left(q \frac{V+JR_s}{n_1 kT} \right)} - 1 \right] - J_{0,bulk} \left[e^{\left(q \frac{V+JR_s}{n_2 kT} \right)} - 1 \right] - \frac{V + J \cdot R_s}{R_p} \quad (3.8)$$

3.4 Shunts

As presented before, an equivalent parallel resistance (Fig. 3.1) is used to simulate the shunt currents in a solar cells. Several studies conclude that the shunt resistance varies with light intensity. For example Mermoud *et al.* [Merm 10] proposed the following equation Equ. 3.9 for the shunt resistance as a function of irradiance:

$$R_p(G) = R_p(G_{ref}) + (R_p(0) - R_p(G_{ref})) \cdot e^{-R_p^{exp} \cdot \left(\frac{G}{G_{ref}} \right)} \quad (3.9)$$

Where G_{ref} is the reference irradiance (generally 1000 W m^{-2}) and G the actual irradiance. They applied this equation especially for thin film solar cells (CIGS, CIS, a -Si:H). Another reference [Boyd 11] proposes:

$$R_p = \frac{G_{ref}}{G} R_{p,ref} \quad (3.10)$$

Sometimes in addition to the parallel shunt resistance R_p , especially for thin-film cells, an additional non-linear shunt current that is symmetric around $V = 0$ is added in the form of $I_{sh} \propto |V|^\beta$ [Dong 10] with $\beta = 1.5 - 3$. This term allows modeling the non-linear shunt behavior at low illumination sometimes encountered (as in our laboratory) for shunted a -Si:H cells. However, later Voswinckel *et al.* [Vosw 13] estimated that for good a -Si:H cells under outdoor conditions the non-linear I_{sh} term and irradiance dependent R_p are not needed. Our fitting experience goes in the same direction. The ohmic interpretation of a constant R_p is sufficient.

3.5 Amorphous silicon solar cell fitting with diode models

3.5.1 One-diode with current loss term

Fitting procedure

Fitting a single measured $I(V)$ curve with the one-diode model including the current loss term (Equ. 3.4) requires an optimization of seven parameters. Moreover, many sets of those parameters could give a good fit, hence the outcome of the fit is not universal. To reduce the order of freedom of the parameters, the $I(V)$ curves are measured under different irradiation intensities (variable intensity measurement: VIM, see Fig. 3.2). Those measurements allow us to determine several parameters independently without using an optimization algorithm (as least square minimization). In this section, we present a developed procedure to fit in a robust way $I(V)$ curves of a -Si:H solar cells.

1. For the built-in voltage we can start by using a value from literature such as $V_{bi} = 1.1$ V. For the thickness of the i -layer d_i we can use the effective thickness of the cell. Note that for fitting we can then fix d_i and only vary $(\mu\tau)_{eff}$ as the two variables are not independent.
2. The shunt resistance R_p may be obtained from the asymptotic value of R_{sc} at low irradiation [Mert 98b] (see part d) of Fig. 3.2).
3. The series resistance R_s , can be fitted at high irradiation intensities using the R_{oc} in function of V_{oc} and the FF in function of J_{sc} (Fig. 3.2, a) and c) very left part).
4. The $(\mu\tau)_{eff}$ product can be fitted from the $R_{sc}(J_{sc})$ curve at high irradiation regime (linear part in log scale in Fig. 3.2, d)). For small forward current values and neglecting R_p and R_s , the short circuit resistance is given by $R_{sc} = \frac{1}{I_{ph}} \frac{(\mu\tau)_{eff} V_{bi}^2}{d_i^2}$ [Mert 98b]. Once $(\mu\tau)_{eff}$ is set, the value of J_{ph} can directly be calculated using Equ. 3.4 at zero bias voltage.
5. The ideality factor n and J_0 can be determined using the $V_{oc}(\ln(J_{sc}))$ plot (Fig. 3.2, b)), in a range where for a good cell, the effect of R_p is negligible which means medium to

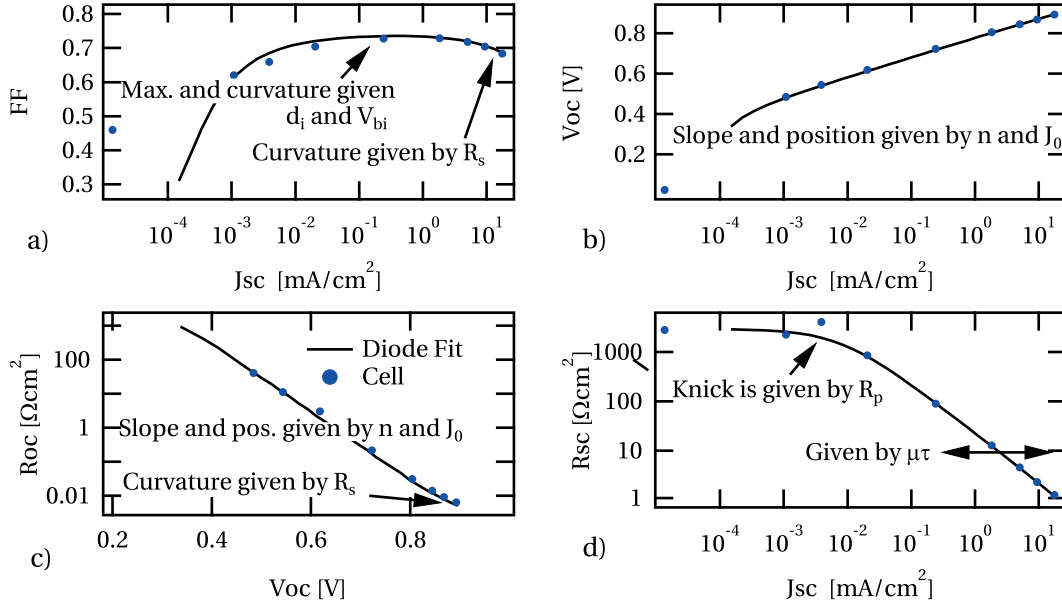


Figure 3.2 – Measured and modeled I(V) curve values. The one-diode model with current loss term is used. a) $FF(J_{sc})$, b) $V_{oc}(J_{sc})$, c) $R_{oc}(V_{oc})$ and d) $R_{sc}(J_{sc})$. Blue points are measured points under different illumination and the black line the modeled values.

high irradiation. We can get an approximation of the $(dV_{oc}/d(\ln(J_{ph})))$ slope². Using Equ. 3.1 we get an expression for the V_{oc} :

$$V_{oc} = \frac{nkT}{q} \ln\left(\frac{J_{ph}^*}{J_0} + 1\right) \quad (3.11)$$

Where $J_{ph}^* = J_{ph} \left(1 - \frac{d_i^2}{(\mu\tau)_{eff}(V_{bi} - V_{oc})}\right)$. We can now differentiate Equ. 3.11 by J_{ph}^* making the assumption that J_{ph}^* is not depending on V_{oc} near V_{oc} :

$$\frac{dV_{oc}}{d(\ln(J_{ph}^*))} = \frac{nkT}{q} \cdot \frac{J_{ph}^*}{J_{ph}^* + J_0} \quad (3.12)$$

As $J_{ph} \gg J_0$ at an irradiance intensity range where R_p is negligible, we can directly extract an approximation of the ideality factor n and the reverse saturation current J_0 (for a defined $(\mu\tau)_{eff}$ and V_{bi}):

$$n = \frac{q \cdot dV_{oc}/d(\ln(J_{ph}^*))}{kT} \quad (3.13)$$

$$J_0 = \frac{J_{ph}^*}{e^{qV_{oc}/nkT}} \quad (3.14)$$

This approximation worked quite well in practice.

²As we already know $(\mu\tau)_{eff}$, we can calculate J_{ph} from J_{sc} .

3.5. Amorphous silicon solar cell fitting with diode models

6. Finally, the value of V_{bi} is adapted such to fit to the $FF(J_{sc})$ on Fig. 3.2 a) curve and to the low forward bias part of the I(V) curve (from 0 V to 0.5 V). Changing V_{bi} implies that we need to adapt slightly $(\mu\tau)_{eff}$ and hence sometimes J_0 and n . This means repeat steps 4 to 6.

Validation of the model

Despite the fact that most assumptions (section 3.2) for the ideal one-diode model are not valid for *a*-Si:H adding the current loss term J_{rec} allows having a remarkable good fit in a large range of irradiation (from below 1 W m^{-2} to more than 1000 W m^{-2}). The IV parameters at STC of the *a*-Si:H cell used in Fig. 3.2 are $V_{oc} = 0.890 \text{ V}$, $FF = 69\%$, $J_{sc} = 17.4 \text{ mA cm}^{-2}$. In this particular example the J_{sc} value is overestimated due to the absence of a mask during I(V) measurements which therefore enhanced light trapping through the glass and hence also lead to an overestimated $P_{mpp} = 107 \text{ W m}^{-2}$ value. The fitted diode parameters are listed in Tab. 3.1.

Diode parameter	TopC	Thin HBG
J_{ph}	18.2 mA cm^{-2}	11.4 mA cm^{-2}
J_0 at 25°C	$7.46 \times 10^{-9} \text{ mA cm}^{-2}$	$1.9 \times 10^{-10} \text{ mA cm}^{-2}$
n	1.6	1.79
$(\mu\tau)_{eff}$	$5.11 \times 10^{-8} \text{ m}^2/\text{Vs}$	$1.67 \times 10^{-8} \text{ m}^2/\text{Vs}$
V_{bi}	1.05 V	1.03 V
R_s	$2.4 \times 10^{-3} \Omega \text{ cm}^2$	$1.3 \times 10^{-6} \Omega \text{ cm}^2$
R_p	$2922 \Omega \text{ cm}^2$	$475 \Omega \text{ cm}^2$
d_i	305 nm	180 nm
E_{act}		1.04 eV

Table 3.1 – Diode parameters for the one-diode model with current loss term J_{rec} . TopC: low band gap top cell of micromorph cells. Thin HBG: thin, high bandgap cells as top cell for triple junction cell after 168 h of degradation under 1 Sun and 50°C .

3.5.2 Temperature fitting of the one-diode model with current loss term

In this section we discuss the temperature dependence of the one-diode model with current loss term (Equ. 3.4). We evaluate two different approaches for implementing temperature dependence in the one-diode model with J_{rec} . The first simple one, assumes that only the J_0 (and T) parameter value depends on temperature. In the second approach, the temperature dependence of each parameter is examined by fitting and then the temperature dependence of the parameter varying significantly with temperature are taken into account.

We begin with the first approach where only the temperature dependence of J_0 is taken into

Chapter 3. Diode equation for solar cells

account. From the ideal one-diode equation, the J_0 equation Equ. 3.2 can be expressed as:

$$J_0 = q \left(\frac{D_n}{L_n N_A} + \frac{D_p}{L_p N_D} \right) n_i^2 \quad (3.15)$$

where n_i is the intrinsic carrier density, $N_{A,D}$ are densities of acceptor and donor atoms. Hence the temperature behavior of J_0 is strongly determined by n_i . By inserting an explicit formula for n_i in Equ. 3.15 we can write (for detailed derivation [Sing 12]).

$$J_0 = CT^3 \exp\left(-\frac{E_g}{kT}\right), \quad (3.16)$$

with E_g the band gap. Green proposed to replace CT^3 by a constant J_{00} [Gree 92]. We will do so to keep the model as simple as possible (even though the following calculation could also be done with CT^3). We therefore assume:

$$J_0 = J_{00} \exp\left(-\frac{E_g}{kT}\right) \quad (3.17)$$

Using a band gap E_g of 1.8 eV (a -Si:H cells) the V_{oc} drop with temperature is strongly underestimated by the model. This fact is not surprising as for a -Si:H, the temperature dependence of the recombination is significantly driven by many parameters and not only by the $n_i(T)$ temperature dependence. Hence we consider E_g as a fitting parameter and rename it to E_{act} . This parameter can be directly calculated as following if the temperature coefficient of the V_{oc} and the J_{sc} are known. By differentiating equation Equ. 3.11, inserting Equ. 3.17 and again making the assumption that J_{ph^*} do not depend on V_{oc} , we get:

$$\frac{dV_{oc}}{dT} = \left(\frac{V_{oc}}{T} \right) - n \frac{E_{act}}{T} + n \frac{dE_{act}}{dT} - \frac{nkT}{q} \left(\frac{1}{J_{ph^*}} \frac{dJ_{ph^*}}{dT} \right). \quad (3.18)$$

If we neglect the temperature dependence of E_{act} , by using 0.3%/°C for the $TC_{V_{oc}}$ and 0.08%/°C for the $TC_{J_{sc}}$ ($\cong \frac{1}{J_{ph^*}} \frac{dJ_{ph^*}}{dT}$), we obtain $E_{act} = 1.04$ eV. With a temperature dependence of $dE_{act}/dT = -0.63$ meV/°C we obtain 0.85 eV. Those values are significantly lower than the bandgap of a -Si:H cells (1.8 eV). Because of assumption of independent J_{ph^*} , E_{act} has to be adapted slightly to fit correctly the I(V) curves.

The fitted parameters for a thin (i -layer of about 180 nm), high bandgap a -Si:H cell (used as top cells in triple junction cells) after one week degradation under 1 Sun and 50 °C are showed in Tab. 3.1 (Thin HBG). Figure 3.3 shows the simulated and the measured temperature behavior of the FF and the V_{oc} . The measured and simulated I(V) curves are also showed. As for the previous example a good fit is obtained with this thin high band-gap cell at several irradiances. The temperature behavior of the V_{oc} can also be well reproduced. However, we see that the simulation shows some slight curvature at low temperature for the $V_{oc}(T)$ curve due to J_{rec} term. The nearer the V_{bi} to the V_{oc} value, the higher is this bending. This bending is not measured and hence the model is no more valid for low temperatures. Interestingly, by tuning

3.5. Amorphous silicon solar cell fitting with diode models

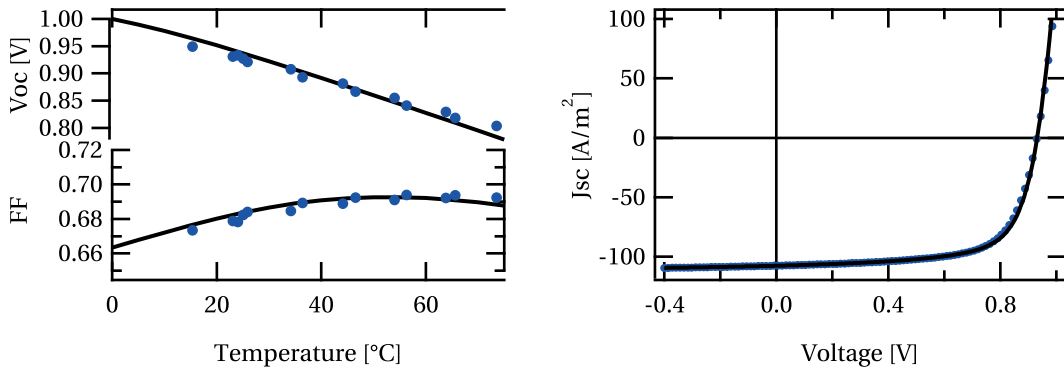


Figure 3.3 – Simulated and simulated (one-diode model J_{rec}) values of a thin, high bandgap a -Si:H cells. Left: The temperature behavior of FF and V_{oc} . Right: $I(V)$ curve at STC.

V_{bi} and $(\mu\tau)_{eff}$ the temperature behavior of $FF(T)$ can also be simulated quite precisely, even the position of the FF maximum. The shift of this maximum to lower temperature with decreasing irradiance intensity can also be well reproduced. This $FF(T)$ curvature is due to the V_{bi} parameter that is constant with temperature. When the temperature decreases, the V_{oc} and V_{mpp} increase. Therefore, the $V_{bi} - (V + JR_s)$ term (from Equ. 3.4) which represents the internal electric field diminishes relatively. As a result the current loss ($J_{ph} * \searrow$) increases relatively and hence the FF decreases. With this diode equation same FF lowering due to electric field lowering with decreasing temperature as described in section 4.2.2 can be simulated.

However, by fitting the same one-diode model with J_{rec} to the same cell (thin HBG) in initial state, the temperature behavior of the FF can no more be approached satisfactorily. The curvature is similar but the maximum value of the FF is 30 °C lower for the modeled curve than for the measured curve. For example at 1000 W m^{-2} and 60 °C the model underestimates the FF by 1 % absolute percent. By fitting the curve at STC conditions, the relative difference between the modeled and measured P_{mpp} is under 1 % until 50 °C and 0.1 suns. Going away from this range of temperature and irradiance values, the error increases up to 4.5 % at 70 °C and below 0.02 suns.

In order to reduce these errors, one can investigate the temperature dependence of the additional fitting parameters as n , $(\mu\tau)_{eff}$, V_{bi} , R_s and R_p . This leads us to the second approach where for several temperatures the one-diode model with J_{rec} is fitted using VIM measurements. We apply the fitting procedures described before to measured $I(V)$ curves at different temperatures. The fit showed that the temperature dependence of the J_0 has an exponential behavior. Therefore Equ. 3.17 can also be used in this approach to describe its temperature behavior and we got a value of the activation energy of $E_{act} = 0.76 \text{ eV}$ for our cell in the degraded and initial state.

Figure 3.4 shows the fitted ideality factor n and the effective mobility lifetime product $(\mu\tau)_{eff}$ as a function of temperature for the a -Si:H cell in initial and degraded state. On the figure we see that the fitted value of n seems to decrease linearly with temperature. Hence we can

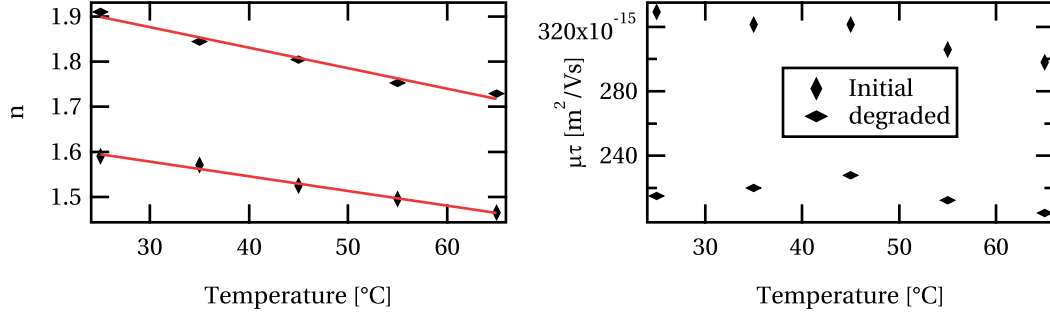


Figure 3.4 – The fitted ideality factor n (left) and the effective mobility lifetime product $(\mu\tau)_{eff}$ (right) as a function of temperature for the one-diode model with J_{rec} . A thin high bandgap a -Si:H cell is fitted in the initial and degraded (168 h and 1 sun at 50 °C) state.

describe its temperature dependence as following:

$$n(T) = n(25^\circ\text{C}) - (T - 25^\circ\text{C}) \cdot TC_n \cdot n(25^\circ\text{C}), \quad (3.19)$$

where TC_n is the temperature coefficient of n . In this case we got $TC_n = 0.20\%/^\circ\text{C}$ and $TC_n = 0.28\%/^\circ\text{C}$ for the initial and degraded states respectively. The value of $(\mu\tau)_{eff}$ decreases slightly with temperature in the initial and degraded state which is in agreements with the reduced recombination observed at higher temperature (see Ch. 4.2). As the variation is relatively small and to keep the model simple we can assume this factor constant. The last fitting factor that varies significantly with temperature is the series resistance R_s that decreases from $2.2 \times 10^{-2} \Omega \text{cm}^2$ at 25 °C to $1.8 \times 10^{-2} \Omega \text{cm}^2$ at 75 °C. By taking into account temperature dependency of n , the cell diode temperature behavior can be fitted satisfactorily. The relative errors between the measured and modeled P_{mpp} are under 1 % for irradiation intensities ranging from 1 Wm^{-2} to more than 1000 Wm^{-2} and temperatures ranging at least from 20 °C to 75 °C in both the initial and the degraded state.

As shown before, a good fit is obtained for thin cells. However, as expected by the constant electric field assumption made for the current loss term, for thicker cells with high defect density, the region around the P_{mpp} cannot be fitted accurately because the field deformation is not taken into account. Therefore the simulated FF is overestimated, as seen in Fig. 3.5, where the fitted $I(V)$ curve of an a -Si:H cell with an i -layer thickness of 300 nm in a degraded state is shown. The circle indicates where the fit diverges. When dividing the term $V_{bi} - (V + JR_s)$ representing the internal electric field by a field deformation factor in the form of $\phi = 1 + A \cdot \exp(-B(V_{bi} - V))$ with A and B as fitting constant, as we propose, the fit improves considerably.

3.5.3 Temperature fitting of the 2 diode model with current loss term

As the one-diode model with J_{rec} without a field deformation factor could not reproduce the $I(V)$ characteristics of cells with low FF , the a -Si:H cell with a 300 nm thick i -layer presented

3.6. Simulating multi-junction solar cells using diode equation based models

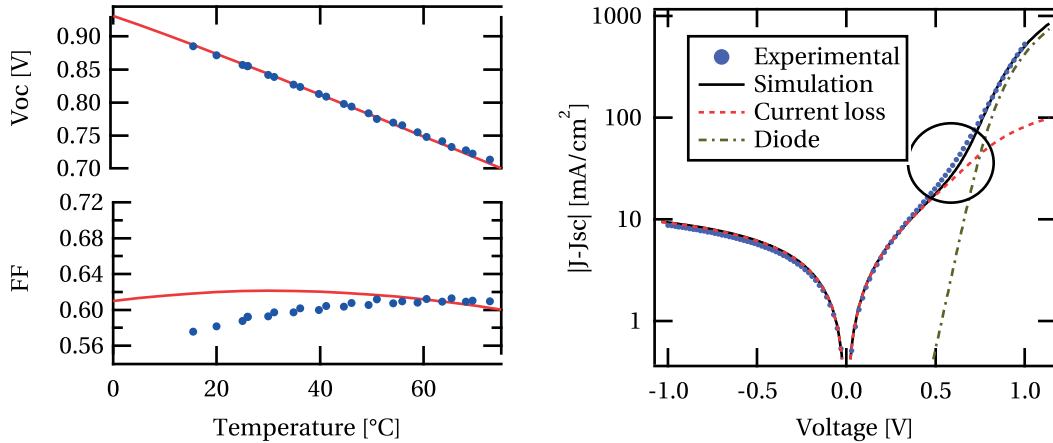


Figure 3.5 – Experimental and simulated (one-diode model with current loss) of a thicker (300 nm i -layer) a -Si:H cell. Left: The temperature behavior of FF and V_{oc} . Right: Absolute value of $I(V)$ curve minus J_{sc} at STC. The contribution of the current loss term and of the diode term are shown as non-continuous lines. The circle shows the region around the P_{mpp} .

before is fitted using the two diode model with current loss term presented in Equ. 3.8. A good agreement between simulation and measured $I(V)$ curve can be obtained by fitting for a specific intensity. However, this fit is only valid for the given intensity. The author could not find a fit which remains good for several intensities. If J_{int} , J_{bulk} , n_1 and n_2 are fitted from the V_{oc} as a function of J_{sc} curve, as for the one-diode model, we overestimate the FF . Hence we also need the ϕ term. However, the second diode is then unnecessary for modeling a -Si:H cells, as the one-diode model becomes sufficient.

3.6 Simulating multi-junction solar cells using diode equation based models

The modeling of the $I(V)$ characteristics of multi-junction cells using diode based models can be done with two different approaches:

- The cell is considered as a mono-junction and the fitting can be done as in the previous chapter with a diode based model. The advantage of this approach is that we limit the number of fitting parameters. However, cell performances variations due to current mismatch (from cell design or by changing spectrum) between the sub-cells are not modeled directly. Moreover the physical meaning is even less meaningful. Therefore we will not use it in our work.
- The cell $I(V)$ curve is simulated by connecting the solar cell diode model of each cell in series (see Fig. 3.6 for a representation of an equivalent circuit). If the spectral response of each sub-cell is known, we can accurately simulate spectral dependent cell performances. However, finding the many fitting parameter of each sub-cell is not

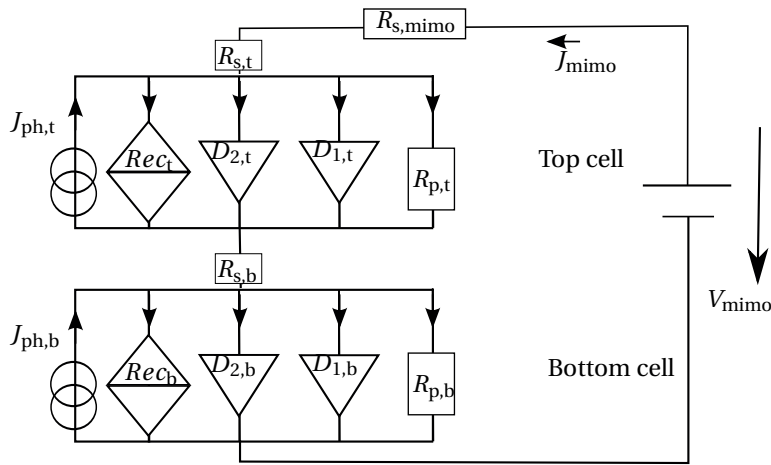


Figure 3.6 – Equivalent circuit of a micromorph cell.

directly possible. We have to extract the parameters from single cell measurements. Spectral dependent $I(V)$ measurement as shown in chapter 4.3 could also help in fitting.

3.7 Conclusion

We presented an overview of different diode based models for simulating solar cells $I(V)$ curves. For simulating thin-film solar cells, adding a irradiation and voltage dependent current recombination term to the standard one-diode model allows having a good fit over several decades of irradiation intensity values and a large temperature range. Even FF as a function of temperature maximum can be reproduced adding temperature dependence to the J_0 and the n fitting parameters. However, for cells with low FF values this model systematically overestimate the FF because electric field deformation are not taken into account. Adding a second diode does not allow reducing significantly this overestimation. However, adding a field deformation factor to the one-diode model allows reducing significantly this overestimation. The diode model with recombination term will be used in chapter 5 to estimate spectral effects on micromorph cells and in chapter 6 to develop a model describing degradation and recovery effect of a -Si:H cells.

4 Temperature dependence of thin-film and crystalline silicon-based solar cells

Summary

To investigate whether *a*-Si:H cells that are optimized for standard conditions (STC) also have the highest energy output, we measured the temperature and irradiance dependence of the different solar cell performance parameters as a function of the temperature for four different deposition parameter series (power and frequency of the PE-CVD generator, the hydrogen-to-silane dilution during the deposition of the intrinsic absorber layer (*i*-layer), and the thicknesses of the *i*-layer and *p*-type doped hydrogenated amorphous silicon carbide layer) in the degraded and annealed state. The results show that the temperature coefficient of the V_{oc} generally varies linearly with the V_{oc} value. The linear J_{sc} increase with temperature is mainly due to temperature-induced bandgap reduction and reduced recombination. The FF temperature dependence is not linear and reaches a maximum at temperatures between 15 °C and 80 °C. Numerical simulations show that this behavior is due to a more positive space-charge density induced by the photogenerated holes in the *p*-layer and to a recombination decrease with temperature. Due to the $FF(T)$ behavior, the $P_{mpp}(T)$ curves also have a maximum, but at a lower temperatures. Moreover, for most series the cells with the highest power output at STC also have the best energy output. However the $P_{mpp}(T)$ curves of two cells with different *i*-layer thicknesses cross each other in the operating cell temperature range indicating that the cell with highest power output could for instance have a lower energy output than the other cell. A simple energy-yield simulation for the degraded and annealed states shows that for Neuchâtel (Switzerland) the best cell at STC also has the best energy output. However for a different climate or cell configuration, this may not be true.

We also compare the temperature behavior of standard μc -Si:H cells with and without *a*-Si:H buffer layer at the *i-n* interface, optimized for high V_{oc} values, and of μc -Si:H solar cells with highly crystallized *i*-layer deposited with silicon tetrafluoride. The temperature behavior is similar to *a*-Si:H cells, there is $FF(T)$ maximum and hence a $P_{mpp}(T)$ maximum but both occurs at lower temperatures. Compared to *a*-Si:H the TC s are slightly lower for μc -Si:H. Hence we suppose that the $FF(T)$ maximum is a consequence of the *p-i-n* nature of those devices. The $TC_{P_{mpp}}$ is mainly driven by the $TC_{V_{oc}}$ which itself is almost linearly dependent on the V_{oc} itself.

To understand the temperature behavior of multi-junction thin-film solar cells we measured those cells at different temperatures and spectra. The temperature dependence of micromorph thin film silicon tandem cells is mainly determined by the TC of its subcells. It is mainly the higher $TC_{J_{sc}}$ of

Chapter 4. Temperature dependence of thin-film and crystalline silicon-based solar cells

the top cell compared to the bottom cells that implies that the $TC_{P_{mpp}}$ of micromorph cells increase when going from bottom to top cell limited case (more bluer to reddish spectrum). However, the better TC at top limited conditions do not counterbalance the P_{mpp} loss due to current mismatch. Hence, if micromorph cells are measured at 25 °C, to reach highest energy outputs, it is still advantageous to be current matched or even slightly bottom limited. The same principle can be applied to triple junction cells.

As for thin film silicon solar cells, silicon heterojunction cells (SHJ) also show a FF as function of temperature maximum. However, this maximum is due to the valence band offset between the a -Si:H i -layer and the c -Si wafer causing a hole accumulation at lower temperature due to less thermionic energy of the carriers. We measured a FF maxima around 20 °C for SHJ cells with a -Si:H p -layers and around -40 °C for cells with a μc -Si:H p -layer. Moreover due to this barrier the $I(V)$ curves become s-shaped at lower temperatures. We propose a new method to calculate an activation energy, using an Arrhenius plot of the $I(V)$ curve slope at the s-shape saddle point. With this method we got activation energies between 0.21 eV and 0.31 eV for the a -Si:H p -layer cells depending on the a -Si:H i -layer characteristics and 0.14 for the μc -Si:H p -layer cells.

Finally, we compare the TC of the previous cell technologies with mono- and multi- c -Si solar cells. In our study, the best $TC_{P_{mpp}}$ (*i.e. highest*) are reached for a -Si:H solar cells principally because of their favorable (high) TC_{FF} . The SHJ cells exhibit the second best $TC_{P_{mpp}}$ also due to their high TC_{FF} . Interestingly, compared to back-contacted mono- c -Si cells with roughly equivalent V_{oc} , their $TC_{V_{oc}}$ is slightly lower. Moreover, due to their particular $FF(T)$ behavior, the $TC_{P_{mpp}}$ of a -Si:H and SHJ solar cells have a relatively higher irradiance dependence than for other cells. However, for estimating the energy output in Switzerland, we calculated that the temperature power losses can be calculated using a constant $TC_{P_{mpp}}$ (measured at STC) without a significant loss in accuracy.

4.1 Introduction

The factor influencing most the efficiency of silicon-based solar cells is the operating temperature. Solar cells are generally optimized for standard test condition (STC: 1000 W/m², AM1.5g, 25 °C) [IEC 08a], and their efficiencies are reported for these conditions. However, in real outdoor operation, solar cells in modules often encounter different operating temperatures which are generally much higher than 25 °C [Kond 97, Jank 13, King 97b, Bogd 10] and this higher operating temperature can lead to a significant reduction of the performance. The yearly energy losses due to temperatures higher than 25 °C can reach over 7 % in Crete for free-standing modules [Kyma 09] or even more than 11% for fully roof-integrated solar modules in central Europe [Nord 03]. Therefore understanding temperature behavior of the solar cell performances allows predicting energy yield (or the yearly energy output) correctly. Furthermore it can help optimize material parameters of cells for a given location with the corresponding operating conditions including temperature variations. The temperature behavior of the different solar cell performance parameters such as the maximum power output (P_{mpp}), the fill factor (FF), the open-circuit voltage (V_{oc}) and the short circuit current density (J_{sc}) can be described using temperature coefficients (TC). For this work, when not stated differently, we determine the TC as the slope of the linear fit over all points within the operating temperature

range of a parameter (Par) divided by the parameter value at 25 °C:

$$TC_{Par} = \frac{1}{Par(25^{\circ}\text{C})} \left. \frac{dPar(T)}{dT} \right|_{T=25^{\circ}\text{C}} \quad (4.1)$$

For example a standard crystalline silicon solar cells (c -Si), the TC of P_{mpp} ($TC_{P_{mpp}}$)¹ is negative with values of $-0.3\%/^{\circ}\text{C}$ to $-0.45\%/^{\circ}\text{C}$ [Skop 09, Smit 12]. In this work, a TC increase or decrease means that the value goes towards $+\infty$ (generally a favorable TC) or $-\infty$ respectively. As well, a low TC is nearer to $-\infty$, whereas a high TC is nearer to $+\infty$.

For silicon-based solar cells the temperature behavior is mainly influenced by the temperature dependence of the V_{oc} ($TC_{V_{oc}}$). At V_{oc} the recombination balances the light and thermally generated currents. By enhancing temperature, the reverse saturation current (J_0) increases because it depends on the np product which itself has an inverse exponential relationship with temperature (see Equ. 3.16 chapter 3.5.1). Hence, the V_{oc} decreases with increasing temperature. The J_{sc} generally increases with temperature because of increased band-to-band absorption due to temperature-induced bandgap reduction. For a standard c -Si solar cell, the temperature behavior of the FF depends mainly on the V_{oc} and $TC_{V_{oc}}$ as showed by an approximate formula presented by Green *et al.* [Gree 82]. However, especially for drift-driven devices as thin-film silicon cells, more parameters influences the temperature behavior of the FF [Gree 03]. The temperature dependence of thin film silicon-based solar cells is not very well understood and only barely treated in literature. Moreover only few studies link material parameter with temperature dependence. The main part of this chapter aims to improve our understanding of the temperature behavior of thin-film silicon solar cells and to relate material properties to temperature behavior.

In section 4.2 we present results of temperature dependent measurement of a -Si:H solar cells. We propose a new explanation of the temperature behavior of the FF , based on measurements and simulations. In addition, we show the influence of different material parameters on the temperature behavior of the solar cells, providing some interpretations. Finally, we quantify the effect of the TC dependence of material parameters on the energy output without considering annealing and degradation effects.

In section 4.3, the temperature behavior of the performances of different type of μc -Si:H solar cells is showed. We also provide some hypothesis allowing to understand the mechanism behind their temperature behavior.

With the help of the two previous sections, the temperature dependence of micromorph tandem cells and triple cells is studied in section 4.4.

In section 4.5, we move to silicon heterojunction cells (SHJ) that are known to have a favorable temperature coefficient principally due to their high V_{oc} [Mish 11, Batz 11]. Investigating the temperature behavior of those cells over a relatively large temperature range (-100°C

¹For PV modules the TC terminology used is generally: $TC_{P_{mpp}} = \gamma$, $TC_{V_{oc}} = \beta$, $TC_{J_{sc}} = \alpha$ and $TC_{FF} = \kappa$

Chapter 4. Temperature dependence of thin-film and crystalline silicon-based solar cells

to 80 °C) allows gaining some insight into materials characteristics. Lowering the operating temperature, the FF deviates from standard c -Si solar cells behavior by having a maximum and decreasing. Moreover an s-shape is appearing on the $I(V)$ curve [Sark 12, Clee 98]. We discuss in detail the temperature and irradiance dependence of each $I(V)$ parameters. We also propose a new method to probe an activation energy that is probably linked to the hole barrier at the p side of the cells. We compare SHJ cells with p - a -Si:H and p - μc -Si:H layer by applying this method.

Finally, in the last section (4.6) we extend the discussion by comparing the TC of thin-film silicon cells and SHJ cells to other silicon-based solar cells as mono and poly- c -Si cells. Moreover, we quantify how the irradiance dependent TC (e.g. as it is the case for SHJ cells) affects the energy yield prediction.

4.2 Amorphous Si cells temperature behavior

Most of the results of this section are published in [Ries 15]. Hydrogenated amorphous silicon (a -Si:H) solar cells are known to have more favorable $TC_{P_{mpp}}$ compared to crystalline silicon (c -Si) cells, reaching values around $-0.2\%/^{\circ}C$ which reduces the energy losses in operation due to temperature compared to c -Si [Virt 13, Akhm 97, Shim 05, Kame 96]. Even positive $TC_{P_{mpp}}$ were measured for cells with high defect densities [Carl 00]. A high $TC_{P_{mpp}}$ can be explained by a high V_{oc} implying a high TC of the V_{oc} ($TC_{V_{oc}}$) [Gree 03], and a high TC of the FF (TC_{FF}). It was proposed that a high TC_{FF} can be explained by a reduction in the contact resistance and an increase in the collection length with temperature [Gree 03, Carl 00]. Stiebig *et al.* [Stie 96] gave some insight into temperature behavior of single-junction a -Si:H cells using simulation and measurements, stating that the decrease of the P_{mpp} value is dominated by the decrease of J_{sc} below room temperature and by the decrease in V_{oc} above room temperature. They measured the maximum efficiency at a temperature of 3 °C.

Some studies have correlated material properties of a -Si:H with the temperature behavior of the corresponding solar cells. For example, Carlson *et al.* [Carl 00] found that a -Si:H solar cells with a thicker absorber layer have a higher $TC_{P_{mpp}}$ than those with a thinner absorber layer. Therefore, thicker absorber layers should be used for warmer climates and thinner for colder climates for maximum energy yield. Sriprapha *et al.* [Srip 08] studied the temperature behavior of silicon thin-film cells on the transition phase from a -Si:H to microcrystalline silicon (μc -Si:H) in the absorber layer by varying the hydrogen-to-silane ratio during deposition. They found that the cells whose absorber was deposited at the transition between a -Si:H and μc -Si:H (called protocrystalline silicon cells) had the best $TC_{P_{mpp}}$. However, a comprehensive study correlating TC with material and solar cell properties is missing to date.

In this section, we² present TC measurements taken at different irradiation levels for several state-of-the-art a -Si:H solar cells series. The investigated parameters are the power, frequency

²Y. Riesen, M. Stuckelberger, F.-J. Haug, C. Ballif and N. Wyrsh

and hydrogen-to-silane dilution during the deposition of the absorber layer (*i*-layer), the thickness of this layer, and the thickness of the *p*-type doped hydrogenated amorphous silicon carbide layer (*p*-(*a*-SiC:H)). We also present numerical simulations and provide physical explanations for the observed trends. Understanding the short-term temperature behavior of an *a*-Si:H cell is a first step for simulating its energy output. The second step would be to take into account degradation and annealing effects (which also depend on temperature but on a longer timescale). This study allows us to assess in a first step whether solar cells optimized for STC also perform best under real conditions, or whether other deposition parameters are better suited for optimum energy output regarding temperature behavior. To have an idea of the resulting energy output range, the simulations are performed for both the annealed and the degraded state.

4.2.1 Experimental details

For this study, we used state-of-the-art *a*-Si:H solar cells (see Sec. 2.1.1) that were optimized for use as the top cell in *a*-Si:H/ μ c-Si:H tandem solar cells and the top cell in a *a*-Si:H/ μ c-Si:H/ μ c-Si:H triple-junction cells. The solar cells were deposited in the *p-i-n* (superstrate) configuration on 0.5-mm-thick Schott AF 32 glass substrates. A 2.3- μ m-thick boron-doped ZnO (ZnO:B) layer deposited by low-pressure chemical vapor deposition (LP-CVD) was used as the front electrode. The following active layers were all deposited by plasma-enhanced chemical vapor deposition (PE-CVD). A *p*-type microcrystalline silicon-oxide layer (*p*-(μ c-SiO:H)) was deposited after the ZnO for a good electrical contact with the front, followed by a wide-bandgap *p*-type *a*-SiC:H layer for a strong electric field. An undoped wide-bandgap *a*-SiO:H buffer layer was deposited at the interface between the *p*- and the *i*-layer. The *a*-Si:H *i*-layer was followed by a *n*-type *a*-Si:H layer and an *n*-type μ c-SiO:H layer at the interface with another 2.3- μ m thick LP-CVD ZnO:B back electrode. These cells were co-deposited with those presented in [Stuc 14d]; further details about the PE-CVD system (Octopus I), the deposition parameters, and substrates can be found elsewhere [Stuc 13, Stuc 14b, Stuc 14c]. Each cell has a nominal area of 0.25 cm².

Based on this high-efficiency solar cell recipe, the following deposition parameters were varied:

1. *i*-layer-thickness (*i*-thick.) series: The *i*-(*a*-Si:H)-layer thickness was varied between 120 nm and 1000 nm.
2. *p*-layer-thickness (*p*-thick.) series: The deposition time of the *p*-(*a*-SiC:H) layer was varied between 0 s and 60 s, corresponding to *p*-layer thickness between 0 and 18 nm [Stuc 14b].
3. Dilution (*dil.*) series: The hydrogen-to-silane flow ratio ($[H_2]/[SiH_4]$) was varied between 0.5 and 64. The bandgaps in terms of E_{04} of the *i*-layers were measured with spectrometric ellipsometry measurements as detailed in [Stuc 14c]. The resulting bandgap values ranged from 1.88 eV to 2.18 eV from lowest to highest dilution and increases almost linearly with the measured V_{oc} values.

Chapter 4. Temperature dependence of thin-film and crystalline silicon-based solar cells

4. *Deposition (dep. rate) series*: The power of the RF generator was varied from 4 W to 80 W at radio frequency (RF, 13.56 MHz) and at very high frequency (VHF, 40.68 MHz), corresponding to deposition rates between 1.5 Å/s and 22 Å/s [Stuc 14c, Stuc 14d].

In addition, for measurements at temperatures as low as $-60\text{ }^{\circ}\text{C}$ (presented in section 4.2.2), reference *a*-Si:H cells with a thin *i*-layer (140 nm) and wide bandgap, optimized for use as the top cell in triple- and quadruple-junction cells [Schu 14, Schu 15], were also used.

Measurements

We measured the current-voltage ($I(V)$) characteristic under a two-lamp solar simulator from Wacom (class AAA). The *i-thick* series and reference cells were also measured with a new hybrid LED-halogen solar simulator (which was not yet available at the beginning of the experiment) built in house, varying the irradiation from about 10 W/m^2 to 1300 W/m^2 . If not stated differently, the temperature was varied between $15\text{ }^{\circ}\text{C}$ and $80\text{ }^{\circ}\text{C}$; the temperature of the cells was controlled with one of the two different setups:

(A) Chuck setup: For good thermal contact between the cells and the chuck, a thermo-conductive sheet was used, which compensated for topological differences from the soldering of the electrical contacts to the solar-cell electrodes. A 5-mm-thick glass was placed over the cell to hold it. A resistance temperature detector (RTD) in contact with the cell was used to measure the cell temperature as it gave more reliable results than using an infrared temperature sensor (measuring through the glass superstrate). The measurement error with the RTD was evaluated at $\pm 2\text{ }^{\circ}\text{C}$.

(B) Oven setup: The cells were mounted on a measurement metal block using spring contact pins. The whole block was inserted in a furnace with a hole allowing the light to enter. Compared to (A), this setup required a longer temperature-stabilization time. The measurements were taken when the difference between the two RTD temperature measurements of the air and of the measurement block was less than $1\text{ }^{\circ}\text{C}$.

A crosscheck confirmed that the temperature control methods of (A) and (B) led to the same results. The *i-thick* series and the reference cell were measured with setup (A) and the hybrid LED-halogen simulator, whereas the other series were measured with setup (B) and the Wacom simulator. The effective irradiance arriving on the cell depends on the setup employed. For instance, the presence of an additional 5-mm-thick glass or the type of back reflector used reduced or enhanced J_{sc} and hence the P_{mpp} values. Therefore, the P_{mpp} values are the measured values if not otherwise indicated. The effective irradiance was calculated according to the ratio between the J_{sc} extracted from $I(V)$ measurements and J_{sc} values extracted from spectral response measurements (considered to correspond to the J_{sc} values at 1000 W m^{-2}). Moreover to allow the comparison of the J_{sc} values between the different series, they were, when indicated, adjusted to the J_{sc} values extracted from the spectral response measurement. Same normalization was used for the P_{mpp} .

For each experiment, we measured one to four cells per substrate. All cells were measured both in the annealed and light-soaked (ls, degraded) states. light-soaking was performed under three-sun-equivalent irradiation (3000 W/m^2 , similar to the AM1.5g spectrum) for 24 h at 50°C using a fully LED-based solar simulator [Stuc 14a].

Simulations

Numerical simulations were performed using the one-dimensional (1-D) simulation package Advanced Semiconductor Analysis (ASA 6.0) developed at Delft University [Zema 97]. The temperature was varied from -70°C to 80°C , taking into account experimentally determined temperature dependencies of the bandgap, refractive index, and extinction coefficient. These temperature dependencies were measured on intrinsic *a*-Si:H layers and are reported in Refs. [Stuc 13, Stuc 14c]. For the bandgap (E_g), the value of -0.63 meV/K was applied to all layers, similar to the values of Overhof *et al.*[Over 89]. Electron and hole mobility and their capture cross sections were assumed constant as no precise literature data was found for those parameters. The simulation input parameters are listed in the appendix. Most of the parameters are the same as used in [Stuc 14b]. However, some parameters were adapted to better fit the data over a large temperature range. This is particularly true for the electron affinities that are now closer to values reported in [Mats 84, Tasa 88]. Bandgaps and activation energies of the *p*-(*a*-SiC:H) layers were also slightly adapted.

4.2.2 Results and discussion

Chapter 4. Temperature dependence of thin-film and crystalline silicon-based solar cells

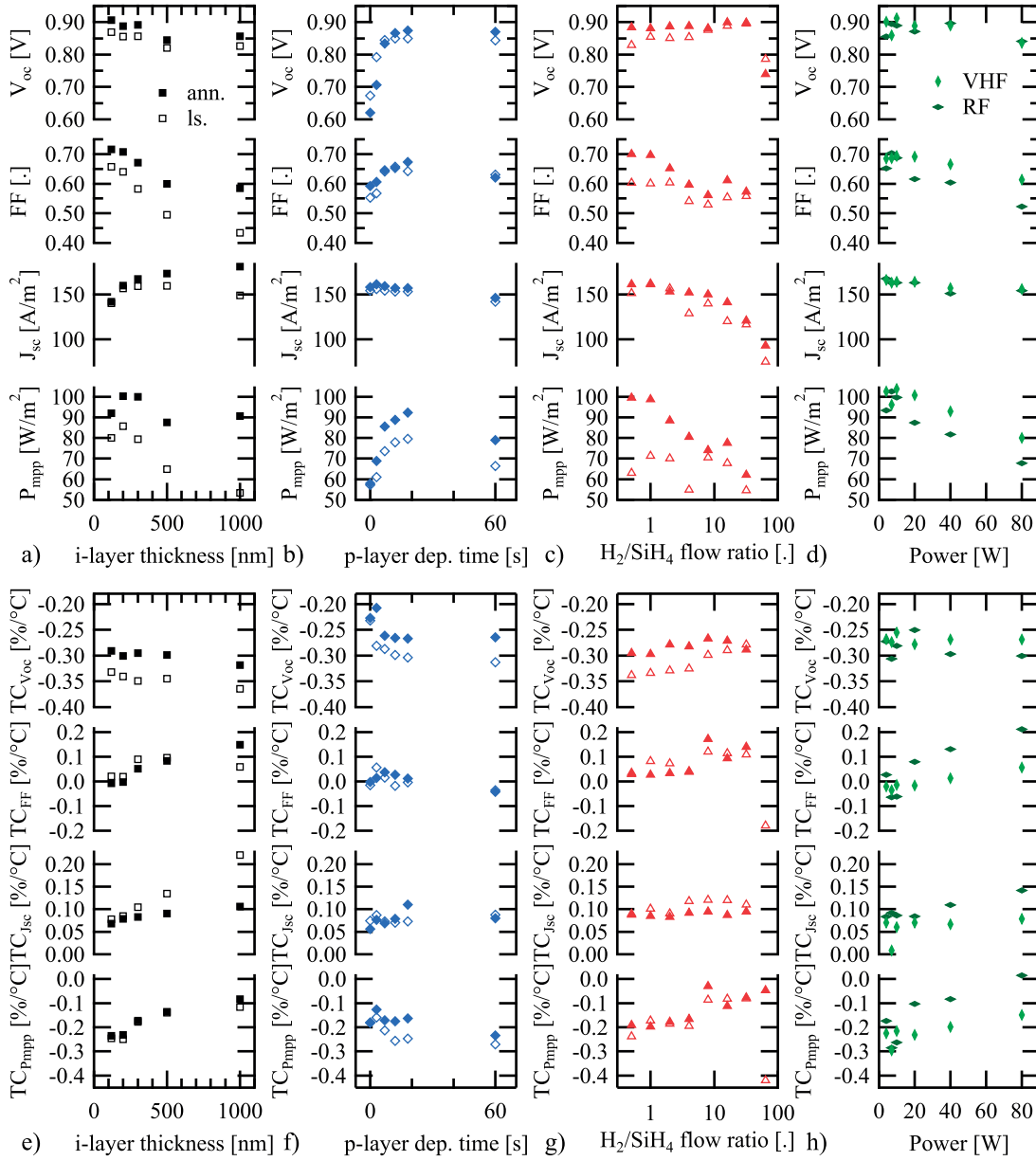


Figure 4.1 – I(V) parameters and their temperature coefficients for *a*-Si:H solar cells varying: a) and e): *i*-layer thickness (*i-thick.* series), b) and f) *p*-layer thickness (*p-thick.* series), c) and g) hydrogen/silane flow ratio (*dil.* Series), d) and h) RF and VHF power during *i*-layer deposition (*dep. rate* series). For a), b), c), e), f) and g) the annealed (solid diamond) and light-soaked (open diamond) states (24 h @ 50 °C, 3 suns) are plotted. For d) and h) only the annealed state is plotted. Each data point represents the mean values between one and four cells. The J_{sc} values are extracted from spectral response measurements and the P_{mpp} values are slightly adjusted to a value corresponding to an irradiance condition of 1000 W m^{-2} .

4.2. Amorphous Si cells temperature behavior

Figure 4.1 shows the I(V) characteristics and their TCs for cells of the four deposition-parameter series (introduced in section 4.2.1) in both the annealed and light soaked states. General trends of the I(V) characteristics and their TCs are summarized in Table 4.1. A TC increase or decrease means that the value goes towards $+\infty$ or $-\infty$ respectively. Each parameter is discussed separately in the next subsections.

Table 4.1 – Summary of the temperature coefficients and I(V) parameters for the analyzed series. " \nearrow ", " \searrow " and "=" mean increases, decreases and is stable with parameter increase respectively..

With	V_{oc}	$TC_{V_{oc}}$	FF	TC_{FF}	P_{mpp}	$TC_{P_{mpp}}$
Thicker <i>i</i> -layer	\searrow	\searrow	\searrow	\nearrow	\searrow	\nearrow
Thicker <i>p</i> -layer	\nearrow	\searrow	\nearrow	=	\nearrow	\searrow
Higher dil.	\nearrow	\nearrow	\searrow	\nearrow	\searrow	\nearrow
Higher dep. rate	=	=	\searrow	\nearrow	\searrow	\nearrow

Temperature coefficient of the open circuit voltage

For all series shown in Fig. 4.1, the V_{oc} decreases linearly with increasing temperature over the full temperature measurement range (15 °C to 80 °C). Therefore, a linear fit leading to the $TC_{V_{oc}}$ adequately describes the temperature behavior of the V_{oc} . $TC_{V_{oc}}$ is on the order of $-0.25\%/^{\circ}\text{C}$ for all series, whereas $TC_{J_{sc}}$ and TC_{FF} are closer to 0. Hence, $TC_{V_{oc}}$ governs $TC_{P_{mpp}}$ in most cases and turns it negative. At open circuit the recombination balances the photo- and thermally generated currents. In a first approximation, for *pn* junction type solar cells, the intrinsic-carrier density increases with temperature resulting in a V_{oc} reduction [Aror 82]. The temperature-induced bandgap reduction also contributes to a non-negligible V_{oc} decrease, however, to a less extent than the intrinsic-carrier increase [Fan 86, Gree 03]. In addition to those effects, especially for *a*-Si:H cells, other temperature dependencies of recombination processes influences the $V_{oc}(T)$ behavior (*e.g.* effects of traps, quasi-Fermi level shift influencing recombination).

Figure 4.2 shows $TC_{V_{oc}}$ in absolute values as a function of the V_{oc} for the *i-thick.* series in the annealed and light-soaked states for different irradiance levels. It shows a linear correlation that seems to follow the V_{oc} dependence described by Green [Gree 03] in Eq. 4.2:

$$\frac{dV_{oc}}{dT} = -\frac{\frac{E_{g0}}{q} - V_{oc} + \gamma \frac{kT}{q}}{T} \quad (4.2)$$

with

$$E_g = E_{g0} + T \frac{dE_g}{dT} \quad (4.3)$$

Chapter 4. Temperature dependence of thin-film and crystalline silicon-based solar cells

and γ a coefficient describing the temperature sensitivity of the mechanism determining the V_{oc} [Dupr 15]. In Fig. 4.2, we can group the TC_{Voc} values around two different lines with an offset in their linear relation: For the annealed state, we observe a generally higher TC_{Voc} than for the light-soaked state and a slightly higher slope of the TC_{Voc} dependence on the V_{oc} . According to Eq. 4.2, the different positions of those lines could for instance be explained by a different γ coefficient between the annealed and light soaked states. Moreover the slightly different slopes indicate that γ also slightly depends on irradiation.

Figure 4.2 (right) shows, similarly to (left), TC_{Voc} in absolute values as a function of V_{oc} for all series at ca. 1-sun intensity. We note that the linear relation also holds for the dilution series. But not the *p-thick.* and *dep. rate* series:

- In the *p-thick.* series, $TC_{Voc}(V_{oc})$ does not follow the general trend for cells, especially for thin *p*-layers. Instead we observe the opposite behavior: TC_{Voc} decreases with increasing V_{oc} (compare also Fig. 4.1c)). For all other series, the V_{oc} is predominantly controlled by the narrow-bandgap *i*-layer, hence, TC_{Voc} is governed by this layer. This is not true for thin *p*-layers, where the V_{oc} and TC_{Voc} are governed by the *p*-layer (*p*-(*a*-SiC:H)) thickness with a different temperature dependence than the one observed when V_{oc} is controlled by the *i*-layer. Thinner *p*-layers lead to a weaker quasi-Fermi-level splitting, hence, the electric field and V_{oc} are reduced [Stuc 10]. We propose two possible explanations for the observation of a decreasing TC_{Voc} with increasing V_{oc} in the *p-thick.* series: (1) Increasing temperature reduces trapped charges in the band tails that shield the electric field [Tayl 72, Stuc 10]. As result the standard decrease in V_{oc} (with the same mechanism as for the other series) is partially counterbalanced by less electric field shielding. (2) Increasing temperature increases the negative space charge in the *p*-layer due to more negatively charged acceptors. This effect increases the quasi-Fermi-level splitting, and hence, the V_{oc} . Those two effects are only significant for cells with thin *p*-layers as for thicker layers the space charge in the *p*-layer is higher and do no more limit the V_{oc} .
- For the *dep. rate* series, cells deposited at VHF follow roughly the linear trend except the cells deposited at high power (80 W). For RF the trend is even less clear. Different material qualities of the *i*-layer (raising deposition rate increases the defect concentration) that change the γ factor (the same effect at the origin of the difference between annealed and light soaked state as seen in Fig. 4.2) could explain this scattering of data points.

The correlation between V_{oc} and TC indicates that TC_{Voc} decreases with the *i*-layer thickness, following the V_{oc} decrease (Fig. 4.1a)). Similarly, TC_{Voc} increases with hydrogen dilution (Fig. 4.1b) due to the wider bandgap, hence higher V_{oc} . Furthermore, TC_{Voc} also decreases with light soaking for the *i-thick.*, *p-thick.* and *dil.* series because of the corresponding V_{oc} drop. Overall, we conclude that for the three series affecting the *i*-layer (*i-thick.*, *dil.*, *dep.*

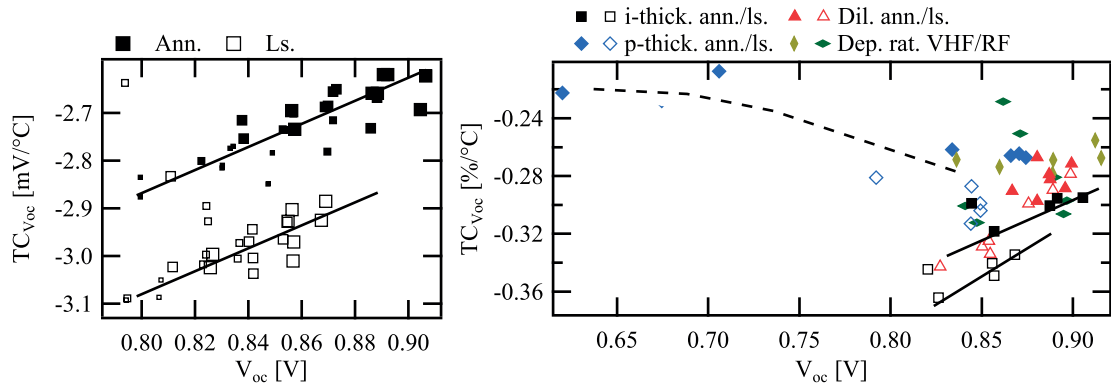


Figure 4.2 – (left) Temperature coefficient in absolute values of the V_{oc} ($TC_{V_{oc}}$) as a function of V_{oc} for the *i-thick.* series at different irradiation levels ($1300 W/m^2$, $800 W/m^2$, $600 W/m^2$ and $300 W/m^2$, marker size is proportional to the irradiation level) in the annealed (solid squares) and light-soaked (open squares) states. Lines are guides for the eyes. (Right) Mean of the temperature coefficient of the V_{oc} ($TC_{V_{oc}}$) values for each deposition parameter at irradiances between $1100 Wm^{-2}$ and $1300 Wm^{-2}$ in the annealed (solid markers) and light-soaked (open markers) states as function of the mean of the V_{oc} values. The solid lines are the same as in left and the dashed line is a guide for the eyes showing the *p-thick.* series trend.

rate), a higher V_{oc} at STC goes along with a higher $TC_{V_{oc}}$, and leads to a greater V_{oc} at higher temperatures. However, this is not the case for cells with thin *p*-layer.

Temperature coefficient of the fill factor: Experimental results

Figure 4.3 (left) shows the temperature dependence of the FF for the *i-thick.* series. In contrast to the $V_{oc}(T)$ curve, the $FF(T)$ curve is generally not linear and seems always to have a maximum (FF_{max}). This maximum depends on the substrate and degradation state and can vary over a large range of temperatures. A quadratic fit could account for the non-linearity, but is appropriate only if the maximum is in the temperature measurement range and the temperature range for fitting is narrow. Therefore, we used a linear fit to calculate TC_{FF} to allow for systematic comparison of the TCs of different cells³. In our case a shift of FF_{max} towards higher temperature enhances the value of TC_{FF} which is calculated using a linear fit in the operating temperature range.

Figure 4.3 (right) compares the linear TC_{FF} values of all cells from different series with the FF values at STC. As a general trend, the TC_{FF} decreases with an FF increase. This trend is significant for the *i-thick.*, *dep. rate* and *dil.* series (cf. Fig. 4.1a, 4.1c and 4.1d): increasing the *i*-layer thickness, the deposition rate, and the hydrogen dilution results in an increase of TC_{FF} (decrease of FF). For the *p-thick.* series, the TC_{FF} does not depend significantly on

³The $I(V)$ curves were measured by first increasing and then decreasing temperature. For cells with low FF , as the cells already degrades during measurements, the $FF(T)$ curve is slightly lower when going down with temperature. For the TC_{FF} fit all points (temperature increase and decrease curve) are taken into account.

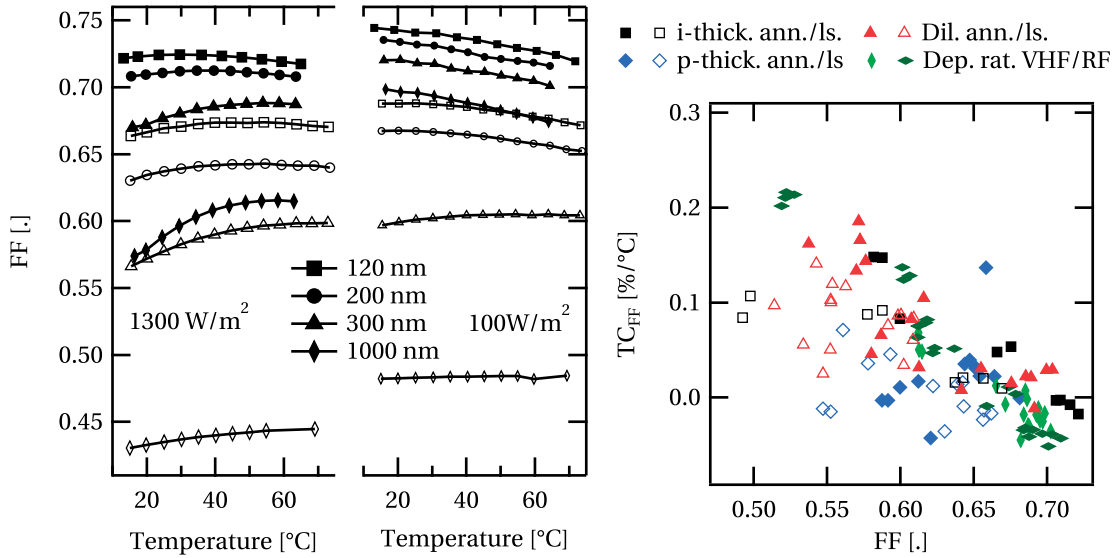


Figure 4.3 – (left) FF dependence on temperature for the *i-thick.* series measured at an irradiance of 1300 W/m^2 (left) and 100 W/m^2 (right) in annealed (solid markers) and light soaked (open markers) state. (right) TC_{FF} vs FF at 25°C for all series at irradiances between 1100 W m^{-2} and 1300 W m^{-2} in the annealed (solid markers) and light-soaked (open markers) states.

the *p*-layer thickness but the FF does. As for the V_{oc} the fact that the *p*-layer limits the FF induces a different temperature response than for *i*-layer-limited cells.

An interesting effect to note is the linear dependence of the $FF(T)$ curve maximum (FF_{max}) as a function of J_{sc} at 25°C , plotted in Fig. 4.4 for the reference cells. Lowering the irradiance pushes FF_{max} to lower temperatures. Here a quadratic fit is used to determine the maximum of the $FF(T)$. Below 2 mAcm^{-2} , the FF_{max} saturates due to the influence of shunts. The highest FF of the reference cell is obtained at J_{sc} of 2 mAcm^{-2} corresponding to about 0.15 suns (Fig. 4.4 right). Likewise, for the *i-thick.* series FF_{max} shifts to lower temperature for thinner *i*-layers as seen in Fig. 4.3. Figure 4.5 shows the I(V) curve of the standard cell at about 1 and 0.1 sun at temperatures from -60°C to 80°C . We see clearly that at very low temperature the curve begin to become S-shape under different illumination. However this is not the case at 0.1.

For the curves whose FF_{max} values are in the temperature measurement range (and can thus be experimentally observed), we see that light soaking shifts FF_{max} towards higher temperatures: For the *i-thick.* series, FF_{max} shifts by 17°C for the thinnest layers and by 5°C for the thickest layers (Fig. 4.3, left). The FF_{max} temperature increase with light soaking is most probably a global trend. Hence for the *i-thick.* and *dil.* series, in most cases, light soaking slightly enhances TC_{FF} . For the thickest cell (1000-nm-*i*-layer) the FF_{max} temperature also increases with light soaking, however the TC_{FF} decreases because the FF dependence becomes weaker at high temperature.

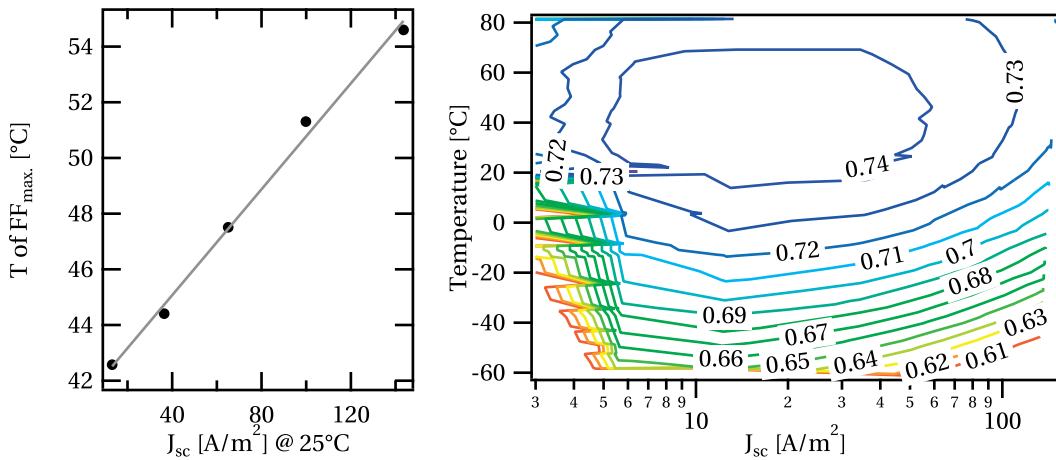


Figure 4.4 – (Left) Temperature of the FF maximum (FF_{max}) as a function of J_{sc} at 25°C for the reference cell (J_{sc} controlled by the illumination intensity). (Right) FF as a function of J_{sc} and temperature of the same cell.

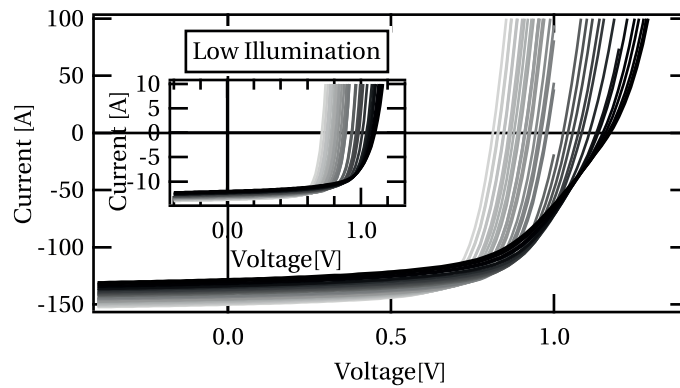


Figure 4.5 – $I(V)$ curve of a reference cell at 1 and 0.1 sun from $-60^{\circ}C$ to $80^{\circ}C$, the darker the colder.

Temperature coefficient of the fill factor: Modeling

In order to understand the existence of a FF_{max} , we simulated the $I(V)$ characteristic with ASA. Figure 4.6 shows the FF dependence on temperature, comparing the simulations with measurements of the reference solar cell. The experimental trends are fairly well reproduced by our model, e.g. the existence of FF and P_{mpp} maxima around $40^{\circ}C$ and $0^{\circ}C$ respectively, with lower FF and P_{mpp} both at lower and at higher temperatures. As observed in the experiment, lower irradiance implies a shift of the $FF(T)$ curve maximum to a lower temperature. The assumption of constant hole and electron mobility with temperature as well as interface effects (such as inhomogeneities, not sharp interface, boron diffusion) and 2-D effects that are not taken into account could explain the discrepancies.

According to our model the FF_{max} value at $40^{\circ}C$ corresponds to the internal electric field

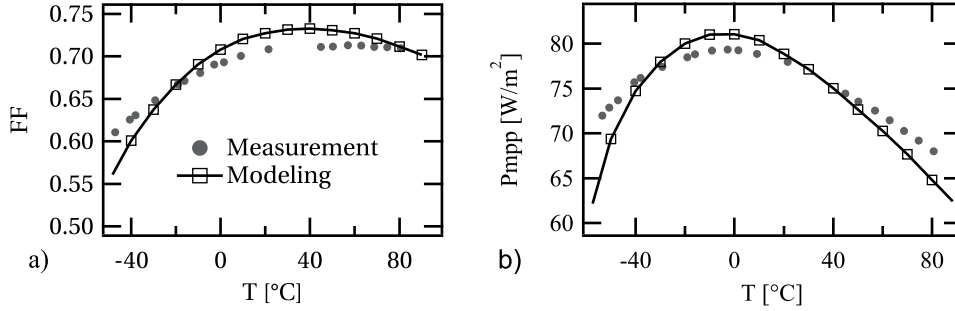


Figure 4.6 – ASA simulated and measured FF a) and P_{mpp} b) as a function of the temperature for the reference cell.

maximum in the central part of the i -layer (highest carrier extraction efficiency). Moving to a higher temperature will decrease the electric field and hence the FF value. The FF decrease is probably due to the V_{oc} decrease with temperature as for c -Si solar cells [Gree 03]. However, in contrast to c -Si cells the decrease is significantly lower. This could be explained by less recombination at higher temperatures due to both, the higher effective mobilities of the carriers [Stre 91] and annealing of dangling bonds. Those two effects are more intense for lower material quality (more defects) and hence explain the higher TC_{FF} for lower FF (Fig. 4.4). In contrast to c -Si cells, there is a certain temperature below which the FF starts decreasing. Considering the simulated band diagram for a forward-bias voltage close to the V_{mpp} (0.4 V) shown in Fig. 4.7, we see that at the p -(a -SiC:H) layer, from 80°C until the FF_{max} temperature (40°C), the quasi-Fermi level of holes (E_F^p) (green ellipse in Fig. 4.7) pins to an energy level defined by the activation energy (given by doping concentration). By further reducing the temperature, the E_F^p energy band is no longer pinned but moves towards the valence band edge and hence to a lower energy than the one defined by the activation energy. At the same bias voltage in the dark, E_F^p remains on the activation energy level. This means that the photogenerated hole concentration is no longer negligible compared to the thermally activated hole concentration as is the case at higher temperatures. Therefore, the space-charge in the p -(a -SiC:H) layer becomes more positive and hence lowers the electric field in the i -layer, which deteriorates the extraction of carriers and hence the FF .

The temperature of FF_{max} is sensitive to different parameters that influence the electrical properties of the interfaces and have an effect on hole accumulations in the p -(a -SiC:H) and p -type μc -Si:H layers. Of particular importance are band offsets (driven by different bandgaps and electron affinities), band-tail properties (through the space charge due to trapped carriers), and the activation energy. For example, an activation-energy increase of the p -(a -SiC:H) layer shifts the maximum to a higher temperature, which is in agreement with the preceding explanations. Accordingly, FF_{max} shifts to lower temperatures when the current density is lowered. This behavior was confirmed both experimentally (cf. Fig. 4.4) and by our simulations (not showed). To verify that this effect is not caused by our specific solar cell design, we simulated the dependence of FF as a function of temperature $FF(T)$ for solar

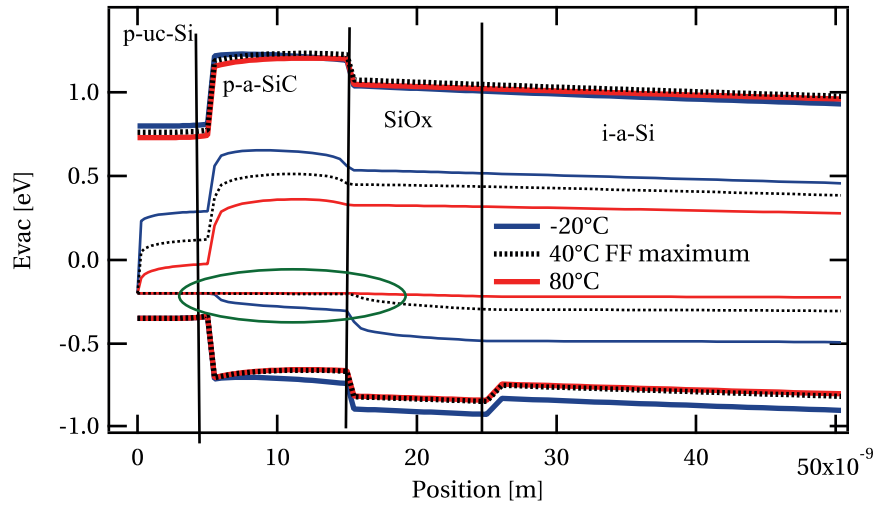


Figure 4.7 – Band diagram of the p -side of the cell from the ASA modeling at a forward-bias voltage of 0.4 V for different temperatures. Thick lines represent the conduction bands (top) and the valence bands (bottom). In between the thin lines represent the quasi-Fermi levels of the electrons and holes. The green ellipse shows the quasi-Fermi levels of holes responsible for the $FF(T)$ curvature.

cells without a -SiO:H layers and found the same trends. Hence, the effect of positive charging of the p -layer causing a drop of the electric field seems to be valid for most state-of-the-art a -Si:H solar cells.

Temperature coefficient of the short circuit current density

For all solar cells series with exception of the p -thick series, we observe a positive linear relation between the J_{sc} and the temperature with $TC_{J_{sc}}$ values that are typically between 0.05 %/°C and 0.13 %/°C. However, the cells with the thickest i -layer had a high $TC_{J_{sc}}$ of 0.2 %/°C in the light-soaked state. Figure 4.8 shows the temperature-dependent external quantum efficiency measurements of cells with an i -layer thickness of 120 nm or 1000 nm in the annealed state. We measured J_{sc} ($TC_{J_{sc}}$) values of 13.7 mA/cm² (0.06 %/°C) and 17.6 mA/cm² (0.11 %/°C) respectively. For the thinner cell, more than 88% of the current increase with temperature originates at wavelengths over 600 nm. Moreover the largest current increase is located at 710 nm (1.75 eV) which is in the range of the bandgap of a -Si:H cells. For the thicker cell, 71% of the current increase originates at wavelengths over 600 nm. Therefore the largest contribution to enhancement of the J_{sc} with temperature seems to come, as explained from the temperature-induced bandgap reduction leading to more absorption in the infrared region. In addition, especially for cells with high defect density and hence low FF , decrease of carrier recombination with temperature (due to higher effective mobility [Stre 91]) also contributes to the $TC_{J_{sc}}$ increase. This can be seen by representing the $TC_{J_{sc}}$ as a function of FF (Fig. 4.9), where the better FF (qualitatively indicating defect density in the i -layer)

Chapter 4. Temperature dependence of thin-film and crystalline silicon-based solar cells

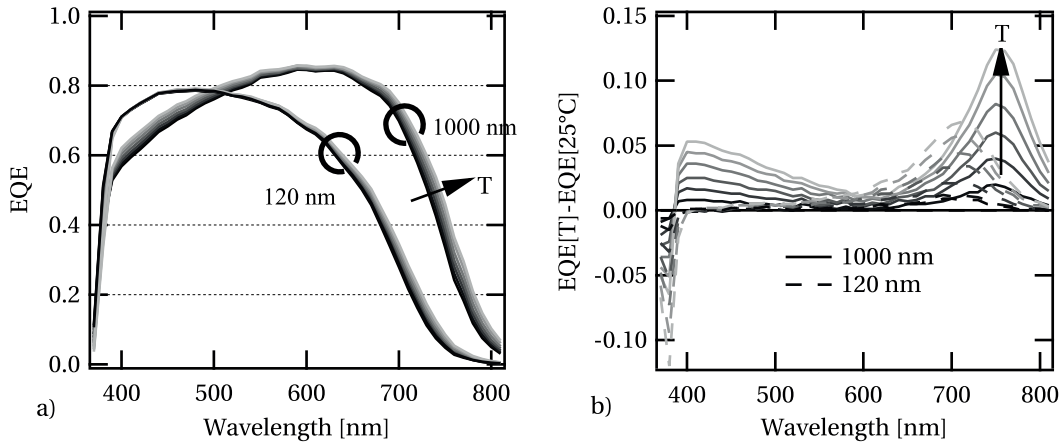


Figure 4.8 – a) External quantum efficiency (EQE) measurement results of annealed solar cells with a 120-nm-thick or 1000-nm-thick *i*-layer as a function of temperature. Black lines correspond to 15 °C and the lightest grey to 75 °C. b) EQE variation with temperature for the two cells. The darker the colder.

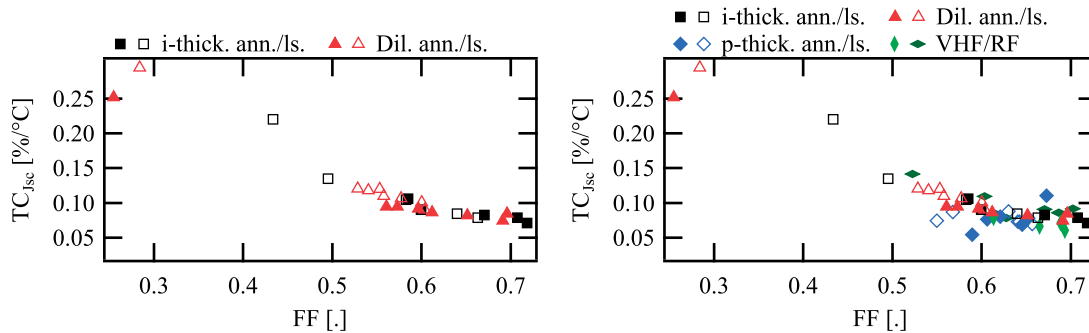


Figure 4.9 – Temperature coefficient of the short-circuit current as a function of FF for the *i*-thick. the *dil.* (left and right), *p*-thick. and *dep. rate* (right) series in the annealed (closed markers) and light-soaked (open markers) states.

corresponds to worse (lower) TC_{Jsc} . This behavior can also be seen in Fig. 4.8 where for the thickest cell (with high recombination and low FF) a current increase between 400 nm and 550 nm was measured. For high- FF (in our case thin) cells with low recombination this effect is smaller.

Temperature coefficient of the maximum power point

By combining the definitions of the FF and the TC , the $TC_{P_{mpp}}$ can be approximated by summing the $TC_{V_{oc}}$, TC_{FF} and TC_{Jsc} . In this work all $TC_{P_{mpp}}$ values were directly extracted from the $P_{mpp}(T)$ curves. The difference between the $TC_{P_{mpp}}$ and the sum of the other TC values was found to be less than 0.01 %/°C which is negligible. Because of the non-linearity of the $FF(T)$ curve, the $P_{mpp}(T)$ curve is also non-linear. The following trends are observed (cf.

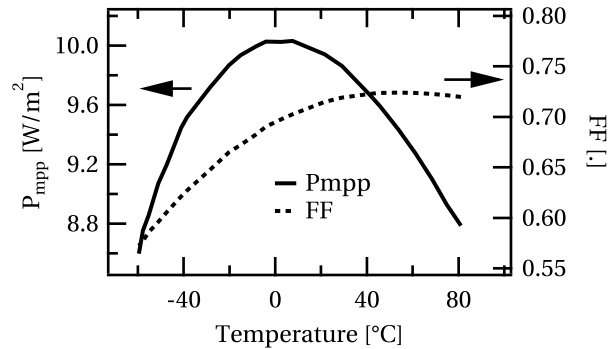


Figure 4.10 – FF and P_{mpp} of the reference a -Si:H cell in the initial state.

Fig. 4.1 and Table 4.1):

- For the *i-thick.*, *dil.* and *dep. rate* series, $TC_{P_{mpp}}$ increases with thickness, dilution and power due to the increase of TC_{FF} which is the TC that varies the most. P_{mpp} decreases.
- For the *p-thick.* series, $TC_{P_{mpp}}$ is governed by TC_{Voc} , hence it decreases with increasing *p*-layer thickness.

The existence of a maximum of FF as a function of temperature and the dominance of the TC_{FF} at low temperature for $TC_{P_{mpp}}$ leads to a $P_{mpp}(T)$ curve maximum which is always at a lower temperature than the temperature of FF_{max} because of the negative TC_{Voc} (see Fig. 4.10). For state-of-the-art cells, the P_{mpp} maximum is typically around 0 °C in agreement with the work of Stiebig *et al.* [Stie 96].

Figure 4.11 (left) shows the interpolated in temperature and irradiance P_{mpp} values (based on measurements) of the *i-thick.* series for three different irradiation intensities (700 W/m², 1000 W/m² and 1300 W/m²). The interpolated efficiency as a function of irradiance for 25 °C and 60 °C is showed in Fig. 4.11 (right). The *i*-layer thickness changes the low light behavior as well as the temperature. These interpolations are used to calculate the energy output in section 4.2.2). For the thickest cell, the $P_{mpp}(T)$ curve reaches a maximum at 35 °C at 1000 W m⁻².

Energy output

If the $P_{mpp}(T)$ curves for the different material parameters never cross each other at any irradiance intensity in the operating temperature range, the cell with the best power rating at STC will also have the best energy output (per m²). For most series there are no such crossings, which means that the best cell at STC also has the best energy output. Only the *i-thick.* series presents such crossings for the 120 nm/1000 nm and the 200 nm/300 nm curves (Fig. 4.11). Moreover, the crossing temperature depends on irradiance. For the *i-thick.* series, to estimate the energy output in Neuchâtel for 2014, we used a very simple model neglecting spectral and angular effects, taking in account only the irradiance and the module

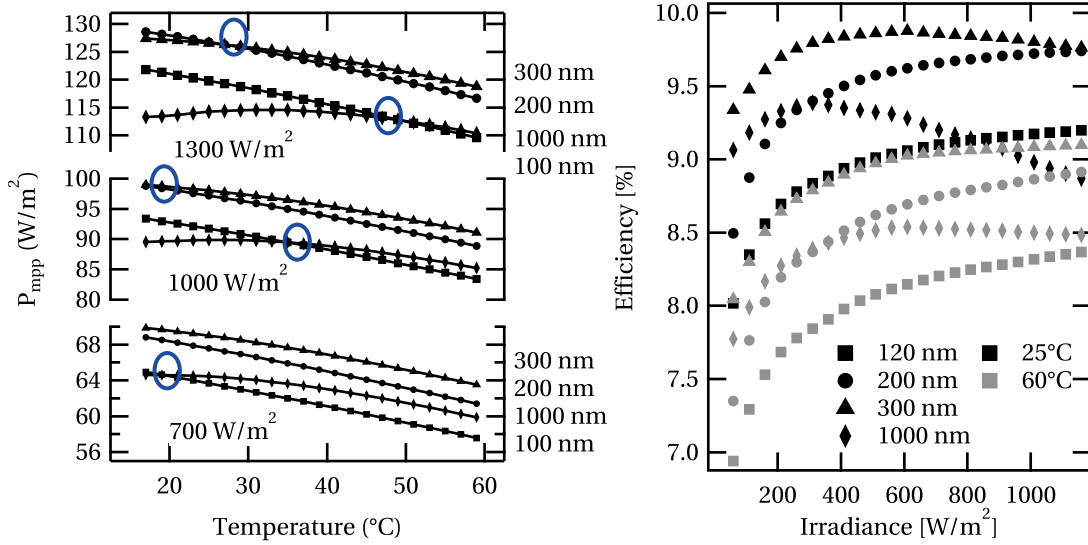


Figure 4.11 – (Left) Interpolated P_{mpp} for the *i-thick*. series at 1300 W/m², 1000 W/m² and 700 W/m² in annealed state. The blue circles indicate the crossing points between two different $P_{mpp}(T)$ curves. (Right) Interpolated efficiency as a function of irradiance at 25 °C (black) and 60 °C (grey).

temperature. Module temperature (using the Sandia module and cell temperature model [King 04]) and in-plane irradiation were derived from global horizontal irradiance (GHI) and the air temperature measurement (with 10 minutes granularity) of the local weather station (MeteoSwiss). The P_{mpp} for each time step was determined by interpolating the $P_{mpp}(T, G)$ (I is the global irradiance) matrix generated from indoor measurements.

By applying this procedure to the *i-thick*. series, in the annealed state, the best cell at STC (W_p) is the 300-nm-*i*-layer cell, which is also the cell with highest energy output (Fig. 4.12) and Table 4.2). The 200-nm-*i*-layer cell has almost the same performance at STC, but the energy output is significantly lower. In the light-soaked state the cell with highest power is

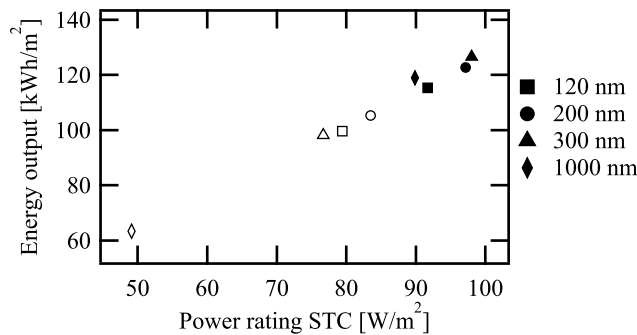


Figure 4.12 – Simulated energy output as a function of P_{mpp} at STC for the *i-thick*. series in the annealed (solid markers) and light soaked (open markers) states.

4.3. Microcrystalline Si cells temperature behavior

again the one producing the most energy but it is now the 200-nm-*i*-layer cell because it degrades less during light soaking. Therefore at this location (Neuchâtel, Switzerland) cells optimized for STC will also have best energy output. However, as there is a crossing near 25 °C between different $P_{\text{mpp}}(T)$ curves, it could be that for slightly different cells the crossing could be significantly above 25 °C for frequent irradiance conditions implying that the cell should be optimized for energy output rather than STC.

Table 4.2 – Power at STC (W_p) and estimation of yearly energy output for the *i*-thick. series.

<i>i</i> -layer (nm)	Annealed		Light soaked	
	W_p (W/m^2)	energy output ($kWh/year$)	W_p (W/m^2)	energy output ($kWh/year$)
120	91.7	115.4	79.4	99.6
200	97.2	122.7	83.5	105
300	98.0	126.5	76.7	98.2
1000	87.2	115.3	64.0	84.0

4.3 Microcrystalline Si cells temperature behavior

There are only few reports on the temperature behavior of microcrystalline silicon (μc -Si:H) solar cells [Meie 98, Yama 99, Srip 07]. To understand their temperature behavior as a function of their material properties, we⁴ measured temperature dependent I(V) characteristics of various solar cells types such as: cells implementing specific buffer layers, high V_{oc} cells, highly crystalline cells based on the use of silicon tetrafluoride and we compared them to standard cells, in *p-i-n* configuration.

4.3.1 Experimental details

For more information on standard μc -Si:H cells refer to chapter 2.1.2.

Cell types and main characteristics

The temperature behavior of the following cell series were analyzed:

Buffer layer series: Amorphous silicon is known to passivate well the surface of *c*-Si and is used in Si heterojunction cells, allowing for V_{oc} values as high as 750 mV [Tagu 14]. Here, *i*-*a*-Si:H/*n*-*a*-Si:H (5 nm to 20 nm/5 nm) layers are introduced at the intrinsic μc -Si:H and *n*- μc -Si:H interface, to enhance the V_{oc} of these cells by passivating the interface [Yue 08, Hann 15]. The *TC* of cells with (*Buffer*) and without (*No Buffer*) these buffer layers, deposited on smooth (*Z5 45*) and rough (*Z5 20*) ZnO front electrodes were measured to test the effect of this buffer layer on the temperature behavior. These cells have an *i*-layer thickness of 1.2 μm .

⁴Y. Riesen, S. Hänni, C. Ballif and N. Wyrsh

Chapter 4. Temperature dependence of thin-film and crystalline silicon-based solar cells

High V_{oc} series: The TC of solar cells with *high* V_{oc} values (above 600 mV) fabricated in our laboratory (Hänni *et al.* [Hann 15]) were measured. These cells have a buffer layer similar to the cells described in the previous paragraph (*Buffer*) but their *i*-layer is thinner (600 nm) to push the V_{oc} to higher values. Again, cells with rough and smooth front electrodes are compared.

High crystallinity series: This series comprises cell with highly crystallized microcrystalline silicon (μc -Si:H) *i*-layers obtained by PECVD using silicon tetrafluoride (SiF_4) as silicon precursor. They are used to assess the potential of μc -Si:H cells with potentially high current due to highly crystalline layers [Hann 14]. Cells deposited on rough and smooth substrate are labeled *HC Z5 20'* and '*HC Z5 45'* respectively. The effect of highly crystallized cells on the temperature behavior is studied.

Standard cell: The temperature dependence of a standard μc -Si:H cells on smooth substrate was measured (*Std Z5 45'*). These cells were deposited after the move of our laboratory and are, therefore, based on an adjusted recipe. Moreover, the cells were deposited with another reactor at a lower frequency than the previous cells.

Measurements

Except for the *Std Z5 45'* cells measured with the cell tester from $-50^\circ C$ to $80^\circ C$ (Fig. 4.13), all μc -Si:H cells were measured with the two lamp solar simulator and the temperature control was done with the oven setup (see section 4.2.1 for more details) from $20^\circ C$ to $80^\circ C$. For each cell type 2-4 cells were measured and we will here plot the mean value with standard deviation.

4.3.2 Results and discussion

Figure 4.13 shows the different IV parameters of the standard μc -Si:H cell at different irradiances ($1320 W m^{-2}$ to $7 W m^{-2}$) from $-50^\circ C$ to $80^\circ C$. We note that:

- The V_{oc} and J_{sc} values follow a linear behavior with respect to temperature on the whole measurement range (as for *a*-Si:H cells see section 4.2.2).
- The FF values as a function of temperature, reach a maximum (FF_{max}) that shifts to lower temperatures when the irradiance is reduced. Despite the fact that μc -Si:H and *a*-Si:H materials are different, we suggest that the same hole accumulation effect as described in section 4.2.2 is responsible for this maximum. This hypothesis is based on the fact that as for *a*-Si:H, μc -Si:H cells exhibit doped layers (*p* and *n*) that are very thin compared to the *i*-layer. However, this maximum occurs at a lower temperature than for most *a*-Si:H cells, i.e. for an irradiance of $1300 W m^{-2}$: the FF_{max} value of the standard μc -Si:H cells is located at a temperature of $0^\circ C$, while for *a*-Si:H it is located at $50^\circ C$. Moreover the FF_{max} shift with irradiance is more than 2 times higher for μc -Si:H than for *a*-Si:H. A probable cause for this lower FF_{max} temperature could be the different

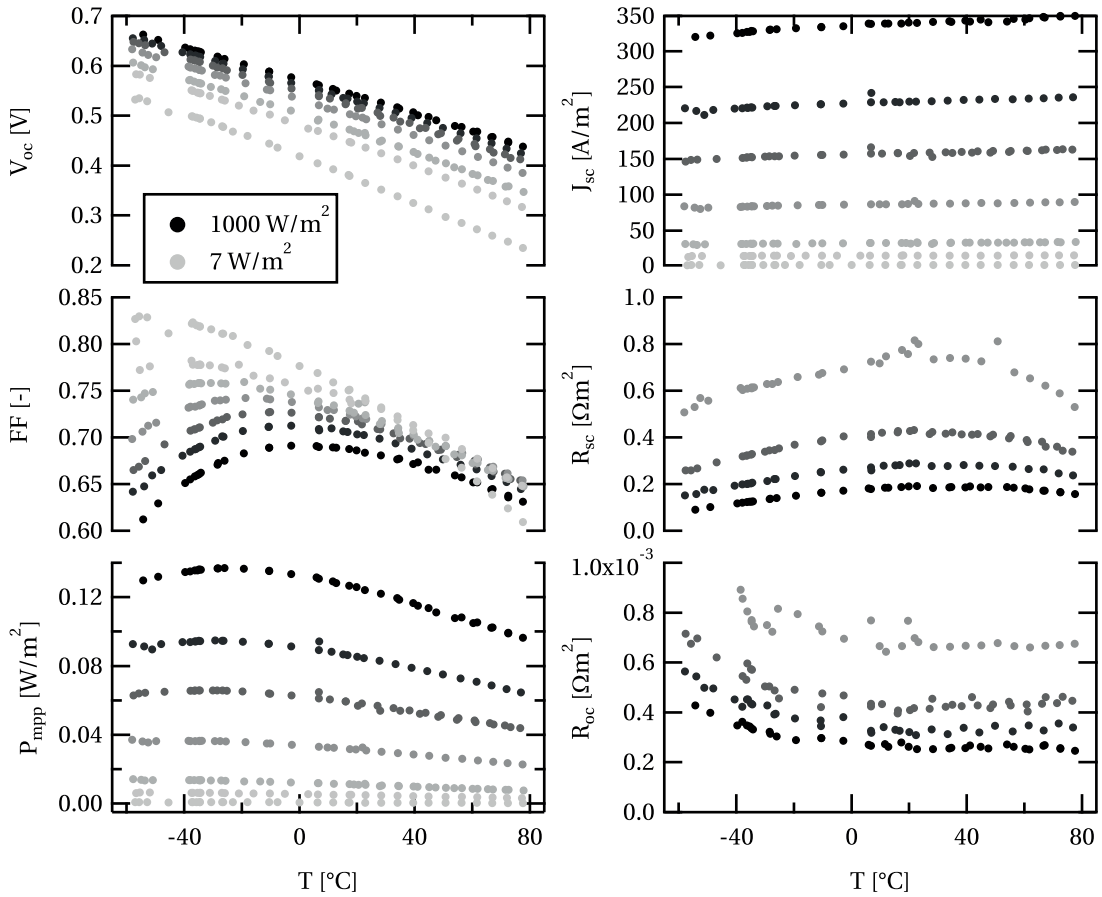


Figure 4.13 – IV parameters of a standard μc -Si:H cell (*Std Z5 45'*) at different irradiation levels (from 1320 W m^{-2} corresponding the black dots to 7 W m^{-2} corresponding to the lightest grey) as a function of temperature.

band mismatch at the p - i interface between a -Si:H and μc -Si:H cells modifying the accumulation of holes mechanism.

- The P_{mpp} values as a function of the temperature reach also a maximum induced by the $FF(T)$ curve. However it occurs at lower temperature (-30°C) than for a -Si:H cells (0°C) because of the lower FF_{max} temperature.
- From 80°C until -20°C the R_{oc} is constant, lowering the temperature further it increases. A higher series resistance in the cell due to charge accumulation at the p - i interface could explain this behavior.
- For all temperatures and irradiance no s-shape is found in the I(V) curves.

Figure 4.14 shows the TC of the I(V) parameters of μc -Si:H cells with different material properties. The TC_{FF} and TC_{Jsc} variation among the different cell type are relatively small (with exception of the TC_{Jsc} of the MBF Z5 20' cells that is two times higher than the others).

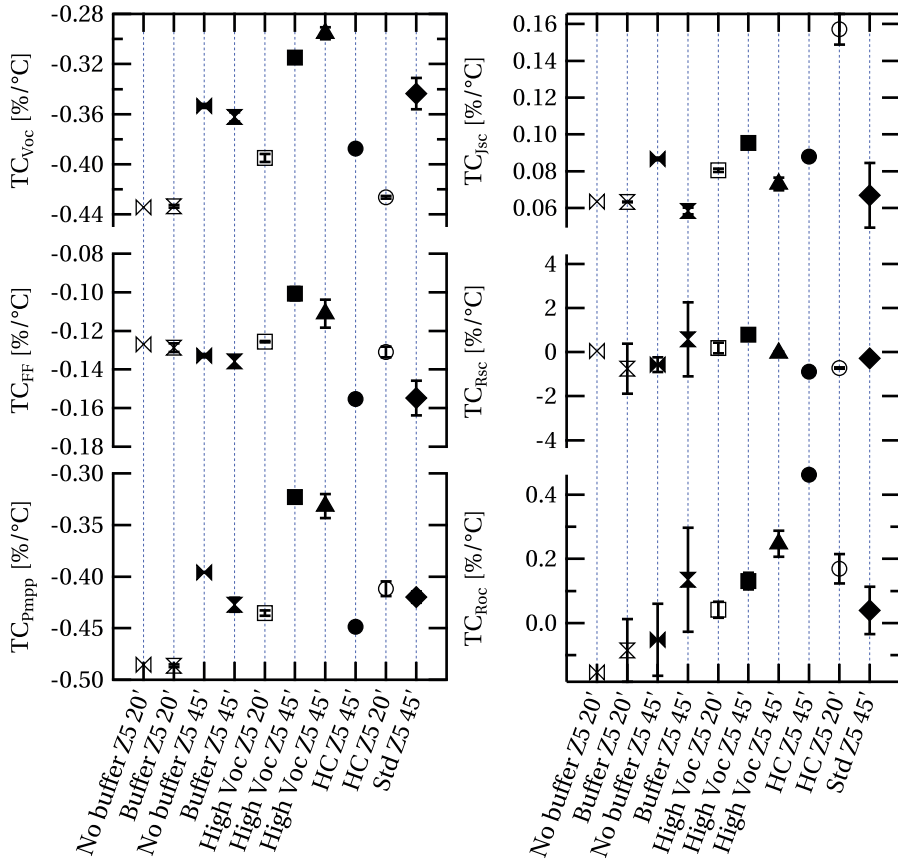


Figure 4.14 – IV parameter's temperature coefficients of the different μc -Si:H cells at an irradiance of about 1000 W m^{-2} except for the standard cell (1300 W m^{-2}). The error bars represents the standard deviation.

However the TC_{Voc} show some variations. For example the difference between the lowest and the highest TC_{Voc} reaches $0.14 \text{ \%}/^\circ\text{C}$. Furthermore the relationship between V_{oc} and TC_{Voc} is linear, as already observed in section 4.2.2 and shown in Fig. 4.15.

The influence of material properties on the TC can be summarized as follows:

- Adding a buffer layer (*Buffer*) do not change significantly the TC compared to the μc -Si:H solar cell *without buffer*. The fact that the buffer layer is introduced at the *i-n* interface could explain that no significant effect is seen for the TC_{FF} (as the TC_{FF} is probably more sensitive to the *p-i*- interface as suggested by the modeling in Sec. 4.2.2). However the front electrode roughness influences the TC_{Voc} value through its influence on V_{oc} . All TC_{Voc} as a function of the V_{oc} data points are on the same line.
- *High V_{oc} Z5 45'* cells have the highest TC_{Voc} values of our experiment ($-0.29 \text{ \%}/^\circ\text{C}$ and hence TC_{Pmp} values ($-0.32 \text{ \%}/^\circ\text{C}$). A rough electrode (*High V_{oc} Z5 20'*) reduces V_{oc} and

4.3. Microcrystalline Si cells temperature behavior

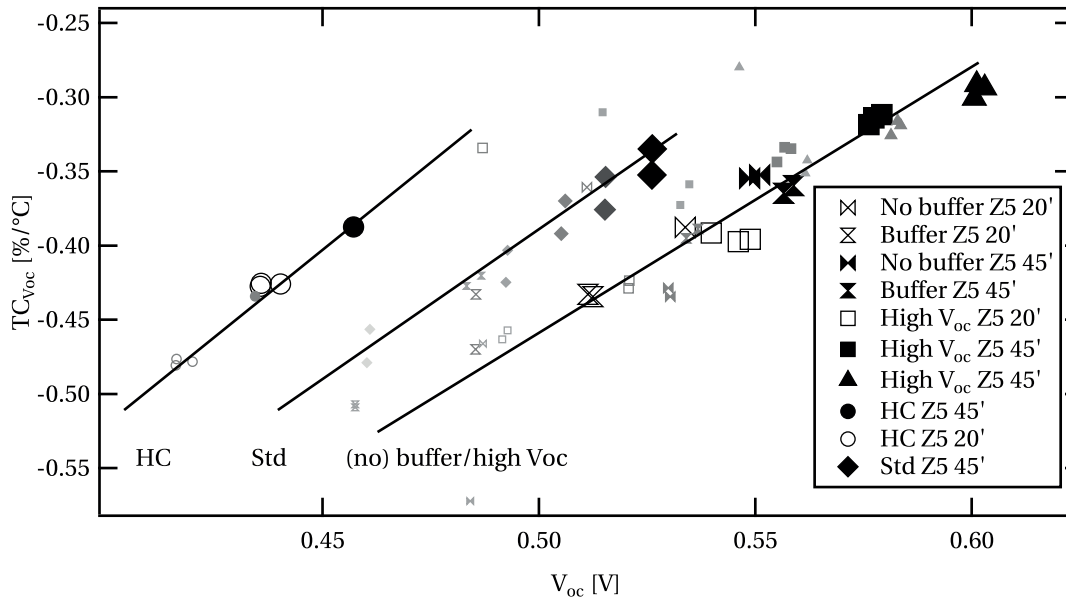


Figure 4.15 – $TC_{V_{oc}}$ as a function of the V_{oc} for the different μc -Si:H cells. The solid and open markers are cells deposited on smooth ($Z5\ 45'$) and on rough ($Z5\ 20'$) front electrodes, respectively. The size of the markers corresponds to the irradiation level, where the biggest markers correspond to the highest irradiation (between 1000 Wm^{-2} and 1300 Wm^{-2}). The lines are guide to the eyes.

as a result the $TC_{V_{oc}}$ decreases.

- Highly crystallized μc -Si:H i -layers (HC) affects the TC values of the solar cells through its V_{oc} variation. However compared to their V_{oc} , the $TC_{V_{oc}}$ values are slightly higher than for *no buffer*, *buffer* and *high V_{oc}* cells.
- The $TC_{V_{oc}}$ of the standard cell as a function of the V_{oc} line is located between the HC series and the others series.

In general, it is mainly the V_{oc} value of μc -Si:H cells that determines the temperature behavior of $P_{m_{pp}}$ in the operating temperature range. It is due to the almost linear dependence of the $TC_{V_{oc}}$ with V_{oc} . As rough electrodes are often leading to the growth of more defective μc -Si:H material [Pyth 09a] and resulting in lower V_{oc} , the $TC_{P_{m_{pp}}}$ values of cells with rough electrodes ($Z5\ 20'$) are lower than the one of cells deposited on smooth electrodes.

In Fig. 4.15 we can separate the data points in three different correlation lines. We draw lines as guide to the eyes:

- The *Buffer*, *no buffer*, *high V_{oc}* cells line at different irradiances and substrate roughness.
- The *Std $Z5\ 45'$* line, which is slightly shifted to the left because the material quality is better due to a lower deposition rate than for the other cells mentioned above. Hence

Chapter 4. Temperature dependence of thin-film and crystalline silicon-based solar cells

the i -layer is more dense and should contain less porous volume.

- The highly crystallized solar cells (HC) with SiF_4 i -layer line is even more shifted to the left, probably because of different material properties.

The different lines reflect the different γ parameter of Equ. 4.2 due to slightly different material properties and hence different related recombination functions. Note that the roughness of the front electrode do not changes significantly the γ despite the fact that it changes the recombination function.

Comparing to a -Si:H solar cells the FF_{\max} and hence the P_{mpp} maximum of μc -Si:H cells is located at temperatures about 30°C lower than for a -Si:H. The $TC_{P_{\text{mpp}}}$ for μc -Si:H has a value between $-0.32\%/^\circ\text{C}$ and $-0.45\%/^\circ\text{C}$ which is lower than the values for a -Si:H (between $-0.1\%/^\circ\text{C}$ and $-0.2\%/^\circ\text{C}$). These lower values seem to be mainly due to the lower TC_{FF} values of μc -Si:H cells induced by their lower FF_{\max} temperature. The $TC_{V_{\text{oc}}}$ values seems also to be slightly higher for a -Si:H (between $-0.25\%/^\circ\text{C}$ and $-0.35\%/^\circ\text{C}$) than for μc -Si:H (between $-0.32\%/^\circ\text{C}$ and $-0.44\%/^\circ\text{C}$), because of the higher V_{oc} values of a -Si:H cells (see equation Equ. 4.2).

4.4 Multi-junction thin-film silicon cell temperature behavior

In this section we present the results of temperature dependent $I(V)$ and spectral response measurements (EQE) for micromorph (a -Si:H/ μc -Si:H) and triple junction (a -Si:H/ μc -Si:H/ μc -Si:H) thin-film silicon solar cells. Only few papers on this subject are found in literature and they generally only report the TC values [Srip 08, Srip 11, Virt 10]. Yunaz *et al.* made some numerical simulation of micromorph solar cells [Yuna 07]. We measured the $I(V)$ characteristics of those cells at different spectra and temperatures to evaluate the temperature dependence of each sub-cells.

4.4.1 Experimental details

The current mismatch is here defined as the difference between the J_{sc} values of the top cell and the J_{sc} value of the bottom cell ($J_{\text{sc,top}} - J_{\text{sc,bot}}$). In our case, it is calculated from the current determined by EQE measurements of the component cells and a simulated spectrum of the solar simulator (inducing some small inaccuracies). The current mismatch is varied by changing the spectrum of the irradiance (using the same principle as the current matching machine, CMM [Bonn 13]). The spectrum was choose such that the sum of the current densities of the two subcells is always equal (25 mA cm^{-2} for this sample). The $I(V)$ measurements were performed by the cell tester setup. The temperature dependence of micromorph tandem solar cells (see section 2.1.2) is investigated by measuring its $I(V)$ characteristic at different temperatures (18°C to 70°C) and current mismatch between the top and the bottom cell (from -7 mA cm^{-2} to 5.5 mA cm^{-2}). At the end of this section, we also show the temperature depen-

4.4. Multi-junction thin-film silicon cell temperature behavior

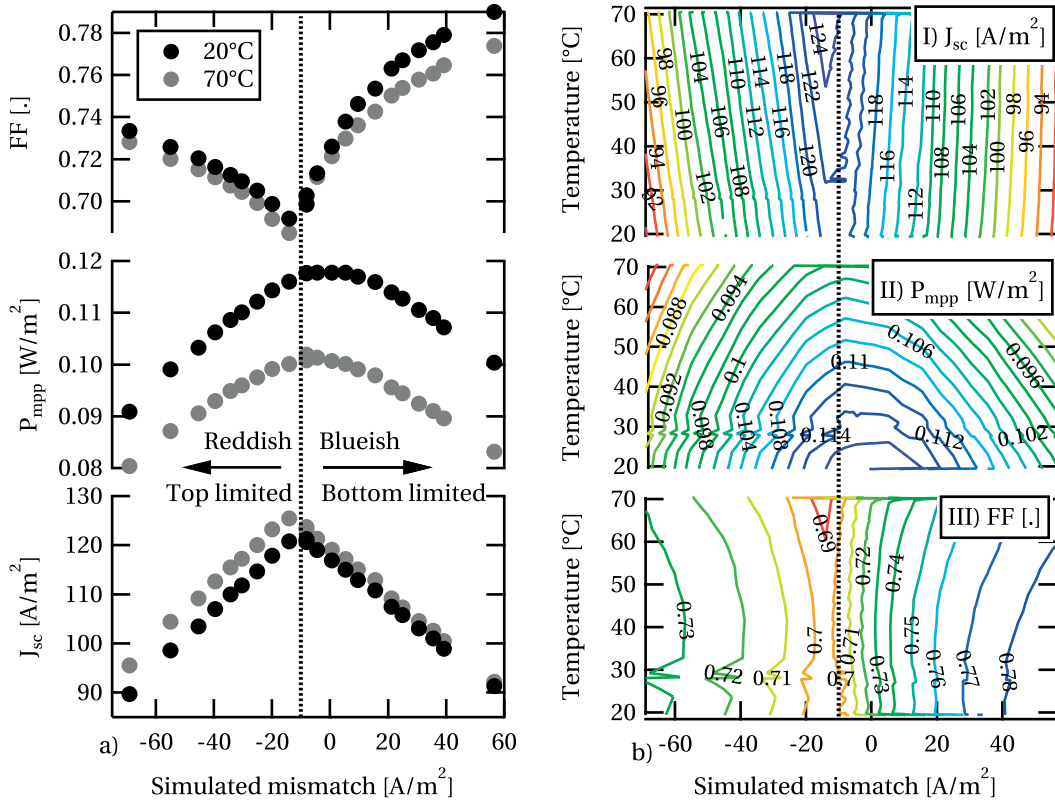


Figure 4.16 – I(V) characteristics as a function of temperature and current mismatch between the top cell (*a*-Si:H) and the bottom cell (μ c-Si:H) of a micromorph thin-film silicon cell. The more negative the mismatch the more reddish is the spectrum of the incoming light. The dashed vertical line represents the x-position where the currents are actually matched at 25 °C.

dence of the performance of thin-film silicon triple-junction cells composed of an *a*-Si:H top cell and μ c-Si:H middle and bottom cells. More details on these devices can be found in [Schu 14, Schu 15]. These cells were measured with the Wacom simulator at 1000 Wm⁻² and with mesh filters for varying irradiance intensities at temperatures from -60 °C to 70 °C.

4.4.2 Results and discussion for micromorph cells

The current densities of the subcells as determined from the EQE for AM1.5G spectrum are $J_{sc,top} = 12.46 \text{ mA cm}^{-2}$ and $J_{sc,bot} = 13.44 \text{ mA cm}^{-2}$, hence the micromorph device is top cell limited. Figure 4.16 shows the *FF*, *P_{mpp}* and *J_{sc}* values as function of the simulated current mismatch and temperature. We notice that the maximum of *J_{sc}* which should correspond to a current-matched condition do not lay at the 0 mA cm⁻² calculated mismatch point as it should be. This shift of 1 mA cm⁻² can be explained by simulated spectrum errors. The slope of *J_{sc}* as a function of mismatch is 0.54 in the top limited and -0.45 in the bottom limited case. As expected the *FF* value increases and the *J_{sc}* value decreases with increasing mismatch. Figure 4.16 b) I) and II) shows that the *J_{sc}* maximum and hence the location of the *P_{mpp}* maximum

Chapter 4. Temperature dependence of thin-film and crystalline silicon-based solar cells

as a function of mismatch, shifts to more reddish spectrum with temperature. This means that the current matched point shifts to a more reddish spectrum. This implies that for an AM1.5g spectrum, the cell becomes more bottom limited or less top limited with increasing temperature. This change of the current distribution between the top and bottom cells with temperature is due to a higher light absorption increase with temperature of the top cell than for the bottom cell (see section 4.4.3 and Fig. 4.18 right). Indeed the gain in current of the bottom cell in the infrared part (due to band-gap narrowing) is partially counterbalanced by the decrease in absorption in the red part of the bottom cell due to increased absorption with temperature of the top cell in this region (due to band-gap narrowing).

Figure 4.17 shows the temperature behavior of the P_{mpp} , FF and J_{sc} in matched, strongly bottom cell limited and strongly top cell limited state and the corresponding TC as a function of the current mismatch. Looking at the FF behavior, we see that in the top cell limited case

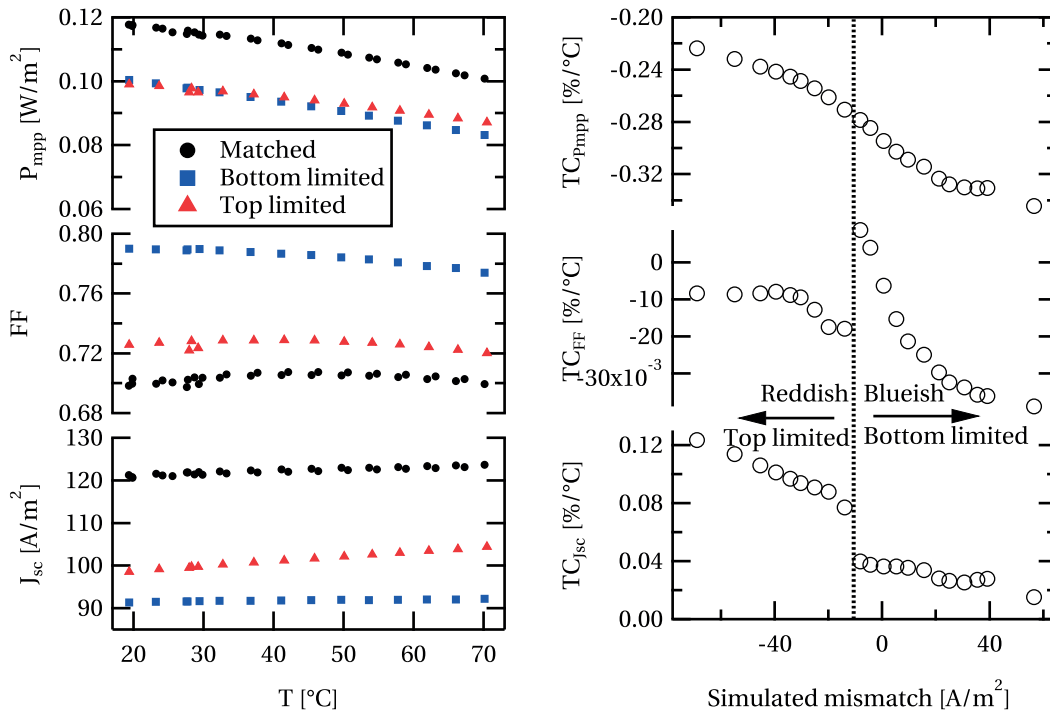


Figure 4.17 – Left: P_{mpp} , FF and J_{sc} as a function of temperature in the current matched, bottom limited and top limited state (simulated mismatch of -0.8 mA cm^{-2} , 5.7 mA cm^{-2} and -5.5 mA cm^{-2}). Right: $TC_{P_{\text{mpp}}}$, TC_{FF} and $TC_{J_{\text{sc}}}$ as a function of simulated mismatch.

(red triangle), the temperature behavior of FF seems to be governed by the a -Si:H subcell. The FF_{max} value is around 45°C and the TC_{FF} value is high ($-0.01 \text{ \%}/^\circ\text{C}$). In the vicinity of the current-matched point we see a discontinuity that is due to the shift of the current matching with temperature as explained previously. Moving further to the bottom (μc -Si:H) limited case, TC_{FF} decreases and FF_{max} moves to lower temperature (blue squares). The TC_{FF} value of the micromorph cells ($-0.05 \text{ \%}/^\circ\text{C}$) decreases towards the value of the TC_{FF} of an μc -Si:H cells,

4.4. Multi-junction thin-film silicon cell temperature behavior

but still remains higher. The value of the TC_{FF} of the micromorph cell is determined by a combination of the $FF(T)$ behavior of each subcells and the FF variation due varying current mismatch with temperature.

In top limited cases, the TC_{Jsc} with values around $0.10\%/^{\circ}C$ is slightly higher than for a good single a -Si:H cells. As for a single cell, there is a current enhancement (in the top cell) with temperature due to enhanced absorption due to temperature-induced bandgap reduction. In addition, as the mismatch diminishes with higher temperature the voltage of the top cell at the J_{sc} point shifts from negative values towards $0V$ and hence the current of the top cell enhances more (as the slope of the $I(V)$ curve at reverse bias is positive). On the other hand, in the bottom limited case the TC_{Jsc} of the micromorph cell is lower than for a single μc -Si:H cells. The current enhancement with temperature in the infrared part due to the temperature-induced bandgap reduction, is partially counterbalanced by less current at higher wavelength due to enhanced absorption in the top cell (as already discussed before, see also Fig. 4.18). The difference between the TC_{Jsc} of a single a -Si:H cell and the TC_{Jsc} of a micromorph cell in the top limited state is linked to the slope of the a -Si:H $I(V)$ curve at reverse bias voltages.

The TC_{Voc} (not shown) exhibit approximately constant value of $-0.32\%/^{\circ}C$ for all spectra. By combining the TC_{Voc} , TC_{Jsc} and the TC_{FF} values, it is evident why TC_{Pmp} decreases from $-0.22\%/^{\circ}C$ to $-0.33\%/^{\circ}C$ moving from top limited to bottom limited conditions. It is mainly the TC_{Jsc} that drives this TC_{Pmp} variation with spectrum (mismatch). At matched conditions the TC_{Pmp} is equal to $-0.28\%/^{\circ}C$.

Regarding temperature, the current matching of the micromorph cell has to be optimized such that the P_{mp} is highest at the production condition leading to the highest energy share. It follows that compared to the optimum at $25^{\circ}C$ the cell should be slightly more top limited as the current matched point shifts to a more redder spectrum with increasing temperature. The matching should then be further optimized to take in account varying spectra (as in our latitude most productive spectra are slightly bluer, the cell should also be slightly more top limited see Chap. 5) and degradation effects (more bottom limited as only the top cell degrades see Chap. 6).

4.4.3 Results and discussion for the triple cells.

The measured triple junction cell has J_{sc} values of 9.9 mA cm^{-2} , 8.9 mA cm^{-2} and 8.3 mA cm^{-2} for the top, middle and bottom cell respectively as calculated from EQE measurements (Fig. 4.18). Hence the cell is bottom limited. As for the micromorph cells presented in the previous section, this triple cell exhibits a FF_{max} situated near $20^{\circ}C$ and the maximum of $P_{mp}(T)$ is situated around $-20^{\circ}C$ (Fig. 4.18 left). The EQE measurements as a function of temperature shows that the top cell loses current with temperature at wavelength around 380 nm due to enhanced absorption of the ZnO front electrode. At a wavelength value of about 600 nm current is gained in the top cell due to bandgap broadening. For the middle and the bottom cell same mechanism occurs. At low wavelength values, the current is loss due to enhanced

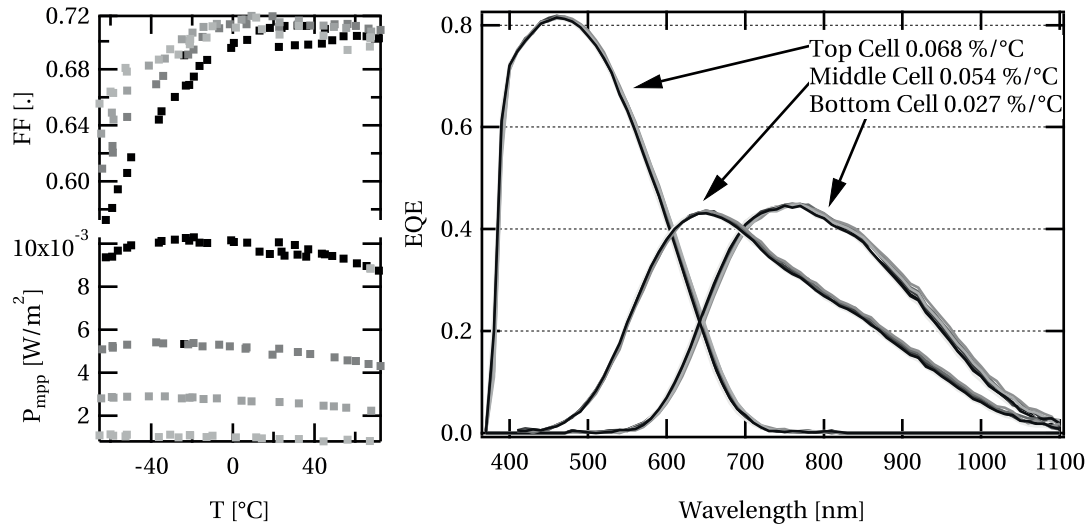


Figure 4.18 – Left: P_{mpp} and FF as a function of temperature at different intensities (black: 1000 $W m^{-2}$ and lightest gray 100 $W m^{-2}$ irradiance). Right: EQE as a function of temperature, black= 10 $^{\circ}C$ and lightest gray = 75 $^{\circ}C$.

absorption of the layer on top, and at larger wavelength there is a current gain. This leads to the highest $TC_{J_{sc}}$ value for the top cell (0.068 $\%/^{\circ}C$), a lower value for the middle cell (0.054 $\%/^{\circ}C$) and the lowest value of 0.027 $\%/^{\circ}C$ for the bottom cell. The $TC_{J_{sc}}$ value of the complete triple cell in the bottom limited state is 0.021 $\%/^{\circ}C$. Similarly to micromorph tandem cells, the $FF(T)$ curve has a maximum dictated by the FF_{max} of the subcells. We observed a $TC_{P_{mpp}}$ value of $-0.28 \%/^{\circ}C$ similarly to micromorph cells.

4.5 Temperature behavior of silicon heterojunction solar cells

Silicon heterojunction cells (SHJ) are known to have a favorable temperature coefficient (compared to other c -Si homojunction solar cells). Their high TC values are principally due to their high V_{oc} [Mish 11, Batz 11]. Investigating the temperature behavior of those cells allows gaining some insight in the materials characteristics. In this section we⁵ study their performance when varying the temperature from $-100^{\circ}C$ to $70^{\circ}C$ as well varying the irradiance intensity.

4.5.1 Experimental details

The 2×2 cm^2 SHJ solar cells made in our laboratory were measured with the cell tester setup (see Sec. 2.2.2). Three different cells were studied. The first one (*SHJCu*) has copper plated fingers [Geis 14] on the front and standard p and i - a -Si:H layers (for more information see section 2.1.4). The second one (*SHJAg*) is very similar to the previous one but was deposited

⁵Y. Riesen, G. Nogay J. Geissbuhler, J. Seif, C. Ballif and N. Wyrsh

4.5. Temperature behavior of silicon heterojunction solar cells

in another deposition system and has screen printed silver fingers. The third one (*SHJAg- μ c*) was deposited in the same reactor as *SHJAg* and is similar to *SHJCu* but with a *p- μ c-Si:H* layer instead of the *p-a-Si:H*, it has also silver fingers (results concerning *SHJAg- μ c* are from Nogay *et al.*, to be published). A summary is shown in Tab. 4.3. During I(V) measurements, the cells temperature were controlled using a chuck (the temperature was measured in the chuck and is assumed to be the cell temperature). The cells were contacted using two kelvin probes at the front contacts and the chuck surface plus a voltage probe for the back contact. For measurements series with temperatures below 10 °C, the whole chuck is placed in a thermal insulated box with a 5-mm glass on top allowing the use of liquid nitrogen to cool the cells.

As the gain in J_{sc} with temperature is mainly due to the temperature-induced bandgap reduction leading to an increase in absorption at wavelength above 1000 nm, the $TC_{J_{sc}}$ depends strongly on the illumination spectrum. Therefore the $TC_{J_{sc}}$ and $TC_{P_{mpp}}$ of *c-Si* solar cells are underestimated if measured with the cell tester. The cell tester's spectrum at wavelength longer than 600 nm is mainly determined by the halogen lamps. At high light intensities the halogen lamps spectrum exhibit a high peak around 680 nm which decreases rapidly when going towards longer wavelengths and only partially reflects the solar spectrum in the infrared region (from 700 nm to 1300 nm). Hence, even if the total current of the cell corresponds to the nominal current at STC, the intensity is in our case more than two times lower around wavelength of 1200 nm than for an AM1.5g spectrum. Going to lower light intensity the peak of the halogen spectrum is reduced compared to the intensity in the infrared part and hence the $TC_{J_{sc}}$ will increase. For example, the $TC_{J_{sc}}$ value measured with the cell tester at 1000 W m^{-2} is $0.02 \text{ \%}/^\circ\text{C}$, however when measured with the Wacom simulator we get $0.06 \text{ \%}/^\circ\text{C}$. The Wacom simulator has a relatively closer to AM1.5g intensity around the wavelength of 1200 nm and gives more accurate results.

4.5.2 Results and discussion

Figure 4.19 shows the I(V) parameters of the *SHJCu* cell from -100°C to 75°C at different irradiation levels. The V_{oc} increases linearly with decreasing temperature as for standard homojunction cells until -20°C where the I(V) curve exhibit a s-shape behavior (see Fig. 4.20 left). However, below this temperature, the $V_{oc}(T)$ curve begins to saturate until -60°C from where the V_{oc} begins to decrease. In literature this s-shape is explained by the hole barrier due to the valence band offset at the *i-a-Si:H/c-Si/* interface at the *p*-side of the wafer [Sark 12, Clee 98]. At low temperatures, holes ceases to have enough thermionic energy to cross this barrier and accumulate. This hole accumulation increases the recombination at forwards bias around the V_{oc} value. As a result, the slope of the I(V) curve taken at V_{oc} decreases and the curve becomes s-shaped. Moreover this enhanced recombination leads also to a drop in V_{oc} .

As for *a-Si:H* cells (see Sec. 4.2.2), the $FF(T)$ curve presents a maximum. For example, for 1260 W m^{-2} the temperature of this maximum (T_{FFmax}) is found at 25°C . This T_{FFmax} decreases

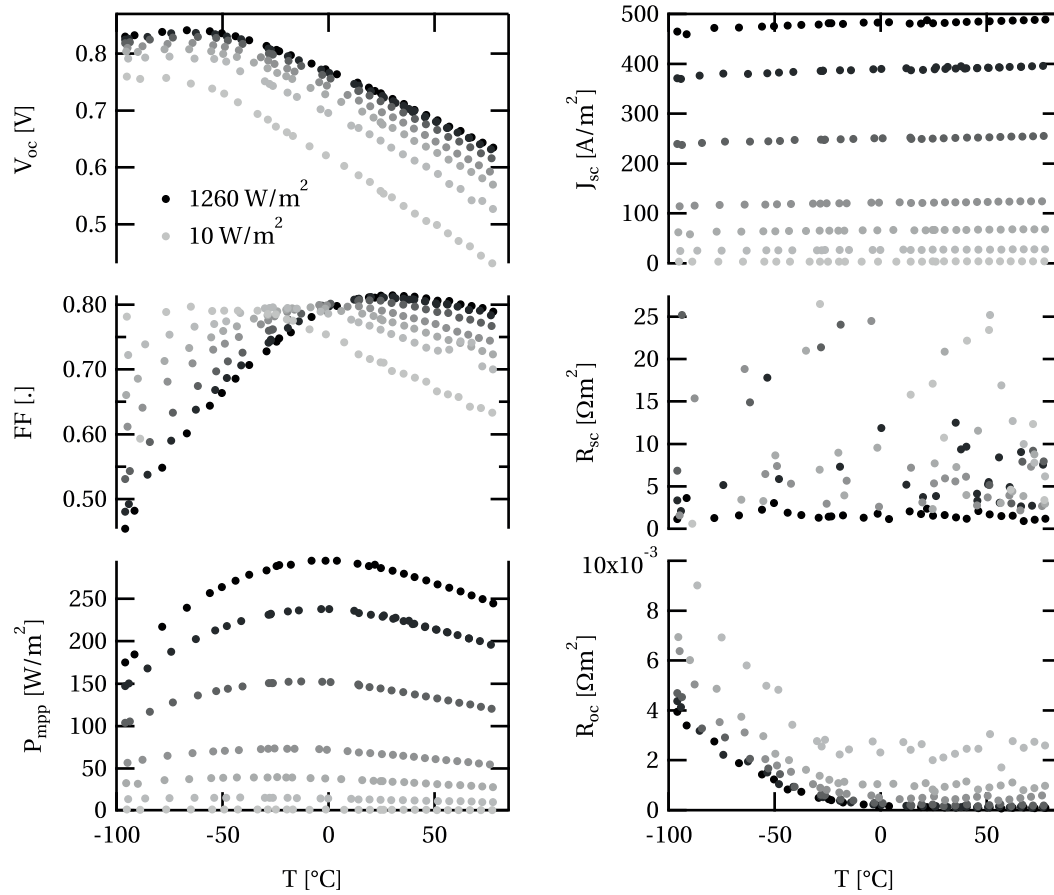


Figure 4.19 – I(V) parameters (V_{oc} , FF , J_{sc} and P_{mpp}) as a function of the SHJCu cell (copper plated cell with p - a -Si:H layer) measured at different irradiation [from 1260 W/m^2 (black dots) to 10 W/m^2 (lightest gray)].

with decreasing irradiance, *e.g.* at 10 W/m^2 $T_{FFmax} = -75^{\circ}\text{C}$. Most probably the valence band offset and the resulting enhanced recombination due to hole accumulation is also the reason for the reduction of FF (see Sec. 2.1.4 for an illustration of the band-diagram). When lowering the irradiance, the critical hole accumulation will only be reached at lower temperature (note that the $V_{oc}(T)$ maximum also decreases with temperature but at a 4 times lower rate). Moreover, the FF maximum is reached at a temperature that is more than 40 $^{\circ}\text{C}$ higher than the temperature where the curve becomes s-shaped and the V_{oc} begins to drop. We believe that the valence band offset affects first the FF , as at V_{mpp} , due to hole currents that cross the barrier, the band bending and hence the hole accumulation could occur already at higher temperatures. As at V_{oc} all carriers recombine in the device, this accumulation occurs only at lower temperatures. It is also interesting to note that for most measured standard SHJ cells made in our laboratory, the T_{FFmax} is around STC temperature (25 $^{\circ}\text{C}$) at an irradiance intensity value of 1000 W/m^2 . It is not clear if this observation is a consequence of the fact that we optimize our cells for STC conditions, the T_{FFmax} is then just at this point which represents

4.5. Temperature behavior of silicon heterojunction solar cells

the best trade-off between good V_{oc} values and FF values or if it has a more fundamental origin. Due to this $FF(T)$ curve shape (Fig. 4.19) the P_{mpp} also has a maximum which is

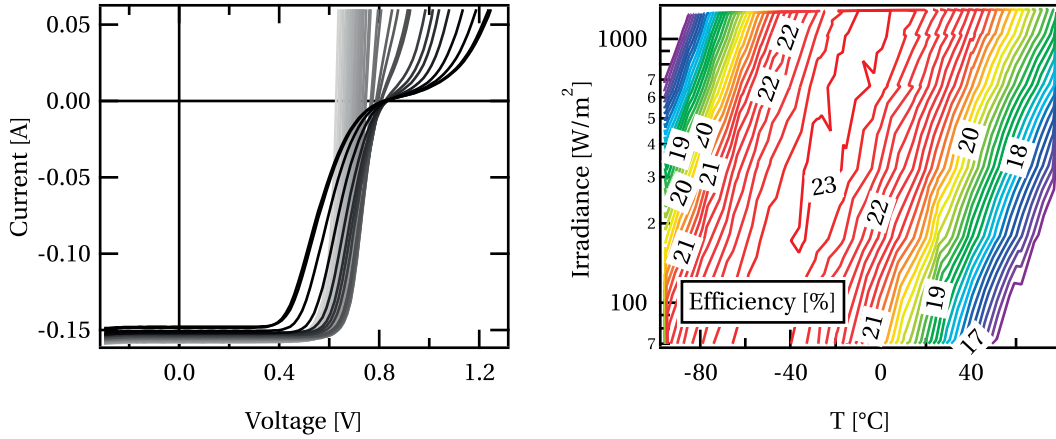


Figure 4.20 – (left) $I(V)$ curve for the $SHJCu$ cell at 1000 Wm^{-2} and different temperatures. Darkest/brightest lines corresponds to $-100 \text{ }^\circ\text{C}$ and $80 \text{ }^\circ\text{C}$. (right) Efficiency as a function of the irradiance (log scale) and temperature.

located at $0 \text{ }^\circ\text{C}$ at 1000 Wm^{-2} . In Fig. 4.20 (right), the efficiency is shown as a function of irradiation intensity (calculated according to the J_{sc} values of the cell, knowing its nominal value) and temperature. We can directly extract that the maximum efficiencies values of over 23% are situated, for irradiation in log scale, on a line going from $-40 \text{ }^\circ\text{C}$ and 200 Wm^{-2} to at least $0 \text{ }^\circ\text{C}$ and 1260 Wm^{-2} . Thus we can directly deduce that the temperature of the P_{mpp} maximum and hence the T_{FFmax} depends logarithmically on irradiance.

The J_{sc} increases linearly with temperature in the measured range. Yet, it is to be noted that the TC_{Jsc} is underestimated as discussed before.

Due to a low lamp stability of the simulator the R_{sc} values are noisy and not completely reliable (sometimes negative values are obtained). However, it is not the case for the R_{oc} . Its values are relatively constant from high temperature until $-20 \text{ }^\circ\text{C}$ where they begin to increase accordingly to the increasing s-shape of the $I(V)$ curve (see Fig. 4.20).

If we assume that this s-shape behavior near V_{oc} is due to a barrier, its effect on the $I(V)$ characteristics is thermally activated and we can extract an activation energy related to the barrier height. Figure 4.21 shows the FF as a function of temperature of the $SHJCu$ and $SHJAg-\mu c$ cells and the natural logarithm of the $I(V)$ curve slope at the saddle point ($ln dj = \ln(\partial I(V)/\partial V)|_{V=V_s}$) as a function of the inverse temperature ($1/T$) at different irradiance values. Lowering the temperature, the FF value of the $SHJAg-\mu c$ solar cell begins to decrease at lower temperature ($-30 \text{ }^\circ\text{C}$) than for the $SHJCu$ and $SHJAg$ cells ($25 \text{ }^\circ\text{C}$ and $40 \text{ }^\circ\text{C}$ respectively). The $FF(T)$ curve of the $SHJCu$ cells is higher than the $SHJAg$ cells mainly because of a lower series resistance. For the $SHJCu$ and $SHJAg$ cells the $ln dj$ values have a linear trend from $-10 \text{ }^\circ\text{C}$ to about $-40 \text{ }^\circ\text{C}$. This linear behavior and the fact that the slopes are similar for

Chapter 4. Temperature dependence of thin-film and crystalline silicon-based solar cells

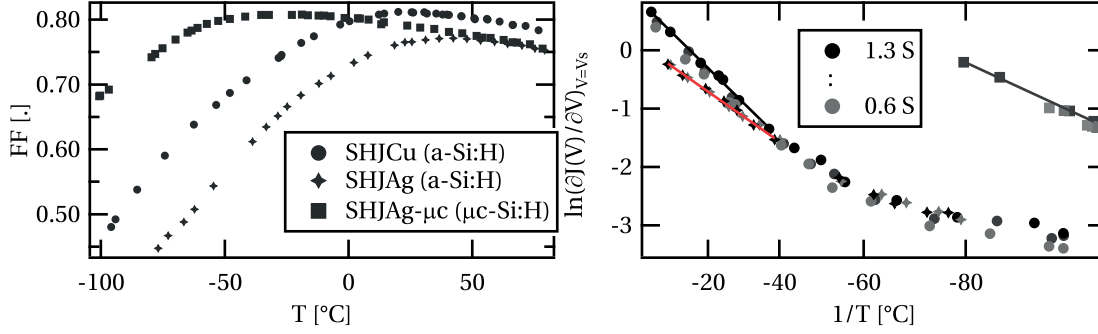


Figure 4.21 – (left) ght: FF as a function of temperature for the three cells. (right) $\ln(\partial I(V)/\partial V)|_{V=V_s}$ at the saddle point (V_s), which is located near the V_{oc} , as a function of the inverse temperature for $SHJCu$, $SHJAg$ and $SHJAg-\mu c$ solar cells. The red lines are the linear fits of the slopes.

different irradiance intensities could for instance validate the existence of a thermally activated process. Decreasing the temperature further, the slope decreases and seems to saturates, this may be explained by a too high barrier compared to the thermionic energy and hence the transport could be mainly driven by another mechanism (*e.g.* trap assisted tunneling because the temperature dependence diminishes). The $\ln dj$ of the $SHJAg-\mu c$ cell is linear with temperature until the minimum measured temperature for the different irradiances. From $E_{act} = \text{slope}(\ln dj(1/T)) \cdot k_B/q$, we get the activation energies (E_{act} listed in Tab. 4.3)

Cell	fingers type	p -layer	Dep. system	$E_{act}[eV]$	$T_{FFmax} [^{\circ}C]$
$SHJCu$	Copper plated	p - a -Si:H	A	0.31	20
$SHJAg$	Screen printed	p - a -Si:H	B	0.21	42
$SHJAg-\mu c$	Screen printed	p - μc -Si:H	A	0.14	-25

Table 4.3 – Activation energies of the s-shape and the corresponding FF maximum temperature.

The activation energies of the $SHJCu$ and $SHJAg$ cells are comparable with the valance band offset (ΔE_{VB}) values given in literature (0.2 eV from a theoretical study [Wall 95] or 0.4 eV found in an experimental study [Schu 11]). The discrepancy between the E_{act} values found between $SHJCu$ and $SHJAg$ probably originates from different p - and i layers characteristics (it is known that the bandgaps differs and hence the ΔE_{VB} [Desc 11, Geis 13]) due to the different deposition conditions between the two reactors⁶. The p - μc -Si:H layer ($SHJAg-\mu c$) influences the T_{FFmax} and also the E_{act} which is the lowest measured value of this study. Notably, there is not a direct correlation between the T_{FFmax} and E_{act} . Hence, we can think that the E_{act} as we defined it, is not the only parameter governing the temperature behavior of the FF . Perhaps as for the $SHJAg-\mu c$ cells higher doping induce a higher band bending reducing the hole

⁶A standard cell deposited with same reactor as $SHJCu$ but with silver screen printing gave an activation energy of 0.28 eV.

accumulation. The valence band barrier at the TCO/*p*-layer interface could also influence this behavior. After these first experimental findings, numerical simulations of such devices are needed to have a better understanding of those effects and to validate the meaning of this activation energy.

4.6 Temperature dependence of silicon-based solar cells

4.6.1 Temperature coefficient comparison

In this part we compare the temperature behavior of different silicon-based solar cells:

Experimental details

The following cells are compared:

- A thin high band gap (170-nm-*i*-layer) (*a*-Si) and a thicker (300-nm-*i*-layer) *a*-Si:H solar cells (*a*-Si2) in initial and degraded state, both are measured with the cell tester.
- A μ c-Si:H standard cell (μ c-Si), corresponding to *Std Z5 45'* in section 4.3, measured with the cell tester.
- A poly-*c*-Si solar cell (*Poly*) measured with the Wacom2 sun simulator.
- A mono-*c*-Si (*Mono*) solar cell⁷ measured with the Wacom2 sun simulator.
- A back-contacted high efficiency mono-*c*-Si cells⁸ measured with the celltester (*BC*).
- A silicon heterojunction cells (SHJ) made in our laboratory corresponding to the one of the previous section (Sec. 4.5). The cells were measured with the cell tester, however the TC_{Jsc} and hence the TC_{Pmpp} were corrected according to the TC_{Jsc} values measured with the Wacom simulator at STC.

The different I(V) parameters at STC are showed in table 4.4:

The TC are fitted from 30 °C to 80 °C to minimize the effects of non-linear $FF(T)$ curves. Moreover in most cases, the operating temperatures during the period when the cell is producing most energy are in this temperature range.

Results and discussion

We first individually go through the TC_{Voc} , TC_{FF} and TC_{Jsc} in order to have a better understanding of the different influences on the TC_{Pmpp} . Figure 4.22 represents the relative TC_{Voc}

⁷Commercial cell from Sunways

⁸Commercial cell from Sunpower

Chapter 4. Temperature dependence of thin-film and crystalline silicon-based solar cells

Label	Cell Type	V_{oc} [mV]	J_{sc} [mA/cm^2]	FF [%]	P_{mpp} [W/m^2]
<i>a-Si(d)</i>	thin high bg <i>a-Si:H</i>	953 (934)	13.1 (12.7)	73.4 (67.1)	91 (80)
<i>a-Si2(d)</i>	300-nm- <i>i</i> -thick	871 (842)	16.3 (15.2)	69.1 (60.2)	98 (77)
μc -Si	μc -Si:H	530	256	69.6	93.9
<i>Poly</i>	Poly- <i>c</i> -Si	619	32.4	77.1	155
<i>Mono</i>	Mono- <i>c</i> -Si	617	36.8	79.1	179
<i>BC</i>	Back cont. mono- <i>c</i> -Si	712	43.0	78.6	240
<i>SHJCu</i>	SHJ copper plated	725	37.7	81.0	220
<i>SHJAg</i>	SHJ standard	714	36.1	77.6	200

Table 4.4 – I(V) parameters of the different silicon-based solar cells. The J_{sc} and P_{mpp} of the *BC* cells are calculated according to data-sheet.

values as a function of the V_{oc} .

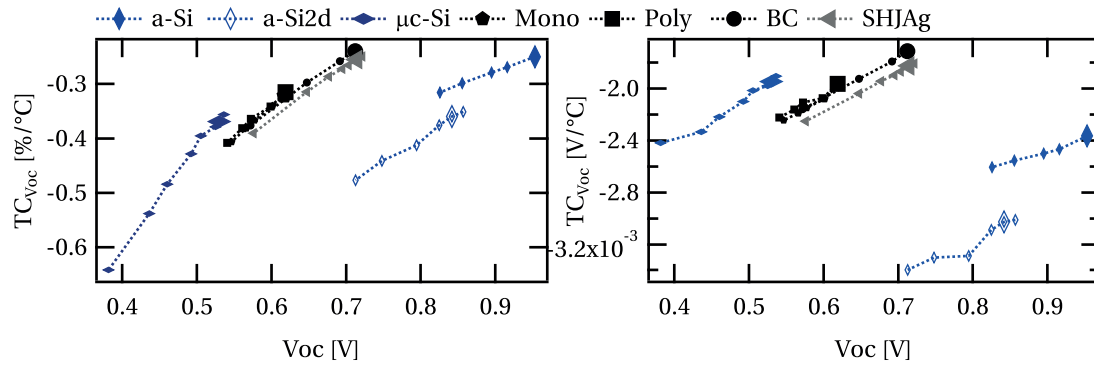


Figure 4.22 – (left) Relative and (right) absolute $TC_{V_{oc}}$ values as a function of their V_{oc} measured on different silicon-based solar cells. The bigger markers indicates the values at STC.

As for thin-film silicon cells (see Sec. 4.2.2, p. 43) the $TC_{V_{oc}}$ of all measured cells at different irradiances behaves linearly as a function of their V_{oc} varied by changing the irradiance. The $TC_{V_{oc}}(V_{oc})$ lines for the *Poly*, *Mono* and *BC* cells are in a first approximation on the same line. Because the V_{oc} of the *BC* cell is higher, its $TC_{V_{oc}}$ ($-0.24\%/^{\circ}C$ at STC) for a same irradiance is higher than for the *Poly* and *Mono* cells (about $-0.32\%/^{\circ}C$ for both). Interestingly, the $TC_{V_{oc}}(V_{oc})$ line of the *SHJAg* cell is slightly shifted downwards. Its $TC_{V_{oc}}$ at STC ($-0.26\%/^{\circ}C$) is slightly lower than for *BC* with almost same V_{oc} at STC but still higher than for the *Poly* and *Mono* because of higher V_{oc} . It can be more clearly seen in Fig. 4.23 (top, left) where the $TC_{V_{oc}}$ is plotted as a function of the J_{sc} in log scale. As already presented in Sec. 4.2, the $TC_{V_{oc}}$ of the *a-Si:H* cells depends considerably on the material properties (mainly the defect density). The *a-Si* cells in initial state with high FF (less recombination) has a $TC_{V_{oc}}$ in the range of the *c-Si* cells ($-0.25\%/^{\circ}C$ at STC), note that in absolute values the $TC_{V_{oc}}$ is significantly lower than for the *c-Si* cells (Fig. 4.22 (right)). The $TC_{V_{oc}}$ of the thicker and in degraded state (*a-Si2d*) cell has a relatively low $TC_{V_{oc}}$ value of $-0.36\%/^{\circ}C$. The $TC_{V_{oc}}$ values of the μc -Si cells are lower than those of *c-Si* cells and similar to the ones of *a-Si2d* in relative values and to the ones of the

4.6. Temperature dependence of silicon-based solar cells

Poly and *Mono* cells in absolute values.

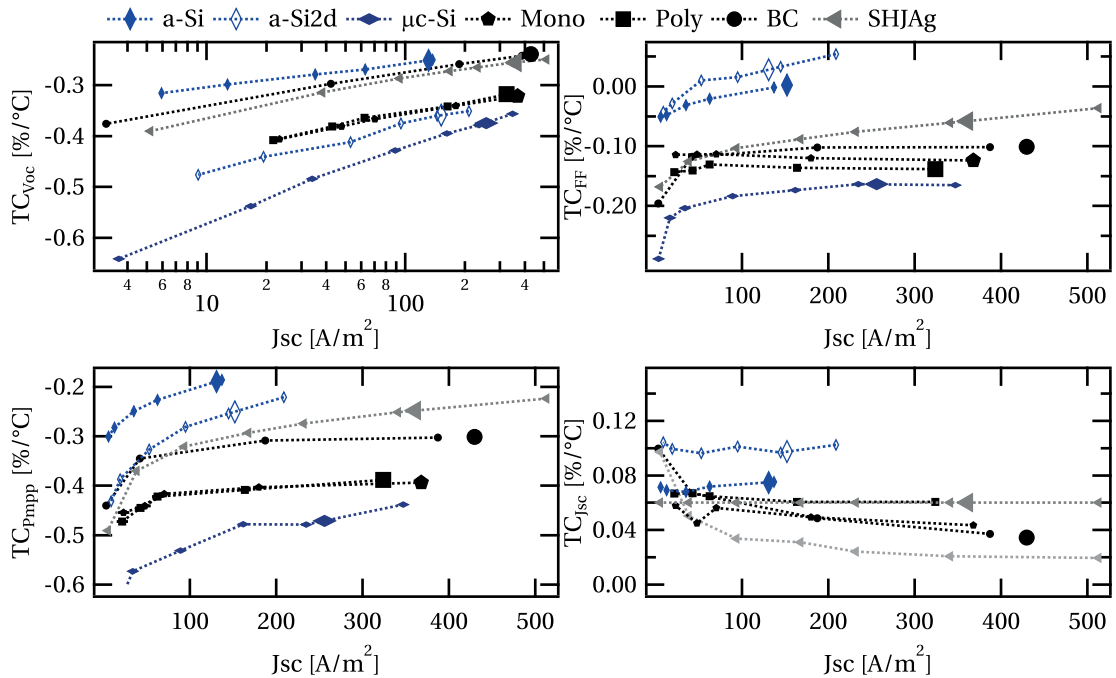


Figure 4.23 – TC_{Voc} , TC_{FF} , TC_{Pmpp} and TC_{Jsc} of silicon-based solar cells as a function of their J_{sc} at different irradiances. The bigger marker indicates the TC at STC. The TC_{Jsc} values of the *SHJAg* cell is corrected according to the TC_{Jsc} measured with the Wacom sun simulator.

The highest TC_{FF} values (in the range of $-0.05\%/^{\circ}C$ to $0.05\%/^{\circ}C$) are obtained with *a-Si:H* cells due to the $FF(T)$ behavior explained before (Sec. 4.2.2, p. 47). It was shown that the TC_{FF} of those cells increases with irradiance because the T_{FFmax} moves then to higher temperatures. The next highest TC_{FF} values are achieved by the *SHJAg* cells ($-0.06\%/^{\circ}C$ at STC) due to this s-shape behavior. Therefore the TC_{FF} increases also with irradiance (gaining $0.002\%/^{\circ}C$ per mA/cm^2). The TC_{FF} of the *Poly*, *Mono* and *BC* cells are in a first approximation constant with irradiance for J_{sc} that are higher than $5 mA/cm^2$ ranging from $-0.13\%/^{\circ}C$ for *Poly* to $-0.10\%/^{\circ}C$ for the *BC* cells. The *μc-Si* exhibit the lowest value of about $0.16\%/^{\circ}C$.

The TC_{Jsc} are as expected constant with irradiance. Most values are around $0.04\%/^{\circ}C$ to $0.06\%/^{\circ}C$ with exception of the *a-Si2d* cell with higher values due to its low FF and hence significant reduced recombination with increasing temperature.

The TC_{Pmpp} is the sum of the TC_{Voc} , TC_{FF} and TC_{Jsc} . Hence for all cells the TC_{Pmpp} increases with irradiance mainly due to the logarithmically TC_{Voc} increase. For the *a-Si:H* and the *SHJ* cells this increase is higher due to the TC_{FF} increase. On the whole the highest TC_{Pmpp} is obtained by the *a-Si* cell followed by the *a-Si2d* cell. The higher TC_{Pmpp} values of the *SHJAg* cells compared to the *BC* cells with about same V_{oc} is principally due to the higher TC_{FF} of the *SHJ* cells. The TC_{Pmpp} at STC are summarized in Tab. 4.5: We note that the TC_{Pmpp} of *Mono* and *Poly* (here measured on cells) are slightly better than those indicated by the

Label	$TC_{P_{mpp}}$ [%/°C]
<i>a-Si</i>	-0.19
<i>a-Si2d</i>	-0.25
<i>SHJAg</i>	-0.25
<i>BC</i>	-0.30
<i>Poly</i>	-0.39
<i>Mono</i>	-0.39
<i>μc-Si</i>	-0.47

Table 4.5 – $TC_{P_{mpp}}$ at STC from highest to lowest

supplier for modules ($-0.42\%/^{\circ}\text{C}$). Moreover, the $TC_{P_{mpp}}$ for the *SHJAg* cells are valid for our laboratory SHJ cells. The $TC_{P_{mpp}}$ can differ for other SHJ cells with different cell design and hence especially a different TC_{FF} behavior.

4.6.2 Impact on the energy yield of irradiance-dependence of the temperature coefficient

Most energy yield models use constant TC to model temperature dependence. In the previous section we observed that the $TC_{P_{mpp}}$ of SHJ cells is not constant with irradiance and we will here analyze the effect on the energy yield and if this has to be taken into account.

We simulate the yearly energy output of a module having the same characteristics than the *SHJAg* cells showed in the previous sections.

Experimental details

We compare the yearly energy output of a module having the same characteristics (in irradiance and temperature) as the *SHJAg* cells showed in the previous sections using four different simulation methods for temperature corrections, for each time step t , the $P_{mpp}(G(t), T(t))$ is calculated as follows :

- *20 % cst. η* , the $P_{mpp}(t)$ is calculated from the given irradiance assuming a constant efficiency (η) of 20 % without taking in account a temperature and irradiance dependence.
- *No T . dep.*, the $P_{mpp}(25^{\circ}\text{C}, G(t))$ is calculated by interpolating the indoor measured P_{mpp} at 25°C for the given irradiance without taking into account a temperature dependence.
- *Cst. TC* , the $P_{mpp}(T(t), G(t))$ calculated with the *No T . dep.* method is corrected to the given temperature ($T(t)$) with the constant $TC_{P_{mpp}}$ (corresponding to the $TC_{P_{mpp}}$ at STC).
- *Var. TC* , the irradiance (or J_{sc}) dependent $TC_{P_{mpp}}(J_{sc})$ showed in Fig. 4.23 is used to linearly correct the $P_{mpp}(T(t), G(t))$ calculated with the *No T . dep.* method.

4.6. Temperature dependence of silicon-based solar cells

- *Interp.*, the $P_{\text{mpp}}(T(t), G(t))$ is calculated by interpolating the indoor measured $P_{\text{mpp}}(G, T)$ at the given irradiance and temperature. This methods should be nearest to the real energy output (or energy yield if we divide the energy yield by the power rating).

The $P_{\text{mpp}}(T(t), G(t))$ of each time step are then integrated in order to calculates the yearly energy output.

The input temperatures ($T(t)$) are taken from measured temperatures of a mono-*c*-Si module monitored on our roof from September 2014 to September 2015 (see Sec. 2.4). The in plane irradiance ($G(t)$) is determined by using the temperature corrected and normalized J_{sc} value of this same module. This methodology, allows obtaining directly the irradiance arriving in the cell from the measured J_{sc} of the module (most angular and glass reflection effects are already taken into account). However, spectral effects resulting from the difference in spectral response between SHJ and mono-*c*-Si are not taken in account. This method is known as self-reference method.

Results and discussion

Figure 4.24 (left) shows the comparison between the measured P_{mpp} and the two simulated (*Cst. TC* and *Var. TC*) P_{mpp} at 500 W m^{-2} irradiance value. Above 25°C the two simulated curves are relatively close to the measured one. By having a closer look, *Cst. TC* curve underestimates the temperature loss and the *Var. TC* curve overestimates the temperature loss because of the non-linearity of the $P_{\text{mpp}}(T)$ curve. Below 25°C , because of a stronger $P_{\text{mpp}}(T)$ curvature both simulated curves overestimates the P_{mpp} . The temperature range used for the *TC* fitting also influences the previous results (in our case we fitted from 30°C to 70°C).

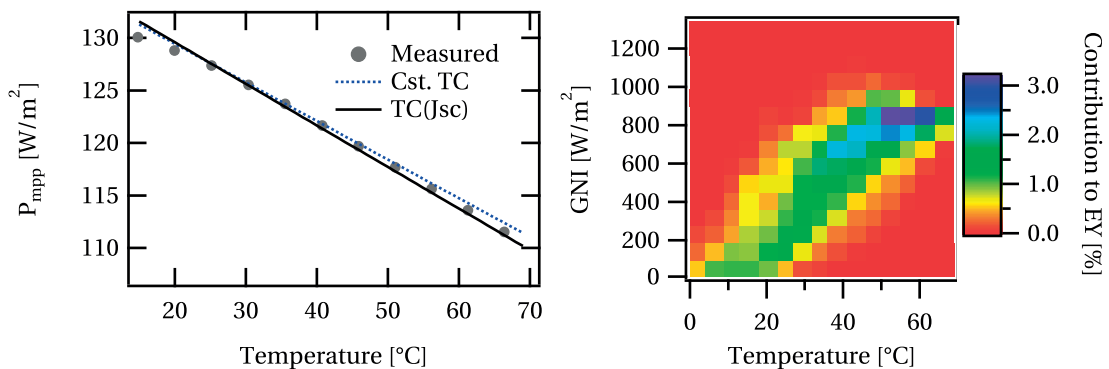


Figure 4.24 – (Left) Measured power, simulated power with constant temperature coefficient and simulated power with a J_{sc} dependent temperature coefficient of the *SHJAg* heterojunction solar cells at an irradiance G of 500 W m^{-2} . (Right) Relative contribution to the yearly in-plane irradiance as a function of different temperature and irradiance conditions in Neuchâtel (CH).

Chapter 4. Temperature dependence of thin-film and crystalline silicon-based solar cells

Figure 4.24 (right) shows the relative contribution to the yearly in-plane irradiation energy of the different temperature and irradiance conditions for one year in Neuchâtel. More than 45 % of the total energy yield is generated at temperatures above 40 °C or more than 35 % are generated during irradiances (G) > 700 Wm⁻². The results of the different simulation are summarized in Tab. 4.6.

20 % <i>cst.</i> η	<i>No T. dep.</i>	<i>Interp.</i>	<i>Cst. TC</i>	<i>Var. TC</i>
247.2 kWh/m ²	242.7 kWh/m ²	233.1 kWh/m ²	233.2 kWh/m ²	232.8 kWh/m ²
106.05 %	104.12 %	100 %	99.87 %	100.04 %

Table 4.6 – Modeled yearly energy output using different methods to correct (or not) temperature and irradiance dependence in absolute and relative to the *Interp.* simulation (which is nearest to the real value).

We lose 1.8 % of the total energy output compared to a constant η cells, if we only take into account efficiency losses due to varying η with irradiances (*No T. dep.*). Adding the temperature losses the total energy output diminish further by 4.1 %. The results of the energy output simulation using the three different temperature corrections (*Cst. TC*, *Var. TC* and *Interp.*) results in almost the same values (0.2 % scattering). Hence for our latitude, it is not necessary to use an irradiance dependent $TC_{P_{mpp}}$ for those cells.

4.6.3 Temperature dependence over a large temperature range

In this subsection, we compare the temperature dependent performances of silicon-based solar cells over a large temperature range including very low temperatures. Figure 4.25 shows the V_{oc} and the FF as a function of temperature. For the *BC* cell, the $FF(T)$ curves is slightly

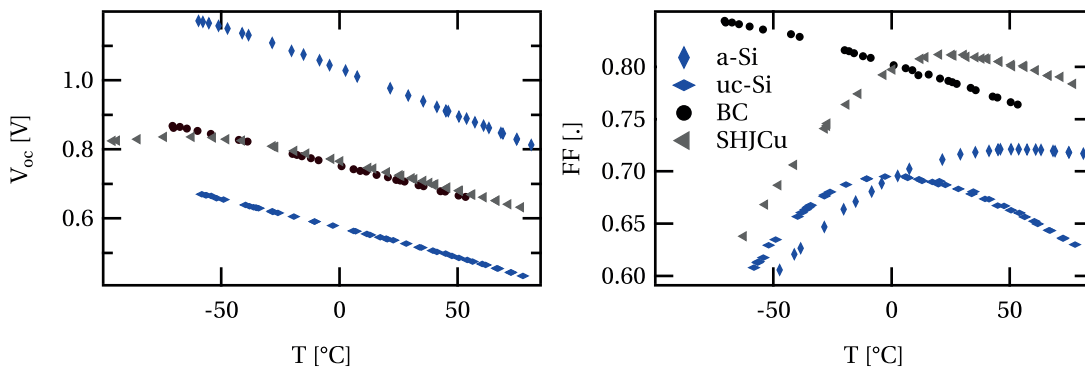


Figure 4.25 – V_{oc} and FF temperature dependence for *a*-Si:H, μ c-Si:H, mono-*c*-Si and SHJ cells.

convex, but is far having a maximum in our measurement range. Hence, the FF reaches a value of 85 % at -60 °C (see Fig. 2.5). Temperature dependent measurements of other homojunction *c*-Si solar cells (not shown here) at these temperatures also shown no FF maximum.

Even though thin-film silicon cells structure is very different from SHJ cells, both have a FF maximum in the same range of temperature (at least for the cells deposited in our laboratory) due to hole accumulation at the p -side. For the first type this accumulation is due to the p - i - n structure and drift driven carrier transport nature of the device and hence the relatively thin p -layer compared to the thicker i -layer where most of the photogeneration occurs (see subsection 4.2.2, p. 47). Whereas for the second type, the hole barrier at the valence band between the a -Si:H i -layer and the c -Si wafer at the p -side is responsible for this accumulation.

4.7 Conclusion

For amorphous silicon cells, we analyzed the impact of the intrinsic layer thickness, p -type a -SiC:H layer thickness, the hydrogen-to-silane flow ratio, and deposition rate on the temperature behavior of the performance of hydrogenated amorphous silicon solar cells. In most cases the TC of the open-circuit voltage (V_{oc}) has a linear dependence with the V_{oc} value. The linear short-circuit current density (J_{sc}) enhancement with temperature is mainly due to temperature-induced bandgap reduction. However a small part is also due to a reduction of the recombination with temperature, which is more important for cells with high defect densities. The fill factor as function of temperature ($FF(T)$) curves are non-linear and have a maximum that could be explained by numerical modeling. This maximum of the FF shifts to lower temperature under reduced irradiation and to higher temperature with degradation. The maximum power point ($P_{mpp}(T)$) curve is hence also not linear and has a maximum that is often below the operating temperature range. For the p -type a -SiC:H layer thickness, the dilution and the deposition rate series, the cells with highest P_{mpp} at 25 °C also perform best at all temperatures in the operating temperature range. This means that despite the fact that the $TC_{P_{mpp}}$ increases with decreasing P_{mpp} (for dilution and deposition rate series), their better TC cannot compensate their worse P_{mpp} (in this temperature range). On the other hand, some of the $P_{mpp}(T)$ curves of the i -layer series cross each other as function of temperature and irradiation levels. According to a simple energy output simulation (that does not take into account degradation and annealing effects) for one year in Neuchâtel (Switzerland) we showed by modeling that the best cell at STC is also best in terms of energy production regarding temperature behavior for both the annealed and light soaked states. However, for cells with slightly different material properties the situation could be different. In this work, we have considered only the temperature behavior of solar cells on a short time scale. For a more complete energy yield model, long-term temperature dependence caused by annealing and degradation effects should be taken into account as well [Vosw 13, Mert 98b, Virt 13]. We will address these aspects in chapter 6.

The temperature behavior of μc -Si:H cells depends mainly on the V_{oc} . The higher the V_{oc} , the higher the $TC_{V_{oc}}$ is and hence the $TC_{P_{mpp}}$. As the roughness has an important influence on the V_{oc} , it determines most the temperature behavior of μc -Si:H cells. Adding a buffer layer does not change significantly the temperature behavior of these cells. However highly crystalline cells have a relatively higher $TC_{V_{oc}}$ compared to their (relatively lower) V_{oc} . The

Chapter 4. Temperature dependence of thin-film and crystalline silicon-based solar cells

temperature behavior of μc -Si:H cells shows similarities with the a -Si:H cells. We assume that same basic mechanism are driving the temperature behavior because of the p - i - n structure.

The evolution of the electrical parameters of tandem and triple junction thin-film silicon cells upon temperature are driven by the temperature behavior of the subcells. The FF as a function of temperature is mainly determined by the limiting cell. Hence there is an $FF(T)$ maximum for those cells. However the TC_{Jsc} value is the highest when the cell is top limited, in that case the TC_{Jsc} of the second or third cell is limited by temperature-induced bandgap reduction of the top cells. Hence the TC_{Pmpp} value decreases continuously when going from top to bottom limited conditions mainly due to the variation with mismatch of the TC_{Jsc} .

We measured the temperature dependence of SHJ solar cells from -100°C to 80°C . Similarly to thin-film silicon-based solar cells, the FF has a maximum and begins to decrease after this point going to lower temperature. The $I(V)$ curve also become s-shape at lower temperature. The s-shaped $I(V)$ curve and the $FF(T)$ behavior seems to be caused by the hole barrier due to the valence band offset at the a -Si:H/ c -Si interface and the band bending in this region. From an Arrhenius plot of the $I(V)$ slope at the saddle point of the s-shape we could extract activation energies that could for instance correspond to the valence band offset. The next step will be to do numerical simulations of such devices at different temperatures to have a better understanding of the experimental results and verify the relationship between band offset and activation energy. Note that the results for SHJ cells are based on our laboratory cells, hence SHJ cells from other laboratory or supplier should be measured in order to generalize those results.

In the last part of this chapter we compared the temperature dependence of the performance of thin-film silicon, SHJ and mono-/poly- c -Si solar cells. We measured best TC_{Pmpp} for the a -Si:H cells mainly due to their high TC_{FF} . The second best TC_{Pmpp} values were obtained for the SHJ cells. Their high V_{oc} only partially explains its high TC_{Pmpp} , because back-contacted mono- c -Si cells with about the same V_{oc} exhibit even slightly higher TC_{Voc} values. However, the TC_{FF} of the SHJ cells are higher (at higher irradiation) than for the back-contacted cells due the $FF(T)$ behavior. Especially for SHJ and thin-film silicon cells, the TC_{Pmpp} increases (improves) significantly with irradiation. However we calculated that for annual energy yield determination in the typical meteorological conditions of Switzerland a constant TC_{Pmpp} with irradiation (*i.e.* TC_{Pmpp} measured at STC) still gives acceptable results and that it is therefore not necessary to take into account the dependence of TC on irradiance.

5 Spectral dependence of micromorph solar cells

Summary

In this chapter, we evaluate the spectral effects on the performance of two micromorph solar cells with different current matching conditions (top and bottom cell limited) using a two diode model with current recombination term. We used the SEDES2 tool [Nann 91] for simulating the sun spectrum depending on measured meteorological inputs and sun position. We observed for both cells that over 88 % of the total yearly energy yield was produced with a solar spectrum that is slightly bluer than the AM1.5g spectrum. Hence, for the top limited cell (under AM1.5g spectrum), the yearly energy yield was 1.6 % higher with the varying (SEDES2) spectra than with constant AM1.5g spectra normalized to give the same global irradiances (integrated values). However, the bottom limited cell gave about the same energy yield under normalized AM1.5g spectrum than with SEDES2 spectrum. This was essentially due to the fact that our bottom cell's efficiency decreases with lower irradiance due to shunt currents (which was not the case for the top limited cell). Hence, when the irradiance is increasing, the higher current mismatch due to the bluer spectrum is counterbalanced by an increase in efficiency due to less importance of the shunt currents.

5.1 Introduction

The irradiation spectrum impacts the output power of solar cells depending on their spectral response (or EQE). Instantaneous solar spectra mainly depend on the air mass of air, meteorological conditions and albedo. For identification of the solar spectrum in clear sky conditions, the air mass (AM_x) coefficient is defined as the portion of atmosphere traveled through by the light beam with $x = 1$ being the vertical atmosphere thickness. Hence an AM0 spectrum corresponds to the solar spectrum outside the atmosphere and AM1 spectrum to the solar spectrum on the earth surface when the sun has a zenith angle of 0° (is perpendicular) [Shah 09]. On the earth surface we can write, $AM = 1 / \cos \alpha$ where α is the angle between a solar ray and a vertical line. The AM1.5g spectrum corresponding to $\alpha \approx 45^\circ$ is the standard value for testing and specification of solar cells [IEC 08a]. The "g" stays for global irradiation (direct beam plus the diffuse irradiation). Under clear sky conditions, the majority of the solar spectral influence can be taken into account by considering only the air mass (AM)

Chapter 5. Spectral dependence of micromorph solar cells

[King 97a, Fann 06]. Hence due to higher air mass in winter or after sunrise or before sunset, the spectrum is then more reddish than at midday (U-shape $AM(t)$). This is a consequence of the Rayleigh scattering [Stru 71]. The water vapor content in the lower atmosphere that varies during the day (in our latitude the spectrum shifts towards blue in the course of the day because of higher vapor content in the afternoon) and the albedo also affects the shape of the spectrum [Gott 03, Pere 07].

The spectrum is often characterized by the APE value [Will 03] which is defined as

$$APE = \frac{\int_0^\lambda G(\lambda) d\lambda}{q \int_0^\lambda \phi(\lambda) d\lambda},$$

where λ is the wavelength, G is the spectral irradiance, q the electronic charge and ϕ the spectral photon flux density. Ishii *et al.* [Ishi 11] showed that APE in cloudy weather is higher (bluer) than in fine weather, because at shorter wavelength below 700 nm the spectral irradiance is much higher than AM1.5g and at longer wavelength above 1200 nm it is lower. Under overcast conditions the spectrum dependence is more difficult to determine [Nann 90, Gott 04, Gott 05, Huld 10] while still important.

Grunow *et al.* showed that during overcast conditions a -Si:H cells could have up to 30% of "spectral" gain in J_{sc} compared to a standard AM1.5g spectrum. When AM is growing the APE is diminishing, which means that the spectrum is more reddish. Even if the APE does not characterize precisely and uniquely a spectrum, Ishii *et al.* state that it is a valid indicator concerning spectral effects on solar cells.

Module and cell technologies shows various spectral sensitivity. Spectral effects influence mainly the J_{sc} of solar cells. They can induce a variation of about 2 %-4 % and 10 %-15 % of the J_{sc} for c -Si, respectively a -Si:H solar cells [Mont 10, Ishi 11, Virt 12]. a -Si:H cells are more sensitive to spectral variations because they use a narrower band in the spectrum than c -Si based solar cells (for example silicon heterojunction cells). Figure 5.1 shows the EQE, the AM1.5g and two different measured sun spectra. Multijunction devices as micromorph cells are also significantly affected by spectrum variations. As both subcells are connected in series, the one with lowest generated current limits the current of the whole cell. Highest performances are reached when the subcells have same currents (are current matched). Hence spectral variations influence the power output of those cells by changing the matching conditions. To illustrate this behavior, Fig. 5.2 shows the efficiency of a 30 x 20 cm² micromorph minimodule monitored on our roof ($B01$ see Sec. 6.3.2) as a function of in plane global irradiance and the ratio between the diffuse (DHI) and global horizontal irradiance (GHI) in gray-scale (black represents mostly clear sky conditions). We observe that below an irradiance of 400 Wm⁻² the efficiency under clear sky conditions drops because of high zenith angle in the mornings or evenings resulting in high AM values. This induce a higher current mismatch between the subcells diminishing its efficiency. However in overcast conditions (brighter points) the spectrum is similar to AM1.5g or even slightly bluer.

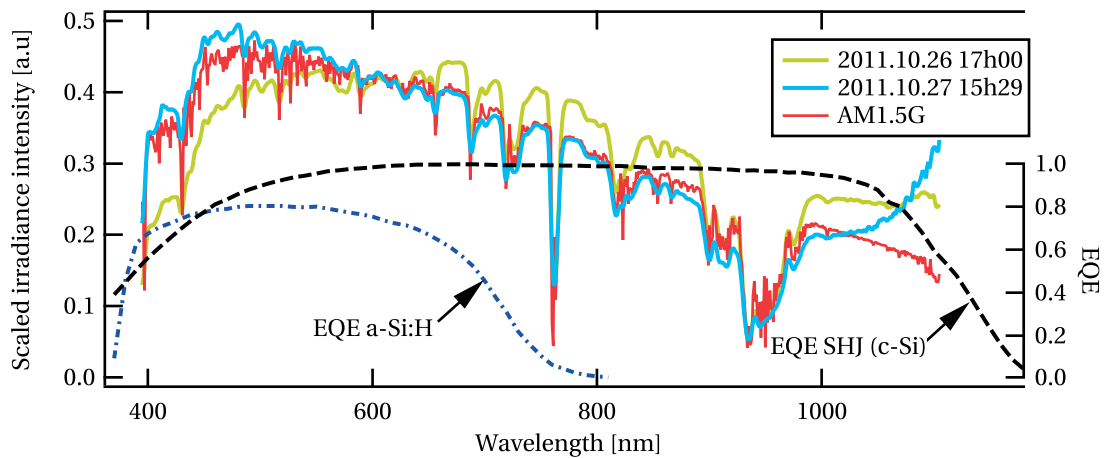


Figure 5.1 – Continuous lines: normalized AM1.5g spectrum and two spectrum measured in Neuchâtel (Switzerland) under different meteorological conditions. Note that the spectrometer used gives reliable spectra until a wavelength of 1000 nm only. Dashed lines: EQE of an *a*-Si:H and a silicon heterojunction cells.

The spectral effects on the energy yield is of the same magnitude as temperature losses and performance reduction in weak light for well oriented thin-film Si modules; it is about 1.3 % for micromorph modules and 3.2 % for *a*-Si:H [Grun 09, Hass 07]. All the results showed before are related to optimally oriented modules, Gueymard *et al.* [Guey 07] showed that for vertically oriented modules spectral effects increases massively (above 30 %). The impact of spectral effects is smaller in southern Europe than in northern Europe [Virt 12].

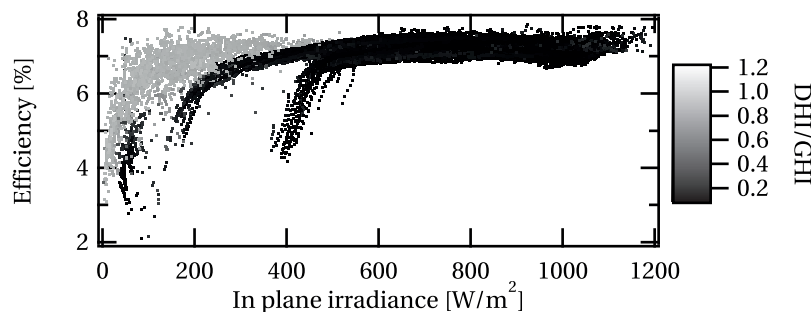


Figure 5.2 – Efficiency of a micromorph minimodule (*B01*) as a function of in plane irradiance (x-axis) and *DHI/GHI* ratio (grayscale). The data points were acquired from June 19, 2015 to September 9, 2015.

Spectral effects for multi-junction solar cells like micromorph and their effect on the current mismatch were *e.g.* discussed in Sutterlueti *et al.* [Sutt 10]. The authors developed a method to evaluate the current mismatch status of micromorph cells under outdoor conditions, in order to separate this effect from degradation, showing that the same cell can switch from a top to a bottom limited regime during seasonal variations. Similar results, but based on simulation were shown by Krishnan *et al.* [Kris 09]. A more precise simulation of spectral effects on

micromorph cells with different thickness was presented by Repmann *et al.* [Repm 03], using a simplified model of the one-diode model with J_{rec} ([Mert 98b], see Sec. 3.5.1) for each subcell. We will here use a similar approach to investigate spectral effects on cell performance.

In this chapter, we¹ quantify the theoretical effects of varying solar spectrum on the energy yield of a micromorph thin-film silicon solar modules in a specific location in Switzerland using a 2 diodes model. We here concentrate on spectral aspects only, temperature and degradation/annealing effects are not considered. We compare the energy yield of a top and a bottom limited micromorph solar cells using simulated varying spectra representing real irradiation conditions and a normalized AM1.5g spectrum representing the case of constant spectral shape of different intensities. The normalization is done in a way to ensure that the energy is kept identical as for the simulated spectrum for the spectral range of the cell (from 350 nm to 1100 nm).

5.2 Model

Firstly we simulated hourly spectrum for one year using the SEDES2 program [Nann 91]. SEDES2² is a semi-empirical model written in Fortran that simulates the irradiation spectrum according to meteorological and geographical inputs. It is based on the SPCTRAL2 model for clear-sky conditions [Bird 86] and with a supplementary cloud modifiers for overcast conditions. The model was calibrated for the location of Stuttgart that we assume to be similar to our location (Bern) in Switzerland. The global horizontal irradiance (GHI), the diffuse horizontal irradiance (DHI), the dew point temperature and the mean of surface pressure for one year used as input are taken from a Meteoswiss³ station located near Bern (CH). To quantify the spectral effects, we generate a second set of hourly spectra generated by scaling the AM1.5g spectrum such that its integral from 350 nm to 1100 nm is equivalent to the integral of the SEDES2 spectrum.

For the cell model, we followed a similar approach to Repmann *et al.* [Repm 03], however we used a 2 diode model with J_{rec} instead of the one-diode model as described in Sec. 3.6. The two diode model was chosen because it was found to be more suitable for $\mu\text{c-Si:H}$ cells as it allows simulating the two current paths through the cell i -layer (bulk $\mu\text{c-Si:H}$ and the porous zone) of such a cell [Pyth 09b]. We fitted the model to a top limited ($\eta = 10.5\%$) and bottom limited ($\eta = 10.2\%$) micromorph cell deposited in our laboratory. Note that top and bottom limited refers to the subcell with the lowest current (that hence limits the total cell current) under the AM1.5g spectrum. The *EQE* of the two cells are shown in Fig. 5.4. The top limited cell has $J_{sc,top} = 10.2 \text{ mA cm}^{-2}$ / $J_{sc,bot} = 13.6 \text{ mA cm}^{-2}$ and the bottom limited cell $J_{sc,top} = 12.8 \text{ mA cm}^{-2}$, $J_{sc,bot} = 12.2 \text{ mA cm}^{-2}$, "top" and "bot" referring to the top and bottom subcells.

¹Y. Riesen, M. Boccard, C. Ballif and N. Wyrsh

²We kindly acknowledge D. R. Myers for giving us the code of SEDES2

³The services have been provided by MeteoSwiss, the Swiss Federal Office of Meteorology and Climatology

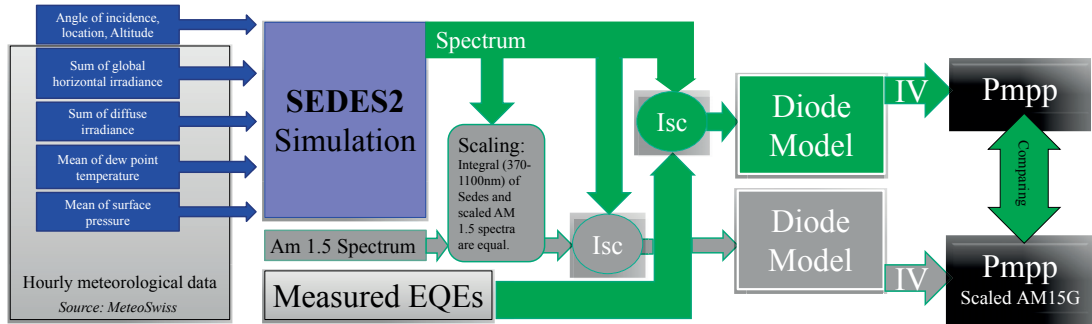


Figure 5.3 – Sketch of the simulation procedure for the study of spectral effects on micromorph solar cells.

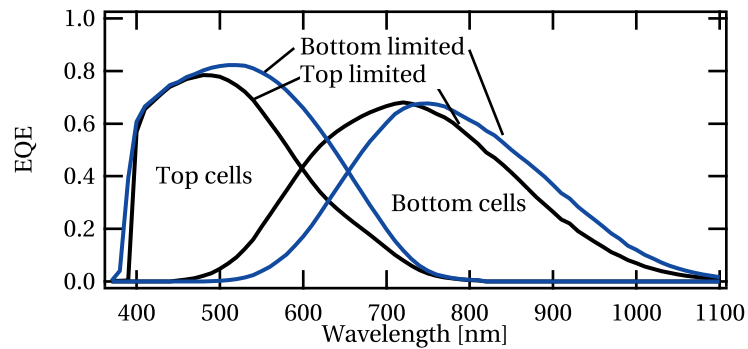


Figure 5.4 – EQE of the top and the bottom limited micromorph cell used for the simulation.

For each time step we calculated the photogenerated currents of the top $I_{ph,top}$ and bottom ($I_{ph,bot}$) cells with the current spectrum convoluted with the measured EQE. Those current values are then used in the diode model to calculate the output power (P_{mpp}) of those cells and ultimately energy yield values.

5.3 Results and discussion

5.3.1 Modeled spectrum

To visualize how the different spectra impacts the energy yield, all SEDES2 spectra for one year were normalized such that their total energy (integrated over all wavelength) are equivalent. The relative contribution of each spectrum shape to the energy yield is then shown in a histogram like plot in Fig. 5.5 left, with the color indicating the relative contribution of those type of spectrum to the total energy yield. On the right of the same graph, the simulated P_{mpp} is plotted as a function of the APE. The color scale of the data points indicates the relative contribution to energy yield of all data points with equal and higher P_{mpp} .

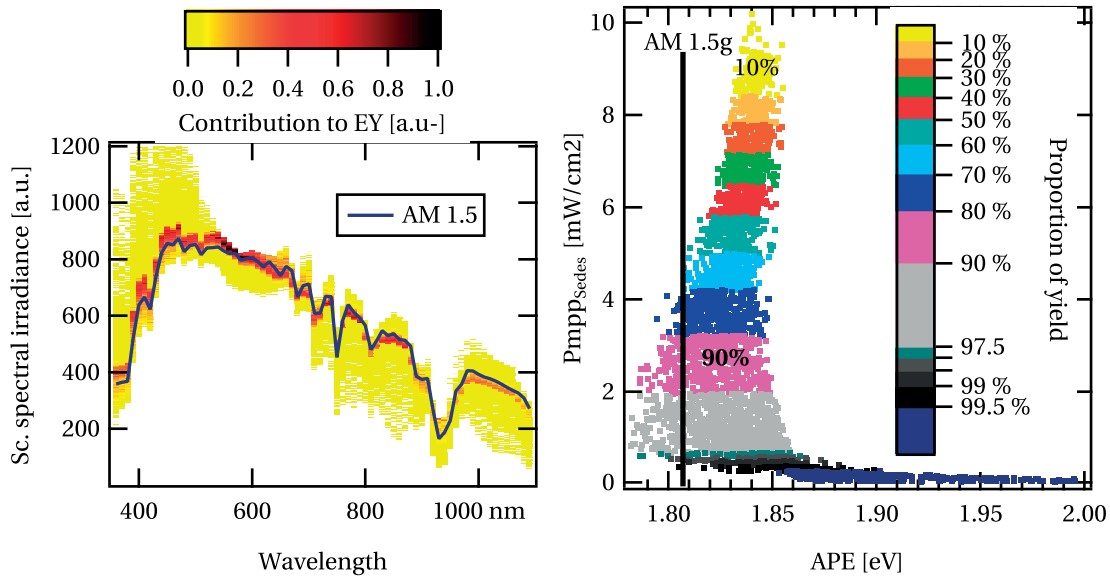


Figure 5.5 – (Left) Contribution to the yearly energy yield of the different spectrum shapes and the AM1.5g spectrum. (Right) simulated P_{mpp} as a function of the APE and their contribution to energy yield (from top to bottom). The height of the color scale bar is proportional to the number of points responsible for this energy yield contribution.

Energy output 2011	SEDES2 [kWh/m ²]	Normalized AM1.5g [kWh/m ²]	relative differences [%]
Top limited	131.9	129.8	1.6
Bottom limited	120.0	120.0	0

Table 5.1 – Energy output simulation (temperature and SWE effects are not taken into account) results for varying spectra and normalized AM1.5g spectrum.

At the simulated location (Bern, Switzerland), 88 % of the total energy yield is produced when the spectrum is bluer (higher APE) than the AM1.5g spectrum. This happens in summer time in the central part of the day. 99 % of the contribution to energy yield is due to spectra with APE values between 1.78 eV and 1.86 eV ($APE(AM1.5g) = 1.81$ eV). To summarize, the spectra that contributes most to energy yield are relatively similar to the AM1.5g spectrum but slightly bluer.

5.3.2 Energy output

The results of the energy output modeling for both, the top and bottom limited cells are presented in Tab. 5.1. The top limited cell has a 1.6 % higher energy energy output using the simulated SEDES2 spectrum (reproducing real spectra) than using a normalized AM1.5g spectrum. This value corresponds to literature values [Grun 09, Hass 07]. The main reason behind this higher value, is the bluer spectrum shifting the cell to less top limited current state

or even to a bottom limited state. Therefore increasing its efficiency (at least when the cell is not too strongly bottom limited). In Fig. 5.6, we see clearly that in summer when the spectrum is bluer due to lower AM, the top limited cell performs better than under an AM1.5g spectrum. For the bottom limited cell, we would expect a lower energy output with the simulated SEDES2 spectrum because the cell is even more limited for bluer spectra, however energy output values are about equal. This is mainly due to the low light performance of this cell. In fact, when lowering the irradiance the expected efficiency gain due to a redder spectrum is often counterbalanced by efficiency losses due to lower illumination. The low performances at low illumination is due to high shunt currents in the $\mu\text{c-Si:H}$ subcell of our test device. For bottom limited cell without high shunt current the energy output calculated with a normalized AM1.5g spectrum should be higher.

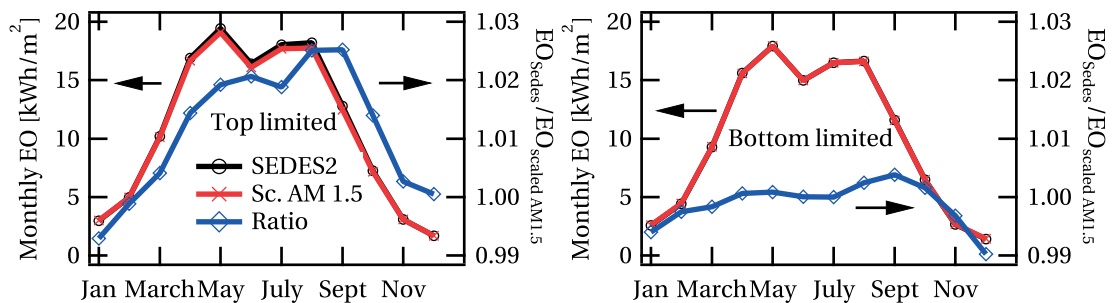


Figure 5.6 – Monthly energy output of top and bottom limited micromorph cells simulated with variable SEDES2 and normalized AM1.5g spectra.

5.4 Conclusion

In order to evaluate the spectral effects on the energy yield calculation of micromorph solar cells we used a 2 diode model with recombination term to simulate the energy output of a top and bottom limited cell. The energy yield was simulated with varying spectrum (simulated using SEDES2 software) and a normalized AM1.5g spectrum. In the first case, more than 88 % of the yearly energy was produced under an irradiation spectrum that is bluer than AM1.5g. Hence, the top limited cell has an energy output that is 1.6 % higher with a varying spectrum than with a normalized AM1.5g. This value is in the range of the spectral effects found in literature. Regarding cell design, this results shows that after taking in account the degradation of the top cell, the micromorph cell should be current matched for a spectrum slightly bluer than the AM1.5g to maximize its energy output. However for the bottom limited cells, we did not observe a difference in energy output between the varying and constant spectra. Lower performances at lower illumination that counterbalance the spectral effects for our cells explains this behavior. This is an interesting case that can happen if there is a low quality bottom cell. However a cell with a better low illumination behavior would give other results.

Chapter 5. Spectral dependence of micromorph solar cells

It has to be noted that the spectra used are simulated, hence inducing some errors. SEDES2 is known to have non-negligible errors in winter [Myer 09]. Ideally, a measured spectrum should be used to calculate the photogenerated currents and evaluate energy yield values.

In this chapter we did not take into account the influences of temperature and metastability (SWE) and we only concentrate on the spectral effects. However, the temperature (see Sec. 4.4) and the SWE influences the current matching conditions of multi-junction solar cells.

Same methodology could be applied to other monolithic multi-junction cells technologies as perovskites-silicon or CIGS tandem solar cells [Lope 14, Todo 15, Mail 15].

6 Annealing and degradation of amorphous silicon solar cells

Summary

Due to the metastable character of the material (as observed in the Staebler-Wronski effect), solar cell performances of *a*-Si:H show degradation or recovery effects following changes in irradiance and/or temperature conditions. The relative variation of the cell's performances (such as V_{oc} , FF and P_{mpp}) extracted from I(V) curve measurements before and after light-soaking depends on the cell temperature and sun simulator irradiance during those measurements. For our cells, the relative variation is more negative (meaning higher degradation) for the V_{oc} but more positive (lower degradation) for the FF , if the temperature is increased during I(V) measurements. These two effects compensate each other to result in a relative variation of the P_{mpp} that is roughly stable with respect to the I(V) measurements temperature and irradiance.

Our indoor light-soaking experiments (for a 20 hours duration) showed that the degradation of the cells performances increases when lowering temperature and increasing irradiance. However for light-soaking at low irradiances (330 W m^{-2}) the relative degradation as a function of temperature is constant and we observed that the higher the temperature the lower the irradiance dependence of the degradation is. At 80°C , the relative degradation no more depends on irradiance. Moreover annealing experiments showed clearly the presence of different defect states.

Outdoor monitoring results of single *a*-Si:H, micromorph and *a*-Si:H/*a*-Si:H tandem cells and modules showed an initial degradation followed by a seasonal variation of the P_{mpp} of more than 4 %, 6 % and 8 % for the *a*-Si:H/*a*-Si:H module, the micromorph module and single *a*-Si:H cells respectively.

Finally, we showed that it is challenging to describe the diode performance evolution (for the purpose of energy yield determination) using a one-diode model comprising a recombination current term using defect density dependent fitting parameters. Indeed the model require not less than four fitting parameters which are all affected by the Staebler-Wronski effect and their relationship with defect density is not trivial.

6.1 Introduction

In 1977, D.L. Stabler and C.R. Wronski discovered that the conductivity of *a*-Si:H layers decreases upon light-soaking and that this change is reversible by heating (annealing) [Stae 77]. This light induced degradation (LID), also called the Stabler-Wronski effect (SWE), affects the performance of *a*-Si:H solar cells. This material is hence metastable as its performance depends on previous irradiation and temperature history. This effect must be accounted when calculating the energy yield of *a*-Si:H based solar modules. We begin this introductory section by a literature review of the SWE effect both at the microscopic and module levels and then investigate its impact on energy yield.

6.1.1 Material level metastability

During light-soaking the defect density of *a*-Si:H increases and during thermal annealing this defect density decreases. The microscopic origin of the *a*-Si:H metastability is still debated in literature. Early on, it was deduced that hydrogen plays an important role in light induced degradation and annealing of *a*-Si:H (see *e.g.* [Stut 85, Powe 02, Mori 05]). From 1985, Stutzmann's breaking of weak Si-Si bonds model [Stut 85] was widely accepted until Branz proposed the "H-collision model" in 1999 [Bran 99]. Overviews of phenomenological and microscopic models are given in [Frit 01, Shim 04, Stra 10]. It is now thought that the nano-structure like nano-voids or di-vacancies play an important role in the metastability of *a*-Si:H [Frit 10, Stra 11, Smet 10]. The different parameters that influence degradation and annealing are: light intensity, illumination conditions (constant or pulsed illumination [Frit 01]), temperature of the sample, electric field in the *i*-layer and the history of the sample [Yang 93, Cuet 99, Roed 00]. The comparison between annealing/degradation in *p-i-n* solar cells and Schottky barrier made by Wronski et al. [Wron 02] indicates that the overall behavior is determined by the bulk rather than interface effects. In most studies, the density of defects or cell performances stabilizes after some time. Park *et al.* [Park 89] observed that this saturation depends on light intensity and is not dependent on the sample temperature up to 70 °C however results of other contributors did not lead to the same results.

Different models were developed to assess the evolution of defect density with LID and annealing:

- Redfield and Bube [Bube 89] introduced an empirical stretched exponential rate equation with terms for light induced creation and annealing, as well as thermal creation and annealing:

$$\frac{dN}{dt} = \left(\frac{t}{P}\right)^{-\alpha} (G_{RB} - DN) \quad (6.1)$$

N is the defect density, t the time, G_{RB} , D and α are constants. Their equation describes that defect generation and annealing are controlled by a dispersive process such as

hydrogen diffusion. However, for some other studies, this model was not able to correctly describe their experimental results [Yang 93, Abra 00].

- For his model Branz [Bran 99] described annealing and degradation with equations of the density of mobile H atoms. According to Shimizu *et al.* the starting assumption that the excitation rate of a mobile H is proportional to the irradiance G and the defect density N is not correct [Shim 04].
- Stutzmann *et al.* [Stut 85, Stut 86], described the time evolution of the defect density based on physical models:

$$\frac{dN}{dt} = ce^{0.04\text{eV}/k_B T} \cdot (G/N)^2 - e^{E_a/k_B T} (N - N(0)) \quad (6.2)$$

where N is the defect density, c a constant, G a parameter describing the irradiance, E_a the activation energy for annealing of the defects and $N(0)$ the starting defect density. The first term of the equation describes light induced defect creation (LID) and the second defect annealing. The authors demonstrated that there is a distribution $N(E_a)$ of activation energies.

- The model of Hata *et al.* [Hata 92] is based on the work of Stutzmann *et al.*. It assumes a Gaussian distribution of potential defect site (also called defect-pool) and annealing energies. The number of potential defect site as a function of the annealing energy (E_{ann}) is expressed by:

$$P(E_{ann}) = N_{sat} \exp[-(E_{ann} - E_0)^2 / 2W^2] / (2\pi W^2)^{1/2} \quad (6.3)$$

Where N_{sat} is the saturated defect density, E_{ann} the activation energy for defect annealing, and E_0 and W are the center and the width of the annealing energy distribution. The envelope of this distribution constitutes the defect pool. Later, Caputo *et al.* [Capu 94] incorporated a light induced annealing effect by adding the ΔE_{ann} term. The change in defect density in time t is then given by:

$$\frac{dN(E_{ann})}{dt} = C_{sw} np [P(E_{ann}) - N(E_{ann})] / N_{max} - N(E_{ann}) / \tau (E_{ann} - \Delta E_{ann}) \quad (6.4)$$

With C_{sw} the Stabler-Wronski coefficient [Stut 85], n and p the free carrier densities of electrons and holes and $E_{ann} - \Delta E_{ann}$ the reduced thermal annealing energy. ΔE_{ann} depends on light intensity and is correlated with the quasi-Fermi level. The thermal annealing term is given by:

$$\tau(E_{ann}) = v^{-1} \exp[(E_{ann})/kT] \quad (6.5)$$

with v the attempt to escape energy. For this model the whole degradation/annealing history has to be taken into account.

- The experimental observation of:

- Two different regimes during LID.
- Degradation kinetics that depends on layers light-soaking history.
- No unique relation between defect densities and the mobility-lifetime product ($\mu\tau$).

led to the suggestion of a two defect state model [Yang 93, Albe 05, Frit 01] based on the assumption that *a*-Si:H based materials have two type of metastable defects state with different annealing kinetics (*i.e.* fast defect states that can be annealed at typical module operating temperatures and slow defect state that do not recover measurably when annealing temperatures are limited to values below 70 °C) [Myon 06, Roed 00]. In this case the total defect density N is given by $N = N_1 + N_2$. The system of equation is:

$$\frac{dN_i}{dt} = G_i(N_T - N_1 - N_2) - A_i N_i \quad (i = 1, 2) \quad (6.6)$$

where G_i and A_i are the constant defect generation and annealing coefficients of the *i*-th component. N_T is the total number of states which can be converted into defects [Yang 93]. This model implies that the degradation annealing history of the cell has to be taken into account. Reasonable fits of data experiments could be obtained [Yang 93]. This two defect state model is a somehow a simplification of Hata's model assuming only two annealing state and not a continuous distribution.

More recently, Melskens *et al.* proposed a nanoscopic model for the creation of light induced defects in *a*-Si:H [Mels 15] especially including the influence of several vacancies and nano-voids [Smet 10]. Their experimental results also support the hypothesis that at least two types of defect are involved.

6.1.2 Module level metastability

After an initial degradation phase, thin film silicon modules efficiency exhibit seasonal fluctuations due to degradation and annealing effects. Literature reports amplitude fluctuations between 5%-10% depending on the sources [Apic 08, Mont 10, Skoc 11, Polv 11, Fann 11, Virt 12, Pier 15]. In winter module efficiency degrades according to LID and in summer, higher efficiencies are reached because of the annealing of the material due to higher operating temperatures. Those metastability effects are more pronounced for *a*-Si:H than multi-junction modules (between 2%-5% less [Skoc 11, Apic 08, Niko 10]). Skoczek *et al.* concluded that for temperate climates, performance gains due to higher operating temperatures of fully-integrated roof systems are higher than losses due to negative temperature coefficients of P_{mpp} [Skoc 11]. For very hot climates, conversion losses due to negative temperature coefficients start to dominate over the positive effect of thermal annealing.

Several degradation and annealing models for energy yield prediction were found in literature and these will be reviewed in the following sections:

Light-soaking and thermal annealing coefficient models

Nikolaeva-Dimitrova *et al.* [Niko 08] light soaked modules at different intensities G (but same temperature of 30 °C) until stabilization of the efficiency was obtained. For all intensities they found a similar stabilized efficiency. From those measurements, they defined a light-soaking (*ls*) coefficient (λ) which is the change in module efficiency per unit time at a given irradiance level¹ (G). They found a linear dependence for $\lambda(G)$. With a similar approach, the thermal annealing (*ta*) coefficient (τ) is defined as the change in efficiency per unit time at a given temperature. It is extracted from controlled thermal annealing of the modules at different temperatures in the dark. They found an exponential growth behavior for $\tau(T)$. Then the daily net effect of the change in efficiency ($\Delta\eta$) is expressed as:

$$\Delta\eta_{\text{daily}} = \sum_i (\lambda_i(G) + \tau_i(T_{\text{mod}})) \Delta t \quad (6.7)$$

Where Δt is the time interval between two measurement points.

Skoczek *et al.* [Skoc 11, Virt 15], presented a similar model which include the stabilized state. The daily Staebler-Wronski state of the module SWE can be described as:

$$dT_{\text{Tot}} = C_{ta} \sum_{i, (T_{\text{mod},i} - T_{\text{min},i}) > 0} (T_{\text{mod},i} - T_{\text{min},i}) \cdot \Delta T + C_{ls} \sum_i G_i \Delta T \quad (6.8)$$

$$d = \begin{cases} SWE_{\text{max}} - SWE_n, & \text{if } dT_{\text{Tot}} > 0 \\ SWE_n - SWE_{\text{min}}, & \text{if } dT_{\text{Tot}} < 0 \end{cases} \quad (6.9)$$

$$SWE_{n+1} = SWE_n + dT_{\text{Tot}} \cdot d, \quad (6.10)$$

with C_{ta} , C_{ls} *ta* and *ls* coefficient, $SWE_{\text{max}}/SWE_{\text{min}}$ the maximum and the minimum state of the module and T_{min} the minimum temperature triggering an annealing effect (typically between 30 °C and 40 °C). Those parameters are determined from controlled indoor measurements.

Polynomial or sinusoidal fit model

Later, the same authors of Equ. 6.7 [Niko 10] developed a simple model based on a sinusoidal function. The amplitude and phase of this function are determined by controlled indoor *ls* and *ta* measurements. Fanni *et al.* [Fann 11] used 4th-grade polynomial fit for one year that interpolates indoor power measurements.

Dose model

Another approach based on the combination of the rate equation of Stutzmann Equ. 6.2 and a dose model was proposed by Zhu *et al.* [Zhu 15]. This model links the defect density with

¹the slope is taken before stabilization

P_{mpp} degradation using the semi-empirical relation from [Smit 85]:

$$\frac{\Delta P}{P_0} = A \log\left(1 + \frac{N}{N_0}\right) \quad (6.11)$$

where ΔP the degradation in P_{mpp} , P_0 the initial device P_{mpp} , N_0 the initial defect density and A a constant. If the LID dominates, this degradation is expressed as:

$$\frac{\Delta P}{P_0} \propto \text{dose} \left(N = G^{2/3} e^{E_{a1}/k_B T} \right) \quad (6.12)$$

with E_{a1} an activation energy.

6.1.3 Motivation and objectives

This literature review showed that the effect of a -Si:H metastability on module performance is generally modeled using phenomenological models (see Sec. 6.1.2) which are able to predict energy yield for a given module (when its performance evolution upon irradiation and temperature change has been fully characterized). The link between material properties and performance metastability is not trivial. There are several models describing the evolution of the defect density N depending on light-soaking and thermal annealing (see Subsec. 6.1.1). An energy yield model of the cell or module encompassing those models would provide more physical insight and enable an extrapolation to other cell design (*e.g.* thicker i -layer). However, it is not straightforward to link defect density to solar cells performance *e.g.* the P_{mpp} .

This link can be done using semi-conductor modeling tools such as ASA (4.2.1, p. 41) [Goer 15]. However many simulation parameters have to be determined, a process prone to errors. This method is also relatively complicated and time consuming. Another way is to use semi-empirical relations such as Equ. 6.11, allowing the use of defect density models, *e.g.* the dose model to calculate energy yield [Zhu 15].

In our approach we want to use the one-diode model with a recombination term (J_{rec}) introduced in Sec. 3.3 (Eq. (3.4)), as it describes satisfactorily the solar cells performance as a function of operating conditions. The advantage of this approach is that, despite the fact that it is semi-empirical (several assumptions are not correct for a -Si:H cells) the parameters employed have a physical meaning. For example, $(\mu\tau)_{\text{eff}}$ can be linked to the defect density. Hence the different models for N evolution with light-soaking and thermal annealing could directly be applied. This model was used to fit I(V) curves and assess the degradation state of a -Si:H modules through the analysis of the evolution of the diode parameters [Mert 98a, Vosw 13] but not to determine energy yield.

In order to develop our model we had to get data on the evolution of cell and module performance upon light-soaking and annealing experiment. We therefore started by measuring the effect of different light-soaking and annealing conditions on the cell performance through several indoor measurements. The results of I(V) measurements before and after light-soaking

and measured in-situ are shown in Sec. 6.2.

In Sec. 6.3, degradation and annealing behavior of outdoor monitored modules are presented. The results of lab-size (0.5X0.5 cm) single *a*-Si:H solar cells, micromorph minimodules (20X30 cm), full size commercial *a*-Si:H/*a*-Si:H and full size micromorph modules are presented. Those results should allow validating the model under real conditions.

Finally in Sec. 6.4 we describe the model that we developed and evaluate its performances and limits.

6.2 Indoor light-soaking and annealing

6.2.1 Experimental details

Experiments were performed on 0.25 cm² thin (180-nm-*i*-layer thickness) high band gap *a*-Si:H solar cells if not stated differently. These solar cells were light-soaked using a fully-LED-based solar simulator [Stuc 14a](see Sec. 2.3), if not stated otherwise. Light-soaking and annealing were carried out at constant irradiance values of about 300 W m⁻², 600 W m⁻², 1000 W m⁻² and 2500 W m⁻² and constant temperatures values of about 20 °C, 50 °C and 80 °C. Most cells were light-soaked and/or annealed during 20 h time steps. We introduce the following notation to describe the light-soaking/annealing conditions of one of these steps: T[temperature]S[irradiance in sun, 1 sun= 1000 W m⁻²]h[duration]. No indication of the time duration will be indicated for the defaults time step of 20 hours (*e.g.* a light-soaking step of 20 hours at 600 W m⁻² and at 50 °C is labeled T50S0.3). For each conditions 2-4 cells deposited on the same substrate are measured. Before and after light-soaking or annealing the I(V) curves of the cells were measured at STC condition using the Wacom solar simulator. Some cells were also measured at different temperatures and irradiation with the cell tester. For annealing in the dark, the cells were kept at constant temperature and I(V) curve were recorded during a light flash of 5 s every minutes.

We here define the relative variation RV_{par} of an I(V) parameter (*par*) as:

$$RV_{par} = \frac{par(t_{\text{after ls/ann}}) - par(t_{\text{before ls/ann}})}{[par(t_{\text{after ls/ann}}) + par(t_{\text{before ls/ann}})] \cdot \frac{1}{2}} \quad (6.13)$$

A negative value indicates degradation and a positive value recovery of the performances.

6.2.2 Results

Dependence of the relative degradation on pre-post I(V) measurements

In this section, we investigate the dependence of the RV of I(V) measurements as a function of temperature and irradiance intensity upon light-soaking for two *a*-Si:H solar cells with different *i*-layer. Both cell were light-soaked at same conditions T50S3. Figure 6.1 shows the

relative degradation for 200- and 300-nm-*i*-layer thickness *a*-Si:H cells of the I(V) parameters measured for three different irradiation intensities as a function of temperature.

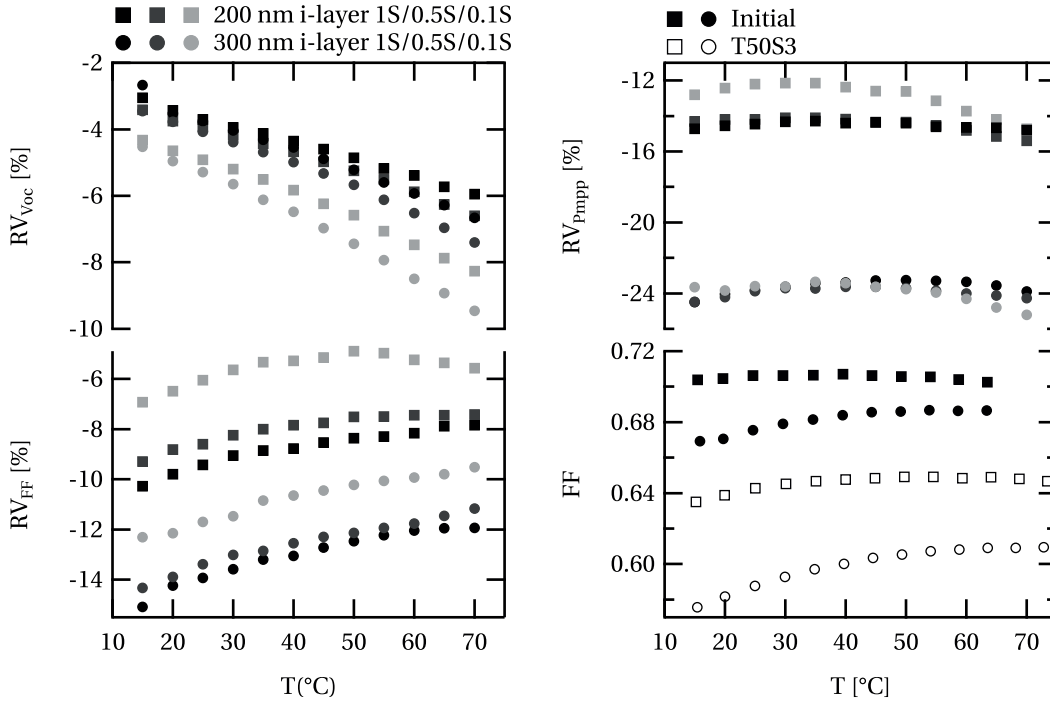


Figure 6.1 – Relative variation of the P_{mpp} , the V_{oc} and the FF values measured as a function of irradiance and temperature following a $T50S3$ light-soaking. The square corresponds to a 200-nm-*i*-layer thick cells and the bullet to 300-nm-*i*-layer thick cells (from *i-thick*. series Sec. 4.2). The FF values measured as a function of the temperature in the initial (full symbols) and degraded (empty symbols) state (lower right figure) are also shown.

The relative variation of the V_{oc} (RV_{Voc}) decreases with temperature (e.g. from -3% at $15\text{ }^{\circ}\text{C}$ to -6.5% at $70\text{ }^{\circ}\text{C}$ for the thicker cell). This behavior is a direct consequence of the lower TC_{Voc} due to a lower V_{oc} in the degraded state (see Sec. 4.2.2, p. 43). Reducing the irradiance also decreases the RV_{Voc} , and this effect increases with increasing temperature, in accordance with the reduction of TC_{Voc} with decreasing irradiance (see Sec. 4.2).

The relative variation of the FF (RV_{FF}), increases generally with temperature (e.g. from -10.5% at $15\text{ }^{\circ}\text{C}$ to -8% at $70\text{ }^{\circ}\text{C}$ for the thicker cell). Again, this behavior is a consequence of the differences (e.g. different T_{FFmax}) between $FF(T)$ curve before and after light soaking [Fig. 6.1 (bottom, right)]. The RV_{FF} seems to increase exponentially when lowering the irradiance (about 3.5% absolute gain from $1000\text{ W m}^{-2}/1\text{S}$ to $100\text{ W m}^{-2}/0.1\text{S}$).

The relative degradation of the J_{sc} (RV_{Jsc}) is relatively constant with temperature and irradiation for the 200-nm-cell. For the thicker cell (300-nm) the RV_{Jsc} values increase by about 1% from $15\text{ }^{\circ}\text{C}$ to $70\text{ }^{\circ}\text{C}$ (not showed).

The relative degradation of the P_{mpp} ($RV_{P_{\text{mpp}}}$) is also approximately constant with measurement temperature and irradiance. Indeed the RV_{FF} difference with temperature and irradiance is balanced by the changes in $RV_{V_{\text{oc}}}$.

Light-soaking at different temperatures and light irradiance

Figure 6.2 shows the time evolution of the V_{oc} , FF and P_{mpp} measured in-situ during light-soaking at two different conditions: $T18S1h500$ and $T50S0.3h500$ of thin high bandgap a -Si:H cells.

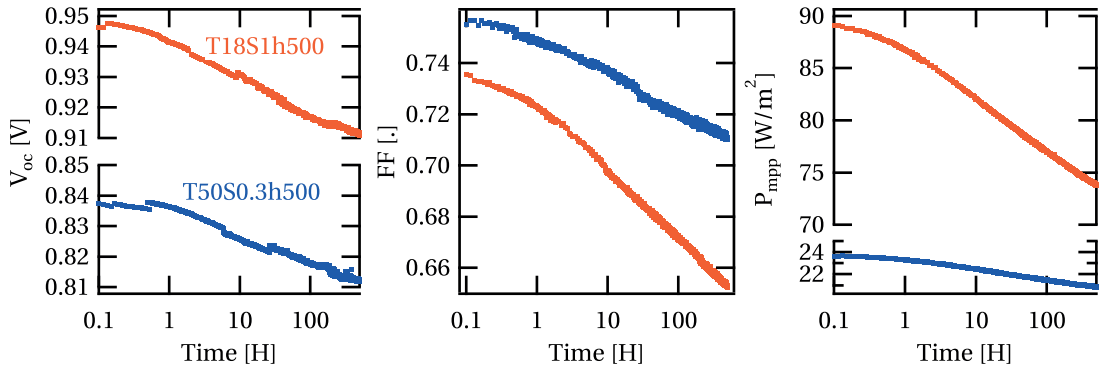


Figure 6.2 – Time evolution of the V_{oc} , FF and P_{mpp} for two different light-soaking conditions during 500h ($T18S1h500$ in red and $T50S0.3h500$ in blue).

The discontinuities seen for the V_{oc} are resulting from small irradiance intensity and temperature variations during the experiments. The P_{mpp} values are adjusted according to the first irradiance values, the latter being continuously measured with a photodiode during light-soaking (to correct irradiance variations). Note, that the in-situ $I(V)$ measurements of the two different curves are taken at different temperature and irradiance conditions (depending on the light-soaking condition). The V_{oc} is higher for the $T18S1h500$ curve due to lower temperature and higher irradiation. Similar observation are made for the other $I(V)$ parameters. For all three $I(V)$ parameters shown in Fig. 6.2, a smaller than logarithmic decrease occurs until about 1 hours for $T18S1h500$ and 10 hours for $T50S0.3h500$ of light-soaking. After this initial period the parameters decrease logarithmically. Between the initial state and the degraded state at 500 h, the P_{mpp} begins to saturate. After 500 h, the P_{mpp} is reduced by $RV_{P_{\text{mpp}}} = -20\%$ for ($T18S1h500$) and by $RV_{P_{\text{mpp}}} = -11\%$ for ($T50S0.3h500$).

In the following part, the cells were light-soaked under different conditions to study the dependence of the $I(V)$ parameters on temperature and irradiance during light-soaking. For practical reasons, most of the cells were light-soaked during 20 h from their initial as deposited state. Figure 6.3 shows the time evolution of the FF and the relative to initial P_{mpp} values under different light-soaking conditions as measured in-situ during light-soaking.

From the time evolution of the FF and the P_{mpp} , we see that the higher the temperature and

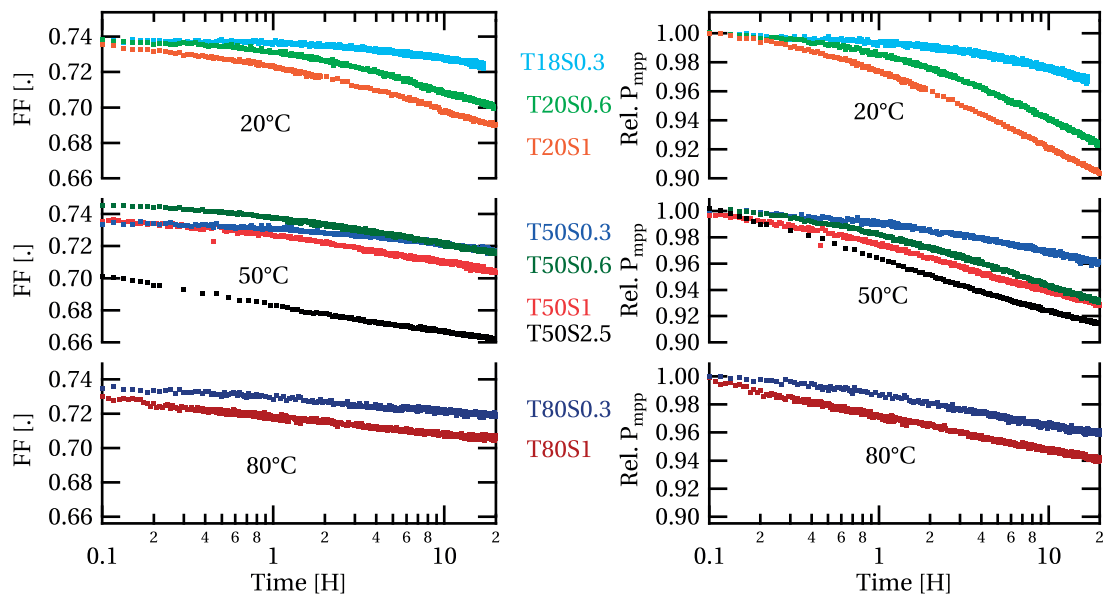


Figure 6.3 – Time evolution of the FF and the relative P_{mpp} for different light-soaking conditions during 20 h (from the initial state).

the higher the irradiance, the quicker the evolution becomes logarithmic. The different RV values as a function of light-soaking temperature are shown in Fig. 6.4 (left). We define the *log slope* parameter as the slope given by a linear fit of the time evolution in log scale of an $I(V)$ parameter from 2 hours to the end of the light-soaking process. The *log slope* allows getting rid of the $I(V)$ measurement scattering (especially for the current) and to directly have an indicator that can be used in a SWE model. This parameter is shown in Fig. 6.4 (right) for the different light-soaking condition.

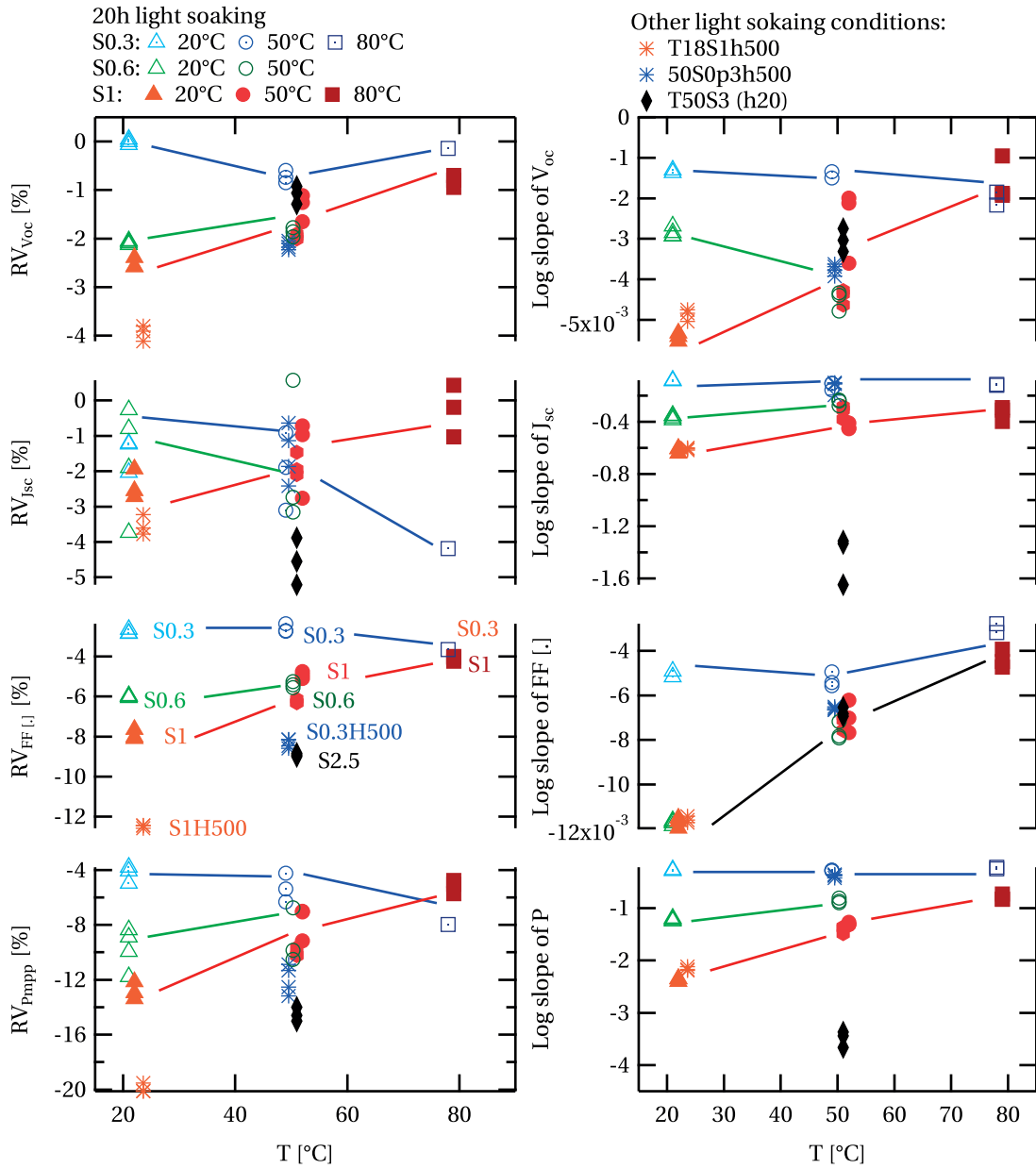


Figure 6.4 – (Left) RV (extracted from $I(V)$ measurement at STC condition before and after degradation) and (right) $log\ slope$ of in-situ measurement of the different $I(V)$ parameters depending on light-soaking temperature and irradiance. Each marker represents one cell hence there are 1 to 4 cells per conditions. The lines are guide for the eyes following same irradiance conditions.

Chapter 6. Annealing and degradation of amorphous silicon solar cells

Let us discuss the result for each I(V) parameter separately:

Within the studied degradation condition window, the RV_{Voc} varies from -4% (*T20S1h500*) through 2.5% (*T20S1*) to 0% (for all low irradiation conditions *S0.3* however as seen for the *log slope* there is still a small degradation). At 20°C , higher irradiances increases the degradation which hence decreases RV_{Voc} . However this RV_{Voc} decrease seems to saturate after a light intensity of $0.6S$. However, at 50°C there is almost no more difference in RV_{Voc} between the different intensities. Even the cells light-soaked during under $2.5S$ irradiance have similar RV_{Voc} as for the other conditions. Furthermore, the statistical deviation of the *log slope* of the V_{oc} measurements appears significant making it difficult to extract some trends. At 80°C , only a small degradation ($RV_{Voc} = -1\%$) of the RV_{Voc} and the *log slope* is observed.

RV_{Jsc} values exhibit a lot of scattering and do not really allow extracting some trends. This noise is thought to be due to the spatial inhomogeneity of light distribution of our sun simulator which is on the order of RV_{Jsc} . However in-situ measurements normalized using the irradiance values recorded by the diode demonstrates clearly that those curve are similar to the *FF* degradation (not shown). Hence, the *log slope* of the J_{sc} gives a better insight. The behavior is similar as for V_{oc} where the degradation increases with an increase in irradiance at 20°C while the value remains stable at higher temperatures. The exception is the *log slope* of the *T50S2.5* cells, which shows a lower RV_{Jsc} .

The RV_{FF} values for $0.3S$ are between 3% and 4% , for the three different temperatures. The highest degradation of the *FF* is encountered for the *T18S1h500* cells with a RV_{FF} of -12% . In general the RV_{FF} are 2-3 times higher than the RV_{Voc} . The general trends of the RV_{FF} are similar to the RV_{Voc} . However, the light-soaking duration has a higher effect on RV_{FF} than for the RV_{Voc} (e.g. the *T50S0.3h500* cells degrades much more than for example the *T50S1* cells). Interestingly, the *log slope* of the *FF* for all degradation conditions higher than $0.3S$ increases linearly with temperature and do not depend on the irradiance anymore.

Within the tested degradation conditions, we measured for the RV_{Pmpp} a minimum degradation of -4% at $0.3S$ and for all temperatures. The RV_{Pmpp} of the *T80S0.3* is certainly underestimated due to the too low RV_{Jsc} induced by the errors during ex-situ I(V) measurements. The lowest RV_{Pmpp} value is found for *T18S1h500* with a value of -20% and the lowest RV_{Pmpp} for 20 h of light-soaking is measured for *T50S2.5*, where $RV_{Pmpp} = -16\%$. To summarize:

- At 20°C the RV_{Pmpp} values increase with irradiance intensity and time.
- Going to higher temperatures those values for irradiance higher than *S0.3* decrease.
- At 80°C , RV_{Pmpp} doesn't evolve anymore as a function of irradiance.

Hence the higher the temperature the lower the irradiance dependence on RV_{Pmpp} and at low irradiance (*S0.3*) the RV_{Pmpp} do not depend much on temperature.

Light-soaking kinetics results with varying a -Si:H cells material parameters or irradiance spectrum can be found in Stükelberger *et al.* [Stuc 13] and Melskens *et al.* [Mels 14].

Annealing after light-soaking

In this experiment the cells are first light-soaked ($T18S1h500$) and then annealed (under the same illumination level, $T80S0.3h118$) in the same light-soaking setup. Figure 6.5, shows the FF and the P_{mpp} values measured in-situ (during light-soaking, small dots) and the $I(V)$ measurement performed with the Wacom simulator at STC (large dots) before and after light-soaking, as well as before, after 20 hours and after 118 hours of annealing.

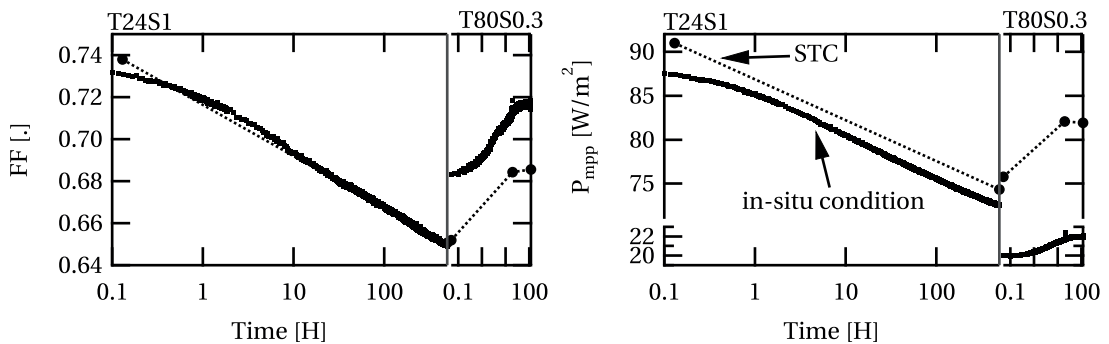


Figure 6.5 – FF and P_{mpp} as function of time for a $T18S1h500$ light-soaking followed by $T80S0.3h118$ annealing step. The large and small dots represent $I(V)$ measurements with the Wacom at STC and in-situ measurements, respectively.

During light-soaking, we observed a $RV_{FF} = -12\%$ as seen in Fig. 6.4. By increasing the temperature and decreasing the irradiance of the light-soaking, the FF increases logarithmically and after about 20 hours it stabilizes, gaining 4.9 % relative variation (RV_{FF}) from degraded state. The same behavior is observed for the P_{mpp} : after losing $RV_{P_{mpp}} = -20\%$ during light-soaking, 8.1 % are recovered during annealing. Note that between the $I(V)$ measurements at STC and the beginning of the degradation, the cell was measured at different irradiance and temperature in the cell tester. During those measurements the cells degraded slightly and this could explain the discrepancy between the STC measurement with the Wacom and the first points in the light-soaking system.

In the next experiment, the cells are first light-soaked ($T50S1h20$) at the same conditions and then annealed at different temperatures and irradiances in the light-soaking setup (for illuminated annealing) or in the cell tester (for dark annealing). The in-situ measurements are shown in Fig. 6.6.

As expected the V_{oc} , FF and P_{mpp} values increase more at 80°C (red curves) than at 50°C (green curves). Interestingly, the performance of the cells subjected to an irradiance higher or equal to $S0.6$, decay again after an initial annealing. The decay is more pronounced at higher irradiances. This behavior reveal that there are more than one annealing mechanism/chan-

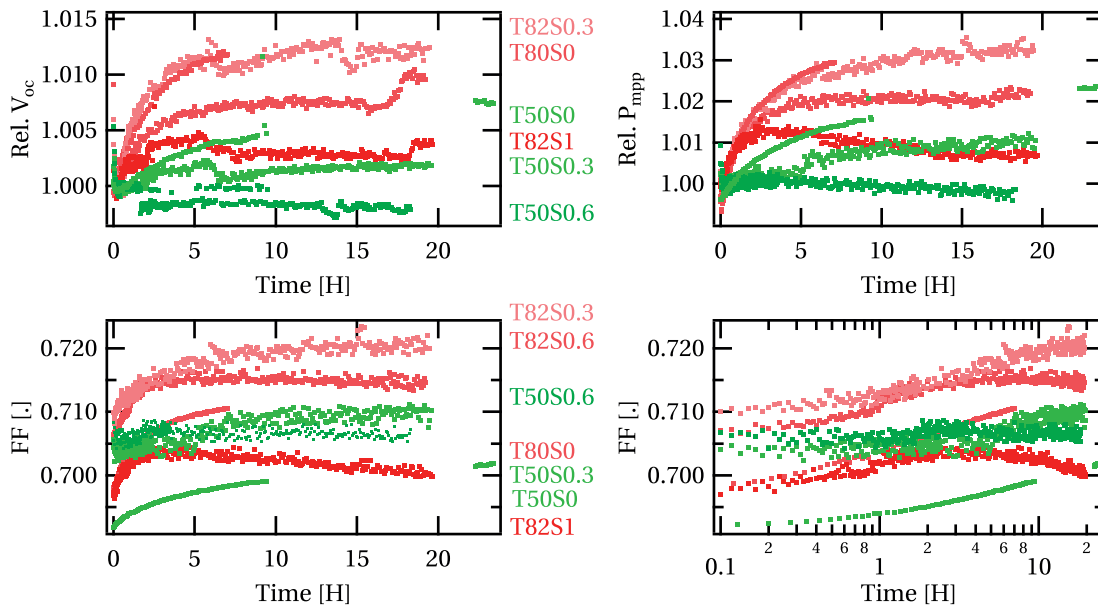


Figure 6.6 – Relative V_{oc} , relative P_{mpp} and FF variation with time during annealing at different temperatures and irradiances after a degradation step of $T50S1h20$ (in-situ measurements under different conditions).

nel as discussed in the literature review 6.1.1 (e.g. fast/slow defects [Roed 00, Myon 06] or activation energy distribution [Stut 86]).

6.3 Outdoor results

In the last section, we characterized the SWE under controlled indoor conditions. Here, we extract the SWE effect from outdoor measurements with varying temperature and irradiation conditions. If a model can be set-up, those data will allow validating the model under real outdoor conditions.

Note that full size modules are kept at the P_{mpp} when not undergoing an I(V) measurement. Alternatively, the other cells and modules are kept at V_{oc} when not measured. This is known to induce slightly higher degradation (due to higher recombination than at P_{mpp}) and also higher cell temperature (meaningful for outdoor monitored cells).

6.3.1 Small amorphous silicon cell monitoring

Experimental details

A $0.5 \times 0.5 \text{ cm}^2$ $a\text{-Si:H}$ cell deposited in our laboratory encapsulated with glue and contacted with ultrasonic soldering was placed in a white box with a 5-mm-thick-glass window. The cell was already slightly light soaked before the outdoor experiment from another experiment. The

temperature of the cell was recorded using an RTD temperature sensor glued on the cell. From mid-September 2014 to mid-September 2015, an I(V) curve and the temperature is recorded every minute. The rest of the time, the cell was left in open-circuit state. Note that the cell was not masked, and light-trapping of the glasses could therefore increase the measured J_{sc} values.

In order to evaluate the degradation and annealing of the cell, the data points that do not respect the following conditions were filtered out:

- The measured J_{sc} is in the range of 3.3 mA to 3.4 mA, which corresponds to an irradiance of 700 W/m^2 to 780 W/m^2 measured with a pyranometer placed just beside the cell with the same orientation². This value was chosen because it is also reached in winter
- The relative variation of the global horizontal irradiance (GHI) measured 10 s and 5 s before/after the I(V) measurement is under 2 %.
- The (calculated) angle of incidence (AOI) is between 35° to 45° to reduce the angular influences on performances.

Moreover, the V_{oc} , FF and the P_{mpp} values were temperature corrected to a temperature of 40°C corresponding to the mean temperature of the filtered data points. The TC were determined by fitting filtered V_{oc} values as a function of temperature. In fact, the $TC_{V_{oc}}$ depends on the degradation states of the cell (as discussed in Sec. 4.2.2) and follows a seasonal variation. In our case it varies from $-0.36 \text{ \%/}^\circ\text{C}$ in November 2014 to $0.39 \text{ \%/}^\circ\text{C}$ in March and June and back to $-0.37 \text{ \%/}^\circ\text{C}$ in August. Same procedure is applied to the P_{mpp} and FF , we got a mean $TC_{P_{mpp}}$ value of $-0.28 \text{ \%/}^\circ\text{C}$ and a TC_{FF} value of $0.1 \text{ \%/}^\circ\text{C}$.

We also normalized the P_{mpp} according to the J_{sc} , to remove spectral effects. However doing so, we removed the contribution of the annealing and degradation of the J_{sc} in the P_{mpp} variation (hence underestimate it). The spectral changes seems to cause variations on the order of 8 %.

Results and discussion

Figure 6.7 shows the mean temperature, the Daily GHI and the variation of the filtered and normalized I(V) parameters.

From mid-September to the beginning of March, the V_{oc} changes by about -12 \% while the FF and the P_{mpp} decrease by -5 \% and -8 \% respectively. Then all parameters stabilize or recover. From end of March until mid-May no data could be recorded because of maintenance and construction work on the roof where the monitoring station is located. In summer due to higher temperatures the I(V) parameters increase notably until a maximum around mid-July. The V_{oc} value then recovers its initial value (which could be verified for several I(V)

²At least from mid-June to mid-September 2015.

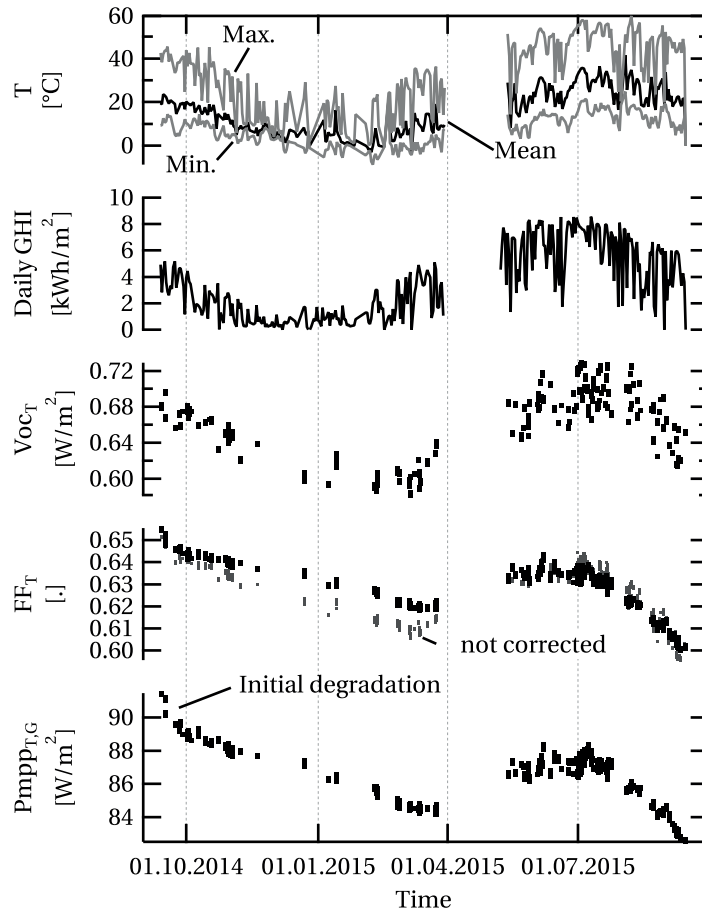


Figure 6.7 – Time evolution of the daily mean temperature (with daily maximum and minimum in grey), daily GHI, the temperature corrected (to 40 °C) V_{oc} , the temperature corrected FF and the normalized J_{sc} and temperature corrected P_{mpp} from outdoor monitoring.

measurements at the identical cell temperatures). However we observe that the FF and the P_{mpp} values do not recover completely (4 % decrease for both).

6.3.2 Micromorph minimodules

Experimental details

Two 30 x 20 cm² encapsulated micromorph mini-modules from an industrial partner were mounted. The first one ($B01_{free}$) was mounted on December 17, 2012 and is free standing. The second one ($B02_{ins}$) was mounted on February 19, 2013 and was isolated with a 8-cm-thick insulating material in order to obtain higher operating temperatures, to compare the degradation/annealing behavior of the modules with different temperatures. Both modules were placed next to each other and south oriented with a 30° tilt. Each minute an IV curve and the temperature of each module were recorded. On December 12, 2013, both modules

were dismantled due to the move of our laboratory to a new building. On July 14, 2014, both modules were mounted on the new building with same tilt but installed with an azimuth of 175° due to mounting constraints. From end of February to mid-July 2015 the modules had to be dismantled due to maintenance and construction work on our roof.

As before the data was filtered to isolate as much as possible the SWE keeping only values with the following conditions:

- The measured J_{sc} has a value between 100 mA and 110 mA corresponding to irradiance values of 690 Wm^{-2} and 760 Wm^{-2} .
- The calculated angle of incidence is between 35° and 45° .

Beside the outdoor measurements both modules were also measured several times indoor using a flat-bed hybrid sun simulator. The module were then measured under different spectra in order to extract the $I(V)$ parameters as a function of current mismatch between the top and bottom cells (as showed in Sec. 4.4). As no EQE results of those modules were available, the mismatch calculation is not precise, and is assumed to be the same for both modules. It is hence more an indication of spectrum variation than reliable mismatch value.

Results and discussion

We here only discuss the FF as it was the only parameter that we could clearly extract from outdoor measurement.

Figure 6.8 (left) shows the FF as a function of mismatch for the first (February 19, 2013) and the last (October 16, 2013) indoor measurements. We see that the current matched point of the two modules differs by about 1 mA cm^{-2} , with the $B02_{ins}$ module being more top limited. Moreover, we see the degradation mostly affects the modules when at top-limited conditions as expected because it is mainly the top $a\text{-Si:H}$ cell that degrades. Moreover in a first approximation, the degradation effect has the same magnitude for all top limited mismatch current values. We also see that the matched point (where the module is neither top nor bottom limited) moves towards a redder spectrum. Figure 6.8 (right) shows the time evolution of the indoor measured minimodules in top-limited condition. The $B01_{free}$ module exhibit a relatively stable FF until end of June. In fall, the FF begins to degrade significantly to reach a total decrease of about 1.5 % compared to its first value measured indoor. The $B02_{ins}$ module (with higher operating temperature) begins to gain almost 1 % of FF and then loses 1.5 % from the first measurement. The higher operating temperature of the $B02_{ins}$ module and resulting higher defect annealing could explain this increase. It has to be noted that the measurement scatterings are relatively important and we estimate (from the observed scattering during measurements) it to be about absolute 0.5 %. The high drop between June 20 and July 1, can be explained by the relative cold period with an average of about 20°C lower daily maximum module temperature compared to the period before).

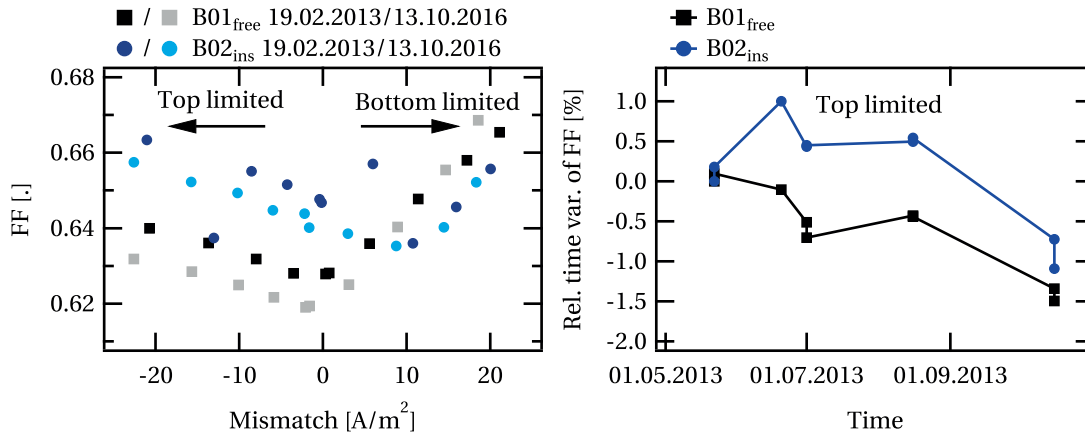


Figure 6.8 – (Left) FF value as a function of mismatch for the first (darkest markers) and last indoor measurements (brightest markers) for the $B01_{free}$ (black) and the $B02_{ins}$ (blue) micromorph modules. (Right) Time evolution of the FF measured indoor in top-limited condition.

The result of the outdoor monitoring are shown in Fig. 6.9. In summer, the maximum instantaneous module temperature of the back isolated $B02_{ins}$ module can reach temperature values that are more than $10\text{ }^{\circ}\text{C}$ higher than for the free-standing $B01_{free}$ module. For $B01_{free}$, we see an initial degradation of about 2% of FF . This seems also be the case for $B02_{ins}$. After this initial period, the $B02_{ins}$ module shows a slightly higher FF gain in summer, gain which is lost again in winter. We also see the FF drop due to colder temperature at the end of June as discussed before. However, the FF of the $B02_{ins}$ module seems to be more stable with the exception of the measurements around mid-February 2015. The origin of this stable behavior is not clear. Less degradation due to higher temperature and/or spectral effects compensating degradation (remember that the matching between the two modules are different) could explain those results. Moreover instantaneous operating temperature influences that were not taken into account could also contribute to this observations.

6.3.3 Micromorph and amorphous tandem module

Experimental details

In this section we present the outdoor monitoring results of full size micromorph and a -Si:H/ a -Si:H tandem module (see Sec. 2.4). Similar to the outdoor monitored a -Si:H small cells, the data points were filtered out as follows:

- The measured J_{sc} were filtered out for values corresponding to an irradiance of 720 W/m^2 to 760 W/m^2 .
- The relative variations between the nearest GHI measured irradiance and the irradiance measured 10 s before and after is smaller than 2%.

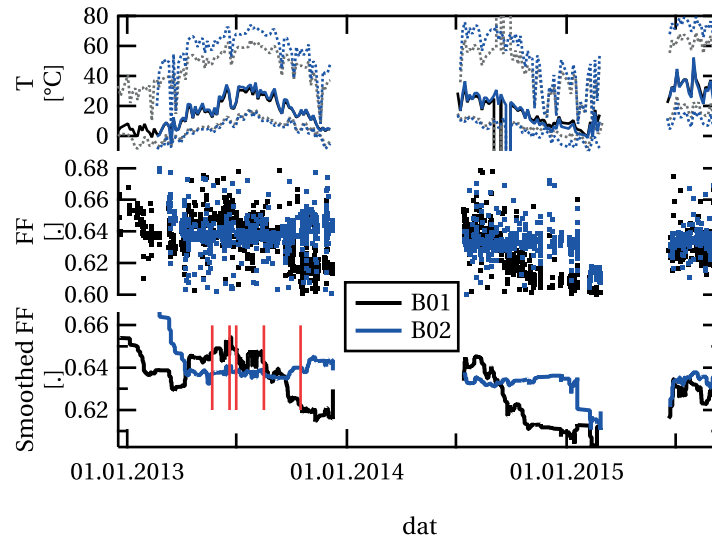


Figure 6.9 – Time evolution of outdoor measured module temperature (maximum, minimum and mean) over 4 days, filtered FF and smoothed (binomial smoothing) filtered FF of the $B01_{free}$ and $B02_{ins}$ micromorph minimodules. The vertical lines corresponds to the indoor measurements dates showed in Fig. 6.8.

- The (calculated) angle of incidence (AOI) is between 37° to 43° .

The temperature dependence of the FF were small and difficult to extract for both module. Hence no temperature correction could be applied to the FF . The P_{mpp} are normalized using the actual J_{sc} over $J_{sc}(@740\text{ W m}^{-2})$ ratio and the temperature values corrected to 45°C using respectively a $TC_{P_{mpp}}$ of $0.28\% / ^\circ\text{C}$ and $-0.27\% / ^\circ\text{C}$ for the micromorph and the $a\text{-Si:H}/a\text{-Si:H}$ modules. Note that we again assume a TC independent of the degradation annealing state, assumption which is not completely true.

The $a\text{-Si:H}/a\text{-Si:H}$ module was measured indoor before installation (July 11, 2014) and on May 6, 2015.

Results and discussion

We begin with the indoor $I(V)$ measurements of the $a\text{-Si:H}/a\text{-Si:H}$ module shown in Tab. 6.1. In 10 month the module lost $RV_{FF}=-18\%$ and $RV_{P_{mpp}}=-19\%$.

	V_{oc} [V]	FF [%]	P_{mpp} [W]	I_{sc} [A]
11.07.2014	42.4	74	123	4.00
06.05.2015	39.8	62	102	4.22
RD	-6.3 %	-18 %	-19 %	-5.4 %

Table 6.1 – IV results of indoor measurements of the $a\text{-Si:H}/a\text{-Si:H}$ module

Figure 6.10 shows the time evolution of the filtered FF and P_{mpp} of the micromorph and a -Si:H/ a -Si:H modules.

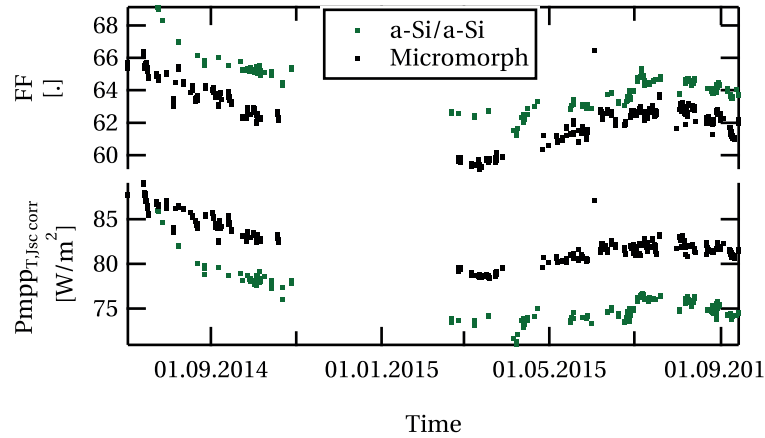


Figure 6.10 – Time evolution of the filtered FF and P_{mpp} measured with the monitoring station. The P_{mpp} are normalized with the J_{sc} ($@750\text{ W m}^{-2}$) and temperature corrected ($@45\text{ }^\circ\text{C}$).

For both module, we see the characteristic initial degradation which is particularly high for the a -Si:H/ a -Si:H module. Then from mid-March 2015, due to higher operating module temperature, the FF and the P_{mpp} of the micromorph and a -Si:H/ a -Si:H modules increase by about 6 % and 4 %, respectively, until beginning of August. Then as expected, the performance of both modules decreases again.

6.4 Diode modeling

In this section we describe our diode model using a defect density dependent one-diode equation with J_{rec} for reproducing the degradation and annealing behavior of a -Si:H solar cells. This model should allow for the determination of device energy yield including the SWE. In a first step we developed a model describing the dependence on defect density (which should represent degradation/annealing state) of different fitting parameters. In a second step, we analyzed, from experimental data, the change of the fitting parameter (before adding defect density dependence) before and after degradation. Finally we check the consistency of the model with the experimental data (from Sec. 6.2). We also evaluate and discuss the limits of this of model.

6.4.1 Description of the model

In Chapter 3, we showed that the one-diode equation with a recombination term J_{rec} is able to reproduce the temperature and irradiance dependence of amorphous silicon solar cells.

This diode equation is repeated here:

$$J(V) = J_{ph} - J_{ph} \frac{d_i^2}{(\mu\tau)_{eff}[V_{bi} - (V + JR_s)]} - J_0 \left[e^{\left(q \frac{V + JR_s}{nkT} \right)} - 1 \right] - \frac{V + J \cdot R_s}{R_p} \quad (6.14)$$

with J the current density, V the voltage, J_{ph} the photogenerated current density, d_i the thickness of the i -layer, $(\mu\tau)_{eff}$ the effective mobility lifetime product, V_{bi} the built-in voltage, R_s the series resistance, R_p the shunt resistance, n the ideality factor, q the unity charge and k_B the Boltzmann constant. We expect that in particular $(\mu\tau)_{eff}$, J_0 and n will depend strongly on the defect density N_r (or recombination center density).

The lifetime can be given by [Stre 82]:

$$\tau_{n,p} = \frac{1}{v_{n,p}\sigma_{n,p}N_r} \quad (6.15)$$

with $v_{n,p} = \sqrt{3kT/m_{p,n}}$ the thermal velocity ($m_{p,n}$ are the effective masses of electrons and holes) and σ the capture cross section. We make the assumption that v and σ do not change with degradation and annealing. We then make the assumption that:

$$(\mu\tau)_{eff}(N_r) = \frac{\mu_{eff}}{v_{eff}\sigma_{eff}N_r} = \frac{C_\mu}{N_r} \quad (6.16)$$

with μ, v, σ_{eff} effective values of the mobility, thermal velocity and capture cross section respectively. In our model we decide to group those three parameters in a fitting parameter C_{mu} .

For the defect density dependency of J_0 , we choose the same dependency as the $J_{0,bulk}$ Eq. 3.7 expression (Sec. 3.3). This was done for two reasons: (1) the main change in recombination rates happens in the i -layer (in the bulk, the role of interfaces is less important) and (2) the fitted ideality factors are nearer to 2 than 1 (an ideality factor of 2 is normally attributed to the $J_{0,bulk}$ [Rech 97, Vosw 13]). We get:

$$J_0 \cong J_{0,bulk} = \frac{q d_i n_i}{\tau} = q d_i n_i v_{eff} \sigma_{eff} N_r = C_J N_r \quad (6.17)$$

where we use $C_j = q d_i n_i v_{eff} \sigma_{eff}$ as a fitting factor and Eq. 6.15.

We did not succeed to find any expression for the ideality factor as a function of N_r .

6.4.2 Before and after degradation fit

Before adding the N_r dependence, discussed before, to the fitting parameters, we fit the one-diode model with a recombination term (J_{rec}) and uses the fitting procedure described in Sec. 3.5.2 to the data of a thin high-bandgap cell in both initial and degraded state (*T23S1h500*). The fitted parameters are shown in Tab. 6.2.

Parameter	Initial	<i>T23S1h500</i>
J_{ph}	13.7 mA cm ⁻²	13.6 mA cm ⁻²
J_0 at 25 °C	1.48×10^{-7} mA cm ⁻²	3.94×10^{-6} mA cm ⁻²
n	1.63	1.86
$(\mu\tau)_{eff}$	3.29×10^{-13} m ² /Vs	2.04×10^{-13} m ² /Vs
V_{bi}	1.2 V	1.07 V
R_s	0.023 Ω cm ²	0.026 Ω cm ²
R_p	1970 Ω cm ²	1970 Ω cm ²
d_i	120 nm	120 nm
E_{act}	0.73 eV	0.73 eV

Table 6.2 – Diode parameters for the one-diode model with current loss term J_{rec} in initial and degraded *T23S1h500* state.

The J_0 increases during light-soaking by more than one order of magnitude. The ideality factor n increases by 0.23 and the $(\mu\tau)_{eff}$ product decreases by 47 %. Additionally, V_{bi} also decreases significantly as it could be expected because of a lower electrical field in the i -layer after light-soaking due to higher charged band tails.

6.4.3 Model validation

Combining Equ. 6.16 and Equ. 6.17 we get:

$$(\mu\tau)_{eff}(t) \cdot J_{0,bulk} = C_\mu C_j. \quad (6.18)$$

According to our model this product should always be constant as it is independent of the defect density. From Tab. 6.2, we directly see that this is not the case, as it increased 14 times upon degradation. This dependence on defect density introduced in our diode model is too simple to reproduce the effects of degradation on the diode I(V) characteristics:

- The assumption of a unique relation between $(\mu\tau)_{eff}$ and the defects density is probably a simplification that do no more allows an acceptable description of this effect. Indeed, Fritzsche *et al.* [Frit 01] pointed out that there is no unique relation between $\mu\tau$ and the defect density.
- The $(\mu\tau)_{eff}$ product is not constant through the whole device.
- Moreover, the assumption that J_0 is only affected by bulk recombination seems also not to be adequate. A more complex model is required that also includes *e.g.* defect states related to open volume deficiencies and charged state located away from midgap as stated by Melskens *et al.* [Mels 14].

Moreover, many assumptions leading to the diode equation are not true for a -Si:H cells. It should be considered as a phenomenological model (although temperature and irradiance de-

pendence could be well reproduced with this model see Sec. 3) resulting in fitting parameters with weaker link to real material parameters. This makes it difficult to relate them to defect densities.

In addition, from Tab. 6.2 we learn that there are at least four fitting parameters that vary with degradation (J_0 , n , $(\mu\tau)_{eff}$ and V_{bi}). In addition to the (too) simple assumptions for the dependence of $(\mu\tau)_{eff}$ and J_0 with N_r , we did not find an expression for n and V_{bi} as a function of N_r . A supplementary step that could be done to model the SWE with the diode equation, would be to measure the kinetics with light-soaking of the different fitting parameters. We saw in Ch. 3 that to be able to uniquely determine the fitting parameter, we need I(V) measurements at different irradiance values. In our indoor light-soaking experiments, we have those data from the measurements before and after light-soaking. During light-soaking we have the I(V) measurements for only one irradiance. However, we could design an experiment with I(V) measurements at different irradiances during light-soaking. However, it would be a phenomenological model with no or very weak link to material properties of the cell.

6.5 Conclusion

Our experimental indoor results, showed that the relative V_{oc} and FF variations depend significantly on the I(V) measurement temperature and irradiance taken before and after light-soaking. Those variations could be linked with the temperature dependence of those factors. The relative variation of the P_{mpp} is less dependent on measurement conditions as the V_{oc} and FF degradation variations compensate each others. However, it is probable that this compensation is not valid for all a -Si:H cells.

Additionally, light-soaking of our cells at different temperatures and irradiances showed that for the V_{oc} , J_{sc} , FF and hence P_{mpp} , the degradation depends on temperature and irradiance. During light-soaking, (1) the higher the temperature, the lower the degradation, and (2) the higher the irradiance, the higher the degradation. Interestingly at higher light-soaking temperatures (80 °C), the degradation dependence on irradiance vanishes. And for light-soaking irradiance equivalent to 0.3 sun the degradation is constant for all temperatures. Hence an annealing degradation model has to take into account temperature and irradiance levels.

From in-situ I(V) measurements with a thermal annealing during light-soaking (constant conditions), we saw that under certain circumstances, the cell first anneals but then degrades after some hours. This confirms that several (or a distribution of) activation energies are involved in the annealing of defects.

The analysis during 14 month of lab-sized single a -Si:H cells, micromorph minimodules, and full sized a -Si:H/ a -Si:H and micromorph commercial modules, all installed outdoor, showed the expected initial degradation and then the seasonal variation of the performance. This variation was of about 2 %-4 % for the FF of the different modules. For all types of modules

Chapter 6. Annealing and degradation of amorphous silicon solar cells

the magnitude of the FF annealing and degradation were comparable. Measurement of the multi-junction devices were problematic as spectral effects (which could not be taken into account) affect the data. For single junction a -Si:H cell, spectrum effects were compensated by a normalization procedure which resulted in the fact that the degradation/annealing of the J_{sc} could not be observed. Installing a filtered c -Si reference cells or a spectrometer would allow taking better into account those spectral effects and to enable a reliable analysis of the J_{sc} variations.

We showed that a reasonable energy yield model based on a one-diode model with J_{rec} with parameters depending on defect density is difficult to achieve. Indeed at least four diode parameters (J_0 , n , $(\mu\tau)_{eff}$ and V_{bi}) are affected by degradation/annealing as showed by fitting experimental $I(V)$ curves in a way that is not known. Moreover, we did not find how the different fitting parameters can be expressed with a common defects density parameter and the measured values were inconsistent with our model. To simulate the effect of SWE on the performances of a -Si:H cells a more complex model is needed taking in account more parameters as charged states located away from the band gap and no unique relation between $(\mu\tau)_{eff}$ and defect densities. Hence complete empirical models are the best alternative for the moment.

7 Photovoltaic generation and the local electricity grid

Summary

In a near future with the expected high PV penetration into the electricity grid, the midday PV production peak could become detrimental for grid stability. In this chapter we investigate how local electric or heat storage, different module orientations or demand-side management could help reducing injected power in the low voltage grid (peak shaving) thus supporting its stability. The present analysis will mainly focus on the role of households.

We developed a simple simulation tool able to model a PV system with local storage (flux model). With this tool we could test different control algorithms or storage strategies for the battery analyzing a case where the power can be fed to the grid without limit and cases where the power is capped. In this latter case, the power exceeding the feed-in power is lost if it cannot be stored locally. In case of no feed-in limit, an electricity pricing including a tax proportional to the daily maximum feed-in power is the best scheme for an efficient peak shaving capability. When a feed-in limit is present storage has to be optimized to minimize energy or financial losses. We tested two different algorithms that optimizes the financial balances due to electrical grid exchange (buying or selling electricity): (a) the first algorithm performs an optimization based on forecast data of the PV production and the load and (b) the second one relies only on a rough clear sky production forecast. We show that algorithm (b) performed almost as well as algorithm (a) when exact forecast are known and much better than algorithm (a) when real forecasts are used. Aggregating several loads (several households on the same low voltage grid) allows diminishing significantly the losses due to the feed-in limit. We also compared battery storage and heat storage using boilers or heat-pumps combined with a hot water reservoir for domestic hot water heating. Generally heat storage performs as well as battery storage in reducing losses due to the presence of a feed-in limit. Moreover, if the power of the heat-pump can be varied (in contrast to a heat-pump with only on/off state - as it is mostly the case) the losses due to peak shaving can be reduced further.

Changing tilt and orientation of the modules allows mainly to reduce losses due to feed-in limits and to reduce the winter/summer production ratio by more than a factor two. However, significantly more PV modules should be installed to achieve the same yearly energy production.

Finally, we developed a statistical method allowing to estimate the usage of different electrical appliances of a household from 15-minutes measured loads, generic time use data and some characteristics of the households (such as number of persons and electrical appliances). Using this method we esti-

mate that about 8 % of the total load could be shifted to the midday period easily and hence reduce accordingly the PV production peak.

Finally, we combine device and system aspects to show that varying cell technology (e.g. with different temperature response) has a limited but not negligible impact on system output.

7.1 Introduction

The new Swiss energy strategy 2050 (decided by the federal council [Mess 13]), implies the shut down of all Swiss nuclear power plants. Consequently, by assuming the same electricity consumption and exchange with other countries as in 2014, 37.9 % (26.4×10^9 kWh) of the yearly Swiss electric production has to be replaced by other power sources.

For planning the future electricity supply of Switzerland, in a very simplified and schematic way (i.e. neglecting power imports and exports), we need to minimize the cost and the environmental impacts (Eco-imp.)¹. The two following objective functions have to be optimized:

$$\min \text{Cost} = \min \sum_{PP} CAPEX_{PP}(IP) + OPEX_{PP}(IP, x) + Grid(PP, IP, x) \quad (7.1)$$

$$\min \text{Eco-imp.} = \min \sum_{PP} CO_2(IP) + EI_{pp} \quad (7.2)$$

The cost can be approximated by the sum of the investment cost (including interest rate, $CAPEX_{PP}$ capital expenditure), the operating cost of the power plant (including fuel and maintenance cost, $OPEX_{PP}$, operating expenditure) and the grid cost. The different costs are mainly a function of the power plant type (PP =hydraulic, thermal, photovoltaic, wind,...) and the respective installed power (IP). Moreover the operating cost also depends on the power plant operation schedule (x) and their geographical distribution. For renewable power sources, because no fuel is used, the operating cost are generally lower (only maintenance). The environmental impact (Equ. 7.2) is reduced by mainly minimizing the CO_2 emission during fabrication (gray energy) and operation. Other ecological impacts (EI) such as toxic or dangerous waste emissions during fabrication, operation and decommission have also to be taken into account. As for any optimization problem there are specific constraints. Some major ones are expressed as follows:

$$\text{Production}(t) = \text{Load}(t) \forall t \quad (7.3)$$

$$\text{Line power}(t)_i \leq \text{Max line power}_i \forall t, i \quad (7.4)$$

$$\text{Trafo power}(t)_j \leq \text{Max trafo power}_j \forall t, j \quad (7.5)$$

$$\text{Generated power}_{PP} \leq P(\text{Irradiance or wind or water flow})_{PP} = \text{PV, wind, hydro,} \quad (7.6)$$

the total produced electricity has to be equal to the total load plus the grid losses at every time

¹It should be stressed that the actual cost structure of electricity does not include externalities, such as the social, environmental and health cost caused by pollution such as the emission in the atmosphere of pollutants and CO_2 (global warming, disease, ...)

t (Equ. 7.3). The maximum power (active and reactive) limits for each transport line of the grid and the transformers (trafo) have always to be respected for each item i, j (Equ. 7.4 and Equ. 7.5). For photovoltaic, wind and hydro the power production is strongly influenced by meteorological conditions such as irradiation, wind speed or rain and exhibit a high degree of variability. Additionally a power reserve is necessary to compensate for forecast errors and load variation. The principal decision variables are:

- The type of power plants (PP), their installed power (IP).
- The production schedule (including on/off and curtailments) for each power plant.
- Location and distribution of the power plants in the grid.

In order to fulfill Equ. 7.3, beside adapting the production (supply-side management), the load can also be adapted. Acting on the load-side is called demand-side management (DSM). Electricity storage is also another way to fulfill this constrain. In Switzerland, pumped hydro is already used as a mean of storing energy.

7.1.1 PV integration in the Swiss grid

As discussed in the general introduction in chapter 1, PV power will certainly play a non-negligible role in the future electricity mix. PV power is not controllable and can only be used directly or curtailed. To have an approximate figure on the share of Swiss electricity demand that PV could supply, we performed a simple simulation using the total Swiss electricity load of 2014 [Swis 15], the weekly run-of-river power plant production [OFEN 14] and a simulated PV production (using irradiance and temperature data from Meteoswiss station in Neuchâtel). No other renewable sources are taken into account. We assumed that the Swiss electric grid is one big copperplate (neglecting grid losses and constraints 7.4, 7.5). Hence we are focusing solely on the constraint described in Equ. 7.3. As for PV, production by run-of-river power plant production is also not controllable. Therefore the excess PV is defined as the amount of production that is higher than the total Swiss load subtracted by the run-of-river power plant production (red area in Fig. 7.1). The PV production is scaled such that the yearly generated energy reaches the given percentage of the total yearly load.

Figure 7.1, shows the simulated PV production scaled such that it covers 20% of the yearly Swiss load, the measured run-of-river power plant production, the measured total electricity load and the excess PV power for a week in May 2014. The peak load coincided temporally with the PV production peak. However, there is still a load at night (around 5 GW to 6 GW). Most of the excess PV power is produced around midday during week-ends (e.g. 17-18 May), as the load is then lower, and can reach more than 2 GW. For comparison, the pumped hydro storage power capacity in Switzerland for 2012 was 1.4 GW and should be 3.5 GW in 2016²

²With the new or extension of Hongrin-Léman, Nant de Drance and Linthal

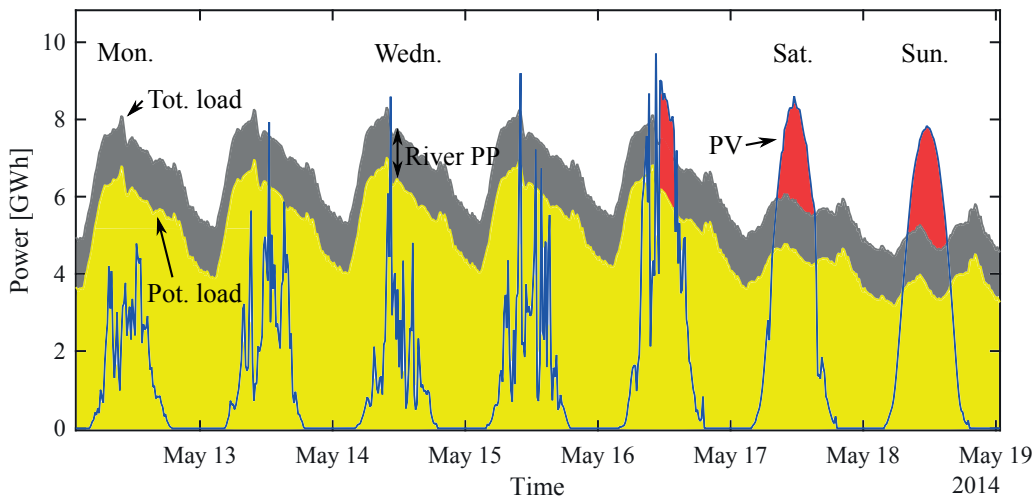


Figure 7.1 – Blue: Simulated PV production with panels facing south and 30° tilt scaled such that it covers 20% of the annual total Swiss load. Top of the gray area: Total Swiss electricity load. Gray area: run-of-river power plant production. Yellow: Potential load that can absorb the produced PV energy (Total load – river power plant production). Red: Excess PV energy.

[Avel 12]. In a more realistic simulation the PV production peak should be lower and larger because of distributed orientation of the panels (in our simple simulation all PV panels are south oriented with a 30° tilt and at a same location).

Figure Fig. 7.2 a), shows the simulated excess PV production relative to the total yearly PV production as a function of the annual PV coverage of the load. Up to 10% of yearly PV coverage, the remaining load (not covered by run-of-the-river hydro plants) can absorb all PV production. At 20% coverage, 6% of the total PV produced energy is exceeding the remaining load. This excess energy could either be curtailed which implies a higher cost for PV electricity (due to wasted energy) or either be stored. This excess energy has only to be stored daily because there is enough load at night to adsorb this excess. A similar analysis performed for the Zurich area can be found in Baumgartner *et al.* [Baum 10] or for the Swiss case in Remund *et al.* [Remu 14].

Beside daily fluctuations there is also a seasonal variation of the PV production. Figure 7.2 b) shows the seasonal variation of the simulated PV production and the load. PV production decreases in winter while the load increases. The PV production variability depends on tilt and orientation distribution of the PV panels. Seasonal storage could be provided for example by power-to-gas [Baum 13].

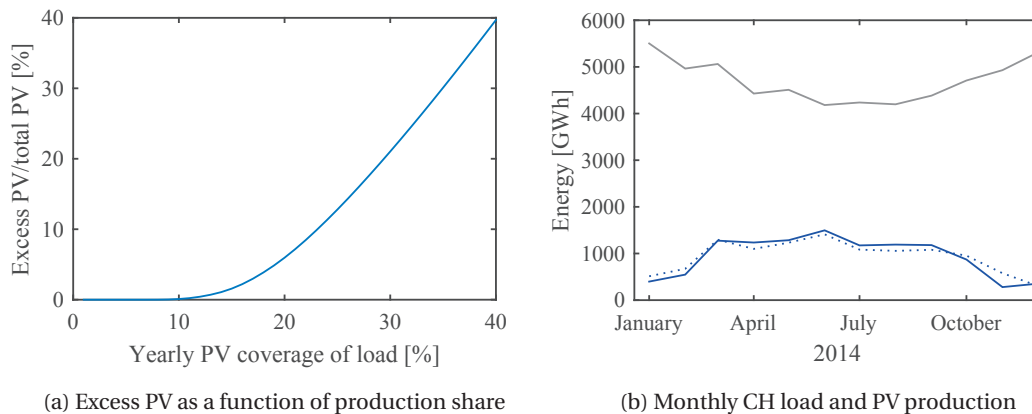


Figure 7.2 – a) Simulated excess PV production as a function of PV coverage of the total Swiss load. b) Monthly Swiss total load in gray and simulated PV production (solid line: for Neuchâtel and dotted line for la Chaux-de-Fonds, south oriented and 30° tilt.) for 20 % PV coverage in blue.

7.1.2 PV integration in the local grid

At local level, in the low voltage grid, high PV penetration may lead to a breach of the constraints Equ. 7.4 and Equ. 7.5. Over-voltage or excess power in low to medium voltage transformer may occur [Denh 07, Buch 13b]. In the framework of the global optimization problem presented in Equ. 7.1 and Equ. 7.2, this chapter focuses on how peak power of PV can be lowered at households level to avoid detrimental effects on the low voltage grid stability, allowing for a larger PV penetration into the grid.

The PV production peaks can be minimized (peak-shaving) by a) storing electricity in a battery [Muld 10, Riff 11, Dunn 11, Schm 10, Alam 13, Appe 12, Brau 09, Mazh 11], b) changing module tilt and orientations or c) by shifting loads to high PV production periods (DSM) [Buch 13a, Caam 09]. These three approaches will be discussed in this chapter. Smart inverter acting on reactive power can also contribute to decrease over-voltage created by PV at the end of distribution lines and thus help improve grid stability [Blet 10, Brau 10]. However, this possible solution will not be treated in this work.

In the first approach a) grid-connected PV-installations with storage can either be locally controlled or centrally remote controlled (e.g. by the utility). In the case of a local control no communication infrastructure is needed and the owners of the system are in general more involved financially. Incentives are either given by the electricity pricing adapted to discourage system owners to feed-in at midday, or by a feed-in curtailment regulation limiting the maximum feed-in power into the grid. Such limit may be defined, as in Germany (and for the present work) by a given ratio of the maximum feed-in power (at the injection point into the grid) to the PV-system nominal power and it easily allows reducing the peak power at midday [Umla 12]. If the system cannot absorb enough power through storage or load

Chapter 7. Photovoltaic generation and the local electricity grid

with respect to the feed-in limit, the excess feed-in power has to be curtailed and is lost (*PV-loss*). In section 7.2, we quantify the performance for peak-shaving of a household with a PV installation and local storage by modeling various system sizes and storage strategies. For this goal we developed a Matlab program able to simulate those systems, it is described in sec. 7.2.1. This program includes decision algorithms controlling the power fluxes in the system, either based on forecast data or only instantaneous data. These algorithms either optimize the electricity cost for the user, minimizing PV-losses due to the feed-in limit (7.2.2) or maximizes self-consumption. We then compare different electricity pricing schemes for their ability to shave peaks (7.2.3) without imposed feed-in limits. Next, in the framework of a possible feed-in limit regulation similar to the German case, we compare two battery control management (*e.g.* two storage strategies) for their ability to minimize *PV-loss* and maximize self-consumption (SC). The first strategy requires PV-power and load forecasts and the second needs only the maximum power curve of the PV system under clear sky condition (7.2.4). The different losses of a PV system with battery are analyzed in subsection 7.2.5. The simulation is then applied to different households to study the sensitivity of the results to the details of the load curves (7.2.6) and to quantify the effect of aggregating several loads for one battery (7.2.7). After that, we discuss a control algorithm that adapts daily its feed-in power limit in such a way that all the excess PV-power can be adsorbed by the storage. Especially for households, excess energy could also be stored (beside batteries) as heat using an electrical water heating (EWH) system or a heat pump (HP) combined to a water storage. In this work we only considered domestic water heating and not household heating. As hot water heating is usually done at night (when electricity price is low), heat storage can also be seen as demand-side management because we shift the load. In subsection 7.2.9, we compare those two storage type in their ability to do peak shaving.

In section 7.3, the effect of module orientations (b) on peak shaving is studied at household level in a feed-in limit context and more generally at Swiss level.

In section 7.4, we present a statistical method for recognition/disaggregation of the different electrical appliances of a household based on measured load curve (with a 15-minute time resolution), time use data and some basic information about the households. Once the time of use of different electrical appliances are known we can estimate the part of the load that can be shifted to PV peak production and hence estimate the potential of demand-side management (c) for shifting loads to PV production period. This method is applied to a sample of about 100 households and the results are discussed.

Finally in section 7.5 we use the result of the precedent chapter to calculate the influence of solar cell temperature and irradiance dependence on self-consumption, *PV-loss* and seasonal PV production ratio. Those results are then compared to the effect of inverter sizing and power rating.

7.2 Photovoltaic and storage for households

Household local electricity storage could contribute to grid stability in case of high photovoltaic (PV) penetration, by absorbing the power peaks around midday. Self-consumption (SC) can also be enhanced, which means that the energy is used where it is produced (allows also to minimize electricity transport losses). In Germany incentive exists to install battery storage if the feed-in power is limited to 60 % of the PV system nominal power [KfW 15]. Till 2015 more than 12'000 such systems were installed in Germany [35 P]. In this section we³ first describe the system considered and the corresponding simulation program developed for this thesis and comment the different control algorithms. We then applies those control algorithms to different cases and discuss the results.

7.2.1 System configurations and description of the simulation

We considered several system configurations comprising a PV system, an electrochemical storage (electrical storage in a battery) and/or a hot water storage (thermal storage in the form of heat). We developed an energy flux simulation with a time step of one minute or 15 minutes and a control algorithm which regulates the energy flux to/out of the battery or the heating state of the boiler each minute.

Electrical storage and electrical converter efficiencies

For the electrical storage simulation we mainly use a DC-link configuration where the battery is connected before the DC/AC converter. The AC-link where the battery is connected through a bidirectional AC/DC inverter can also be simulated (Fig. 7.3). The results between the two configurations are very similar, hence we will only show the studies using the DC-link configuration. The efficiencies of the DC-DC converter and the DC-AC inverter are calculated according to typical curves of commercially available systems [Nott 10] (see appendix C). If not stated differently the converter and inverter nominal power are equal to the DC nominal power of the PV installation. Only input power dependence of the converter efficiency is taken into account (temperature and voltage dependence are neglected). We use a very simple battery model with a fixed round-trip efficiency of 90 % which is in the range of standard Li-Ion battery. The choice of a Li-Ion battery is motivated by potentially less cost in the long term due to higher cycle number and hence lifetime [Thia 09]. In this work, the storage capacity is defined as the effective battery capacity. For example a battery of 10 kWh storage capacity and a minimal possible state of charge (depth of discharge) of 80 % has an effective capacity of 8 kWh.

³Y. Riesen, S. Monnier, C. Ballif and N. Wyrsh

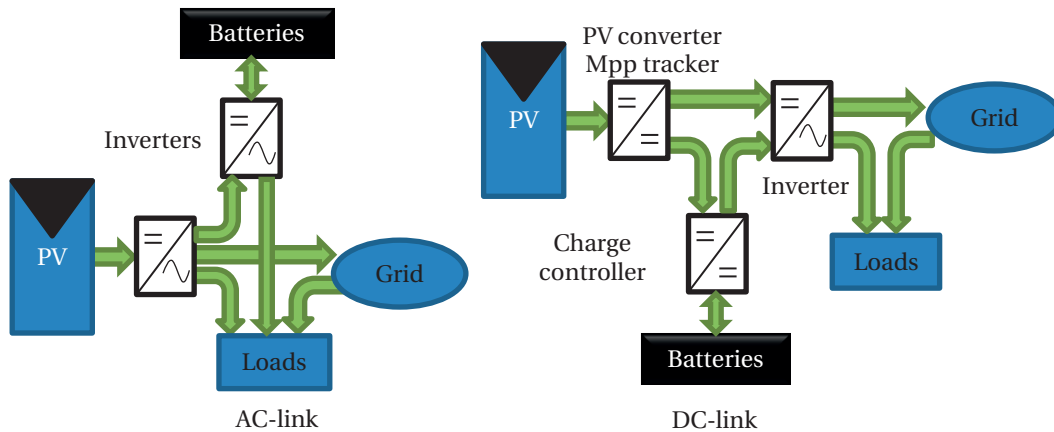


Figure 7.3 – Schematic of two different configurations of a PV system with battery: (left) AC-link and (right) DC-link.

Thermal storage

For heat storage system we considered electrical water heating using boiler (EWH) or heat pumps (HP) electrically connected to the AC side (Fig. 7.3). The energy is stored in the form of

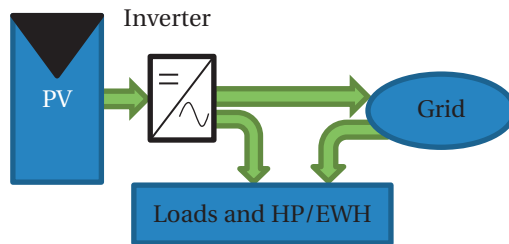


Figure 7.4 – Schematic of PV system with heat storage (heat pump and electrical water heating).

heat in a water tank. The water tank is modeled according to this simple equation 7.7 which does not take into account temperature stratification [Ceri 13, Paul 10]:

$$m \cdot c \frac{dT_w}{dt} = \dot{Q}_{el} - h(T_w - T_{inf}) + \dot{m}_{dem}(h_{in} - h_{out}), \quad (7.7)$$

where $m \cdot c$ is the mass times heat storage capacity of the water, T_w is the water temperature, \dot{Q}_{el} is the electrical input power, \dot{m}_{dem} is the enthalpy transfer due to hot water consumption, $h = A / (\frac{1}{h_1} + \sum \frac{l_i}{k_i} + \frac{1}{h_2})$ is the heat transfer characteristic with a value of $h = 1.2$ taken from [Paul 10]. The electrical input power is given for EWH by $\dot{Q}_{el} = x(t) \cdot P_{el}$ where $x(t)$ is on/off state (0 or 1) and P_{el} is the electrical power of the heater. For HP it is given by $\dot{Q}_{el} = x(t) \cdot P_{el} \cdot COP$, where the coefficient of performance COP is given by a linear approximation $COP = d_0 + d_1 \cdot T_w + d_2 \cdot T_i$ [Verh 10], where $d_0 = 5.6$, $d_1 = -0.066$, $d_2 = 0.057$ are the different coefficients and T_i the inlet

temperature. For HP we modeled two different cases: classical on/off HP where, $x(t)$ is 0 or 1 and the continuous HP (variable power or inverter HP) where $x(t)$ lies between a defined minimum and 1.

Data sources

The main load profiles used are:

Reference load is based on data measured at one minute interval of a Swiss household of five people (family house with central oil heating, including domestic hot water), from April 2012 to March 2013 located near to Neuchâtel. The annual load consumption was 4943 kWh.

Flexi loads is based on data measured with smart meters at 15 minutes interval in a village in canton de Neuchâtel. Most measurement are loads of family households and apartments.

The PV production curve was generated with the PV-lib toolbox [Stein 15], using real global horizontal irradiance and temperature data recorded at a 10-minute-interval by a MeteoSwiss station. For the calculation, we assumed a 270-W-multi-crystalline silicon modules taken from the PV-lib toolbox library and if not stated differently, a module tilt angle of 30° and a south orientation. The resulting module power was then interpolated to the simulation time step.

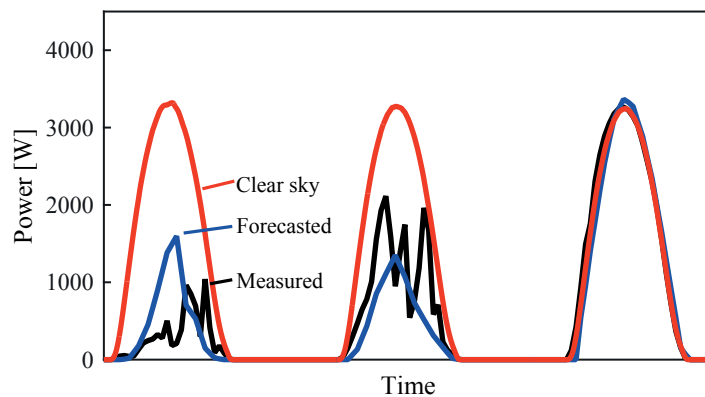


Figure 7.5 – Forecast, measured and clear sky PV production for 3 days

The real PV forecast is based on historical forecast data from Meteotest (48h ahead in 1 hour time steps). The forecasts were interpolated to 30 minutes time step data (see Fig. 7.5). The load forecast was generated by averaging for each 30 minutes the historical load profiles of each day of the week for each season. During days when the household was unoccupied a special holiday average load curve was generated. To compare the effect of forecast errors, we

introduce an exact forecast having the same format as the real forecast, but using the effective production and loads and hence no forecast errors (exact forecast).

7.2.2 Control algorithms

Three different optimization objectives were used:

- Maximize self-consumption (*max. sc.*).
- Minimize PV-losses due to feed-in limit (*min. PV-loss*).
- Optimize financial balance (*cost minimization*) due to electricity exchange with the grid (buying or selling electricity, cashflow). In the presence of a feed-in limit this is equivalent to first minimize the losses due to feed-in power curtailment and then enhance self-consumption. For this objective we developed three different versions/strategies:
 - Cost minimization (*co. opt.*) based on PV production and load forecast.
 - Cost minimization without forecast (*opt. both.*), requiring only clear sky PV production data; this version makes sense only if a feed-in limit exists.
 - Cost minimization with variable feed-in limit, based on PV production and load forecast.

Those strategy are only useful if the battery cannot absorb the complete daily PV production.

For HP/EWH a scheduled operation control algorithm is used for comparison (HP/EWH are switched on every day from 11h00 until the maximum temperature is reached in the water storage). The different control algorithms relevant for these optimization objectives are detailed below.

Maximize self-consumption

The battery is charged (if state-of-charge allows) as soon as PV-power exceeds load (or consumption) and is discharged as soon as PV-power is lower than consumption. This strategy is best for maximizing self-consumption (*max. sc.*).

Minimize PV-losses

Excess PV-power that would be curtailed by the feed-in limit is stored (if state-of-charge allows) in the battery. The battery is discharged as soon as PV-power is lower than consumption. This strategy is best for minimizing PV-losses (*min. PV-loss*) and is only applicable in the context of a feed-in limit.

Cost minimization with forecast

This control algorithm optimizes the gain or cost (*co. opt.*) due to exchange with the grid (selling or buying electricity) and depends on feed-in tariff and electricity costs. This algorithm is valid with and without feed-in limit and need some form of forecasts. A schematic representation can be found in Fig. 7.6.

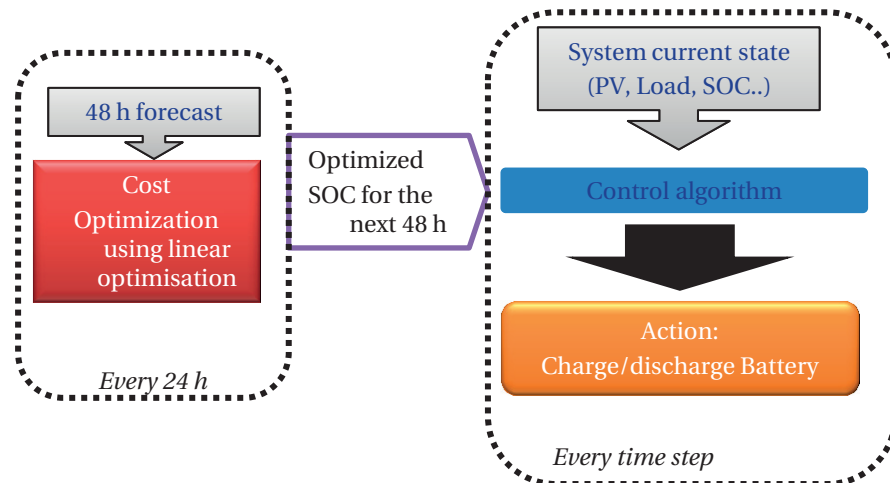


Figure 7.6 – Schematic representation of the cost minimization algorithm with forecast (*co. opt.*) algorithm.

The developed algorithm is the following: Each 24 h, a cost optimization of the energy flux is done with forecast data for the next 48h of PV-production, household load and buying/selling prices (generally with 30 minutes forecast time step). Then, for each simulation time step (generally 1 or 15 minutes time step), the control algorithm defines the battery flux or the HP/EWH state in order to try to reach the optimized state of charge (SOC) for batteries or temperature for hot water storage calculated during the previous cost optimization step based on the forecasts. The control algorithm is constrained to the following rules:

- The resulting energy fluxes have to respect the different given limits of the system (inverter power limit, power flux limits of the battery, battery size, temperature limit of the water tank. . .).
- If there is a feed-in limit the PV power exceeding the limit is stored as long as the previously cited constraints are met. If it is not possible this excess PV power is lost (considered as *PV-loss*); In practice, this means that the maximum power tracker of the PV system is no more operated at maximum point.

For electrical storage, a linear programming algorithm optimizing the electricity financial bal-

Chapter 7. Photovoltaic generation and the local electricity grid

ance for the user is applied. The inverter and converter efficiencies are considered as constant (do not dependent on the input power) to allow a linear optimization. This is considered as an acceptable approximation as the power flux intensities that give most contribution are on the flat part (high input power) of the efficiency curve of the inverter.

For heat storage we wrote our own optimization algorithm because, with HP, the problem cannot be linearized anymore. Furthermore, for this on/off problem, the mixed integer problem optimization function built-in in Matlab gave poor results. Our optimization algorithm works as follow: at each time step of the forecast, beginning from $t = 0$, it checks, if the tank temperature is under the minimum. If this is the case, the algorithm tests for each time between $t = 0$ and actual time step what would be the cost per gained degree if HP is turned on at his time. Then the HP is effectively turned on at the time where the cost per gained degree has its minimum. This procedure is done again until the temperature for this time step crosses the lower temperature limit. Finally we get HP states that are very close to the optimized states for a cost balance optimization.

Cost minimization without forecast

This newly developed simple algorithm optimizes the financial balance due to grid exchange in the presence of feed-in limits and constant electricity/feed-in prices without the need for forecast (*opt. both.*). In this context optimizing costs is equivalent to first minimize the losses due to feed-in power curtailment and then enhance self-consumption. This algorithm needs only the theoretical maximum PV-production curve to minimize PV-losses and maximize self-consumption. For this purpose, the maximum clear-sky PV-production is calculated for each minute using the PV-lib toolbox [Ste1 15]. The battery is controlled as follow:

- Excess PV-power that would be curtailed by the feed-in limit is stored (if state-of-charge allows) in the battery. Moreover, if the battery capacity is sufficient to absorb the maximum excess PV production (calculated with the clear sky PV-production) of the next 10 hours, the battery is charged further until this limit.
- If PV power is higher than the load power the battery is only charged if its capacity is sufficient to absorb the maximum excess PV of the next 10 hours.
- If PV-power is lower than the load power the battery is discharged.
- The system boundaries must be satisfied (battery capacity, inverter power limits)

Cost minimization with variable feed-in

The cost minimization with variable feed-in algorithm is similar to the cost minimization without forecast algorithm. For each day, the feed-in limit is fixed as the maximum limit for which all excess PV production can be stored for the given battery size. Hence forecasts are needed. Weniger *et al.* developed a similar approach [Weni 14].

7.2.3 Comparison of different electricity pricing scheme for peak-shaving

In this section we compare the peak shaving capability of different electricity pricing using the *co. opt.* control algorithm and the *max. sc.* algorithm with no feed-in limit (discussed in more details later Sec. 7.2.4)

Simulation details

As data source the *reference load* (1 single household) and the PV production described in section 7.2.1 are used. The PV system is sized to 5 kWp (approximately covering the yearly household consumption with a yearly PV production of 1000 kWh/kWp) nominal power and the battery capacity is 10 kWh. An exact forecast is used. The following four different cases are analyzed:

Case 1 The *max. sc.* algorithm is used and is independent of pricing.

Case 2 The *co. opt.* algorithm is used with a day/night tariff scheme.

Case 3 The *co. opt.* algorithm is used with an electricity and feed-in price proportional to the load minus PV-production. The feed-in price is always 10 cts/kWh lower than the electricity price in absolute values. At high PV injection the feed-in and electricity prices are low.

Case 4 The *co. opt.* algorithm is used, the electricity price is constant in time. However, a tax proportional to the daily highest feed-in power is introduced. Under those constant price conditions the amount of this tax do not play a role.

Results and discussion

Figure 7.7, shows the result of the simulations for two days. Case 1 that uses *max. sc.* algorithm charges the battery until it is full. But then all excess power is fed into the grid. Hence, there is still a peak in the afternoon. Case 2, does not completely shave peaks. Case 3, with pricing depending on feed-in without battery, charges the battery only when the prices is lowest. Hence peaks are appearing at the beginning and end of the day. Case 4, where the user has to pay a tax which is proportional to the highest daily power peak, successfully achieves peak shaving. Those results are similar to [Umla 12]. This clearly highlights the advantage of using a daily power tax system for an efficient peak shaving strategy.

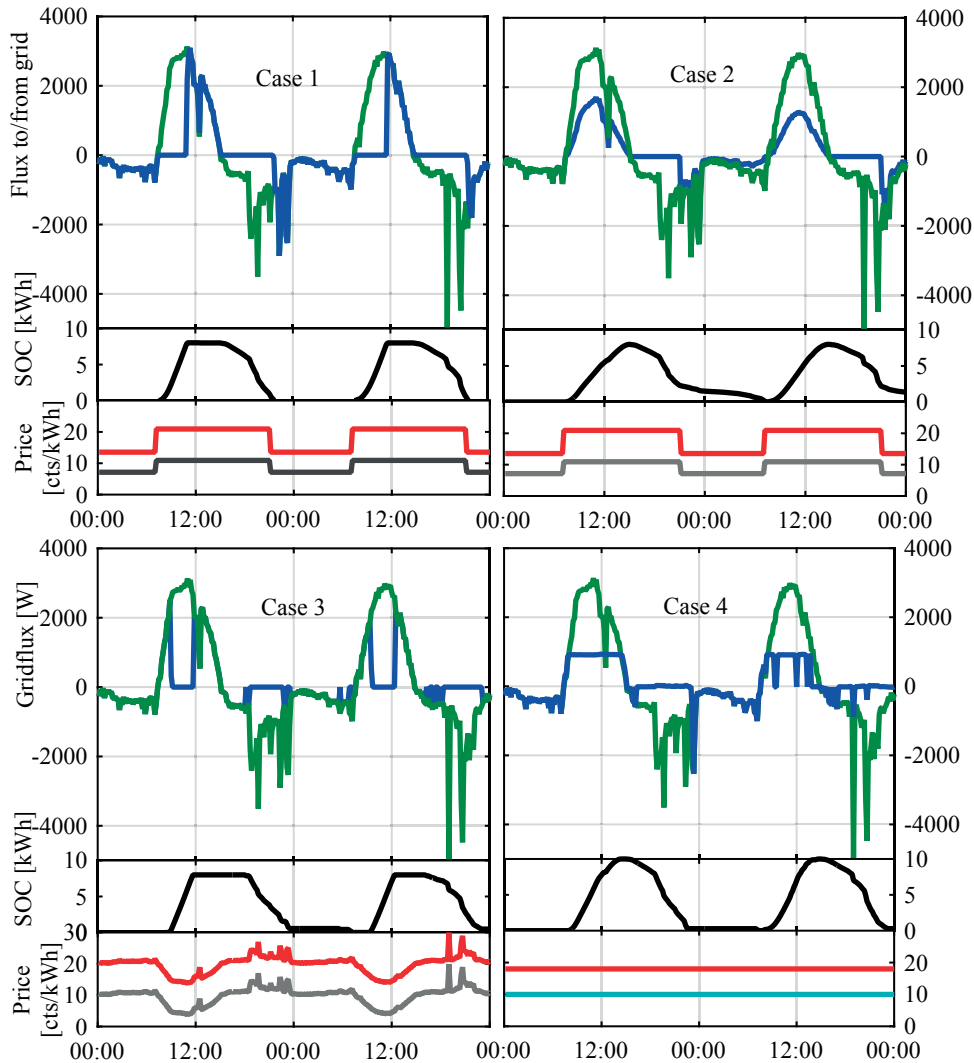


Figure 7.7 – Green: Electricity flux (*gridflux*) with the grid without storage, blue: *gridflux* with storage, black: battery state of charge (SOC), red: electricity price, gray: feed-in tariff, for the different pricing cases and control algorithms.

7.2.4 Comparison of the different control algorithms with feed-in limit

Imposing a feed-in limit is a simple and efficient method to avoid high injection peaks. The first purpose of this section is to compare the performance in peak shaving and enhancing self-consumption (or cost optimization) of two different algorithms (already introduced in Sec. 7.2.2) controlling the charge and discharge behavior of the batteries in the presence of a feed-in limit and constant electricity and feed-in prices. The first algorithm is based on forecast and performs a linear optimization to maximize the financial gain *co. opt.*. The second algorithm needs only the theoretical maximum PV-production curve to minimize PV-losses and maximize self-consumption *opt. both.*. This algorithm is therefore independent of forecast accuracy. For comparison purposes, the results of the basic control algorithm

maximizing only self-consumption (*max. sc.*) and another minimizing only PV-losses (*min. PV-loss*) are also showed. Moreover, for the first algorithm we compare the results using real forecast and an optimal exact forecast in order to isolate the errors due to forecast inaccuracies. Those results are partially based on [Ries 13].

Simulation details

The *reference load* with a 1 minute time step is used. The PV system size is adapted such that the total yearly PV production is equivalent to the total electricity consumption (Sec. 7.2.1) and hence sized to 4.2 kWp. Notably, the system is not allowed to charge or discharge the battery directly into or from the grid.

Results and discussion

The histogram in figure 7.8 a) shows the distribution of the daily excess energy due to the feed-in limit of 60 %.

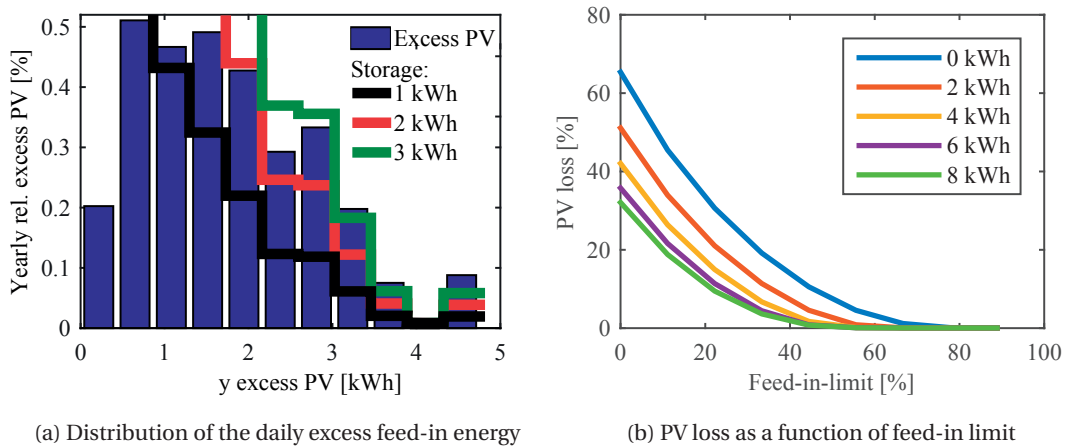


Figure 7.8 – a) Distribution of the daily excess feed-in energy as a function of excess in percentage of the total PV production from April 2012 to March 2013 for 60 % feed-in limit. The areas above the different lines represent the PV-loss corresponding to the respective storage size. b) PV-loss as a function of feed-in limit for different storage capacities.

By summing up the area above the different lines corresponding to the different storage capacities we get the PV-loss energy for the studied period as a function of these storage capacities. We see that only few days have an excess PV energy above 3 kWh. Therefore for this case study, storage sizes above 3 kWh do not bring much for reducing PV-loss. Figure 7.8 b) shows the PV loss as a function of the feed-in limit for different storage capacities. Without storage and a feed-in limit of 0 % which means that all production has to be self-consumed, we get a PV-loss of 70 %. With a storage of 4 kWh we can reduce this value to 42 %. Increasing

Chapter 7. Photovoltaic generation and the local electricity grid

the feed-in limit reduces rapidly the *PV-loss* for each storage size. At a feed-in limit of 80 % there is almost no more losses even without storage. Note that the feed-in limit effect depends strongly on the orientation of the modules as the feed-in limit is expressed in ratio of the nominal power.

Figure 7.9 shows the *PV-loss* and the self-consumption (SC) for a feed-in-limit of 40 % as a function of the battery capacity.

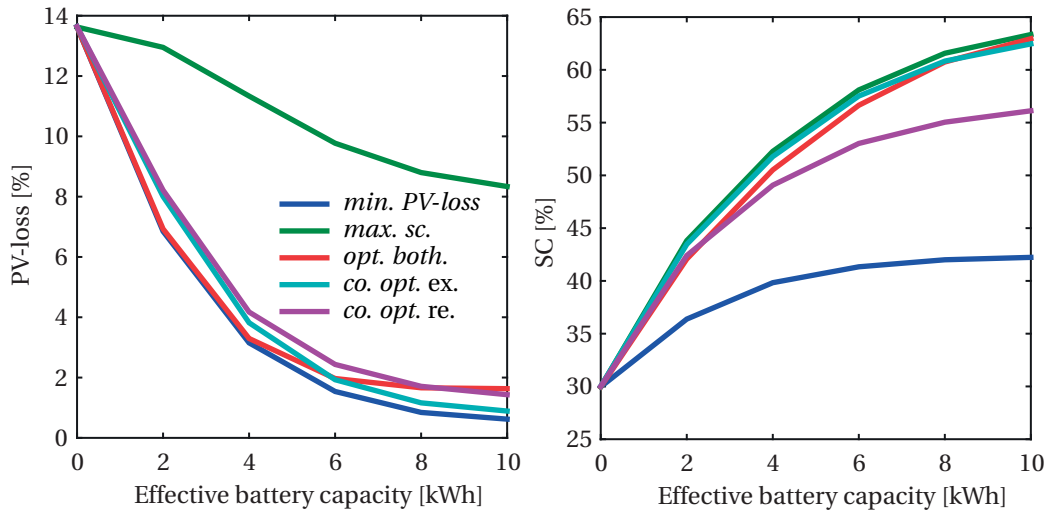


Figure 7.9 – *PV-loss* and self-consumption (SC) for a single household using the different battery control algorithm as a function of battery effective capacity with a feed-in limit of 40 %.

As expected the *PV-loss* is smallest for the *min. PV-loss* algorithm. Until a battery capacity of 5 kWh, the optimize both algorithm without forecast (*opt. both.*) performs almost as well as the best (*min. PV-loss*) case. At higher than 5 kWh storage capacities, the battery is no more always empty in the morning. However the algorithm assumes that it is the case and hence underestimates the storage needed for peak shaving and as a consequence the *PV-loss* do not diminish further. As the discharging power of the battery is limited by the DC/AC inverter, increasing its nominal power could, in a limited extend, empty the battery faster during peak consumption and slightly diminish the *PV-loss* for high storage capacities. Theoretically, the cost minimization with exact forecast case (*co. opt. ex.*) should give equal *PV-loss* values as the *min. PV-loss* case. This is almost the case: the differences are due to the different time steps of the optimization algorithm (30 minutes) and the simulation time step (1 minute) and the constant inverter efficiency approximation which result in slightly higher *PV-loss* for the *co. opt. ex.* case. With real forecast (*co. opt. re.*) the *PV-loss* are higher; for example with a 3 kWh battery, they are more than two times higher than for *min. PV-loss*. Those higher losses arise at days when the forecast amount of excess PV is underestimated and therefore the storage is already full when it is needed.

SC increases from 30 % without battery to over 60 % for storage capacities above 7 kWh. The

co. opt. ex. mode is almost as well as the best case (*max. sc.*), even without exact forecasts. However, the *co. opt.* mode with real forecasts has a lower SC than the two others. The difference can reach 8 % in absolute.

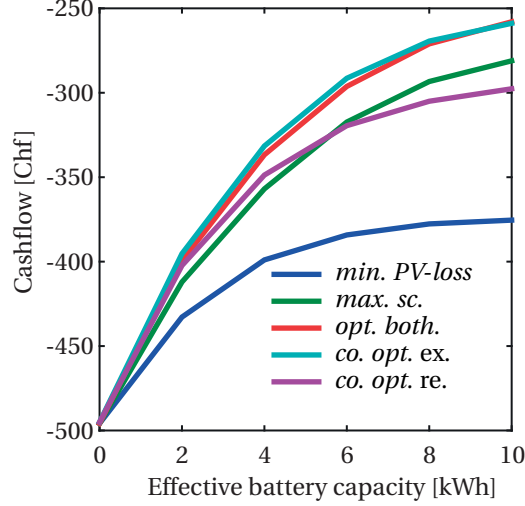


Figure 7.10 – Cashflow due to the electricity flux with the grid for the five different control algorithms. With an electricity price of 20 cts/kWh, a feed-in tariff of 8 cts/kWh and a feed-in limit of 40 %.

As we set the condition that the battery cannot charge or discharge directly from the grid, we can link the *PV-loss* and the *SC* to the financial balance due to grid exchange (*cashflow*). Given the *SC* (Equ. 7.8) and the *PVloss* (Equ. 7.9) we can calculate the cashflow C for any feed-in tariff F^+ and electricity price F^- :

$$SC = \frac{\sum_t L_t + \sum_t (PV_t - L_t + B^+) |_{(PV_t - L_t) < 0}}{\sum_t PV_t} \quad (7.8)$$

$$PV_{loss} = \frac{\sum_t (PV_t - L_t + B^-) |_{(PV_t - L_t + B^-) > F_{limit}}}{\sum_t PV_t} \quad (7.9)$$

$$C = \sum_t (PV_t - L_t + B^-) |_{(PV_t - L_t) > 0} \cdot F^+ + \sum_t (PV_t - L_t + B^+) |_{(PV_t - L_t) < 0} \cdot F^- \quad (7.10)$$

$$= SC \cdot PV_{tot} (F^- - F^+) + PV_{tot} (1 - PV_{loss}) \cdot F^+ - B_{loss} F^+ - L_{tot} \cdot F^- \quad (7.11)$$

where L_t is the load at time t , PV_t is the PV production at time t , B^+ is the battery discharging energy at time t (positive value), B^- is the battery discharging energy at time t (negative value), $B_{loss} = \sum B^+ + \sum B^-$, $L_{tot} = \sum L_t$ and $PV_{tot} = \sum PV_t$, SC the *SC* and PV_{loss} the *PV loss*. In order to visualize of adding new battery capacity we can write Equ. 7.11 in differences:

$$\Delta C = PV_{tot} (\Delta SC \cdot (F^- - F^+) - \Delta PV_{loss} \cdot F^+) - \Delta B_{loss} F^+ \quad (7.12)$$

Chapter 7. Photovoltaic generation and the local electricity grid

In our case, with ($F^+ < F^-$) and Fig. 7.9 we see in Equ. 7.12 that the SC value mainly influences the cashflow. If we set the electricity price to $F^- = 20$ cts/kWh and the feed-in tariff to $F^+ = 8$ cts/kWh. We get the result showed in Fig. 7.10.

The *co. opt. ex.* algorithm performs best but is closely followed by the *opt. both.* algorithm needing no forecast. However, as for SC , the algorithm with real forecast (*co. opt. re.*) as it would be the case in real condition, is financially less favorable than the *opt. both.* algorithm. Therefore the *opt. both.* control algorithm is the best choice and will be used for the next simulations presented in this chapter. Those results are independent on pricing as far as the electricity price is higher than feed-in price and the prices are constant in time.

7.2.5 Loss analysis

In order to compare the different losses, the 1-minute-*reference load* is used. The simulation is run with a feed-in limit of 50 %, a yearly PV production and load of 4924 kWh, a PV size of 4.2 kWp and the *opt. both.* algorithm is used. The battery size is 1 kWh/kWp (corresponding to 4.2 kWh).

Figure 7.11, shows the monthly relative to total PV production losses due to feed-in limitation (*PV-loss*), due to the DC/AC and the DC/DC conversion and the battery losses. The monthly PV production is represented as a blue line. The highest losses are due to the DC/AC conversion

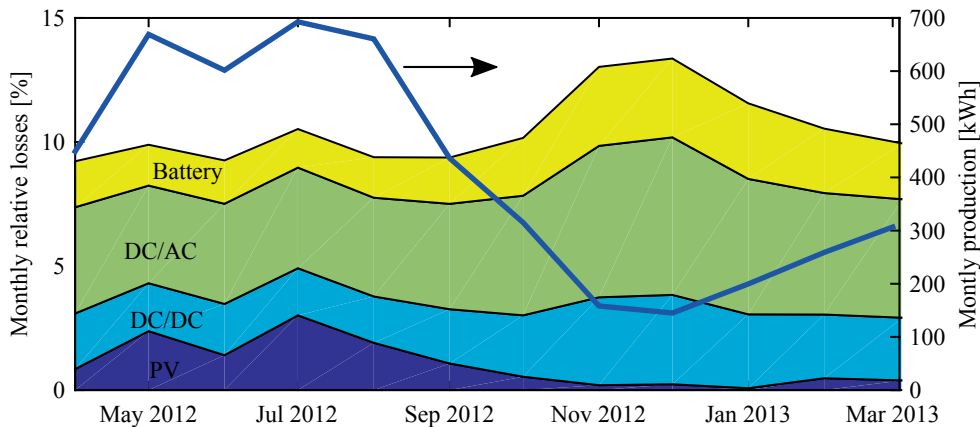


Figure 7.11 – Monthly losses relative to the total PV production of the the feed-in limit (*PV-loss*), the DC/DC converter, the DC/AC converter and the battery. Based on 1-minute data with a feed-in limit of 50 % and a battery size of 1 kWh/kWp. The blue line represents the total monthly PV production.

despite the fact its efficiency can reach 95 % (see appendix C). In our simulated case, 4.4 % of the total PV production for one year is lost in the converter. A high fraction of energy is produced when the power is below 20 % of the nominal power where the inverter efficiency drops and those losses are higher during the low irradiation period (winter). A smarter control

algorithm that discharge the battery only when higher power is needed could reduce those losses. Reducing the nominal power of the inverter could also help. However, if this power is too low, two additional losses occur: – if the battery is full and the production is higher, the excess is lost. – As the discharge of the battery is limited, during sunny periods, the battery cannot be discharged completely before a new PV production peak occurs. An optimal sizing of this inverter can be found and depends mainly on the irradiation distribution, the battery size, the feed-in limit and the load power distribution.

For the investigated year, 2.2 % of the PV production is lost in the DC/DC converter. The battery losses account for 2.0 % of the total PV production. In absolute values less energy is lost in the battery in winter due to less charging/discharging cycles, however relative to (the lower) production, the loss is higher. As the present battery model is very simple, those battery losses values should only be taken as an approximation.

The *PV-loss* reaches 1.5 % for a battery size of 4.2 kWh and a feed-in limit of 50 %. Most of the loss arises in the sunniest months. For the chosen battery size those losses are relatively low compared to the battery and inverter/converter losses.

7.2.6 Load shape sensitivity analysis

In this section we will again use the *opt. both.* control algorithm which is the best choice between the presented control algorithm in the presence of a feed-in limit as established in section 7.2.4. In the previous chapter the algorithms were applied to only one household using the *reference load* (7.2.1). In this section we apply the *opt. both.* control algorithm to 44 different loads (*flexi loads*) to do a sensitivity study on the different load shapes (most of them from households). The feed-in limit is fixed to 50 % and the PV installation nominal power is fixed such that the yearly PV produced energy is equal to the total yearly consumption.

Figure 7.12 shows the mean, median, maximum and minimum values of the *PV loss* and *SC* as a function of the relative to nominal PV power battery size. For the *PV loss* and the *SC* values, the maximum and minimum difference is about 5 % and 12 %. Otherwise same behaviors as for the reference load is seen.

7.2.7 Household local storage compared to district storage

Aggregating loads also allows reducing power peaks. In this section we quantify the gain of applying the control algorithm to aggregated loads compared to the case where all households have their own individual batteries and apply the optimization only for themselves (distributed optimization). Aggregated loads means that the feed-in limit is applied to the sum of all loads and that either all batteries are centrally controlled or that there is one central battery. The *opt. both.* control algorithm is applied and the feed-in limit is set to 50 %. The generated yearly PV energy equals in each case the total yearly consumption.

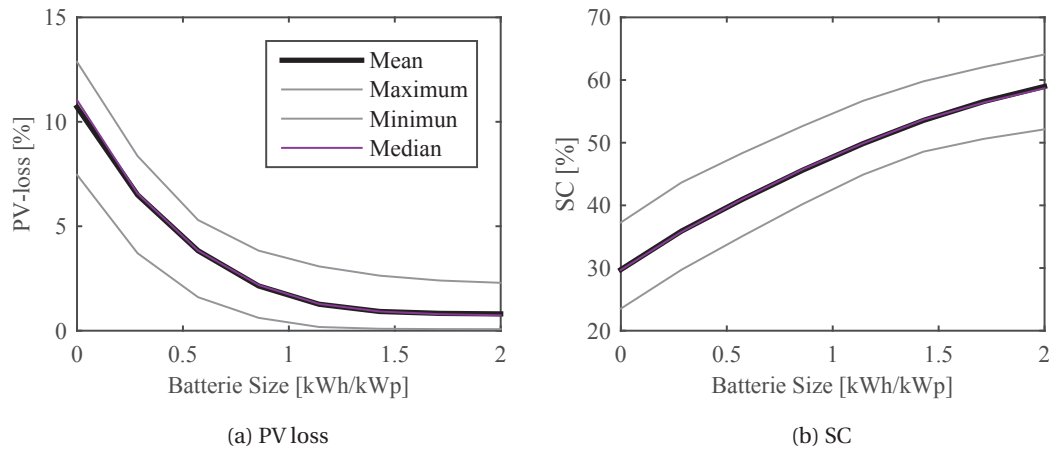


Figure 7.12 – Maximum, minimum, mean and median of the *PV loss* and the *SC* as a function of the battery size divided by the nominal PV power for 44 different loads. The feed-in limit is 50 %.

In Fig. 7.13 a) the *PV loss* is plotted as a function of the number of aggregated loads (same 44 loads used in Sec. 7.2.6). For both relative battery sizes, the *PV loss* decays rapidly by more than 0.4 % absolute till 4 households and then continue decaying slightly with fluctuations. The *SC* as a function of loads remains more or less stable and varies according to the mean of the individual *SC*.

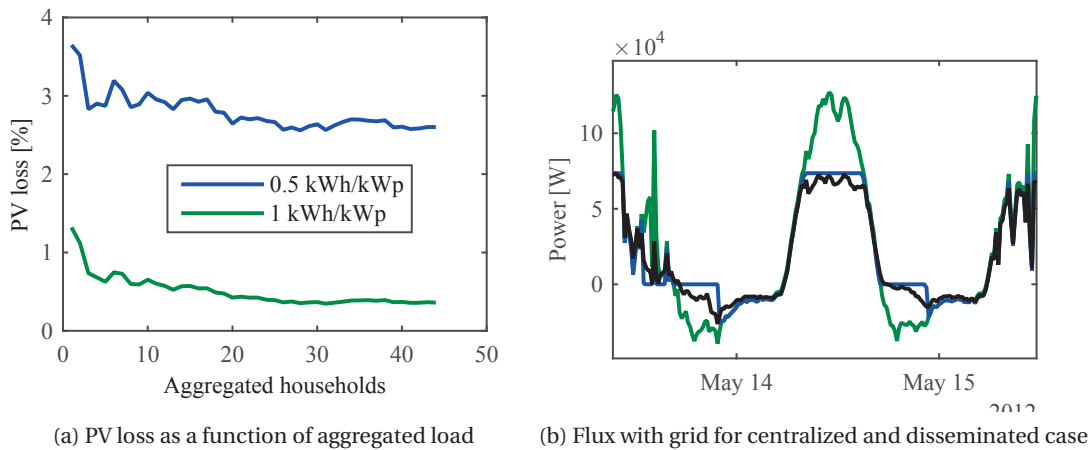


Figure 7.13 – a) *PV loss* as a function of the number of aggregated loads for two different storage capacities. b) Electricity flux with grid for one day for the initial case (blue), disseminated (black) and central (blue) storage.

For comparison, the *opt. both.* control algorithm is applied individually to the 44 different loads and PV sizes and to the case of a PV-field that has the same total energy production than the cumulative PV production of all loads and a centralized storage. The total PV production is

7.2. Photovoltaic and storage for households

equal to the total yearly consumption (190 000 kWh). For this example we use a storage size of 1 kWh/KWp and a feed-in limit of 50 %. Figure 7.13 b) shows the flux with the grid for a clear sky day. The total *PV-loss*, *SC* and *cash-flow* are presented in Tab. 7.1. The *SC* is also slightly

	Disseminated	centralized
<i>PV-loss</i>	1.6 %	0.4 %
<i>SC</i>	49.8 %	51.3 %
<i>Cash-flow</i>	-11 525 CHF	-10 750 CHF

Table 7.1 – *PV-loss*, *SC* and cash-flow for comparison between disseminated and centralized storage.

(1.5 %) higher for the aggregated case. The gain with aggregation for the *PV-loss* is larger, the higher is the load compared to the nominal PV power. Because, on a local level, only the load is smoothed by aggregation and not the PV production as we assume the same irradiation for all modules.

In the presence of a feed-in limit, *e.g.* 50 %, aggregation allows reducing the *PV-loss* and in some case to enhance the *SC*. Moreover, in addition to the more favorable cashflow, maintenance and investment cost should be lower for a centralized storage compared to a distributed one.

7.2.8 Variable feed-in limit

In this section we present the results of the cost minimization with variable feed-in limit control algorithm (see sec. 7.2.2, p.118). This algorithm gives nearly same results as the *co. opt.* algorithm with a power tax proportional to the daily highest feed-in power (Sec. 7.2.3). This algorithm maximizes *SC* and limits the feed-in power as much as the battery allows it.

Simulation details

The algorithm is applied separately to each of the 44 *flexi loads*. The PV systems are sized such that to cover their annual total consumption. For each household, the battery is sized to 1 kWh/kWp. For the following simulation we used exact forecasts to study the optimal case.

Results

The histogram in Fig. 7.14 shows the number of days corresponding to the global feed-in limit (the calculated feed-in limits of each household in power units are summed and divided by the aggregated PV-nominal power). During almost 150 days the batteries could store all produced energy and hence the daily feed-in limit is fixed to 0. Not more than 60 % of the nominal PV power is fed into the grid with this battery size. Now we discuss the local feed-in limit. The mean *SC* of the 44 households has a value of 49.7 % (maximum: 57.0 %, minimum: 44.2 %). The *PV-loss* are under 1 % for each household. Ideally, it should be zero. However due to the

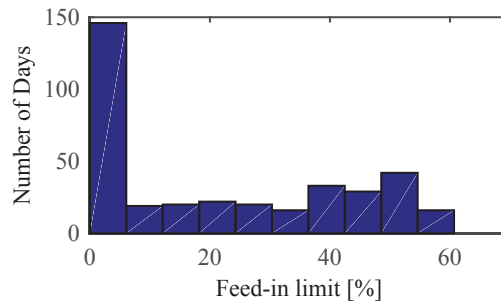


Figure 7.14 – Occurrence in days of a given daily feed-in limit using the variable feed-in limit algorithm with a relative battery size of 1 kWh/kWp.

fact that some days the battery cannot be completely discharged the value is different from zero.

7.2.9 Electricity and heat storage comparison

For a Swiss household, 70 % of its energy consumption is used for room heating and 12.5 % for water heating [Kemmler 14]. Through heat pumps (water and room heating) or electrical water heating, PV can also contribute to reduce CO₂ emission in this sector. Moreover, in Switzerland, where 25 % of the energy used for water heating of private household is obtained by electrical water heating systems [BFE 12], heat energy storage method for electricity peak shaving would require only limited investment and adaptation.

Simulation and data sources

For this subsection, the *reference load* curve was used and the hot water consumption profile was estimated from a survey. The same profile was used for each day and normalized such that the total heating energy equals 6500 kWh per year for the given household⁴. The PV installation was sized such that the annual energy output equals the total yearly consumption. Without taking in account HP/EWH loads, this corresponds to a 4.2 kWp installation. With a HP the total yearly consumption depends on the control algorithm, but is approximately 6600 kWh. A 5.5 kWp PV installation can cover on an annual basis this consumption. For EWH, we have a yearly consumption of about 9600 kWh which corresponds to a PV system of 8 kWp.

For heat storage, we simulated a 300 l water tank with water temperature limits between 55 °C and 80 °C (see section 7.2.1). This tank can store about 8.7 kWh of thermal energy for EWH and about half for HP because the mean COP is around 2. The continuous HP can vary its power from 10 % to 100 % of P_{el} (see Fig. 7.15). In our case the HP is assumed to only heat hot water.

⁴This is slightly higher than the Swiss average [Kemmler 14]

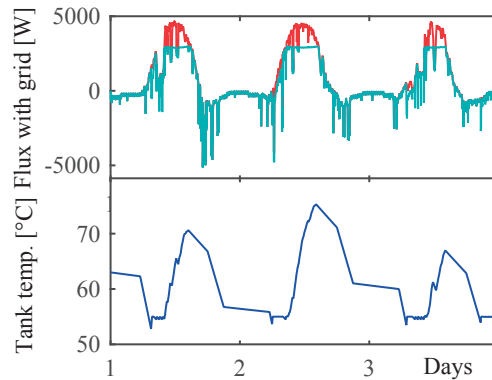


Figure 7.15 – Continuous 3 kW HP and a feed-in limit of 60 % using the *min. PV-loss* algorithm. Top: power flux with grid (with (blue)/without (red) storage and feed-in limit), bottom: water tank temperature.

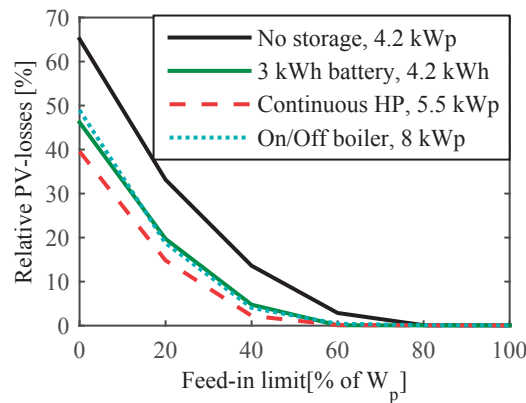


Figure 7.16 – PV-loss as a function of the feed-in limit for electric and heat storage. The *min. PV-loss* algorithm is used

Results and discussions

Figure 7.16 shows the *PV-loss* modeled for HP, EWH and battery as a function of the feed-in limit. Table 7.2 shows same data complemented by the other scenarios for a feed-in limit of 60 %. For this calculation the battery effective capacity was 3 kWh and the HP/EHW power (P_{el}) set to 2 kW. The *PV-loss* minimization control algorithm was used (see section 7.2.2). Compared to the case without storage, all scenarios (even the scheduled one) reduce *PV-loss* by a factor 2 or more. The smallest losses are obtained with heat storage and continuous HP because its storage capacity is bigger than that of the battery. On/Off heating induces higher *PV-losses* because the power is fixed and cannot be adjusted to the excess power. Therefore the sizing of the On/Off HP/EHW (P_{el}) has to be adapted according to the feed-in limit such that its value is in the order of the mean excess PV power in order to minimize *PV-losses*. Considering everything, heat storage for hot water is an efficient and potentially low cost peak

Mode	PV rating [kWp]	PV-loss	
		[%] at 60 %	[%] at 40 %
No storage	4.2	2.9	13.6
3 kWh battery	4.2	0.1	4.8
Continuous HP	5.5	0.1	2.2
On/Off HP	5.5	0.8	5.7
Scheduled HP	5.5	1.2	7.4
Scheduled EWH	8	1.0	6.6
On/Off EWH	8	0.4	4.0

Table 7.2 – Relative PV-loss with a 60 % and 40 % feed-in limit, using PV-loss minimization algorithm and for comparison a scheduled operation (heating from 11h00). HP or EWH $P_{el} = 2$ kW.

shaving solution.

7.3 Module orientation and peak shaving

Changing module orientation can also contribute to lower the midday production peak and also reduce the seasonal production variation. However more PV modules (higher nominal PV power) are needed to keep same yearly produced energy. In this section, we quantify the effect on SC and $PV-loss$ of different orientations for single households in a first step. In a second step, we analyze the effect of different module orientation configurations on the excess PV related to the total Swiss load.

7.3.1 Simulation details

For the simulation at household level, the yearly PV production equals the total yearly consumption. The *opt. both.* control algorithm (see section 7.2.2) is used. The algorithm is applied separately to each of the 44 *flexi loads*. Three different module orientation configurations are simulated:

- All modules are south oriented with a 30° tilt (S30°). In total 147 kWp are needed.
- Modules are east and west oriented with a 30° tilt, each side producing half of the yearly PV energy (EW30°). 175 kWp are needed.
- Modules are east and west oriented and vertically tilted (90°)(EW90°). 196 kWp are needed.

Figure 7.17 shows the three configuration at clear-sky condition for the 21 of June, September and December 2012. For each household, the simulations are run with two different feed-in limit configurations. First, the relative feed-in limit is set to 50 % of the nominal power for

all module configuration. Second, the feed-in limit absolute value is equal for all module configurations and corresponds to 50 % of the nominal power of the south oriented with a 30° tilt configuration. For the east and west oriented configuration with 30° and 90° it corresponds to value of feed-in limits of 42 % and 37.5 % respectively. The second approach allows having a better comparison regarding peak shaving for each configuration.

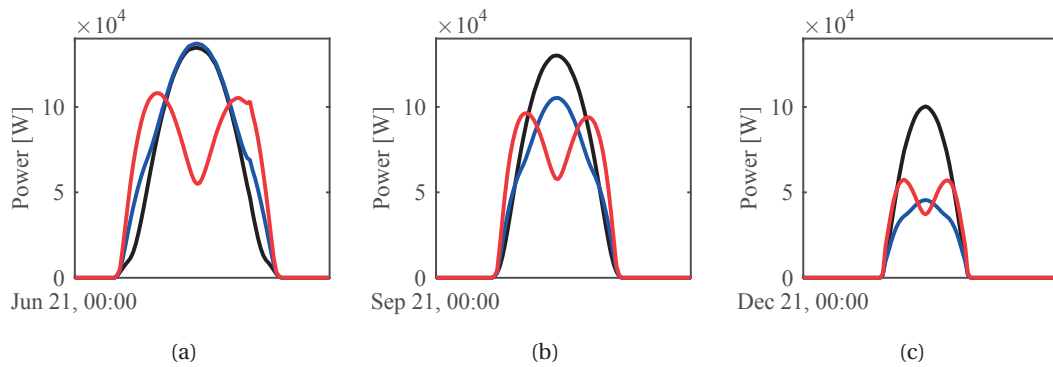


Figure 7.17 – Simulated clear sky PV-production at 21 of June, 21 of September and 21 of December for: (black) south oriented 30° tilt, (blue) east-west oriented 30° tilt and (red) east-west oriented 90° tilt.

For the simulation at Swiss level, the PV production is sized such that it produces 20 % of the total Swiss load of 2014 (without excess PV). We define the orientation ratio as the ratio of the energy produced by the east-west oriented modules and the total PV production (0: all modules are south oriented, 1 all modules are east-west oriented). Note that the yearly PV production of the east is sized such to be equal to the west production. The tilt is always the same for all modules. We varied the orientation ratio from 0 to 1 and the tilt from 0° to 90°. As in section 7.1.1 the excess power is defined as the PV power exceeding the power of the total Swiss load minus the power of the run-of-river plant.

7.3.2 Households level results

The *PV-loss* and *SC* as a function of storage size (compared to the nominal power in the S30° case) for the three module orientation configurations and the absolute equal feed-in limit are shown in Fig. 7.18. Using the same absolute feed-in value for the three module orientations, the *PV-loss* are highest for the S30° orientation, followed by the EW30° and is lowest for the EW90° configuration for all battery sizes. With no storage, comparing to the S30° configuration, there are 3 % absolute less *PV-loss* for the EW30° configuration but we need relative 17 % higher nominal power. The difference between the configurations reduces with increasing battery size. If the relative feed-in limits are set to 50 % for each configuration the *PV-loss* will even be smaller for the east west orientation configurations.

Without battery, the *SC* is only improved by 1 % and 1.1 % for the EW30° and the EW90° compared to the S30°. This small improvement is certainly due to the relative small broadening of

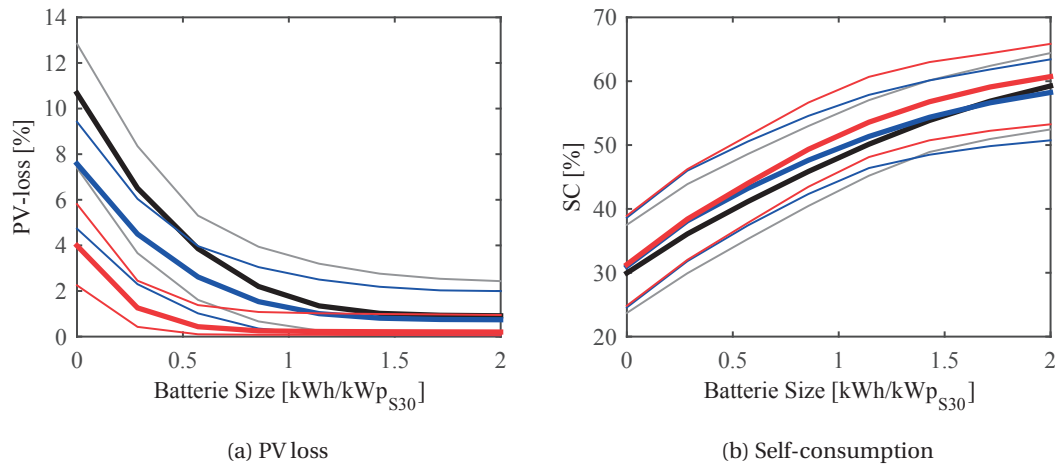


Figure 7.18 – *PV-loss* and *SC* as a function of the relative battery size to the nominal PV power in the $S30^\circ$ case for: (black) south oriented and 30° tilt, (blue) east-west oriented and 30° tilt and (red) east-west oriented and 90° tilt. The thicker lines is the mean of all households and the thinner lines the maximum and minimum values.

the peak as seen in Fig. 7.17. Increasing the battery size increases the *SC* until a maximum of 2 % and 4 % absolute improvement for the $EW30^\circ$ and the $EW90^\circ$ compared to the south oriented module for a battery size of 0.5 kWh/kWp_{S30} and 1 kWh/kWp_{S30}. Increasing the battery size further, implies a smaller *SC* increases. At battery sizes higher than 1.5 kWh/kWp_{S30} the $S30^\circ$ *SC* even exceed the *SC* of $EW30^\circ$. Essentially the seasonal variation between the three orientation configurations explain this *SC* behavior.

7.3.3 Swiss level results

Figure 7.19 shows the relative excess PV power (a), the ratio of the energy produced during the months of November, December and January and during May, June and July 2014 (b), the installed PV power (c) and the normalized compensated PV power (d) are shown as a function of the orientation ratio and the tilt of the PV modules. We define the normalized compensated PV power as the PV power that should be installed to reach the 20 % of the total electricity consumption by taking in account the losses divided by the minimum of the installed PV power⁵. The monthly energy production for three different PV module orientations and the monthly total Swiss load are shown in Fig. 7.20.

The excess power has a minimum value of less than 5 % for a tilt of 90° and an orientation ratio of 0.6. The excess increase until a value of more than 12 % in the case of horizontally tilted modules. The PV energy produced in the three months with lowest irradiation (November-January)

⁵In fact, we used a linear approximation and calculated this factor as following normalized compensated PV power = $\frac{[Installed\ PV \cdot (1 + excess\ PV / (20\% \cdot Tot.\ consumption))]}{\min_{tilt,OR}(Installed\ PV)}$

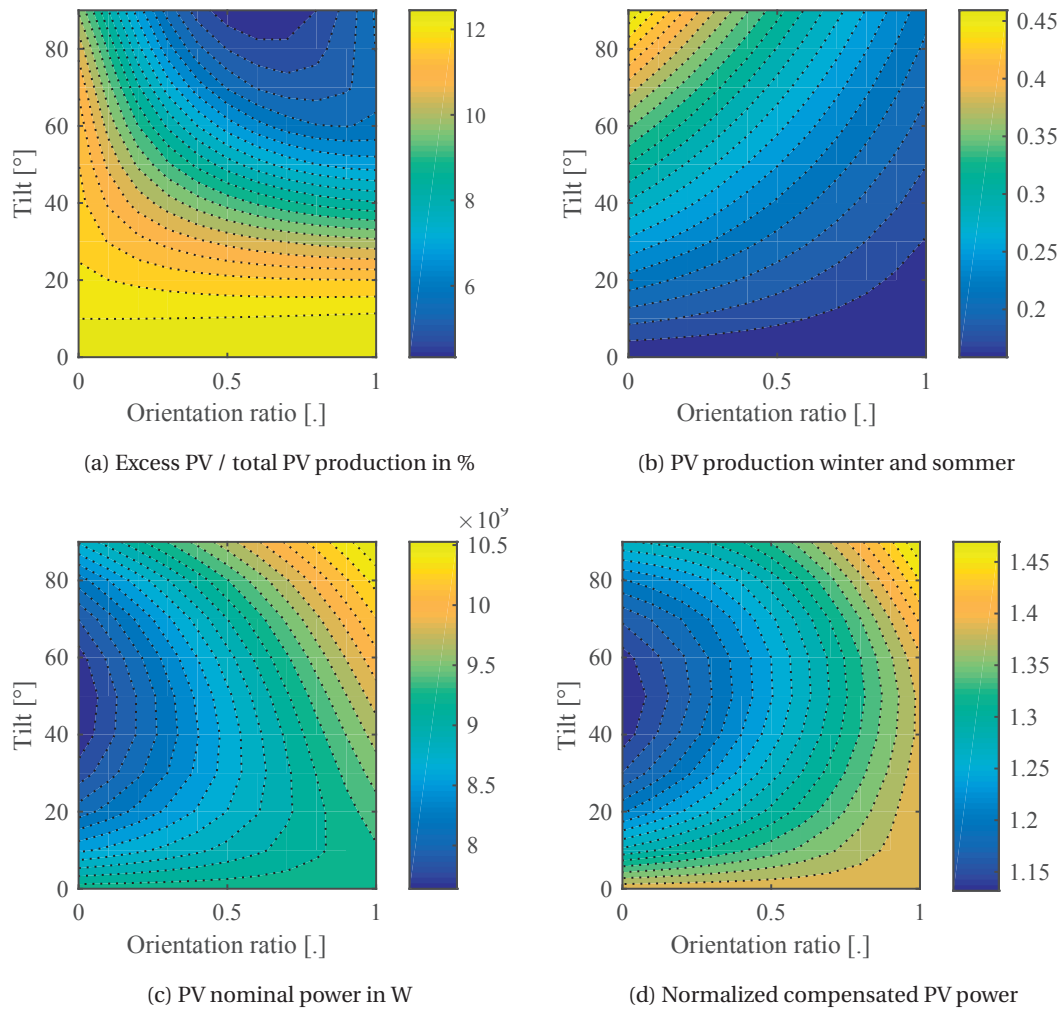


Figure 7.19 – Excess PV, PV production ratio between the months of November, December, January and during May, June and July, PV nominal power and normalized compensated PV power as a function of tilt angle and azimuth share (0 only south oriented and 1 only west/east oriented modules). The PV nominal power is adapted such that 20% of total Swiss load is covered by solar power. Simulation is based on 2014 Swiss load and Neuchâtel irradiation.

reaches only 15% of the PV production during the three months with highest irradiation (May-July) in 2014 for horizontally tilted panels. However this value reaches 45% for south oriented vertically tilted modules. If the modules would be in La Chaux-de-Fonds (14 km north and 500 m higher altitude than Neuchâtel) this value could even reach 68% because of the less foggy weather condition during fall and winter. For the selected module (see Sec. 7.2.1), a minimum of 7.5 GWp has to be installed to cover 20% of the yearly load with only south oriented modules and a tilt of 45°. Going away from this module configuration increases the needed nominal PV power until 10 GW. The normalized compensated PV power represents the additional PV power that has to be installed to compensate the losses in order to fulfill

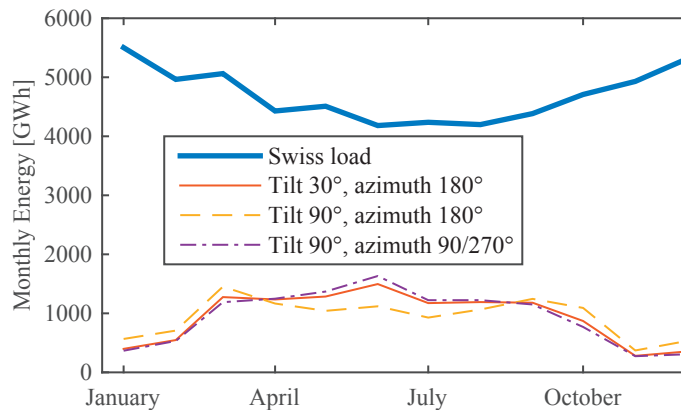


Figure 7.20 – Monthly PV production for three different PV module orientations such that for each configuration the total PV production is equivalent to 20 % of the annual Swiss load and the total Swiss load.

the 20 % of annual electricity consumption load. Dividing this compensated PV power by the minimum installed PV power of all orientations and tilt allows comparing the different configuration directly. The minimum of this factor is found for south oriented modules with 45° tilt as for the PV nominal power. Here we need to install 11 % more PV to compensate the losses. Hence this factor represents in a very first approximation (assuming that the price per installed PV power do not depend on module tilt and neglecting the grid cost) the cost of PV energy if the excess cannot be stored or sold to other countries.

Those simulations on Swiss level only give a rough estimate of the effect of PV system orientation on the grid. In reality, the costs and excess PV energy depend on many more parameters such as installation costs depending on module orientation and tilt, the details of the Swiss distribution grid (local variations, distribution losses, etc), of the type and capacities of the other power plants and the power exchange with other countries.

7.4 Demand-side management potential for households

As mentioned at the beginning of this chapter, the PV production peaks injected into the grid can be lowered by shifting loads to this production period. The Flexi project [Perr 15] aimed to determine the flexibilization potential of the electricity demand for households. For the socio-economical part of the study, 105 households were divided in three groups:

- The *flexi* group that received monthly a financial incentive if they performed among the best households of the group in terms of *midday ratio* (defined below).
- The *invoice* group that just received monthly information of how much and when during the day they consume electrical energy. They were just encouraged to enhance *midday*

ratio (with no financial incentive).

- The *Control* group receiving no information on the goal of the project or on their consumption/behavior.

The goal was to measure if and how the *flexi* or *invoice* group could enhance their *midday ratio*. The group received their score or information from January 2014 to December 2014. The results are detailed in [Perr 15]. In the technical part of this project one of our⁶ goal was to evaluate theoretically the share of the electricity consumption that can be shifted to midday period when PV production should be highest. In this work we define as *midday ratio* the ratio of the electricity consumption between 11:00 and 15:00 and the total electricity consumption. A sample of ca. 300 households loads with a time step of 15 minutes from the village of Cernier (CH) was available. Moreover, out of this sample 105 households answered a detailed survey with a description of the inhabitants, their occupation and description of the existence and use of domestic electrical appliances. To quantify the amount of load than could be shifted, we classified the different appliances in three categories; easily shift-able, hardly shift-able and non shift-able. The time of use of each load should be known. The survey answers could already give some hint of the time use, however not very accurately. The 15-minute-load curve do not really allows assessing which appliances are used. Hence we developed a new hybrid method using the 15-minutes-load curves, Markov chain based "human behavior model" and "time use data" that was then applied to the 105 households which answered the survey⁷.

7.4.1 Methodology

For each household a synthetic load curve is generated that allows extracting the time use of each appliances (Fig. 7.21). To build this curve the following inputs are used:

- The number of persons and the electrical appliances available which are extracted from the survey.
- Time use data which is a list of activities coupled with time for a sample of persons during a given period. As not such data exists for Switzerland we used a time use data from the Netherlands [Neth 05] as input. From time use data we can extract the probability for each activity at each time of the day and the probability to move from one to another activity (Markov chain approach [Torr 14])
- The mean consumption values of the different appliances mean values from different sources [Trac, Beta, Comp].
- The recorded 15-minutes load curves.

The synthetic load curve of one household is generated for one day as following:

⁶Y. Riesen, R. F Tschui, C. Ballif and N. Wyrsh

⁷The code was mainly written by Raffael Tschui during his civil service

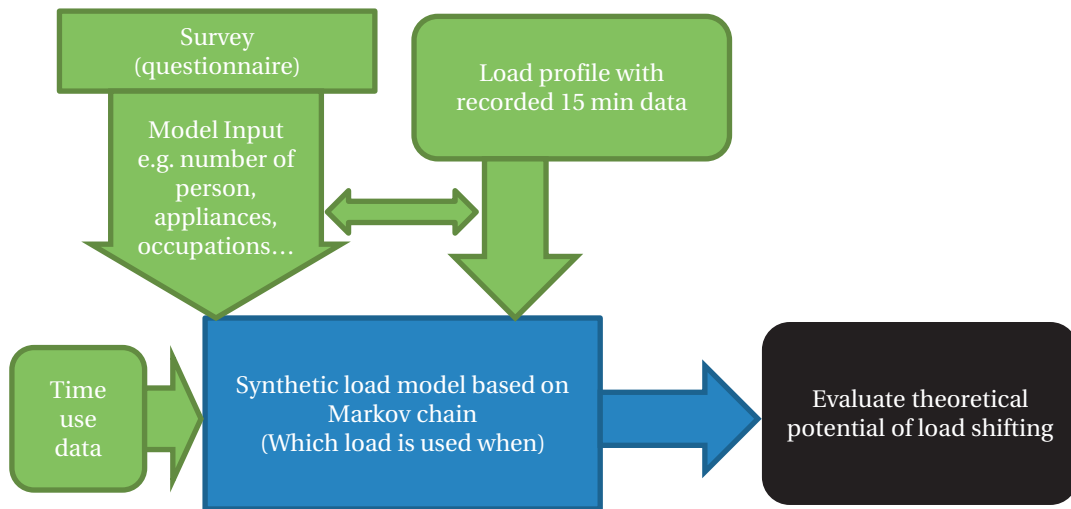


Figure 7.21 – Schematic of the methodology used to recognize appliances.

1. The standby power is determined as the minimum recorded load value of the current day. It is then subtracted from the recorded load curve.
2. Periodic loads as fridge and freezers are recognized and also subtracted from the recorded load.
3. If no other consumption peak is detected, it is assumed that no one is in the house. Only standby and fridge consumption are used for the load curve of this day. The algorithm goes to the next day.
4. The light are assumed to be on between sunset and sunrise if at least one person is at home and not resting.
5. If the survey indicates that there are children in the house a random activity sequence is generated for them.
6. For adults in the households, the best load curve fit to the measured curve is iteratively found by generating synthetic loads constructed with a chain of activities based on probabilities that are determined with the following inputs:
 - If the household own such a device based on the survey (if not the probability for using this device is 0).
 - During the consumption peak detected on the measured load curve, the probability for high consuming activities is increased.
 - During low consumption period the probability of big consumers is low.
 - Markov chain model for human behavior [Torr 14] based on the time use data [Neth 05]. Weekends and weekdays are distinguished are handled separately but no seasonal effect in terms of behavior is taken into account

7.4. Demand-side management potential for households

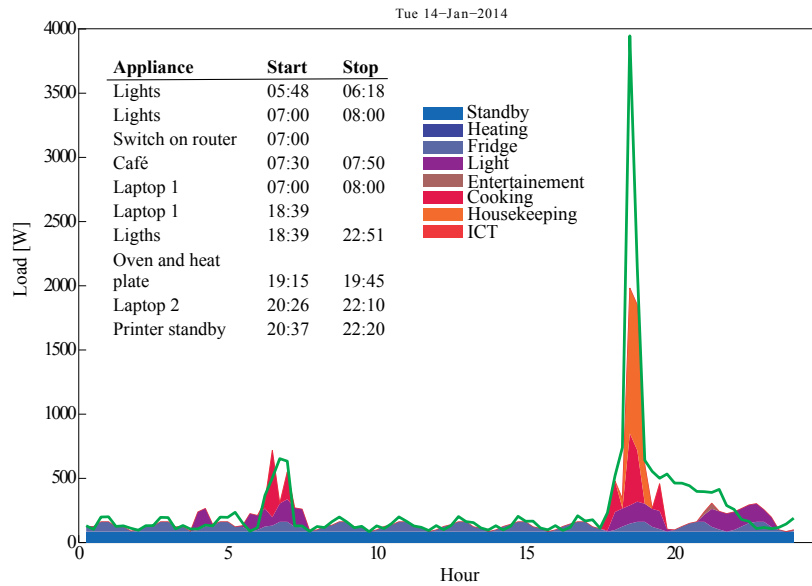


Figure 7.22 – Measured (yellow) and reconstructed synthetic load of an apartment with 2 person. The time use for the different devices is also added.

A classification of the activities and their related loads can be found in the appendix B.

For this analysis, heat pumps or EHW are not taken into account, as almost all households of this sample have oil based central heating.

7.4.2 Results

The simulated synthetic load results in 13.4 % less yearly consumed energy than the measured electrical consumption for a 2-person household and 15.7 % for a 4-person household. The more person living in a household the worse is the fit. The simulated *midday ratio* values are slightly lower (17 % to 20 %) than the measured one (20 % to 25 %) because the synthetic load often underestimate power peaks which are frequent around midday. Comparing the total consumed energies between measured and synthetic load curve only partially allows validating the model. Moreover, the modeled time use of the different appliances should be compared with the real time use. As this is a very demanding task for a household to keep record of all activities and appliances used as a function of time, this was only checked for one household during two days. Figure 7.22 shows the measured and the reconstructed load for one day. The real time use of the different appliances is added as text in the figure. The standby and the fridge/freezers loads are well reproduced. The main peaks are also reproduced quite well. However for the peak occurring around 19h00, the intensity is not completely correct as well as the activity was only cooking and not housekeeping at this time in reality.

For a better validation more device time use data of the measured households are needed.

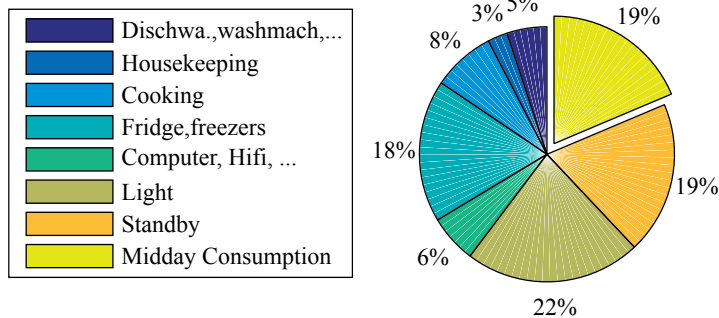


Figure 7.23 – Relative consumption of each appliance types outside the 11:00 to 15:00 period and the total midday consumption as determined from August 2013 to December 2014 and all household that filled the survey.

The dependence of the result on the input time use data has also to be further investigated. Nevertheless we still assume that those synthetic loads and the corresponding device time use could statistically represent the reality. We therefore applied it to the 105 households that answered the survey.

Figure 7.23 shows the relative consumption of each device types for all households outside the 11:00 to 15:00 period and the total midday consumption from August 2013 to December 2014. The results can only be approximately compared to existing studies [Nipk 13, Kemm 14] as the context analysis are different (for example the standby are treated differently). 19% of the total electricity is already consumed during midday. The rest of the day:

- 22% of the energy is used for light. This proportion seems to be relatively high compared to existing studies [Nipk 13]. The lamp consumption is quite difficult to simulate accurately as it depends strongly on the type of lamps used and household type. This load is considered as not shift-table.
- The standby consumption reaches 19% and the fridge and freezers consumption 18%. Hence 37% of electric energy is constituted of appliances that are always on. They are considered as not flexible. Even if technically it is possible to shift a fridge consumption by some hours. Also, despite the fact that we consider standby consumption as not flexible, diminishing its load will logically enhance *midday ratio*.
- Cooking has a part of 8% of the total electric consumption outside the midday period. For people eating lunch at home it could be classified as hard shift-able otherwise it is not shift-able.
- Computer, Hi-Fi and other electronic devices, dishwasher/wash-machine/tumbler and housekeeping appliances reaches 6%, 5% and 3% of the load respectively. Computer

7.4. Demand-side management potential for households

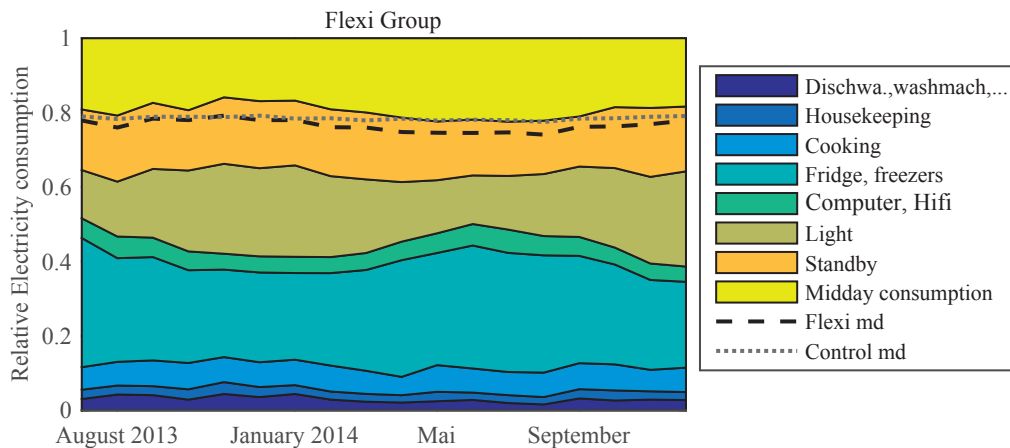


Figure 7.24 – Simulated monthly electrical device category share use for the flexi group. The measured *midday ratio* for the flexi (dashed line) and the control group (dotted line) are also plotted.

and Hi-Fi can be considered as hardly shift-able. Housekeeping, dishwasher, wash-machine can be considered as easy shift-able.

Considering everything, with our classification, 8% of the consumption can be easily shifted to the midday period and 6% hardly shifted. The 67% consumption left are considered as non-shift-able.

Figure 7.24 shows the monthly simulated electricity share for the *flexi* group and the measured *midday ratio* for the *flexi* and the *control* group. We note that as already discussed the simulated *midday ratio* is slightly lower than the measured one. However for the simulation as well for the measurement the *midday ratio* enhances after January (start of the experiment with the monthly financial incentives). While the *midday ratio* of the control group remains stable. From now on we discuss the simulated values. The light (as expected) and standby part diminish in summer and increase again in winter (it is also the case in absolute values). The diminution of the standby could partially be explained by the electricity used during the cold period to supply the circulation pump for heating. The fridge/ freezers consumption part is increased in summer, however its absolute value oscillate over the same value during the whole year. Housekeeping and dishwashers/wash-machine devices categories which are considered as flexible exhibit a relative lower consumption from January to September. This is coherent with *midday ratio* enhancement.

For the 105 households, in the idealized case of completely controllable loads, the 8% easily shift-able part is roughly equivalent to the peak shaving capability of a storage size of 0.3 kWh/kWp for 30° tilted south oriented modules (see Sec. 7.2.6 and 7.2.8).

7.5 Solar cells influence on self-consumption, PV-loss and seasonal production

In this section, we quantify the effect of solar cell's temperature and irradiation behavior on self-consumption, *PV-loss* in the presence of a feed-in limit and winter/summer PV production ratio ($E_{\text{wint.}}/E_{\text{summ.}}$). For this purpose, we modeled the power production over the year of poly-crystalline silicon (*Poly*), silicon heterojunction (*SHJAg*), thin-high-band gap single-junction amorphous silicon (*a-Si*) in initial state and a thick single-junction amorphous in degraded state (*a-Si2d*) solar modules. The simulation is based on the cells measured in Sec. 4.6. Moreover, the impact of the DC/AC inverter on those results is also studied. For simplification we don't consider storage.

7.5.1 Simulation details

The power output as a function of irradiance and temperature ($P_{\text{mpp}}(G, T)$) of those four different solar modules is calculated by interpolating the indoor measurement results (at different T and G) of the corresponding solar cells. We apply the same procedure as for the *Interp.* case in Sec. 4.6.2 for determining the irradiance and the temperature:

- The in-plane irradiance as a function of time $G(t)$ is determined by the temperature corrected and normalized J_{sc} value of a *c-Si* module monitored on our roof in Neuchâtel (Switzerland) from September 2014 to September 2015 (see Sec. 2.4). This methodology, allows using directly the irradiance on cells (most angular, glass reflection and soiling effects are therefore already taken into account). However, due to the different spectral response of the two *a-Si:H* cells compared to the *c-Si* modules, spectral effects are not taken into account for those cells (see Ch. 5). As a consequence, for clear sky conditions, we slightly overestimate their output power in winter and slightly underestimate it in summer.
- The module temperature used in the simulation $T(t)$ is extracted from the back-of-module temperature of the monitored *c-Si* module. Hence we are neglecting the difference between back-of-module temperature and the cell temperature. Moreover, we do not take into account the fact that the module temperature also depends on the module's efficiency (indeed a module with higher efficiency will heat less due to lower thermal losses). However, we estimate that these errors are negligible compared to the effect of using real measured module temperatures and considering their influence on module performances instead of STC performances.

For simplicity and to avoid effect of module design, we decided to use same module temperature and irradiance inputs for all four simulated modules. The choice of two different *a-Si:H* cells is motivated by the fact that we then have a best case: the thin *a-Si* module in initial state and a worse case with the thicker *a-Si2d* module. During the simulation period, 23 days

7.5. Solar cells influence on self-consumption, PV-loss and seasonal production

had to be removed due to no available monitoring data. Note that degradation and recovering effects for *a*-Si:H based modules (see Ch. 6) are not directly taken into account.

To assess the impact of the DC/AC inverter we simulate the power output of the PV system with and without taking into account the DC/AC converter losses (see Sec. 7.2.1). The maximum inverter power ($P_{inv,max}$) is sized such as maximizing the total energy output for each technology in the case of no feed-in limit. Moreover, the PV system is sized such that the total PV production after the converter⁸ is equivalent to the total electricity consumption during this period. We used the load of the same household as the *Reference load* but for another period (September 2014 to September 2015). The total consumption without the removed 23 days reaches 3350 kWh. The self-consumption (SC) was calculated for a case without feed-in limit and the *PV-loss* was calculated for a feed-in limit of 50 %.

7.5.2 Results

Inverter losses and sizing

Table 7.3 shows the Efficiency and temperature coefficient of P_{mpp} (TC_{Pmpp}) at STC (η_{stc}) together with the relative $P_{inv,max}$ and the relative to total PV production inverter losses.

	η_{stc} [%]	TC_{Pmpp} %/°C	$P_{inv,max}/P_{nom}$ [%]	Inv. loss [%]
<i>Poly</i>	15.3	-0.39	105	3.95
<i>SHJAg</i>	20.0	-0.25	107	3.98
<i>a-Si</i>	9.14	-0.19	109	3.99
<i>a-Si2d</i>	7.70	-0.25	107	3.98

Table 7.3 – Efficiency at STC (η_{stc}) and TC_{Pmpp} from Sec. 4.6. Optimized relative $P_{inv,max}$ to nominal PV power and the inverter losses from the simulation.

From this table we can extract following results:

- The optimal $P_{inv,max}/P_{nom}$ is correlated with the TC_{Pmpp} of the cells. The higher (more favorable) the TC_{Pmpp} the higher is this ratio because the power production peaks are higher (during production peaks the cell temperature is generally high). The power rating ($P_{inv,max}$) of commercially available converters is defined by the manufacturers at given values. Hence the $P_{inv,max}$ cannot be adapted continuously and those $P_{inv,max}/P_{nom}$ variation are negligible.
- Inverter losses depend on the temperature behavior, as well as on low light behavior of the modules. The fact that the thick *a-Si2d* has a better low light behavior than the thin *a-Si* explains that their inverter losses are equal despite their different TC_{Pmpp} .

⁸Not as in Sec. 7.2

SC, PV-loss and PV sizing

Table 7.4 shows the simulation results for the SC and the PV-loss depending on module types with and without inverter losses. The installed PV capacity needed to produce the same energy as the electric consumption is shown as well.

	SC		PV-loss		P_{nom} inv. W_p
	no inv. [%]	inv.	no inv. [%]	inv.	
<i>Poly</i>	28.0	27.8	10.4	10.7	2946
<i>SHJAg</i>	27.9	27.7.0	11.5	11.7	2918
<i>a-Si</i>	27.7	25.0	12.0	12.2	2881
<i>a-Si2d</i>	27.7	25.0	11.4	11.6	2933

Table 7.4 – SC without feed-in limit and PV-loss with a feed-in limit of 50 % with and without inverter losses. Installed PV capacity (P_{nom}) to reach an annual PV production that is equivalent to the consumed electricity.

The module type influences barely the SC in this case, although we still notice an increase of absolute 0.1 % in SC for the *Poly* module due to its lower TC_{Pmpp} reducing injection peaks. The inverter losses reduce the SC by absolute 3 % for all modules due to higher inverter losses at low irradiation condition where the self-consumption is relatively higher than for high irradiances.

Without inverter losses the PV-loss values are as expected lowest (10.4 %) for the module with lowest TC_{Pmpp} (*Poly*) and highest (12 %) for the *a-Si* module with highest TC_{Pmpp} . Adding inverter losses increases the PV-loss by absolute 2.7 % to 4.2 % depending on the module type. The PV-loss increases because the feed-in limit in power is lower in the case of taking in account inverter losses due to the fact that the feed-in limit is calculated by taking 50 % of the nominal power after the inverter. If it was 50 % of the nominal power before the inverter losses, the PV-loss would be lower in the range of 10 %. Those results also depends on several factors as excess injection power distribution and the P_{mpp} as a function of irradiance behavior of the different modules.

Winter to summer production ratio

The ratio between the total energy produced by the modules from October 29, 2014 to February 2, 2015 and from May 7, 2015 to August 8, 2015 (90 days with available monitoring data for each period) with and without inverter losses are presented in table 7.5. Note that no feed-in limit is used in this case.

As expected due to the more negative TC_{Pmpp} , the $E_{wint.}/E_{summ.}$ of the *Poly* is highest (51.2 %) and lowest for *a-Si2d* (47.5 %). As for the PV-loss, it is essentially the temperature behavior that influences most this ratio, however the irradiance behavior also plays a non-negligible

	$E_{\text{wint.}} / E_{\text{summ.}}$	
	no inv.	inv.
	[%]	
<i>Poly</i>	51.2	50.4
<i>SHJAg</i>	48.8	48.0
<i>a-Si</i>	48.0	47.2
<i>a-Si2d</i>	47.5	46.7

Table 7.5 – Ratio of the energy output between the 90 days with lowest sun (above the clouds) irradiance and highest sun irradiance ($E_{\text{wint.}} / E_{\text{summ.}}$).

role. Moreover for the *a-Si:H* cells this ratio would even be about 4 % higher due to seasonal variation induced by the Staebler-Wronski effect (see Sec. 6.3.1).

7.6 Conclusion

In this chapter we discussed how midday PV production peaks injected into the grid can be lowered (peak-shaving), hence supporting the low voltage grid by avoiding over-voltage and too high reverse power flows through the transformers. The analysis was done by considering the consumption of households. Peak shaving capability of local storage, module orientation variation, demand-side management and influences of solar cell characteristics were discussed and quantified. As reference case for the presented results, we sized the PV nominal power such that its total energy output covers its yearly electricity consumption. We developed a Matlab program able to simulate a PV system with a battery or a heat storage. This program allows us quantifying the capability of peak-shaving of such systems. With this tool we first testes several electricity price schemes encouraging households inhabitant to do feed-in peak-shaving. The best price scheme that minimizes the maximum feed-in power is established to be a proportional to the daily feed-in maximum power tax. Other price scheme such as a feed-in and electricity price inversely proportional to the PV production do not shave completely all feed-in peaks. Introducing a fix feed-in limit also allows encouraging owner of PV systems to limit their feed-in power. If the feed-in limit is set to 50 % of the nominal PV power, with no batteries about 7 % to 12 % of the total PV power has to be curtailed and is lost as shown for a sample of 44 loads (households and some shops). Adding a storage allows reducing significantly those losses. For example, a battery capacity of 1 kWh/kWp reduces those losses to values of 0.5 % to 4 %. In the presence of a feed-in limit with constant electricity prices, optimizing the cashflow is equivalent to first minimizing losses due the feed-in limit and to then maximizing self-consumption. We compared a control algorithm optimizing cashflow due to the electrical flux with grid needing PV production and load forecast (*co. opt.*) with a simple developed control algorithm needing only a simulated clear sky maximum PV production (*opt. both.*). The *opt. both.* algorithm performs almost as well as the *co. opt.* algorithm using an exact forecast (best case) and significantly better than the *co. opt.* algorithm with real forecast. As in real condition no real forecast is possible, the *opt. both.* algorithm

Chapter 7. Photovoltaic generation and the local electricity grid

using no forecast is best suited. Loss analysis of such a system shows that the DC/AC inverter sizing is crucial to optimize the system efficiency. For more realistic system efficiency analysis, power flow simulation are not enough, voltages and currents should be taken into account as well as a more precise battery model.

Furthermore, we evidenced the advantage of using load aggregation in the framework of feed-in limits. When the control algorithm is applied to the sum of several loads, only one central battery or distributed batteries but with a central control can be used. Aggregating loads mainly diminish the *PV-loss*, the higher the load compared to the PV production the higher the *PV-loss* diminution. Moreover in real conditions, one centralized battery should be more cost effective than distributed systems. However one possible disadvantage of centralized battery could be the loss of concern of the involved people or household owners. Using heat pump or electrical water heating system and a water tank as heat storage is also a very effective way to do peak shaving. Our case study showed that if heat storage is only used for domestic water heating, heat storage performs as well as or even better than a 0.7 kWh/kWp battery storage. In this context, continuous heat pump performs best as the power can be adapted to the excess feed-in. When using ON/OFF heaters with fix power, either more or less of the excess feed-in can be stored. As a summary, a relatively small heat or battery storage is enough to already significantly diminish the power peaks around midday.

In the second part of this chapter, we simulated the effect of module orientation on peak shaving for households and at Swiss level. For households in the presence of a feed-in limit of 50 %, we compared south oriented modules at 30° tilt, with west/east oriented modules with same tilt. The later configuration allows reducing the *PV-loss* by 3.1 % absolute percent and the *SC* by 1 % absolute percent. However, 17 % more modules have to be installed. Adding storage will reduce the difference in *PV-loss* between the different orientations but increase the gain in *SC* for east-west orientation. At Swiss level, we simulated the excess PV power defined as the instantaneous PV power exceeding the total load subtracted by the run-of-river plant. This excess power, assuming that the PV production covers 20 % of the yearly Swiss load, can be reduced from 12 % for horizontal modules to 5 % for vertical tilted modules mainly west/east orientated. Tilting the modules more vertically allows reducing by more than a factor two the difference in PV production between the three month with highest and lowest irradiation. Knowing the financial value of peak shaving and storage those results allows assessing if it is worth or not to encourage the installation of modules at a different orientation than south.

To quantify the shift-able electrical load for households, we developed a specific algorithm. The latter uses as input 15-minutes loads, some characteristics of the households (such as number of persons and electrical appliances available) and time use data. Using a few judicious assumptions, the algorithm is then able to roughly reproduce the measured load curve and estimate the share of shift-able load. However, to validate the model more device time use data of the households sample are needed. The result indicated that beside the 19 % share of the load that is already consumed during midday (11:00 to 15:00), 8 % could be easily shifted and while 5 % is hardly shift-table. Note that for this study heat pumps and

electrical water heating which are potentially very flexible loads in households are not taken into account as they were very rare in the considered sample.

Finally, we quantified the effect of solar cells temperature and irradiance dependence on *SC*, *PV-loss* and winter to summer production ratio. We observed that a more negative temperature coefficient increases slightly *SC* (e.g. 0.1 % in absolute between a poly-*c*-Si and an heterojunction solar cell, SHJ) and decreases *PV-loss* (e.g. 1.1 % less *PV-loss* for a poly-*c*-Si compared to a SHJ cell). A lower temperature coefficient also increases the winter over summer production ratio. The performance dependence on irradiance also influences those results but in a reduced amount compared to the temperature. Those effects are relatively small compared to other system effects as inverter efficiency and sizing, however they are not completely negligible.

8 Conclusion

Improvements of PV systems have so far mainly focused on the cell or module efficiency. However the system energy yield should be more relevant and its importance has been widely overlooked. In this thesis we therefore studied the effect of the main parameters influencing the useful energy production of a photovoltaic system at both cell and system levels. The influence of module design on energy yield was not considered.

We focused specifically on thin-film silicon solar cells and we were able to link material parameters and cell design to the temperature behavior of thin-film silicon solar cells, allowing the optimization for energy output at specific location. We also studied spectral effects as a function of the current matching configuration of silicon thin-film multi-junction solar cells (micromorph) aiming at designing devices with optimum energy production. The energy yield of *a*-Si:H is also sensitive to degradation or recovery effects (related to the Staebler-Wronski effect) of the solar cell performance following changes in irradiance and/or temperature conditions. Even though we were able to document in detail the device evolution under various operating conditions, we were not able to model these effects using a simple diode model approach taking into account the defect states in the device. Nevertheless the obtained indoor and outdoor experimental results combined with temperature dependence results opens the way for developing a more precise model (or improving existing models) with other approaches.

To achieve high PV penetration into the electrical grid, PV systems have to be optimized to minimize energy losses and to therefore maximize the useful energy generated. In this context, we evaluated system losses resulting directly from measures to limit the peak rate of PV energy injection on clear middays; such measures comprised battery storage, module orientation variations or demand-side management. At the same time, we evaluated these measures in their ability to support the electrical grid for enhanced PV integration. Lastly, we quantified – based on cell level results – the influence of solar cell technology on grid integration.

More detailed conclusions and perspectives are detailed in the next sections:

8.1 Cell level

8.1.1 Temperature dependence

We measured the temperature and irradiance dependences of different *a*-Si:H solar cell performance parameters for four different cell series prepared with different deposition parameters (power and frequency of the PE-CVD generator, the hydrogen-to-silane dilution during the deposition of the intrinsic absorber layer (*i*-layer), and the thicknesses of the *i*-layer and *p*-type doped hydrogenated amorphous silicon carbide layer) in an annealed and degraded state. With the only exception being the *i*-layer thickness series, the cells that performed best at STC also showed the most favorable temperature behavior. It follows that optimizing these fabrication parameters for best efficiency at STC will also lead to the optimum energy output, independent of the device operating temperature. For the *i*-layer series this correlation has yet to be confirmed. Cell thickness thus is a crucial parameter for optimizing the cells. It has to be noted that we did not take into account dynamic degradation and recovery behavior for that part of the study. Moreover, based on numerical simulations and experimental results we showed that the peak in the *FF* as a function of temperature (often occurring between 0 °C and 80 °C) correlates with more positive space-charge in the *p*-layer induced by the photo-generated holes. We also observed that the $TC_{V_{oc}}$ dependence on irradiance and material parameters generally increases linearly with the V_{oc} . Degrading a cell increase the (is favorable for) $TC_{J_{sc}}$ and TC_{FF} but the $TC_{V_{oc}}$ get worse (because the V_{oc} decreases with degradation) resulting in a $TC_{P_{mpp}}$ that becomes slightly worse.

The temperature dependence of microcrystalline silicon μc -Si:H solar cells exhibit a similar behavior due to its similar geometry – with thin doped layers compared to a relatively thick *i*-absorber layer. The temperature behavior of μc -Si:H cells is most sensitive to the roughness of the transparent conductive oxide substrate because of its influence on V_{oc} which itself impacts the temperature coefficient of the V_{oc} . The temperature dependence of thin film silicon micromorph and triple junction solar cells can be understood by the temperature behavior of their sub-cells (*a*-Si:H and μc -Si:H). Hence, we now have a better and comprehensive understanding of the different mechanism influencing the temperature dependence of thin-film silicon cells. This should benefit their design with optimum energy yield for specific climate conditions.

We could also show that for *a*-Si:H solar cells with relatively high *FF*, a good fit of their I(V) characteristic over orders of irradiation intensity and a wide range of temperatures can be obtained with a 1-diode model containing a current loss term and temperature dependent saturation current and ideality factor. For cells with lower *FF*, a field deformation factor is required to obtain an acceptable fit.

Silicon heterojunction solar cells (SHJ) also exhibit a *FF* maximum with temperature mainly due to the hole barrier (band offset between the *a*-Si:H-*i* layer and the *c*-Si wafer) in the valence band. This effect also renders I(V) curves to be s-shaped at low temperatures. We here

proposed a method that allows the extraction of an activation energy from those $I(V)$ curves. However the link between the activation energy and the band offset is not yet clear. Numerical simulations are needed to clarify the correlations.

Finally we compared the previous results with the temperature behavior of other silicon crystalline (c -Si) solar cells (mono-, multi- c -Si and back contacted mono- c -Si). For c -Si solar cells, the $TC_{V_{oc}}$ vs. V_{oc} curves (the V_{oc} is varied by changing irradiance) for each device are almost superposed. As back-contacted and SHJ cells have a higher V_{oc} , their $TC_{P_{mpp}}$ are more favorable (higher) than for the technologies with lower V_{oc} . Between those two high V_{oc} cells the SHJ has an even better $TC_{P_{mpp}}$ due to the temperature dependence of the FF . For this study the SHJ cells were fabricated in our laboratory, and the last conclusion should be verified with other commercial SHJ devices since this $FF(T)$ behavior depends on cell design.

8.1.2 Spectral dependence

We also evaluate the effect of varying spectra (simulated with SEDES2 software model) on micromorph (a -Si:H/ μc -Si:H multi-junction) solar cells using a 2-diode model with a current loss term. We found that over 88 % of the total energy yield was produced with a solar spectrum that is bluer than the AM1.5g spectrum (for an installation located in Bern, Switzerland). Since with a bluer spectrum, a top limited cell become less top limited, we calculated that the multijunction cell's energy yield increases by 1.6 % due to the spectral effects. We conclude that to maximize the energy yield in our location, the cells have to be matched for a slightly bluer spectrum than AM1.5g. It is relatively easy to calculate spectral effects on solar cells knowing their spectral response if the sun spectra are known. Therefore the highest challenge for evaluating the spectral effects on energy yield is to simulate or measure the spectral irradiance shape as a function of meteorological conditions, especially for overcast situations.

8.1.3 Annealing and degradation

Our 20-hours indoor light-soaking kinetics experiments showed that, as expected, the degradation of cell performance increases when lowering temperature and increasing irradiance. However for light-soaking at low irradiances (330 W m^{-2}) the relative degradation was observed to be almost independent of temperature, and at high temperature (80°C), it was almost independent of irradiance. Outdoor monitoring results of single a -Si:H, micromorph and a -Si:H/ a -Si:H tandem cells and modules showed an initial degradation followed by a seasonal variation of the P_{mpp} of more than 4 %, 6 % and 8 % for the a -Si:H/ a -Si:H module, the micromorph module and single a -Si:H cells respectively. Those results confirm observation of previous studies.

In literature, this effect was either modeled using completely phenomenological models or by complicated and time consuming numerical models linking detailed material properties with solar cell performances. We choose to take a median approach using a diode model with

parameters depending on defect density. However, we showed that it is challenging to model the Stabler-Wronski effect with such a diode model and a simple defect density model. Indeed, at least four diode parameters (J_0 , n , $(\mu\tau)_{eff}$ and V_{bi}) are affected by degradation/annealing in a way that is not clearly known. Moreover the complexity and multiple effects (charged state, multiple dependence of the $(\mu\tau)_{eff}$ product with defect density) involved in the SWE cannot be simplified with a single defect density variable. Hence completely empirical models are the best alternative for the moment.

8.2 System level

With high PV penetration into the electrical grid, the midday peak production could become detrimental for the electrical grid stability if it cannot be absorbed locally. We focused on three possible solutions for households to diminish this peak injection into the low-voltage electrical grid and evaluated their respective induced losses (i.e., their quantitative effect on net system useful).

Local storage We developed a simulation tool able to model a PV system with local storage. Grid operators can introduce a feed-in limit to encourage system owners to reduce their peak injection using e.g. a battery. We developed a control algorithm that minimizes the losses due to feed-in limits and maximizes the self-consumption. This algorithm needs no production forecast and performs as good as a control algorithm with forecasts. We also evaluate the system losses as function of this particular and other control algorithms. For example, with a feed-in limit of 50 % of the nominal installed PV power, a battery size of 1 kWh/KWp reduces the losses due this feed-limit from 4 % to 0.4 %. Hence, a feed-in limit allows reducing significantly peak-injection with relatively small net useful energy loss, and the loss could be further significantly reduced with a relatively low storage capacity. We also demonstrated that heat storage using a boiler or heat pump performs as well as battery storage. Aggregating loads also allows diminishing the loss and increasing self-consumption. In this thesis we only used storage for peak-shaving. However it could also be used for additional grid support, such as supplying reactive power or frequency control, adding even more value to storage. Including this aspect, the next step would be to compare a feed-in limit regulation with a centrally-controlled battery bank to allow more services to the grid under optimal control. However, the latter scheme does not offer very much interest to the end-user seeking to maximize the percentage of self-consumption.

Module orientation Changing tilt and orientation of the modules allows reducing losses due to feed-in limits and to reduce the winter/summer production ratio by more than a factor two. However, more PV modules are needed to achieve the same production and the detailed economic aspects are therefore critical. Those results can help one to assess if and how different module orientations present advantages.

Demand-side management We developed a statistical method that estimates the usage time of different electrical appliances of a household from 15-minutes measured loads. We applied this method to a sample of 105 households (with detailed information on the household size, inhabitants and electrical appliances) to estimate the share of the total load that could be shifted to the peak PV production period modeled as 11:00 to 15:00). We calculated that about 8 % of the total load could be easily shifted and 5 % additional load could be shifted with more challenges. Note that already 19 % of the total load is used in this target time period. Moreover, heat pump or boiler heating were not considered as in this sample almost all households are using oil for heating. With electrical heating (e.g. using a heat pump) the easy shiftable load would increase significantly. With those results we can evaluate by which amount load shifting (demand-side management) can reduce the midday injection peak.

Solar cell influence on grid integration Finally we combined the device and system part of this thesis to quantify the effect of cell technology on self-consumption, peak-shaving and winter/summer production ratio. A lower (more negative) $TC_{P_{mpp}}$ reduces the midday peaks and winter/summer production ratio by a few percent. The module technology has a limited but not negligible impact on system output compared to other influences (e.g. system, configuration, electricity management, inverter sizing).

8.3 Outlook

By analyzing separately the temperature, spectral and degradation/recovery dependence of thin-film silicon cells, we provide the building blocks needed to predict more precisely the energy yield of thin-film silicon solar cells as a function of operating conditions. Moreover, the new insights gained by linking material properties and cell design to spectral and temperature performance behavior allows highlighting the critical parameters in solar cell design that should be adapted differently for maximizing energy output for conditions other than for STC efficiency. Hence those results provide tools for optimizing solar cells for best energy production in specific climates.

We also showed that it is challenging to describe degradation/recovery dependence of a -Si:H solar cells with a diode model. However our collected experimental results could be used to calibrate existing empirical degradation/recovery models to increase their accuracy.

Our analysis of the temperature dependence of SHJ cells provides a basis for optimizing device design for specific operating conditions. By combining those results with numerical simulations of their electrical characteristics, we should for instance be able to link the s-shape behavior of the device $I(V)$ curve to the valence-band offset of the material. Understanding this link will allow for going towards optimizing cells for given operation conditions.

On cell level, the developed experimental and data analysis methodology can be applied to other solar cells technologies. For example regarding multi-junction cells, this methodology

Chapter 8. Conclusion

could easily be applied to other tandem cells such as perovskites-c-Si solar cells to optimize their energy yield.

The results of the system level portion of the thesis enables a global overview of how high injection peaks can be reduced at household level and help for planning the future electrical grid. Hence we provide tools to quantify how much PV power can be absorbed by the electrical grid on a global level. Based on those general guidelines, we can then focus on the best methods to reduce those peaks, performing a more specific local evaluation that takes into account the local grid topology as well as reactive power. More precise results on the losses of a PV system with battery storage could be achieved by a model that takes into account current and voltage (and not only a simple power flux model) and a more sophisticated battery model. While full validation is still required, our original approach for assessing the load shifting potential is a valuable tool for the analysis of demand side management measures which are of paramount importance to insure large and smooth PV grid integration. However, the time use data (from a Dutch study) used for this work should also be adapted for the Swiss situation.

Throughout this thesis, we quantified the different losses occurring during the conversion of solar energy into useful electric energy from cell to system level. Owing to this wide perspective, the losses with highest reduction potential, from material properties to grid integration constraint, can be targeted.

A ASA simulation input parameters

We present here the input parameters we used for ASA simulations of *a*-Si:H solar cells. Values indicated as VARIABLE are the values varied with temperature.

```
C Device structure;
layers electrical=6 front=2 back=1;
grid[1] d=5e-9 spaces=20;
grid[2] d=10e-9 spaces=20;
grid[3] d=10.0e-9 spaces=20;
grid[4] d=220.0e-9 spaces=200;
grid[5] d=6.0e-9 spaces=20;
grid[6] d=30.0e-9 spaces=20;
grid[f.1] d=0.5e-3;
grid[f.2] d=2.00e-06;
grid[b.1] d=2.00e-6;

C Optical properties;
optical[1] lnk.file=Lj_p-ucSi.nk;
optical[2] lnk.file=tud_p-aSiC.nk;
optical[3] lnk.file=input/i-aSi_MS_VARIABLE.nk;
optical[4] lnk.file=input/i-aSi_MS_VARIABLE.nk;
optical[5] lnk.file=tud_n-aSi.nk;
optical[6] lnk.file=tud_n-aSi.nk;
optical[f.1] ext.coeff=0 ref.index=1.5 incoherent;
optical[f.2] lnk.file=ZnoOz2min0.nk;
optical[b.1] lnk.file=ZnoOz2min0.nk;

C Semiconductor properties;
doping[1] e.act.acc=0.15;
doping[2] e.act.acc=0.45;
doping[5] e.act.don=0.15;
doping[6] e.act.don=0.05;

bands[1] e.mob=1.12-VARIABLE chi=4.05 nc=2.5E+26 nv=1.2E+26 epsilon=7.2;
bands[2] e.mob=1.9-VARIABLE chi=3.65 nc=6.0E+26 nv=6.0E+26 epsilon=7.2;
bands[3] e.mob=1.9-VARIABLE chi=3.80 nc=2.0E+26 nv=2.0E+26 epsilon=11.9;
bands[4] e.mob=1.8-VARIABLE chi=3.80 nc=2.0E+26 nv=2.0E+26 epsilon=11.9;
bands[5] e.mob=1.9-VARIABLE chi=3.80 nc=6.0E+26 nv=6.0E+26 epsilon=11.9;
bands[6] e.mob=1.12-VARIABLE chi=4.05 nc=6.0E+26 nv=6.0E+26 epsilon=11.9;

mobility[1] mu.e=10.0e-4 mu.h=1.0e-4;
mobility[2] mu.e=10.0e-4 mu.h=1.0e-4;
mobility[3] mu.e=20.0e-4 mu.h=5.0e-4;
mobility[4] mu.e=20.0e-4 mu.h=5.0e-4;
mobility[5] mu.e=10.0e-4 mu.h=1.0e-4;
mobility[6] mu.e=10.0e-4 mu.h=1.0e-4;

C Description of DOS;
vbtail[all] e.range=0.5 levels=50 c.neut=0.7e-15 c.pos=0.7e-15;
vbtail[1] n.emob=1.0e28 e.char=0.090;
vbtail[2] n.emob=1.0e28 e.char=0.090;
vbtail[3] n.emob=1.0e27 n1.emob=1.0e27 e.char=0.043 e1.char=0.043;
vbtail[4] n.emob=1.0e27 n1.emob=1.0e27 e.char=0.043 e1.char=0.043;
vbtail[5] n.emob=1.0e28 e.char=0.090;
```

Appendix A. ASA simulation input parameters

```
vbtail[6] n.emob=1.0e28 e.char=0.090;

cbtail[all] e.range=0.5 levels=50 c.neut=0.7e-15 c.neg=0.7e-15;
cbtail[1] n.emob=5.0e27 e.char=0.070;
cbtail[2] n.emob=5.0e27 e.char=0.070;
cbtail[3] n.emob=2.0e27 e.char=0.030;
cbtail[4] n.emob=2.0e27 e.char=0.030;
cbtail[5] n.emob=1.0e28 e.char=0.080;
cbtail[6] n.emob=1.0e28 e.char=0.080;

dbond[all] levels=40 e.corr=0.2;
dbond[1] n=1e21 e.neut=-0.70 ce.pos=200.0e-15 ce.neut=1.0e-15 ch.neg=100.0e-15 ch.neut=1.0e-15;
dbond[2] n=1e25 e.neut=-0.70 ce.pos=200.0e-15 ce.neut=1.0e-15 ch.neg=100.0e-15 ch.neut=1.0e-15;
dbond[3] n=3e22 e.neut=-0.88 ce.pos=200.0e-15 ce.neut=1.0e-15 ch.neg=100.0e-15 ch.neut=1.0e-15;
dbond[4] n=3e22 e.neut=-0.88 ce.pos=200.0e-15 ce.neut=1.0e-15 ch.neg=100.0e-15 ch.neut=1.0e-15;
dbond[5] n=5e23 e.neut=-1.40 ce.pos=200.0e-15 ce.neut=1.0e-15 ch.neg=100.0e-15 ch.neut=1.0e-15;
dbond[6] n=1e21 e.neut=-1.40 ce.pos=200.0e-15 ce.neut=1.0e-15 ch.neg=100.0e-15 ch.neut=1.0e-15;

variable Wt=0.040;
variable Ech0=sqrt(Wt^2-(k*363.15/q)^2);
variable Ech=sqrt(Ech0^2+(k*300/q)^2);
vbtail[1] e.char=Ech;
cbtail[1] e.char=Ech;

C Numerical settings;
model[all] amorphous;
model[all] external;

settings newton gummel.starts=2;
settings damp=3 max.iter=50;
settings sr.flux=1.0e16;
settings Rs=3e-4;
settings temp=VARIABLE;

optigen spectrum=am15.dat genpro3 mult=1.0;
```

B Activity and load classification

This part lists the activity categories, the considered activities (indicated in italic below) and the corresponding appliances or devices for the synthetic load recognition method (7.4.1) related to the time use data [Neth 05]:

Heating Space and Water heating are not implemented here, because most of the households have oil-heating. However, the function is used to simulate the hairdryer.

Cooking *Cooking and eating*. Devices: Cooking group, cooking oven, coffee machine, kettle, microwave.

Housekeeping *Cleaning, set table/wash dishes, laundry/ironing/clothing repair*. Devices: washing machine, dish washer, Tumble Dryer and vacuum cleaner.

Entertainment *Cook, eat, shower, work at home, use computer, TV, radio and indoor activities*. Devices: TV, HiFi system, DVD-player, Game, console and TV Box.

ICT *Work at home and use computer*. Devices: Desktop PC, Printer/Scanner/Fax and laptop.

C Inverter efficiencies

Inverter efficiency curves used in chapter 7. The curve are taken from [Nott 10].

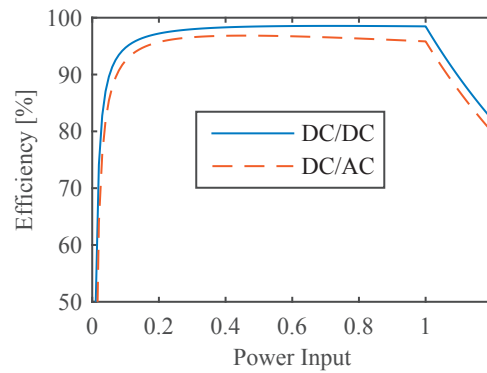


Figure C.1 – DC/DC converter and DC/AC inverter efficiencies.

Glossary

APE Average photon energy

a-Si:H Hydrogenated amorphous silicon

c-Si Crystalline silicon

DHI Diffuse horizontal irradiance

E_{act} Activation energy

E_{F}^n Quasi-Fermi level of electrons

E_{F}^p Quasi-Fermi level of holes

E_{g} Band gap

EQE Quantum efficiency (from spectral response)

FF Fill factor

GHI Global horizontal irradiance

I(V) Current as a function of voltage curve

J_{mpp} Current density at the maximum power point

J_0 Reverse saturation current

J_{rec} Voltage-dependent recombination current (from [Mert 98b])

J_{sc} Short circuit current density

ls light-soaking

max. sc. Maximize self-consumption battery control algorithm

min. PV-loss Minimize losses due to feed-in limit battery control algorithm

n Ideality factor

opt. both. Minimize loss due to feed-in limit and maximize self-consumption algorithm (no forecast needed)

co. opt. Optimize financial flux due to electricity exchange with the grid battery control algorithm (forecast needed).

P_{mpp} Power at the maximum power point
 $PV\text{-loss}$ Losses due to feed-in limit
 RV Relative variation of a parameter before/after light soaking or thermal annealing
 R_{oc} Resistivity at the open circuit point
 R_{p} Parallel resistance
 R_{s} Series resistance
 R_{sc} Resistivity at the short circuit point
 SC Self-consumption
 TC Temperature coefficient
 ta Thermal annealing
 T_{FFmax} Temperature of the FF maximum (or peak)
 $\mu c\text{-Si:H}$ Microcrystalline silicon
 V_{mpp} Voltage at the maximum power point
 V_{oc} Open-circuit voltage
SHJ Silicon heterojunction solar cells
STC Standard testing conditions (25 °C, 1000 W m⁻² and AM1.5g spectrum)

Bibliography

- [35 P] “35 Prozent mehr Solarstromspeicher”. Online, accessed 28.08.2015. <http://die-sonne-speichern.de/pressemeldungen/35-prozent-mehr-solarstromspeicher/>.
- [Abra 00] A. Abramov, A. Kosarev, and P. R. i Cabarrocas. “Kinetics of defects and electron, hole diffusion lengths during light soaking and consequent annealing”. *Journal of Non-Crystalline Solids*, Vol. 266, No. 0, pp. 419 – 422, 2000.
- [Akhm 97] K. Akhmad, A. Kitamura, F. Yamamoto, H. Okamoto, H. Takakura, and Y. Hamakawa. “Outdoor performance of amorphous silicon and polycrystalline silicon PV modules”. *Solar Energy Materials and Solar Cells*, Vol. 46, No. 3, pp. 209 – 218, 1997.
- [Alam 13] M. Alam, K. Muttaqi, and D. Sutanto. “Mitigation of Rooftop Solar PV Impacts and Evening Peak Support by Managing Available Capacity of Distributed Energy Storage Systems”. *Power Systems, IEEE Transactions on*, Vol. 28, No. 4, pp. 3874–3884, Nov 2013.
- [Albe 05] M. Albert, J. Deng, X. Niu, J. Pearce, R. Collins, and C. Wronski. “The Creation and Annealing Kinetics of Fast Light Induced Defect States created by 1 Sun Illumination in a-Si:H”. *MRS Online Proceedings Library*, Vol. 862, 2005.
- [Apic 08] F. Apicella, V. Giglio, M. Pellegrino, S. Ferlito, F. Tanikawa, and Y. Okamoto. “Thin Film Modules: Long Term Operational Experience in Mediterranean Climate”. In: *23rd European Photovoltaic Solar Energy Conference and Exhibition, 1-5 September 2008, Valencia, Spain*, 2008.
- [Appe 12] J. von Appen, A. Schmiegel, and M. Braun. “Impact of PV Storage Systems on Low Voltage Grids: A Study on the Influence of PV Storage Systems on the Voltage Symmetry of the Grid”. In: *27th European Photovoltaic Solar Energy Conference*, 2012.
- [Aror 82] N. Arora and J. Hauser. “Temperature dependence of silicon solar cell characteristics”. *Solar Energy Materials*, Vol. 6, No. 2, pp. 151 – 158, 1982.
- [Avel 12] F. Avellan. “Evolution des groupes de pompage-turbinage”. *Bulletin electro suisse, AES*, Vol. 2, p. 38, 2012.

-
- [Batz 11] D. Bätzner, Y. Andrault, L. Andreetta, A. Büchel, W. Frammelsberger, C. Guerin, N. Holm, D. Lachenal, J. Meixenberger, P. Papet, B. Rau, B. Strahm, G. Wahli, and F. Wunsch. "Properties of high efficiency silicon heterojunction cells". *Energy Procedia*, Vol. 8, pp. 153 – 159, 2011. Proceedings of the SiliconPV 2011 Conference (1st International Conference on Crystalline Silicon Photovoltaics).
- [Baum 10] Baumgartner, F.P., Achtnich, T., Remund, J., Gnos, S., Nowak, and S. "Steps towards integration of PV-electricity into the GRID". *Progress in Photovoltaics: Research and Applications*, Vol. n.a., p. n.a, 2010. <http://dx.doi.org/10.1002/pip.1047>.
- [Baum 13] C. Baumann, R. Schuster, and A. Moser. "Economic potential of power-to-gas energy storages". In: *European Energy Market (EEM), 2013 10th International Conference on the*, pp. 1–6, May 2013.
- [Beta] "Betatronics". Online, accessed 28.08.2015. <http://www.beta-a2.com/EE-photos.html>.
- [BFE 12] BFE. "Analyse des schweizerischen Energieverbrauchs 2000 - 2011 nach Verwendungszwecken". Tech. Rep., Bundesamt für Energie, 2012.
- [Bird 86] R. E. Bird and C. Riordan. "Simple solar spectral model for direct and diffuse irradiance on horizontal and tilted planes at the earth's surface for cloudless atmospheres". *J. Climate Appl. Meteor.*, Vol. 25, pp. 87–97, 1986.
- [Blet 10] B. Bletterie, A. Gorsek, B. Uljanic, B. Blazic, A. Woyte, T. V. Van, F. Truyens, and J. Jahn. "Enhancement of the Network Hosting Capacity " Clearing Space for/with PV". In: *5th World Conference on Photovoltaic Energy Conversion, 6-10 September 2010, Valencia, Spain*, 2010.
- [Bogd 10] N. Bogdanski, W. Herrmann, F. Reil, M. Köhl, K.-A. Weiss, and M. Heck. "PV Reliability (Cluster II): Results of a German Four-Year Joint Project - Part II, Results of Three Years Module Weathering in Four Different Climates". In: *EUPVSEC Valencia 2010*, 2010.
- [Boli 15] M. Bolinger and J. Seel. "Utility-Scale Solar 2014: An Empirical Analysis of Project Cost, Performance, and Pricing Trends in the United States". Tech. Rep., Lawrence Berkeley National Laboratory, 09/2015 2015.
- [Bonn 13] M. Bonnet-Eymard, M. Boccard, G. Bugnon, F. Meillaud, M. Despeisse, F.-J. Haug, and C. Ballif. "Current matching optimization in high-efficiency thin-film silicon tandem solar cells". In: *Photovoltaic Specialists Conference (PVSC), 2013 IEEE 39th*, pp. 0184–0187, June 2013.
- [Boyd 11] M. T. Boyd, S. A. Klein, D. T. Reindl, and B. P. Dougherty. "Evaluation and Validation of Equivalent Circuit Photovoltaic Solar Cell Performance Models". *Journal of Solar Energy Engineering*, Vol. 133, No. 2, p. 021005, 2011.

- [Bran 99] H. M. Branz. “Hydrogen collision model Quantitative description of metastability in amorphous silicon”. *Phys. Rev. B*, Vol. 59, pp. 5498–5512, Feb 1999.
- [Brau 09] M. Braun, K. Büdenbender, D. Magnor, and A. Jossen. “Photovoltaic Self-Consumption in Germany - Using Lithium-Ion Storage to Increase Self-Consumed Photovoltaic Energy”. In: *24th European Photovoltaic Solar Energy Conference, 21-25 September 2009, Hamburg, Germany*, 2009.
- [Brau 10] M. Braun, T. Stetz, and K. Büdenbender. “Multifunctional PV inverters”. In: *Electric Cars and integration of Renewable Energy at the 2020 horizon*, 2010.
- [Brey 13] C. Breyer and A. Gerlach. “Global overview on grid-parity”. *Progress in Photovoltaics: Research and Applications*, Vol. 21, No. 1, pp. 121–136, 2013.
- [Broh 06] P. Brohan, J. J. Kennedy, I. Harris, S. F. B. Tett, and P. D. Jones. “Uncertainty estimates in regional and global observed temperature changes: A new data set from 1850”. *Journal of Geophysical Research: Atmospheres*, Vol. 111, No. D12, pp. n/a–n/a, 2006. D12106.
- [Bube 89] R. H. Bube and D. Redfield. “Kinetic and steady-state effects of illumination on defects in hydrogenated amorphous silicon”. *Journal of Applied Physics*, Vol. 66, No. 2, pp. 820–828, 1989.
- [Buch 13a] C. Bucher, G. Andersson, and L. Küng. “Increasing The PV Hosting Capacity Of Distribution Power Grids: a Comparison Of Seven Methods”. In: *EUPVSEC Paris*, 2013.
- [Buch 13b] C. Bucher, J. Betcke, G. Andersson, B. Bletterie, and L. Kueng. “Simulation of distribution grids with photovoltaics by means of stochastic load profiles and irradiance data”. In: *EUPVSEC Paris 2013*, 2013.
- [Bugn 13] G. Bugnon. *High-Quality Microcrystalline Silicon for Efficient Thin-Film Solar Cells*. PhD thesis, STI, EPFL, Lausanne, 2013.
- [Burg 15] B. Burger, K. Kiefer, C. Kost, S. Nold, S. Philips, R. Preu, T. Schegl, G. StryuHipp, G. Willeke, H. Wirth, I. Brucker, A. Haeberle, V. Schacht, W. Warmuth, and C. Moreno. “Photovoltaics Report”. Presentation, 2015. Fraunhofer Institute for Solar Energy Systems ISE.
- [Caam 09] E. Caamano-Martin, D. Masa, A. Gutiérrez, F. Monasterio, M. Castillo, J. Jiménez-Leube, and J. Porro. “Optimizing pv use through active demand side management”. In: *24th European Photovoltaic Solar Energy Conference*, 2009.
- [Capu 94] D. Caputo, J. Bullock, H. Gleskova, and S. Wagner. “Toward a Practical Model of a-Si:H Defects in Intensity-Time-Temperature Space”. In: *Symposium Amorphous Silicon Technology - 1994*, 1994.

-
- [Carl 00] D. Carlson, G. Lin, and G. Ganguly. "Temperature dependence of amorphous silicon solar cell PV parameters". In: *Photovoltaic Specialists Conference, Conference Record of the Twenty-Eighth IEEE*, pp. 707–712, 2000.
- [Ceri 13] I. D. de Cerio Mendaza, B. Bak-Jensen, and Z. Chen. "Electric Boiler and Heat Pump Thermo-Electrical Models for Demand Side Management Analysis in Low Voltage Grids". *International Journal of Smart Grid and Clean Energy*, Vol. 2, pp. 52–59, 2013.
- [Clee 98] M. W. M. van Cleef, F. A. Rubinelli, R. Rizzoli, R. Pinghini, R. E. I. Schropp, and W. F. van der Weg. "Amorphous Silicon Carbide/Crystalline Silicon Heterojunction Solar Cells: A Comprehensive Study of the Photocarrier Collection". *Japanese Journal of Applied Physics*, Vol. 37, No. 7R, p. 3926, 1998.
- [Clim 15] "Climatic Research Unit, University of East Anglia". Database, 2015. <http://www.cru.uea.ac.uk/cru/data/temperature/>.
- [Comp] "Computer Power Usage". Online, accessed 28.08.2015. <https://secure.www.upenn.edu/computing/resources/category/hardware/article/computer-power-usage>.
- [Cuet 99] J. A. del Cueto and B. von Roedern. "Temperature-induced changes in the performance of amorphous silicon multi-junction modules in controlled light-soaking". *Progress in Photovoltaics: Research and Applications*, Vol. 7, No. 2, pp. 101–112, 1999.
- [De W 12] S. De Wolf, A. Descoedres, Z. C. Holman, and C. Ballif. "High-efficiency Silicon Heterojunction Solar Cells: A Review". *green*, Vol. 2, 2012.
- [DeGr 10] D. DeGraaff, S. Caldwell, R. Lacerda, G. Bunea, A. Terao, and D. Rose. "Qualification, manufacturing, and reliability testing methodologies for deploying high-reliability solar modules". In: *25th European Photovoltaic Solar Energy Conference and Exhibition / 5th World Conference on Photovoltaic Energy Conversion, 6-10 September 2010, Valencia, Spain, 2010*.
- [Denh 07] P. Denholm and R. M. Margolis. "Evaluating the limits of solar photovoltaics (PV) in electric power systems utilizing energy storage and other enabling technologies". *Energy Policy*, Vol. 35, No. 9, pp. 4424 – 4433, 2007.
- [Desc 11] A. Descoedres, L. Barraud, S. De Wolf, B. Strahm, D. Lachenal, C. Gérin, Z. C. Holman, F. Zicarelli, B. Demareux, J. Seif, J. Holovsky, and C. Ballif. "Improved amorphous/crystalline silicon interface passivation by hydrogen plasma treatment". *Applied Physics Letters*, Vol. 99, No. 12, pp. –, 2011.
- [Desp 14] M. Despeisse, A. Lo, M. Bonnet-Eymard, Y. Riesen, P. J. Alet, and C. Ballif. "Large-Area LED/Halogen hybrid solar simulator and Silicon Heterojunction solar mod-

- ules indoor to outdoor performance monitoring”. In: *6th World Conference on Photovoltaic Energy Conversion(WCPEC-6), Kyoto (JP)*, 2014.
- [Ding 13] L. Ding. *Low-Pressure Chemical Vapor Deposited Zinc Oxide Films*. PhD thesis, STI, Lausanne, 2013.
- [Domi 09] D. Dominé. *The role of front electrodes and intermediate reflectors in the optoelectronic properties of high-efficiency micromorph solar Cells*. PhD thesis, Université de Neuchâtel, Switzerland, 2009.
- [Dong 10] S. Dongaonkar, J. D. Servaites, G. M. Ford, S. Loser, J. Moore, R. M. Gelfand, H. Mohseni, H. W. Hillhouse, R. Agrawal, M. A. Ratner, T. J. Marks, M. S. Lundstrom, and M. A. Alam. “Universality of non-Ohmic shunt leakage in thin-film solar cells”. *Journal of Applied Physics*, Vol. 108, No. 12, p. 124509, 2010.
- [Droz 04] C. Droz, E. Vallat-Sauvain, J. Bailat, L. Feitknecht, J. Meier, and A. Shah. “Relationship between Raman crystallinity and open-circuit voltage in microcrystalline silicon solar cells”. *Solar Energy Materials and Solar Cells*, Vol. 81, No. 1, pp. 61 – 71, 2004.
- [Dunl 06] E. D. Dunlop and D. Halton. “The performance of crystalline silicon photovoltaic solar modules after 22 years of continuous outdoor exposure”. *Progress in Photovoltaics: Research and Applications*, Vol. 14, No. 1, pp. 53–64, 2006.
- [Dunn 11] B. Dunn, H. Kamath, and J.-M. Tarascon. “Electrical Energy Storage for the Grid: A Battery of Choices”. *Science*, Vol. 334, No. 6058, pp. 928–935, 2011.
- [Dupr 15] O. Dupré, R. Vaillon, and M. Green. “Physics of the temperature coefficients of solar cells”. *Solar Energy Materials and Solar Cells*, Vol. 140, No. 0, pp. 92 – 100, 2015.
- [Fan 86] J. C. Fan. “Theoretical temperature dependence of solar cell parameters”. *Solar Cells*, Vol. 17, No. 23, pp. 309 – 315, 1986.
- [Fann 06] A. H. Fanne, M. W. Davis, B. P. Dougherty, D. L. King, W. E. Boyson, and J. A. Kratochvil. “Comparison of Photovoltaic Module Performance Measurements”. *Journal of Solar Energy Engineering*, Vol. 128, No. 2, pp. 152–159, 2006.
- [Fann 11] L. Fanni, A. Virtuani, and D. Chianese. “A detailed analysis of gains and losses of a fully-integrated flat roof amorphous silicon photovoltaic plant”. *Solar Energy*, Vol. 85, No. 9, pp. 2360 – 2373, 2011.
- [Fran 10] P. Frankl and S. Nowak. “Technology Roadmap: Solar photovoltaic energy”. Tech. Rep., International Energy Agency, 2010.
- [Fran 12a] A. Franco, Y. Riesen, M. Despeisse, N. Wyrsh, and C. Ballif. “High Spatial Resolution of Thin-Film-on-ASIC Particle Detectors”. *IEEE Transactions on Nuclear Science*, Vol. 59, No. 5, pp. 2614–2621, 2012.

-
- [Fran 12b] A. Franco, Y. Riesen, N. Wyrsh, S. Dunand, F. Powolny, P. Jarron, and C. Ballif. “Amorphous silicon-based microchannel plates”. *Nuclear Instruments and Methods in Physics Research Section A: Accelerators, Spectrometers, Detectors and Associated Equipment*, Vol. 695, pp. 74–77, 2012.
- [Frit 01] H. Fritzsche. “Development in understanding and controlling the Staebler-Wronski effect in a-Si : H”. *Annual review of materials research*, Vol. 31, pp. 47–79, 2001.
- [Frit 10] H. Fritzsche. “A New Perspective on an Old Problem: The Staebler-Wronski Effect”. *MRS Online Proceedings Library*, Vol. 1245, pp. null–null, 2010.
- [Geis 13] J. Geissbühler, S. De Wolf, B. Demareux, J. P. Seif, D. T. L. Alexander, L. Barraud, and C. Ballif. “Amorphous/crystalline silicon interface defects induced by hydrogen plasma treatments”. *Applied Physics Letters*, Vol. 102, No. 23, p. 231604, June 2013.
- [Geis 14] J. Geissbuhler, S. De Wolf, A. Faes, N. Badel, Q. Jeangros, A. Tomasi, L. Barraud, A. Descoedres, M. Despeisse, and C. Ballif. “Silicon Heterojunction Solar Cells With Copper-Plated Grid Electrodes: Status and Comparison With Silver Thick-Film Techniques”. *Photovoltaics, IEEE Journal of*, Vol. 4, No. 4, pp. 1055–1062, July 2014.
- [Geis 15] J. Geissbühler, J. Werner, S. M. De Nicolas, L. Barraud, A. Hessler-Wyser, M. Despeisse, S. Nicolay, A. Tomasi, B. Niesen, S. De Wolf, *et al.* “22.5% efficient silicon heterojunction solar cell with molybdenum oxide hole collector”. *Applied Physics Letters*, Vol. 107, No. 8, p. 081601, 2015.
- [Ghos 80] A. K. Ghosh, C. Fishman, and T. Feng. “Theory of the electrical and photovoltaic properties of polycrystalline silicon”. *Journal of Applied Physics*, Vol. 51, No. 1, pp. 446–454, 1980.
- [Goer 15] M. Goerig and P. Bart E. “Development and validation of a phenomenological model describing degradation and annealing of a-si:h solar cells”. In: *31st European Photovoltaic Solar Energy Conference and Exhibition Hamburg*, 2015.
- [Gott 03] R. Gottschalg, D. Infield, and M. Kearney. “Experimental study of variations of the solar spectrum of relevance to thin film solar cells”. *Solar Energy Materials and Solar Cells*, Vol. 79, No. 4, pp. 527 – 537, 2003.
- [Gott 04] R. Gottschalg, T. R. Betts, D. G. Infield, and M. J. Kearney. “On the importance of considering the incident spectrum when measuring the outdoor performance of amorphous silicon photovoltaic devices”. *Measurement Science and Technology*, Vol. 15, No. 2, p. 460, 2004.
- [Gott 05] R. Gottschalg, T. Betts, D. Infield, and M. Kearney. “The effect of spectral variations on the performance parameters of single and double junction amorphous silicon

- solar cells”. *Solar Energy Materials and Solar Cells*, Vol. 85, No. 3, pp. 415 – 428, 2005.
- [Gree 03] M. A. Green. “General temperature dependence of solar cell performance and implications for device modelling”. *Progress in Photovoltaics: Research and Applications*, Vol. 11, No. 5, pp. 333–340, 2003.
- [Gree 82] M. Green, K. Emery, and A. Blakers. “Silicon solar cells with reduced temperature sensitivity”. *Electronics Letters*, Vol. 18, No. 2, pp. 97–98, January 1982.
- [Gree 92] M. Green. *Solar Cells; Operating Principles, Technology and Practice*. Bridge Printery, university of new south wales Ed., 1992.
- [Grun 09] P. Grunow, A. Preiss, S. Koch, and S. Krauter. “Yield and Spectral Effects of a-Si Modules”. In: *24th European Photovoltaic Solar Energy Conference, 21-25 September 2009, Hamburg, Germany, 2009*.
- [Guey 07] C. A. Gueymard. “Spectral effects on latitude-tilt and vertical PV modules as affected by latitude, air mass, and climate”. In: D. R. Myers, Ed., *San Diego, CA, USA*, p. 66520C, SPIE, 2007.
- [Hann 14] S. Hänni. *Microcrystalline Silicon for High-Efficiency Thin-Film Photovoltaic Devices*. PhD thesis, EPFL, Lausanne, 2014.
- [Hann 15] S. Hänni, M. Boccard, G. Bugnon, M. Despeisse, J.-W. Schüttauf, F.-J. Haug, F. Meillaud, and C. Ballif. “Microcrystalline silicon solar cells with passivated interfaces for high open-circuit voltage”. *physica status solidi (a)*, Vol. 212, No. 4, pp. 840–845, 2015.
- [Hass 07] B. H. Hassanzadeh, A. de Keizer, and W. v. S. N.H. Reich. “The effect of a varying solar spectrum on the energy performance of solar cells”. In: *22nd European Photovoltaic Solar Energy Conference, milan, 2007*.
- [Hata 92] N. Hata and S. Wagner. “A comprehensive defect model for amorphous silicon”. *J. Appl. Phys.*, Vol. 72, No. 7, pp. 2857–2872, 1992.
- [Hubi 92] J. Hubin, A. V. Shah, and E. Sauvain. “Effects of dangling bonds on the recombination function in amorphous semiconductors”. *Philosophical Magazine Letters*, Vol. 66, No. 3, pp. 115–125, 1992.
- [Huld 10] T. Huld, R. Gottschalg, H. G. Beyer, and M. Topic. “Mapping the performance of PV modules, effects of module type and data averaging”. *Solar Energy*, Vol. 84, No. 2, pp. 324 – 338, 2010.
- [IEC 08a] “IEC 60904-3: Photovoltaic devices - Part 3: Measurement principles for terrestrial photovoltaic (PV) solar devices with reference spectral irradiance data”. 2008.

-
- [IEC 08b] “IEC 60904-9: Photovoltaic devices - Part 9: Solar simulator performance requirements”. IEC, 2008.
- [Ishi 11] T. Ishii, K. Otani, T. Takashima, and Y. Xue. “Solar spectral influence on the performance of photovoltaic (PV) modules under fine weather and cloudy weather conditions”. *Progress in Photovoltaics: Research and Applications*, Vol. n/a, pp. n/a–n/a, 2011.
- [Jank 13] M. Jankovec and M. Topic. “Intercomparison of Temperature Sensors for Outdoor Monitoring of Photovoltaic Modules”. *Journal of Solar Energy Engineering*, Vol. 135, p. 3, April 2013.
- [Jord 13] D. C. Jordan and S. R. Kurtz. “Photovoltaic Degradation Rates-an Analytical Review”. *Progress in Photovoltaics: Research and Applications*, Vol. 21, No. 1, pp. 12–29, 2013.
- [Kame 96] M. Kameda, S. Sakai, M. Isomura, K. Sayama, Y. Hishikawa, S. Matsumi, H. Haku, K. Wakisaka, M. Tanaka, S. Kiyama, S. Tsuda, and S. Nakano. “Efficiency evaluation of a-Si and c-Si solar cells for outdoor use”. In: *Photovoltaic Specialists Conference, 1996., Conference Record of the Twenty Fifth IEEE*, pp. 1049–1052, May 1996.
- [Kemmm 14] A. Kemmler, A. Piegsa, A. Ley, P. W. M. Keller, M. Jakob, and G. Catenazzi. “Analyse des schweizerischen Energieverbrauchs 2000 - 2013 nach Verwendungszwecken”. Tech. Rep., BFE, 2014.
- [KfW 15] “KfW-Programm Erneuerbare Energien "Speicher"”. 2015. <https://www.kfw.de/>.
- [King 04] D. L. King. “Photovoltaic array performance model”. Tech. Rep., Sandia National Laboratories, Albuquerque, NM, 2004.
- [King 97a] D. L. King, J. A. Kratochvil, and W. E. Boyson. “Measuring Solar Spectral and Angle-of-Incidence Effects on Photovoltaic Modules and Solar Irradiance Sensors”. In: *26th IEEE Photovoltaic Specialists Conference, September 29- October 3, 1997, Anaheim, California, 1997*.
- [King 97b] D. King, J. Kratochvil, and W. Boyson. “Temperature coefficients for PV modules and arrays: measurement methods, difficulties, and results”. In: *Photovoltaic Specialists Conference, 1997., Conference Record of the Twenty-Sixth IEEE*, pp. 1183–1186, sep-3 oct 1997.
- [Kipp] “Kipp and Zonen”. <http://www.kippzonen.com> accessed on 23.10.2015.
- [Kond 97] M. Kondo, H. Nishio, S. Kurata, K. Hayashi, A. Takenaka, A. Ishikawa, K. Nishimura, H. Yamagishi, and Y. Tawada. “Effective conversion efficiency enhancement of amorphous silicon modules by operation temperature elevation”. *Solar Energy Materials and Solar Cells*, Vol. 49, No. 1?4, pp. 1 – 6, 1997.

- [Kris 09] P. Krishnan, J. Schüttauf, C. van der Werf, B. H. Hassanzadeh, W. van Sark, and R. Schropp. "Response to simulated typical daily outdoor irradiation conditions of thin-film silicon-based triple-band-gap, triple-junction solar cells". *Solar Energy Materials and Solar Cells*, Vol. 93, No. 6-7, pp. 691 – 697, 2009.
- [Kyma 09] E. Kymakis, S. Kalykakis, and T. M. Papazoglou. "Performance analysis of a grid connected photovoltaic park on the island of Crete". *Energy Conversion and Management*, Vol. 50, No. 3, pp. 433 – 438, 2009.
- [Lo 10] A. Lo, M. Despeisse, R. Theron, and C. Ballif. "An hybrid LED/halogen large-area solar simulator allowing variable spectrum and variable illumination pulse shape". In: *25th EU PVSEC Proc*, 2010.
- [Lope 14] P. Loper, B. Niesen, S.-J. Moon, S. Martin De Nicolas, J. Holovsky, Z. Remes, M. Ledinsky, F.-J. Haug, J.-H. Yum, S. De Wolf, and C. Ballif. "Organic 2013;Inorganic Halide Perovskites: Perspectives for Silicon-Based Tandem Solar Cells". *Photovoltaics, IEEE Journal of*, Vol. 4, No. 6, pp. 1545–1551, Nov 2014.
- [Mail 15] J. P. Mailoa, C. D. Bailie, E. C. Johlin, E. T. Hoke, A. J. Akey, W. H. Nguyen, M. D. McGehee, and T. Buonassisi. "A 2-terminal perovskite/silicon multijunction solar cell enabled by a silicon tunnel junction". *Applied Physics Letters*, Vol. 106, No. 12, pp. –, 2015.
- [Masu 14] K. Masuko, M. Shigematsu, T. Hashiguchi, D. Fujishima, M. Kai, N. Yoshimura, T. Yamaguchi, Y. Ichihashi, T. Mishima, N. Matsubara, T. Yamanishi, T. Takahama, M. Taguchi, E. Maruyama, and S. Okamoto. "Achievement of More Than 25Crystalline Silicon Heterojunction Solar Cell". *Photovoltaics, IEEE Journal of*, Vol. 4, No. 6, pp. 1433–1435, Nov 2014.
- [Mats 84] H. Matsuura, T. Okuno, H. Okushi, and K. Tanaka. "Electrical properties of nanoamorphous crystalline silicon heterojunctions". *Journal of Applied Physics*, Vol. 55, No. 4, pp. 1012–1019, 1984.
- [Mazh 11] E. Mazhari, J. Zhao, N. Celik, S. Lee, Y.-J. Son, and L. Head. "Hybrid simulation and optimization-based design and operation of integrated photovoltaic generation, storage units, and grid". *Simulation Modelling Practice and Theory*, Vol. 19, No. 1, pp. 463 – 481, 2011. Modeling and Performance Analysis of Networking and Collaborative Systems.
- [Meie 94] J. Meier, S. Dubail, R. Flueckiger, D. Fischer, H. Keppner, and A. Shah. "Intrinsic Microcrystalline silicon - a promising new thin film solar cell Material". In: *First world conference on Photovoltaic Energy conversion*, 1994.
- [Meie 98] J. Meier, H. Keppner, S. Dubail, Y. Ziegler, L. Freitknecht, P. Torres, C. Hof, U. Kroll, D. Fisher, J. Cuperus, J. A. Selvan, and A. Shah. "Microcrystalline and Micromorph Thin-Film Silicon Solar cells". In: *2nd World conference on Photovoltaic Energy Conversion Vienna*, 1998.

-
- [Mels 14] J. Melskens, M. Schouten, A. Mannheim, A. Vullers, Y. Mohammadian, S. Eijt, H. Schut, T. Matsui, M. Zeman, and A. Smets. “The Nature and the Kinetics of Light-Induced Defect Creation in Hydrogenated Amorphous Silicon Films and Solar Cells”. *Photovoltaics, IEEE Journal of*, Vol. 4, No. 6, pp. 1331–1336, Nov 2014.
- [Mels 15] J. Melskens, A. Schnegg, A. Baldansuren, K. Lips, M. P. Plokker, S. W. H. Eijt, H. Schut, M. Fischer, M. Zeman, and A. H. M. Smets. “Structural and electrical properties of metastable defects in hydrogenated amorphous silicon”. *Phys. Rev. B*, Vol. 91, p. 245207, Jun 2015.
- [Merm 10] A. Mermoud and T. Lejeune. “Performance Assessment of a Simulation Model for PV Modules of Any Available Technology”. In: *25th European Photovoltaic Solar Energy Conference and Exhibition / 5th World Conference on Photovoltaic Energy Conversion, 6-10 September 2010, Valencia, Spain, 2010*.
- [Mert 98a] J. Merten and J. Andreu. “Clear separation of seasonal effects on the performance of amorphous silicon solar modules by outdoor I/V-measurements”. *Solar Energy Materials and Solar Cells*, Vol. 52, No. 1?2, pp. 11 – 25, 1998.
- [Mert 98b] J. Merten, J. Asensi, C. Voz, A. Shah, R. Platz, and J. Andreu. “Improved equivalent circuit and analytical model for amorphous silicon solar cells and modules”. *IEEE Transactions on Electron Devices*, Vol. 45, No. 2, pp. 423–429, 1998. cited By (since 1996) 61.
- [Mess 13] “Message relatif au premier paquet de mesures de la Stratégie énergétique 2050 et à l’initiative populaire fédérale Pour la sortie programmée de l’énergie nucléaire”. September 2013. Conseil Fédérale Suisse, <https://www.admin.ch/opc/fr/federal-gazette/2013/6771.pdf>.
- [Metz 15] A. Metz, G. Demenik, A. Richter, T. Vlasenko, I. Buchovskaya, M. Zwegers, H. Xu, A. Luan, R. Wertz, A. Stassen, H. Forstner, W. Jooss, J. Haase, E. Dornberger, S. Raithel, J. Szlufcik, G. Coletti, Sinke, Wim, P. Wyers, J. Zhu, S. Zhang, Guo, Aaron, L. Maosheng, J. Xia, Y. Zhang, J. Dong, C. Jian, S. Li, Y. Jiang, X. Aimin, G. Xing, M. Fischer, P. Engelhard, A. Gerlach, K. Petter, T. Spiess, A. Metteand, M. Mette, K. Wang, L. Chi-Chun, Y. Wan, G. Li, K. C. Lin, K. C. Lin, and S. Julsrud. “International Technology Roadmap for Photovoltaic Results 2014 Rev 1”. Tech. Rep., SEMI and VDMA, 2015.
- [Mish 11] T. Mishima, M. Taguchi, H. Sakata, and E. Maruyama. “Development status of high-efficiency {HIT} solar cells”. *Solar Energy Materials and Solar Cells*, Vol. 95, No. 1, pp. 18 – 21, 2011. 19th International Photovoltaic Science and Engineering Conference and Exhibition (PVSEC-19) Jeju, Korea, 9-13 November 2009.
- [Mont 10] D. F. Montoro, M. Latour, and P. Vanbuggenhout. “IP Performance”. Tech. Rep., Sixth framework Programme, 2010.

- [Mori 05] K. Morigaki, K. Takeda, H. Hikita, and P. Roca I Cabarrocas. “Light-induced defect creation in hydrogenated polymorphous silicon during repeated cycles of illumination and annealing”. *Philosophical Magazine*, Vol. 85, No. 29, pp. 3393–3407, 2005.
- [Muld 10] G. Mulder, F. D. Ridder, and D. Six. “Electricity storage for grid-connected household dwellings with PV panels”. *Solar Energy*, Vol. 84, No. 7, pp. 1284 – 1293, 2010.
- [Myer 09] D. R. Myers. “Terrestrial solar spectral distributions derived from broadband hourly solar radiation data”. *Solar Radiation Measurements and Modeling Applications II*, Vol. 7410, No. 1, p. 74100A, 2009.
- [Myon 06] S. Y. Myong and K. S. Lim. “Modeling of annealing kinetics for hydrogenated-amorphous-silicon-based solar cells using two-component metastable defects”. *Applied Physics Letters*, Vol. 88, No. 24, p. 243510, 2006.
- [Nann 90] S. Nann and C. Riordan. “Solar spectral irradiance under overcast skies [solar cell performance effects]”. In: *Photovoltaic Specialists Conference, 1990., Conference Record of the Twenty First IEEE*, pp. 1110 –1115 vol.2, may 1990.
- [Nann 91] S. Nann and C. Riordan. “Solar spectral irradiance under clear and cloudy skies: measurements and a semiempirical model”. *Journal of Applied Meteorology*, Vol. 30, No. 4, pp. 447–462, 1991. Cited By (since 1996): 46.
- [Neth 05] M. Netherland. “Time data from Netherland”. MTU Netherland, 2005. www.timeuse.org/information/access-data.
- [Niko 08] M. Nikolaeva-Dimitrova, R. P. Kenny, and E. D. Dunlop. “Controlled conditioning of a-Si:H thin film modules for efficiency prediction”. *Thin Solid Films*, Vol. 516, No. 20, pp. 6902 – 6906, 2008. Proceedings on Advanced Materials and Concepts for Photovoltaics EMRS 2007 Conference, Strasbourg, France.
- [Niko 10] M. Nikolaeva-Dimitrova, R. Kenny, E. Dunlop, and M. Pravettoni. “Seasonal variations on energy yield of a-Si, hybrid, and crystalline Si PV modules”. *Progress in Photovoltaics: Research and Applications*, Vol. 18, No. 5, pp. 311–320, 2010. cited By (since 1996) 0.
- [Nipk 13] J. Nipkow. “Typischer Haushalt-Stromverbrauch”. Tech. Rep., BFE, 2013.
- [Nord 03] T. Nordmann and L. Clavadetscher. “Understanding temperature effects on PV system performance”. In: *Photovoltaic Energy Conversion, 2003. Proceedings of 3rd World Conference on*, pp. 2243–2246 Vol.3, May 2003.
- [Nott 10] G. Notton, V. Lazarov, and L. Stoyanov. “Optimal sizing of a grid-connected PV system for various PV module technologies and inclinations, inverter efficiency characteristics and locations”. *Renewable Energy*, Vol. 35, No. 2, pp. 541 – 554, 2010.

-
- [Nuge 14] D. Nugent and B. K. Sovacool. "Assessing the lifecycle greenhouse gas emissions from solar {PV} and wind energy: A critical meta-survey". *Energy Policy*, Vol. 65, pp. 229 – 244, 2014.
- [OFEN 14] OFEN. "Mittwochproduktion 2014". Tech. Rep., OFEN, 2014.
- [OFEN 15] OFEN. "Statistique globale suisse de l'énergie 2014". Report, 2015.
- [Over 89] H. Overhof and P. Thomas. *Electronic Transport in Hydrogenated Amorphous Semiconductors*. Springer Berlin Heidelberg, 1989.
- [Pach 14] R. Pachauri and L. Meyer. "Climate Change 2014: Synthesis Report. Contribution of Working Groups I, II and III to the Fifth Assessment Report of the Intergovernmental Panel on Climate Change". Tech. Rep., IPCC, IPCC, Geneva, Switzerland, 2014. <http://www.ipcc.ch/>.
- [Park 15] G. Parkinson. "Record low solar prices heralds power shift from fossil fuels". Website, January 2015.
- [Park 89] H. R. Park, J. Z. Liu, and S. Wagner. "Saturation of the light-induced defect density in hydrogenated amorphous silicon". *Applied Physics Letters*, Vol. 55, No. 25, pp. 2658–2660, 1989.
- [Paul 10] L. Paull, H. Li, and L. Chang. "A novel domestic electric water heater model for a multi-objective demand side management program". *Electric Power Systems Research*, Vol. 80, No. 12, pp. 1446 – 1451, 2010.
- [Pere 07] J. J. Pérez-López, F. Fabero, and F. Chenlo. "Experimental solar spectral irradiance until 2500nm: results and influence on the PV conversion of different materials". *Progress in Photovoltaics: Research and Applications*, Vol. 15, No. 4, pp. 303–315, 2007.
- [Perr 15] L. Perret, J. Fahrni, N. Wyrsh, Y. Riesen, S. Puddu, S. Weber, and D. P. Barzallo. "FLEXI, Determining the flexibilization potential of the electricity demand - Final report". Tech. Rep., OFEN, 2015.
- [Phil 14] C. Philibert. "Technology Roadmap: Solar photovoltaic energy". Tech. Rep., International Energy Agency, 2014.
- [Pier 15] M. Pierro, F. Bucci, and C. Cornaro. "Impact of light soaking and thermal annealing on amorphous silicon thin film performance". *Progress in Photovoltaics: Research and Applications*, pp. n/a–n/a, 2015. A lire absolutent.
- [Polv 11] D. Polverini, T. Huld, and R. Kenny. "Effects of operating conditions on thin film amorphous and microcrystalline silicon module performance". In: *26th European Photovoltaic Solar Energy Conference and Exhibition*, 2011.

- [Powe 02] M. J. Powell, S. C. Deane, and R. B. Wehrspohn. “Microscopic mechanisms for creation and removal of metastable dangling bonds in hydrogenated amorphous silicon”. *Phys. Rev. B*, Vol. 66, p. 155212, Oct 2002.
- [Pyth 08] M. Python, E. Vallat-Sauvain, J. Bailat, D. Dominé, L. Fesquet, A. Shah, and C. Ballif. “Relation between substrate surface morphology and microcrystalline silicon solar cell performance”. *Journal of Non-Crystalline Solids*, Vol. 354, No. 19, pp. 2258–2262, 2008.
- [Pyth 09a] M. Python, O. Madani, D. Dominé, F. Meillaud, E. Vallat-Sauvain, and C. Ballif. “Influence of the substrate geometrical parameters on microcrystalline silicon growth for thin-film solar cells”. *Solar Energy Materials and Solar Cells*, Vol. 93, No. 10, pp. 1714 – 1720, 2009.
- [Pyth 09b] M. Python. *Microcrystalline silicon solar cells: growth and defects*. PhD thesis, Institut de Microtechnique, Université de Neuchâtel, 2009.
- [Rech 97] B. Rech. *SolarSolarzellen aus amorphen Silizium mit hohem stabilen Wirkungsgrad Zum Einfluss des ϕ -Grenzflaechenbereichs und der intrinsische und der Absorber schicht*. PhD thesis, Forschungszentrum Jülich, 1997.
- [Remu 14] J. Remund, A. Shah, and N. Wyrsh. “Energy transition from nuclear to solar: the case of switzerland”. In: *Conference: 6th World Conference on Photovoltaic Energy Conversion, At Kyoto, Japan*, 2014.
- [Repm 03] T. Repmann, J. Kirchhoff, W. Reetz, F. Birmans, J. Muller, and B. Rech. “Investigations on the current matching of highly efficient tandem solar cells based on amorphous and microcrystalline silicon”. In: *Photovoltaic Energy Conversion, 2003. Proceedings of 3rd World Conference on*, pp. 1843 –1846 Vol.2, may 2003.
- [Ries 13] Y. Riesen, P. Ding, S. Monnier, N. Wyrsh, and C. Ballif. “Peak Shaving Capability Of Household Grid-connected Pv-system With Local Storage: A Case Study”. In: *28th European Photovoltaic Solar Energy Conference*, 2013.
- [Ries 15] Y. Riesen, M. Stuckelberger, F.-J. Haug, C. Ballif, and N. Wyrsh. “Temperature Dependence of Hydrogenated Amorphous Silicon Solar Cell Performances”. *Journal of applied physics* 2015. Submitted.
- [Ries 16a] Y. Riesen, C. Ballif, and N. Wyrsh. “Importance of PV forecast for an optimal management of grid connected PV systems with batteries in the presence of a feed-in limit”. 2016. In preparation.
- [Ries 16b] Y. Riesen, N. G., J. Cattin, F.-J. Haug, C. Ballif, and N. Wyrsh. “Comparison of temperature dependence on performances of silicon based solar Cell.”. 2016. In preparation.

-
- [Ries 16c] Y. Riesen, M. Stuckelberger, N. Wyrsh, and C. Ballif. "Assessment of one-diode model with recombination term for modeling amorphous silicon solar cells long term performance in operating conditions.". 2016. In preparation.
- [Riff 11] Y. Riffonneau, S. Bacha, F. Barruel, and S. Ploix. "Optimal Power Flow Management for Grid Connected PV Systems With Batteries". *Sustainable Energy, IEEE Transactions on*, Vol. 2, No. 3, pp. 309–320, July 2011.
- [Roed 00] B. v. Roedern and J. A. del Cueto. "Model for Staebler-Wronski Degradation Deduced from Long-Term, Controlled Light-Soaking Experiments". *MRS Online Proceedings Library*, Vol. 609, pp. null–null, 2000.
- [Sah 57] C.-T. Sah, R. Noyce, and W. Shockley. "Carrier Generation and Recombination in P-N Junctions and P-N Junction Characteristics". *Proceedings of the IRE*, Vol. 45, No. 9, pp. 1228–1243, Sept 1957.
- [Sai 15] H. Sai, T. Matsui, T. Koida, K. Matsubara, M. Kondo, S. Sugiyama, H. Katayama, Y. Takeuchi, and I. Yoshid. "Triple-junction thin-film silicon solar cell fabricated on periodically textured substrate with a stabilized efficiency of 13.6%". *Applied Physics Letters*, Vol. 106, No. 21, pp. –, 2015.
- [Sark 12] W. G. J. H. M. van Sark, L. Korte, and F. Roca. *Physics and Technology of Amorphous-Crystalline Heterostructure Silicon Solar Cells*. Springer Berlin Heidelberg, 2012.
- [Schm 10] A. Schmiegel, K. Koch, A. Meissner, P. Knaup, C. Jehoulet, H. Schuh, M. Landau, M. Braun, K. Büdenbender, R. Geipel, C. Vachette, D. Sauer, D. Magnor, and J.-C. Marcel. "The Sol-Ion System, an Integrated PV-System with Lithium Ion Batteries System Performance". In: *25th European Photovoltaic Solar Energy Conference and Exhibition*, 2010.
- [Schu 11] T. F. Schulze, L. Korte, F. Ruske, and B. Rech. "Band lineup in amorphous/crystalline silicon heterojunctions and the impact of hydrogen microstructure and topological disorder". *Phys. Rev. B*, Vol. 83, p. 165314, Apr 2011. Barrier height.
- [Schu 14] J.-W. Schüttauf, G. Bugnon, M. Stuckelberger, S. Hänni, M. Boccard, M. Despeisse, F.-J. Haug, F. Meillaud, and C. Ballif. "Thin-Film Silicon Triple-Junction Solar Cells on Highly Transparent Front Electrodes With Stabilized Efficiencies up to 12.8%". *IEEE Journal of Photovoltaics*, Vol. 4, No. 3, pp. 757–762, 2014.
- [Schu 15] J.-W. Schüttauf, B. Niesen, L. Loefgren, M. Bonnet-Eymard, M. Stuckelberger, S. Hänni, M. Boccard, G. Bugnon, M. Despeisse, F.-J. Haug, F. Meillaud, and C. Ballif. "Amorphous silicon germanium for triple and quadruple junction thin-film silicon based solar cells". *Solar Energy Materials and Solar Cells*, Vol. 133, No. 0, pp. 163–169, 2015.
- [Shah 09] A. Shah. *Thin-Film Silicon Solar Cells. Engineering Sciences: Micro- And Nanotechnology*, Taylor & Francis, 2009.

- [Shim 04] T. Shimizu. “Staebler-Wronski Effect in Hydrogenated Amorphous Silicon and Related Alloy Films”. *Japanese Journal of Applied Physics*, Vol. 43, No. 6A, pp. 3257–3268, 2004.
- [Shim 05] M. Shima, M. Isomura, K. ichiro Wakisaka, K. Murata, and M. Tanaka. “The influence of operation temperature on the output properties of amorphous silicon-related solar cells”. *Solar Energy Materials and Solar Cells*, Vol. 85, No. 2, pp. 167 – 175, 2005.
- [Sing 12] P. Singh and N. Ravindra. “Temperature dependence of solar cell performance?an analysis”. *Solar Energy Materials and Solar Cells*, Vol. 101, No. 0, pp. 36 – 45, 2012.
- [Skoc 11] A. Skoczek, A. Virtuani, T. Cebecauer, and D. Chianese. “Energy Yield Prediction of Amorphous Silicon PV Modules Using Full Time Data Series of Irradiance and Temperature for Different Geographical Locations”. In: *26th European Photovoltaic Solar Energy Conference and Exhibition*, 2011.
- [Skop 09] E. Skoplaki and J. Palyvos. “On the temperature dependence of photovoltaic module electrical performance: A review of efficiency/power correlations”. *Solar Energy*, Vol. 83, No. 5, pp. 614 – 624, 2009.
- [Smet 10] A. H. Smets, C. R. Wronski, M. Zeman, and M. van de Sanden. “The Staebler-Wronski Effect: New Physical Approaches and Insights as a Route to Reveal its Origin”. *MRS Online Proceedings Library*, Vol. 1245, pp. null–null, 2010.
- [Smet 12] A. Smets, M. Wank, B. Vet, M. Fischer, R. van Swaaij, M. Zeman, D. Bobela, C. Wronski, and R. van de Sanden. “The Relation Between the Bandgap and the Anisotropic Nature of Hydrogenated Amorphous Silicon”. *Photovoltaics, IEEE Journal of*, Vol. 2, No. 2, pp. 94 –98, april 2012.
- [Smit 12] D. Smith, P. Cousins, A. Masad, A. Waldhauer, S. Westerberg, M. Johnson, X. Tu, T. Dennis, G. Harley, G. Solomon, S. Rim, M. Shepherd, S. Harrington, M. Defensor, A. Leygo, P. Tomada, J. Wu, T. Pass, L. Ann, L. Smith, N. Bergstrom, C. Nicdao, P. Tipones, and D. Vicente. “Generation III high efficiency lower cost technology: Transition to full scale manufacturing”. In: *Photovoltaic Specialists Conference (PVSC), 2012 38th IEEE*, pp. 001594–001597, June 2012.
- [Smit 85] Z. E. Smith, S. Wagner, and B. W. Faughnan. “Carrier lifetime model for the optical degradation of amorphous silicon solar cells”. *Applied Physics Letters*, Vol. 46, No. 11, pp. 1078–1080, 1985.
- [Sola] “Solaronix”. <http://www.solaronix.ch/> accessed 23.10.2015.
- [Srip 07] K. Sriprapha, I. A. Yunaz, S. Hiza, K. H. Ahn, S. Y. Myong, A. Yamada, and M. Kona-gai. “Temperature Dependence of Silicon-based Thin Film Solar Cells on Their Intrinsic Absorber”. *MRS Online Proceedings Library*, Vol. 989, pp. null–null, 2007.

-
- [Srip 08] K. Sriprapha, S. Inthisang, S. Y. Myong, S. Miyajima, A. Yamada, P. Sichanugrist, and M. Konagai. "Development of amorphous silicon-based thin-film solar cells with low-temperature coefficient". *Photovoltaic Cell and Module Technologies II*, Vol. 7045, No. 1, p. 70450C, 2008.
- [Srip 11] K. Sriprapha, C. Piromjit, A. Limmanee, and J. Sritharathikhun. "Development of thin film amorphous silicon oxide/microcrystalline silicon double-junction solar cells and their temperature dependence". *Solar Energy Materials and Solar Cells*, Vol. 95, No. 1, pp. 115 – 118, 2011. <ce:title>19th International Photovoltaic Science and Engineering Conference and Exhibition (PVSEC-19) Jeju, Korea, 9-13 November 2009</ce:title>.
- [Stae 77] D. L. Staebler and C. R. Wronski. "Reversible conductivity changes in discharge-produced amorphous Si". *Applied Physics Letters*, Vol. 31, pp. 292–294, 1977.
- [Ste1 15] J. Stein, D. Riley, and C. W. Hansen. "PV LIB Toolbox". Sandia National Laboratories, 2015. Website: <http://pvpmc.org>.
- [Stie 96] H. Stiebig, T. Eickhoffa, J. Zimmera, C. Benekinga, and H. Wagnera. "Measured and Simulated Temperature Dependence of A-Si:H Solar Cell Parameters". In: *MRS Spring Meeting*, 1996.
- [Stra 10] P. Stradins. "Staebler-Wronski defects: Creation efficiency, stability, and effect on a-Si:H solar cell degradation". In: *Photovoltaic Specialists Conference (PVSC), 2010 35th IEEE*, pp. 000142 –000145, June 2010.
- [Stra 11] P. Stradins, D. Bobela, and H. Branz. "Reduced light-induced degradation in a-Si:H: The role of network nanostructure". In: *Photovoltaic Specialists Conference (PVSC), 2011 37th IEEE*, pp. 003343 –003347, June 2011.
- [Stre 82] R. A. Street. "Trapping parameters of dangling bonds in hydrogenated amorphous silicon". *Applied Physics Letters*, Vol. 41, No. 11, pp. 1060–1062, 1982.
- [Stre 91] R. Street. *Hydrogenated amorphous silicon*. Cambridge Solid State Science Series, 1991.
- [Stru 71] J. Strutt. "On the light from the sky, its polarization and colour". *Philosophical Magazine*, Vol. 41, pp. 107–120, 1871.
- [Stuc 10] M. Stükelberger, A. Shah, J. Krc, M. Despeisse, F. Meillaud, and C. Ballif. "Internal electric field and fill factor of amorphous silicon solar cells". In: *Photovoltaic Specialists Conference (PVSC), 2010 35th IEEE*, pp. 001569–001574, IEEE, 2010.
- [Stuc 12] M. Stuckelberger, Y. Riesen, B. Perruche, M. Despeisse, N. Wyrsh, and C. Ballif. "Charge collection in amorphous silicon solar cells: Cell analysis and simulation of high-efficiency pin devices". *Journal of Non-Crystalline Solids*, Vol. 358, No. 17, pp. 2187–2189, 2012.

- [Stuc 13] M. Stuckelberger, M. Despeisse, G. Bugnon, J.-W. Schüttauf, F.-J. Haug, and C. Ballif. “Comparison of amorphous silicon absorber materials: Light-induced degradation and solar cell efficiency”. *Journal of Applied Physics*, Vol. 114, No. 15, pp. –, 2013.
- [Stuc 14a] M. Stuckelberger, B. Perruche, M. Bonnet-Eymard, Y. Riesen, M. Despeisse, F.-J. Haug, and C. Ballif. “Class AAA LED-Based Solar Simulator for Steady-State Measurements and Light Soaking”. *Photovoltaics, IEEE Journal of*, Vol. 4, No. 5, pp. 1282–1287, Sept 2014.
- [Stuc 14b] M. Stuckelberger, Y. Riesen, M. Despeisse, J.-W. Schüttauf, F.-J. Haug, and C. Ballif. “Light-induced Voc increase and decrease in high-efficiency amorphous silicon solar cells”. *Journal of Applied Physics*, Vol. 116, No. 9, pp. –, 2014.
- [Stuc 14c] M. Stuckelberger. *Hydrogenated amorphous silicon*. PhD thesis, EPFL, Lausanne, 2014.
- [Stuc 14d] M. Stuckelberger, A. Billet, Y. Riesen, M. Boccard, M. Despeisse, J.-W. Schüttauf, F.-J. Haug, and C. Ballif. “Comparison of amorphous silicon absorber materials: Kinetics of light-induced degradation”. *Progress in Photovoltaics: Research and Applications*, 2014.
- [Stut 85] M. Stutzmann, W. B. Jackson, and C. C. Tsai. “Light-induced metastable defects in hydrogenated amorphous silicon: A systematic study”. *Phys. Rev. B*, Vol. 32, pp. 23–47, Jul 1985.
- [Stut 86] M. Stutzmann, W. B. Jackson, and C. C. Tsai. “Annealing of metastable defects in hydrogenated amorphous silicon”. *Phys. Rev. B*, Vol. 34, pp. 63–72, Jul 1986.
- [Stut 99] U. Stutenbaeumer and B. Mesfin. “Equivalent model of monocrystalline, polycrystalline and amorphous silicon solar cells”. *Renewable Energy*, Vol. 18, No. 4, pp. 501 – 512, 1999.
- [Sutt 10] J. Sutterlueti, R. Kravets, M. Keller, H. Knauss, I. Sinicco, and A. Huegli. “Energy Yield Optimization and Seasonal Behavior of Micromorph Thin Film Modules”. In: *25thEUPVSEC2010*, 2010.
- [Swis 15] Swissgrid. “Energieuebersicht Schweiz 2014”. 2015. <https://www.swissgrid.ch/swissgrid/de/home/reliability/griddata/generation.html> [accessed 18.08.2015].
- [Tagu 14] M. Taguchi, A. Yano, S. Tohoda, K. Matsuyama, Y. Nakamura, T. Nishiwaki, K. Fujita, and E. Maruyama. “24.7% Record Efficiency HIT Solar Cell on Thin Silicon Wafer”. *IEEE Journal of Photovoltaics*, Vol. 4, No. 1, pp. 96–99, 2014.
- [Tana 93] M. Tanaka, M. Taguchi, T. Takahama, T. Sawada, S. Kuroda, T. Matsuyama, S. Tsuda, A. Takeoka, S. Nakano, H. Hanafusa, and Y. Kuwano. “Development of a new heterojunction structure (ACJ -HIT) and its application to polycrystalline silicon

-
- solar cells”. *Progress in Photovoltaics: Research and Applications*, Vol. 1, No. 2, pp. 85–92, 1993.
- [Tasa 88] H. Tasaki, W. Y. Kim, M. Hallerdt, M. Konagai, and K. Takahashi. “Computer Simulation Model of the Effects of Interface States on Higher Performance Amorphous Silicon Solar Cells”. *Journal of Applied Physics*, Vol. 63, No. 2, pp. 550–560, 1988.
- [Tayl 72] G. Taylor and J. Simmons. “Basic equations for statistics, recombination processes, and photoconductivity in amorphous insulators and semiconductors”. *Journal of Non-Crystalline Solids*, Vol. 8-10, pp. 940–946, jun 1972.
- [Thia 09] Y. Thiaux, L. Schmerber, J. Seigneurbieux, B. Multon, and H. B. Ahmed. “Comparison between Lead-Acid and Li-Ion Accumulators in Stand-Alone Photovoltaic System Using the Gross Energy Requirement Criterion”. In: *24th European Photovoltaic Solar Energy Conference, 21-25 September 2009, Hamburg, Germany, 2009*.
- [Tied 84] T. Tiedje, E. Yablonovitch, G. Cody, and B. Brooks. “Limiting efficiency of silicon solar cells”. *Electron Devices, IEEE Transactions on*, Vol. 31, No. 5, pp. 711–716, May 1984.
- [Todo 15] T. Todorov, T. Gershon, O. Gunawan, Y. S. Lee, C. Sturdevant, L.-Y. Chang, and S. Guha. “Monolithic Perovskite-CIGS Tandem Solar Cells via In Situ Band Gap Engineering”. *Advanced Energy Materials*, pp. n/a–n/a, 2015.
- [Torr 14] J. Torriti. “A review of time use models of residential electricity demand”. *Renewable and Sustainable Energy Reviews*, Vol. 37, pp. 265 – 272, 2014.
- [Trac] “Tracebase”. Online, accessed 28.08.2015. <https://www.tracebase.org/>.
- [Tsao 06] J. Tsao, N. Lewis, and G. Crabtree. “Solar FAQs”. web, 2006. <http://www.sandia.gov/jytsao/Solar>
- [Umla 12] A. Umland, M. Rothert, A.-S. Bukvic-Schäfer, M. Walter, J. Laschinski, and F. Kever. “Local Energy Storage ? The Next Level of PV Grid Integration”. In: *27th European Photovoltaic Solar Energy Conference and Exhibition, 2012*.
- [Vall 00] E. Vallat-Sauvain, U. Kroll, J. Meier, A. Shah, and J. Pohl. “Evolution of the microstructure in microcrystalline silicon prepared by very high frequency glow-discharge using hydrogen dilution”. *Journal of Applied Physics*, Vol. 87, No. 6, pp. 3137–3142, 2000.
- [Verh 10] C. Verhelst, D. Axehill, C. N. Jones, and L. Helsen. “Impact of the cost function in the optimal control formulation for an air-to-water heat pump system”. In: *8th International Conference on System Simulation in Buildings, Liege, December 2010*.

- [Virt 10] A. Virtuani, D. Pavanello, and G. Friesen. “Overview of Temperature Coefficients of Different Thin Film Photovoltaic Technologies”. In: *25 EU PVSEC - September 2010, Valencia*, 2010.
- [Virt 12] A. Virtuani and L. Fanni. “Seasonal power fluctuations of amorphous silicon thin-film solar modules: distinguishing between different contributions”. *Progress in photovoltaics: research and applications*, Vol. –, pp. 1–10, 2012.
- [Virt 13] A. Virtuani, D. Strepparava, and G-Friesen. “A Simple Approach to Model the Performance of Amorphous Silicon PV Module in Operations”. In: *28th European Photovoltaic Solar Energy Conference and Exhibition*, 2013.
- [Virt 15] A. Virtuani, A. Skoczek, and D. Strepparava. “Modeling The Performance Of Amorphous Silicon Photovoltaic Modules For Different Geographical Locations In North-America”. In: *42 ieee-pvsc.*, 2015.
- [Vosw 13] S. Voswinckel, V. Wesselak, and B. Lustermann. “Behaviour of amorphous silicon solar modules: A parameter study”. *Solar Energy*, Vol. 92, No. 0, pp. 206 – 213, 2013.
- [Wall 95] C. G. Van de Walle and L. H. Yang. “Band discontinuities at heterojunctions between crystalline and amorphous silicon”. *Journal of Vacuum Science & Technology B*, Vol. 13, No. 4, pp. 1635–1638, 1995.
- [Weni 14] J. Weniger, J. Bergner, T. Tjaden, and V. Quaschnig. “Bedeutung von prognosebasierten Betriebsstrategien für die Netzintegration von PV-Speichersystemen”. In: *29. Symposium Photovoltaische Solarenergie, Kloster Banz, Bad Staffelstein*, 2014.
- [Wild 13] M. M. de Wild-Scholten. “Energy payback time and carbon footprint of commercial photovoltaic systems”. *Solar Energy Materials and Solar Cells*, Vol. 119, pp. 296 – 305, 2013. Thin-film Photovoltaic Solar Cells.
- [Will 03] S. Williams, T. Betts, T.Helf, R. Gottschalg, G. Beyer, and D. Infield. “Modelling long-term module performanc based on realistic reporting conditions with consideration to spectral effects”. In: *3rd Conference in Photovoltaic Energy Conversion, Osaka, Japan*, 2003.
- [Wolf 77] M. Wolf, G. Noel, and R. Stirn. “Investigation of the double exponential in the current Voltage characteristics of silicon solar cells”. *Electron Devices, IEEE Transactions on*, Vol. 24, No. 4, pp. 419 – 428, apr 1977.
- [Wron 02] C. R. Wronski, J. M. Pearce, R. J. Koval, X. Niu, A. S. Ferlauto, J. Koh, and R. W. Collins. “Light Induced Defect Creation Kinetics in Thin Film Protocrystalline Silicon Materials and Their Solar Cells”. *MRS Online Proceedings Library*, Vol. 715, pp. null–null, 2002.

-
- [Wurf 15] U. Wurfel, A. Cuevas, and P. Wurfel. "Charge Carrier Separation in Solar Cells". *Photovoltaics, IEEE Journal of*, Vol. 5, No. 1, pp. 461–469, Jan 2015.
- [Wyr 11] N. Wyrch, A. Franco, Y. Riesen, M. Despeisse, S. Dunand, F. Powolny, P. Jarron, and C. Ballif. "Amorphous silicon based particle detectors". In: *MRS Proceedings*, pp. mrss11–1321–a13–06, Cambridge Univ Press, 2011.
- [Wyr 13a] N. Wyrch, Y. Riesen, A. Franco, S. Dunand, H. Kind, S. Schneider, and C. Ballif. "Amorphous silicon based betavoltaic devices". *MRS Proceedings*, Vol. 1536, pp. mrss13–1536, 2013.
- [Wyr 13b] N. Wyrch, Y. Riesen, and C. Ballif. "Effect of the Fluctuations of PV Production and Electricity Demand on the PV Electricity Self-Consumption". In: *Proceedings of the 28th European Photovoltaic Solar Energy Conference and Exhibition*, p. 4322 - 4324, 2013.
- [Wyr 15a] N. Wyrch, Y. Riesen, and R. Tschui. "Flexibilisation de la consommation électrique des ménages". *Bulletin Revue spécialisée des associations electro suisse et AES*, 2015.
- [Wyr 15b] N. Wyrch, Y. Riesen, R. Tschui, C. Boillat, and C. Ballif. "Demand side management for enhanced integration of photovoltaics into grid". In: *31th European Photovoltaic Solar Energy Conference, Hamburg*, 2015.
- [Yama 99] K. Yamamoto, M. Yoshimi, Y. Tawada, Y. Okamoto, A. Nakajima, and S. Igari. "Thin-film poly-Si solar cells on glass substrate fabricated at low temperature". *Applied Physics A: Materials Science & Processing*, Vol. 69, pp. 179–185, 1999. 10.1007/s003390050988.
- [Yang 93] L. Yang and L. Chen. "'Fast' and 'slow' metastable defects in hydrogenated amorphous silicon". *Applied Physics Letters*, Vol. 63, No. 3, pp. 400–402, 1993.
- [Yue 08] G. Yue, B. Yan, C. Teplin, J. Yang, and S. Guha. "Optimization and characterization of i/p buffer layer in hydrogenated nanocrystalline silicon solar cells". *Journal of Non-Crystalline Solids*, Vol. 354, pp. 2440 – 2444, 2008. Amorphous and Nanocrystalline Semiconductors Proceedings of the 22nd International Conference on Amorphous and Nanocrystalline Semiconductors - Science and Technology 22nd International Conference on Amorphous and Nanocrystalline Semiconductors - Science and Technology Reference thpse.
- [Yuna 07] I. A. Yunaz, K. Sriprapha, S. Hiza, A. Yamada, and M. Konagai. "Effects of Temperature and Spectral Irradiance on Performance of Silicon-Based Thin Film Multijunction Solar Cells". *Japanese Journal of Applied Physics*, Vol. 46, No. 4A, pp. 1398–1403, 2007.
- [Zema 97] M. Zeman, J. Willemen, L. Vosteen, G. Tao, and J. Metselaar. "Computer modelling of current matching in a-Si : H/a-Si : H tandem solar cells on textured {TCO} substrates". *Solar Energy Materials and Solar Cells*, Vol. 46, No. 2, pp. 81 – 99, 1997.

- [Zhu 15] J. Zhu, M. Bliss, T. R. Betts, and R. Gottschalg. “Towards modelling realistic ageing rates of amorphous silicon devices in operational environment”. *Japanese Journal of Applied Physics*, Vol. 54, No. 8S1, p. 08KG03, 2015.

Acknowledgment/Remerciements

Cette thèse n'aurait pas été possible ni ces quatre années de travail si exceptionnelles sans le soutien de nombreuses personnes. Ainsi, bien que je vais oublier quelques personnes auxquelles je demande d'ores et déjà de bien vouloir m'excuser, j'aimerais particulièrement remercier :

- Mes directeurs de thèse : Prof. Christophe Ballif de m'avoir donné l'opportunité d'accomplir ce travail dans son laboratoire à la pointe de la recherche photovoltaïque, au sein d'une équipe motivée et compétente. Son enthousiasme et son engagement pour le photovoltaïque et une production énergétique renouvelable sont une source de motivation et d'inspiration. Nicolas Wyrsh, pour sa confiance, sa disponibilité et son soutien constant. Je lui suis profondément reconnaissant de m'avoir partagé ses connaissances et d'avoir répondu à mes nombreuses questions tout comme de m'avoir généreusement soutenu pendant l'écriture de ma thèse.
- Les membres du jury de thèse : Prof. P. Mural, Prof. R. Gottschalg et Prof. M. K. Nazeerudin pour les discussions constructives et de s'être déplacé jusqu'à Neuchâtel. Je voudrais aussi remercier particulièrement Dr. A. Virtuani pour ses nombreuses remarques et corrections qui ont permis d'améliorer significativement ce manuscrit.
- EOS Holding, OFEN (dans le cadre du projet Flexi) et la CTI (dans le cadre du projet SCCER-Furies) pour leur soutien financier.
- Les membres du PV-LAB et PV-center grâce auxquels j'ai pu apprendre énormément tant au niveau scientifique que humain. Ils m'ont permis de passer des moments agréables au labo (mais aussi en dehors) dans une excellente ambiance de travail : Adrian, Aïcha, Alo, Ana, Andrea F. (ta motivation constante, tes encouragements et discussions étaient des ingrédients précieux de la vie au labo), Andrea T., Antoine, Antonin, Bénédic (qui m'a fait découvrir des montagnes plus hautes que le Chasseral), Benoît, Bertrand, Björn, Céline, Christian, Corsin, Didier, Eleonora, Esteban, Etienne, Fabien, Fanny, Federico, Franz (j'ai beaucoup appris au travers de nos discussions sur les propriétés physiques du silicium amorphe, mais aussi concernant les bons plans en montagne), Gian Luca, Gizem, Greg B., Jacques, Jan, Jan-Willem, Jason, Jean, Joël, Johannes (tes nombreux coups de main et informations sur les cellules SHJ étaient précieux, les balades en VTT

ou à pieds également), Jonas (merci pour les nombreux services rendu et les randonnées en montagne), Jonathan, Josua, Julien, Karin, Lara, Laura, Linus, Loris, Mathieu B., Mathieu C., Matthieu D., Mario, Max (c'était un plaisir de bidouiller ces fameux setups IV avec toi), Michael (qui m'a beaucoup appris), Monica, Nicolas, Niels, Peter, Petra, Philippe L., Philippe W., Pierre-Jean, Pricille, Quentin (ton soutien et tes tuyaux pour bien finir ma thèse m'ont beaucoup aidé), Randy (thanks for the last corrections), Rémi, Saba, Ségolène, Silvia, Simon (le co-tramelot, merci pour les astuces de doctorant, cellules uc-Si et nombreuses discussions), Stefaan, Sylvain, Valentin, Vincenzo, Yann, Zachary...

- L'équipe technique de m'avoir initié en électronique et mécanique, mais aussi pour tous les coups de main : Cédric, Jérémie, Lionel, Joël et Jean-Luc et Réto.
- Mary-Claude pour toute la gestion administrative et son soutien.
- Toutes les civilistes et étudiant de master avec qui j'ai pu travailler, sans vous on n'aurait jamais pu avancer autant : Christophe, Cyril, Loïc, Marc, Pengcheng, Raffael, Samuel M., Samuel et Virginien.
- L'équipe qui fait en sorte que l'on puisse travailler dans des locaux propres et un bâtiment qui fonctionne, je pense en particulier à Céleste, Cyril et Thierry.
- Fabio, Noël et ma belle-famille pour leur précieux soutien.
- Toutes les personnes déjà citées qui ont relu une partie de ma thèse, vos remarques constructives ont été très utiles.
- Mes parents et mes sœurs pour leurs encouragements et soutien continue depuis les débuts de ma vie.
- Mon épouse Florine, pour tous ce qu'elle m'apporte chaque jour, pour son soutien fidèle depuis le début et aussi de m'avoir supporté lors des moments un peu plus stressants.

Publications as first authors:

Riesen, Y.; Stuckelberger, M.; Haug, F.-J.; Ballif, C. & Wyrsh, N.
Temperature Dependence of Hydrogenated Amorphous Silicon Solar Cell Performances, *Journal of Applied Physics*, submitted

Riesen, Y.; Ballif, C. & Wyrsh, N.
Importance of PV forecast for an optimal management of grid connected PV systems with batteries in the presence of a feed-in limit, in preparation

Riesen, Y.; Stuckelberger, M.; Wyrsh, N. & Ballif, C.
Assessment of one-diode model with recombination term for modeling amorphous silicon solar cells long term performance in operating conditions, in preparation.

Riesen, Y.; G., N.; Catton, J.; Haug, F.-J.; Ballif, C. & Wyrsh, N.
Comparison of temperature dependence on performances of silicon based solar Cell, in preparation.

Riesen, Y.; Ding, P.; Monnier, S.; Wyrsh, N. & Ballif, C.
Peak Shaving Capability Of Household Grid-connected Pv-system With Local Storage: A Case Study *Proceedings of the 28th European Photovoltaic Solar Energy Conference, 2013*

Publications as co-author:

Wyrsh, N.; Riesen, Y.; Tschui, R.; Boillat, C. & Ballif, C.
Demand side management for enhanced integration of photovoltaics into grid
31th European Photovoltaic Solar Energy Conference, Hamburg, 2015, in print

Wyrsh, N.; Riesen, Y. & Tschui, R.
Flexibilisation de la consommation électrique des ménages
Bulletin Revue spécialisée des associations electro suisse et AES, 2015

Stuckelberger, M.; Riesen, Y.; Despeisse, M.; Schüttauf, J.-W.; Haug, F.-J. & Ballif, C.
Light-induced Voc increase and decrease in high-efficiency amorphous silicon solar cells
Journal of Applied Physics, 2014, 116, - [Link]

Stuckelberger, M.; Perruche, B.; Bonnet-Eymard, M.; Riesen, Y.; Despeisse, M.; Haug, F.-J. & Ballif, C.
Class AAA LED-Based Solar Simulator for Steady-State Measurements and Light Soaking
Photovoltaics, IEEE Journal of, 2014, 4, 1282-1287 [Link]

Wyrsh, N.; Riesen, Y.; Franco, A.; Dunand, S.; Kind, H.; Schneider, S. & Ballif, C.
Amorphous silicon based betavoltaic devices
MRS Proceedings, Cambridge Univ Press, 2013, 1536, mrs13--1536

Wyrsh, N.; Riesen, Y. & Ballif, C.
Effect of the Fluctuations of PV Production and Electricity Demand on the PV Electricity Self-Consumption
Proceedings of the 28th European Photovoltaic Solar Energy Conference and Exhibition, p. 4322 - 4324, 2013

Stuckelberger, M.; Despeisse, M.; Bugnon, G.; Schuettauf, J.-W.; Haug, F.-J. & Ballif, C.
Comparison of amorphous silicon absorber materials: Light-induced degradation and solar cell efficiency
Journal of Applied Physics, 2013, 114, - [Link]

Stuckelberger, M.; Riesen, Y.; Perruche, B.; Despeisse, M.; Wyrsh, N. & Ballif, C.
Charge collection in amorphous silicon solar cells: Cell analysis and simulation of high-efficiency pin devices

Journal of Non-Crystalline Solids, Elsevier, **2012**, 358, 2187-2189

Franco, A.; Riesen, Y.; Wyrsh, N.; Dunand, S.; Powolny, F.; Jarron, P. & Ballif, C.

Amorphous silicon-based microchannel plates

Nuclear Instruments and Methods in Physics Research Section A: Accelerators, Spectrometers, Detectors and Associated Equipment, Elsevier, **2012**, 695, 74-77

Franco, A.; Riesen, Y.; Despeisse, M.; Wyrsh, N. & Ballif, C.

High Spatial Resolution of Thin-Film-on-ASiC Particle Detectors

IEEE Transactions on Nuclear Science, IEEE-INST ELECTRICAL ELECTRONICS ENGINEERS, **2012**, 59, 2614-2621

Wyrsh, N.; Franco, A.; Riesen, Y.; Despeisse, M.; Dunand, S.; Powolny, F.; Jarron, P. & Ballif, C.

Amorphous silicon based particle detectors

MRS Proceedings, Cambridge Univ Press, **2011**, 1321, mrss11-1321-a13-06

Presentations

Oral presentation at the 28th EUPVSEC in Paris 2013: Peak Shaving Capability Of Household Grid-connected Pv-system With Local Storage: A Case Study

Poster presentation at the 29th EUPVSEC in Amsterdam 2014, Is PV forecast needed for an optimal control management for grid connected PV systems with batteries?

Poster presentation at the at 11^e *Symposium photovoltaïque national 2013* "PV Systems with Local Storage for Mass Integration into Electricity Networks presented "

Poster presentation at the *International Workshop on Modeling of Thin Film Silicon Solar Cells* , 2012. Simulation of Spectral Effects on the Energy Yield of Micromorph Thin-film Silicon Solar Modules.

Yannick S. RIESEN

Grand-Rue 174
2720 Tramelan
Switzerland

yannick.riesen@gmail.com

29 years old
Swiss
Married

Education

2010-present	École polytechnique fédérale de Lausanne (EPFL) : PhD candidate in Materials Science
2004-2010	Eidgenössische Technische Hochschule Zürich (ETHZ): BSc and MSc ETH in Physics
2001-2004	Gymnase Français de Bienne : Matura
Computer skills	Igor pro, LabView, Matlab, LaTeX, MS Office suite and ASA: good knowledge C/C++, Arduino, Inventor, Python, MySQL, PHP and Linux: basic knowledge
Language skills	French / Swiss German: mother tongue German / English: fluent

Experience

2011-2015	PhD candidate at PV-LAB, EPFL: “Energy Yield and Electricity Management of Thin-Film and Crystalline Silicon Solar Cells: from Devices to Systems”: <ul style="list-style-type: none">- Solar cell characterisation- Responsible of several sun simulators, wrote many LabView and Igor programs for data acquisition, characterisation and measurements. Solved several calibration issues- Partial set up and maintenance of an outdoor PV monitoring station (pyranometers, temperature sensors, I(V))- Configuration, commissioning and debugging of a household battery storage system- Datamining and database experience gained from analysis of monitoring station and several hundred of household smart meter results- Supervised several master students and civilist working on different projects- Teaching assistant for the lecture “Opto- and Microelectronic materials”- Performing solid state physics simulation (ASA, Casino) and system level simulations
2010-2011	Service civil and internship at PV-LAB, EPFL: Setup of an EBIC (Electron Beam Induced Current) technique for thin film silicon cells and particle detectors.
2008	Master thesis, ETHZ: “Analysis of spin polarized current in non-magnetic metals”: Elaboration and measurement of samples in ultra-high vacuum and developing analysis tools in Matlab and Labview.
2007-2008	Semester thesis at CERN for the Institute for Particle Physics, ETHZ
2008-2009	Teaching assistant for “Analysis I for Chemist”, ETHZ
2009-2010	Intermittent teaching of mathematics and physics at high school level: Gymnase français de Bienne, EMSp Moutier and Haute École Arc de Gestion in Delémont

Scientific contribution

I co-authored 10 scientific journal contributions included 1 as first author; further articles are in the publication process. I took part to 4 international conferences, gave 1 presentations and presented several posters.

Miscellaneous

I co-organised several summer camps and week-end for children and teenager. I like outdoor activities as hiking, cross-country skiing and biking.